3D and 4D printed meta-biomaterials for bone tissue engineering

Yarali, E.

DOI
10.4233/uuid:99ffee1f-ab8d-41c7-8b98-07165d5788b6

Publication date
2025

Document Version
Final published version

Citation (APA)
Yarali, E. (2025). *3D and 4D printed meta-biomaterials for bone tissue engineering*. [Dissertation (TU Delft), Delft University of Technology]. https://doi.org/10.4233/uuid:99ffee1f-ab8d-41c7-8b98-07165d5788b6

3D and 4D printed meta-biomaterials for bone tissue engineering

Ebrahim Yarali

3D and 4D printed meta-biomaterials for bone tissue engineering

3D and 4D printed meta-biomaterials for bone tissue engineering

Dissertation

for the purpose of obtaining the degree of doctor

at Delft University of Technology,

by the authority of the Rector Magnificus prof. dr. ir. T.H.J.J. van der Hagen,

chair of the Board of Doctorates,

to be defended publicly on

Thursday 24 April 2025 at 12:30 o' clock

by

Ebrahim YARALI

This dissertation has been approved by the promotors.

Composition of the doctoral committee:

Rector magnificus,	chairperson
Prof. dr. A.A. Zadpoor,	Delft University of Technology, promotor
Dr. A. Accardo,	Delft University of Technology, copromotor
Dr. M.J. Mirzaali Mazandarani,	Delft University of Technology, copromotor

Independent members:

Prof. dr. H.E.J. Vegeer,	Delft University of Technology,
Prof. dr. J. Moran Mirabal,	McMaster University, Canada,
Prof. dr. G.J.V.M. van Osch,	Delft University of Technology/ Erasmus Medical Center,
Prof. dr. ir. H.H. Weinans,	Delft University of Technology,

Other member:

Dr. J. Zhou,	Delft University of Technology,

The research leading to these results was funded by the ME cohesion granted awarded by Dr. M.J. Mirzaali Mazandarani and Dr. A. Accardo.

Keywords: Meta-biomaterials; mechanobiology; Poisson's ratio; micro-fabrication; two-photon polymerization; 4D bioprinting

Cover illustration: Mahdi Ghezelseflo
Printed by: Gildeprint (https://www.gildeprint.nl/)

ISBN 978-94-6496-389-2
An electronic version of this dissertation is available at http://repository.tudelft.nl/

Summary

A complex interplay of material, mechanical, and biological factors governs the performance of bone implants and scaffolds. Key determinants include surface functionalization, Young's modulus of the base material (*e.g.,* metals, or polymers), morphometric properties (*e.g.,* curvature, porosity), mechanical features (*e.g.,* effective elastic modulus, and Poisson's ratio, defined as the negative ratio of transverse strain to longitudinal strain), and mass transport parameters (*e.g.,* permeability). All these properties are often designed to enhance osseointegration significantly within the context of both bone replacement and regeneration. Regarding Poisson's ratio, auxeticity (*i.e.,* negative values of Poisson's ratio) is a distinct property of trabecular bone, which assumes a high relevance for implant design.

To address these challenges, meta-biomaterials offer a unique opportunity to tune all the above-mentioned properties, enhancing the rate of tissue regeneration. These designer materials derive their effective properties mainly from their engineered microarchitecture rather than solely from their material composition. This has led to the development of meta-implants, a new generation of bone implants that exhibit rare or unprecedented functionalities. Conventional solid hip joint implants are mainly under mechanical bending, and due to their design, a physical gap may be created between the surrounding bone and the implant in such conventional implants. Under such circumstances, the particles released from the bearing surfaces may enter the gap and trigger an inflammatory response, replacing the bone tissue with fibrous tissue around the implant, a process known as osteolysis. On the other hand, meta-implants minimize the risk of such physical gaps between the surrounding bone and implants, thereby reducing the risk of implant loosening.

While the next generation of "*hip meta-implants*" addresses this issue by using auxeticity to minimize the risk of gaps forming, a fundamental challenge remains: "*How can the effects of auxeticity on cell and tissue response be studied in isolation from many intrinsically coupled properties of meta-biomaterials (e.g., elastic/shear moduli, porosity, pore size, permeability)?"* This question forms the core of my dissertation, which focuses on decoupling Poisson's ratio from interdependent scaffold properties to achieve tunable auxetic behavior while preserving structural and functional integrity. Beyond structural design, understanding how Poisson's ratio influences bone cell mechanobiology is vital for ensuring meta-implants promote healthy tissue regeneration. This leads to a key sub-question: "H*ow does Poisson's ratio affect bone cell response in meta-biomaterials?*" Exploring this extends the research into the biological implications of meta-biomaterials.

Addressing these challenges demands an interdisciplinary approach, including *i.* mechanical design to isolate Poisson's ratio from all other scaffold properties, *ii.*

additive manufacturing (AM) of meta-biomaterials and their mechanical characterizations, *iii.* bone cell culture of meta-biomaterials and their cellular assessments, and *iv.* creating shape-morphing meta-biomaterials via 4D bioprinting for prospective dynamic cell culture studies.

After the introductory **Chapter 1**, we review auxeticity as a mechanobiological tool to create meta-biomaterials in **Chapter 2**. More specifically, we focus on the effects of Poisson's ratio (negative to positive values) on the (bone) cell responses. We also briefly discuss how Poisson's ratio can influence the cell response in meta-biomaterials under dynamic conditions.

In **Chapter 3**, we report on the development of 3D meta-biomaterials featuring Poisson's ratios within the range of -0.74 and +0.74. The Poisson's ratio of these meta-biomaterials is nearly isolated from other parameters, including porosity, pore size, and effective elastic modulus. The 3D meta-biomaterials featuring complicated microarchitectures are additively manufactured using two-photon polymerization (2PP). We also characterize their mechanical properties at the microscale under compression loading. The meta-biomaterials are seeded with murine preosteoblast cells using *in vitro* cell culture models to assess their interaction with cells. Meta-biomaterials with positive Poisson's ratios (PPRs) resulted in higher metabolic activity and larger cell-induced deformations than those with negative values. We also study the osteogenic differentiation of the preosteoblast cells seeded on the meta-biomaterials using Runx2 immunofluorescence staining and matrix mineralization (*i.e.,* Alizarin red staining) assays. The outcome indicate that the meta-biomaterials provide an environment for the preosteoblast cells to differentiate, showing the significant potential impact of 3D meta-biomaterials in engineering the bone tissue. However, the main drawback of the study in this Chapter was the partial isolation of the Poisson's ratio.

In the subsequent research in **Chapter 4**, we improved the isolation of the Poisson's ratio using a systematic multi-objective design approach. This Chapter focuses on computational modeling and design of meta-biomaterials with extensive simulations to isolate the Poisson's ratio as much as possible. We introduce non-stochastic unit cells featuring reduced anisotropy with three orthotropic planes of symmetry, making isolation of Poisson's ratio less challenging. To explore the design space of our meta-biomaterials, we explicitly establish the required geometrical relationships and thus generated 43,000 number of designs. The generated meta-biomaterials are simulated using a numerical homogenization method based on a 3D voxelization approach. We successfully isolate the Poisson's ratio from other mechanical properties (*i.e.,* effective elastic and shear moduli and anisotropy level), morphological properties (*i.e.,* relative density, pore size, tortuosity, surface-to-volume ratio, and connectivity) and mass transport parameters (*i.e.,* permeability) with an average deviation below 9% using a multi-objective optimization technique. The 3D meta-biomaterials are selectively

fabricated using PolyJet 3D printing and 2PP techniques at the macro- and microscales, respectively. We also characterize their mechanical properties by measuring their effective elastic modulus, to validate the predictions of our computational models.

Chapter 5 focuses on the dynamic aspect of this research project, namely, 4D bioprinting in biomedical applications, particularly in bone tissue engineering. This is because meta-implants and meta-biomaterials are under dynamic loading and deformation in cell culture environments. Therefore, in this chapter and Chapter 6, we aim to understand "*how does 4D printing create dynamic meta-biomaterials?*". Chapter 5 first provides the various types of smart (bio)materials, external stimuli, and mechanical design used in 4D bioprinting. Then, we critically review the biomedical applications of 4D printing and discuss biomedical research's future directions. These directions include *in vivo* tissue engineering, multi material implementations with reversible shape morphing, fast responses, micro scalability, remote activation, and the applications of multi-physics-based modeling and machine learning to predict the structure-property and design–shape morphing relationships of 4D (bio)printed constructs.

In **Chapter 6**, we take a step forward through 4D printing of dynamic microstructures, such as meta-biomaterials, via 2PP from a biocompatible poly(N-isopropylacrylamide), pNIPAM,-based hydrogel. Systematic studies were first performed to evaluate the correlation between the printing parameters (*i.e.,* laser power, scanning speed, and hatching angle) and the density of pNIPAM components (*i.e.,* monomer and crosslinker) in terms of shape morphing and printability. The thermomechanical properties of the hydrogels, including the elastic modulus, thermal expansion coefficients, and angular deflection, were also measured at different printing doses and activation temperatures. Based on these experimental characterizations, we developed a thermomechanical model to predict shape morphing in 4D printed soft microstructures under the applications of soft grippers, drug delivery systems, and meta-biomaterials.

Chapter 7 provides conclusions and recommendations regarding the promising avenues for future research. Our research has opened a new pathway in bone tissue engineering, particularly when developing meta-implants. We concluded that isolating Poisson's ratio from other mechanical, morphometric, and mass transport properties is possible. Second, the Poisson's ratio significantly affects the bone cell response, including metabolic activity, cell adhesion, cell morphology, and cell differentiation. Moreover, it is possible to create meta-biomaterials with shape-morphing capability such that their Poisson's ratio changes over time.

Samenvatting

Een complex samenspel van materiaal, mechanische en biologische factoren bepaalt de prestaties van botimplantaten en scaffolds. Belangrijke determinanten zijn onder meer oppervlaktefunctionaliteit, de Young-modulus van het basismateriaal (*bijv.,* metalen of polymeren), morfometrische eigenschappen (*bijv.* kromming, porositeit), mechanische kenmerken (*bijv.* effectieve elasticiteitsmodulus en Poisson's ratio, gedefinieerd als de negatieve verhouding van transversale rek tot longitudinale rek), en massatransportparameters (*bijv.*, permeabiliteit). Al deze eigenschappen zijn vaak ontworpen om osseointegratie significant te verbeteren in de context van zowel botvervanging als regeneratie. Wat de Poisson's ratio betreft, is auxeticiteit (*d.w.z.,* negatieve waarden van de Poisson's ratio) een kenmerkende eigenschap van trabeculair bot, die zeer relevant is voor het ontwerp van implantaten.

Om deze uitdagingen aan te pakken, bieden meta-biomaterialen een unieke kans om alle bovengenoemde eigenschappen af te stemmen, waardoor de snelheid van weefselregeneratie wordt verbeterd. Deze ontworpen materialen ontlenen hun effectieve eigenschappen voornamelijk aan hun ontworpen microarchitectuur in plaats van uitsluitend aan hun materiaalsamenstelling. Dit heeft geleid tot de ontwikkeling van meta-implantaten, een nieuwe generatie botimplantaten die zeldzame of ongekende functionaliteiten vertonen. Conventionele massieve heupgewricht implantaten staan voornamelijk onder mechanische buiging, en door hun ontwerp kan er een fysieke kloof ontstaan tussen het omliggende bot en het implantaat in dergelijke conventionele implantaten. Onder dergelijke omstandigheden kunnen de deeltjes die vrijkomen van de lage oppervlakken de kloof binnendringen en een ontstekingsreactie uitlokken, waarbij het botweefsel wordt vervangen door fibreus weefsel rond het implantaat, een proces dat bekend staat als osteolyse. Aan de andere kant minimaliseren meta-implantaten het risico op dergelijke fysieke kloven tussen het omliggende bot en de implantaten, waardoor het risico op losraken van het implantaat wordt verminderd.

Terwijl de volgende generatie "*heup meta-implantaten*" dit probleem aanpakt door auxeticiteit te gebruiken om het risico op het ontstaan van kloven te minimaliseren, blijft er een fundamentele uitdaging: "*Hoe kunnen de effecten van auxeticiteit op de cel- en weefselrespons worden bestudeerd in isolatie van de vele intrinsiek gekoppelde eigenschappen van meta-biomaterialen (bijv., elastische/schuifmoduli, porositeit, poriegrootte, permeabiliteit)?*" Deze vraag vormt de kern van mijn proefschrift, dat zich richt op het ontkoppelen van de Poisson's ratio van onderling afhankelijke scaffold-eigenschappen om instelbaar auxetisch gedrag te bereiken met behoud van structurele en functionele integriteit. Naast structureel ontwerp is het begrijpen hoe de Poisson ratio de mechanobiologie van botcellen beïnvloedt van vitaal belang om ervoor te zorgen dat meta-implantaten gezonde weefselregeneratie bevorderen. Dit leidt tot een belangrijke deelvraag: "*Hoe beïnvloedt de Poisson's ratio de respons van botcellen*

in meta-biomaterialen?" Het verkennen hiervan breidt het onderzoek uit naar de biologische implicaties van meta-biomaterialen.

Het aanpakken van deze uitdagingen vereist een interdisciplinaire benadering, waaronder: *i.* mechanisch ontwerp om 'de Poisson's ratio te isoleren van alle andere scaffold-eigenschappen, *ii.* additieve manufacturing (AM) van meta-biomaterialen en hun mechanische karakteriseringen, *iii.* botcelcultuur van meta-biomaterialen en hun cellulaire beoordelingen, *iv.* het creëren van vormveranderende meta-biomaterialen via 4D-bioprinten voor prospectieve dynamische celcultuurstudies.

Na het inleidende **Hoofdstuk 1** bespreken we in **Hoofdstuk 2** auxeticiteit als een mechanobiologisch tool om meta-biomaterialen te creëren. Meer specifiek richten we ons op de effecten van de Poisson's ratio (van negatieve tot positieve waarden) op de respons van (bot)cellen. We bespreken ook kort hoe de Poisson's ratio de celrespons in meta-biomaterialen onder dynamische omstandigheden kan beïnvloeden.

In **Hoofdstuk 3** rapporteren we over de ontwikkeling van 3D meta-biomaterialen met Poisson ratios in het bereik van -0,74 tot +0,74. De Poisson's ratio van deze meta-biomaterialen is bijna geïsoleerd van andere parameters, waaronder porositeit, poriegrootte en effectieve elasticiteitsmodulus. De 3D meta-biomaterialen met gecompliceerde microarchitecturen worden additief vervaardigd met behulp van two-photon polymerization (2PP). We karakteriseren ook hun mechanische eigenschappen op microschaal onder compressiebelasting. De meta-biomaterialen worden bezaaid met murine preosteoblast cellen met behulp van *in vitro* celcultuurmodellen om hun interactie met cellen te beoordelen. Meta-biomaterialen met positieve Poisson's ratios (PPRs) resulteerden in hogere metabole activiteit en grotere, door-cellen-veroorzaakte vervormingen dan die met negatieve waarden. We bestuderen ook de osteogene differentiatie van de preosteoblast cellen die op de meta-biomaterialen zijn gezaaid met behulp van Runx2 immunofluorescentie staining en matrix mineralisatie (*d.w.z.,* Alizarin red staining) assays. De uitkomsten geven aan dat de meta-biomaterialen een omgeving bieden voor de preosteoblast cellen om te differentiëren, wat de significante potentiële impact van 3D meta-biomaterialen aantoont in het engineeren van botweefsel. Echter, het belangrijkste nadeel van de studie in dit Hoofdstuk was de gedeeltelijke isolatie van de Poisson ratio.

In het daaropvolgende onderzoek in **Hoofdstuk 4** hebben we de isolatie van de Poisson's ratio verbeterd met behulp van een systematische multi-objectieve ontwerpaanpak. Dit hoofdstuk richt zich op computationele modellering en ontwerp van meta-biomaterialen met uitgebreide simulaties om de Poisson's ratio zo veel mogelijk te isoleren. We introduceren niet-stochastische eenheidscellen met verminderde anisotropie en drie orthotrope symmetrievlakken, waardoor de isolatie van de Poisson's ratio minder uitdagend wordt. Om de ontwerpruimte van onze meta-biomaterialen te verkennen, hebben we expliciet de vereiste geometrische relaties vastgesteld en zo 43,000 ontwerpen gegenereerd. De gegenereerde meta-biomaterialen worden gesimuleerd

met behulp van een numerieke homogenisatie methode gebaseerd op een 3D voxelization benadering. We isoleren succesvol de Poisson's ratio van andere mechanische eigenschappen (*d.w.z.,* effectieve elasticiteits- en schuifmoduli en anisotropie niveau), morfologische eigenschappen (d.w.z. relatieve dichtheid, poriegrootte, tortuositeit, oppervlak-tot-volume verhouding en connectiviteit) en massatransportparameters (*d.w.z.,* permeabiliteit) met een gemiddelde afwijking van minder dan 9% met behulp van een multi-objectieve optimalisatietechniek. De 3D meta-biomaterialen worden selectief vervaardigd met behulp van PolyJet 3D printen en 2PP technieken op respectievelijk macro- en microschaal. We karakteriseren ook hun mechanische eigenschappen door hun effectieve elasticiteitsmodulus te meten, om de voorspellingen van onze computationele modellen te valideren.

Hoofdstuk 5 richt zich op het dynamische aspect van dit onderzoeksproject, namelijk 4D bioprinten in biomedische toepassingen, met name in botweefsel engineering. Dit is omdat meta-implantaten en meta-biomaterialen onder dynamische belasting en vervorming staan in celcultuuromgevingen. Daarom streven we in dit hoofdstuk en Hoofdstuk 6 ernaar te begrijpen "*hoe creëert 4D printen dynamische meta-biomaterialen?*". Hoofdstuk 5 geeft eerst de verschillende soorten smart (bio)materialen, externe stimuli en mechanisch ontwerp die worden gebruikt in 4D bioprinten. Vervolgens beoordelen we kritisch de biomedische toepassingen van 4D printen en bespreken we de toekomstige richtingen van biomedisch onderzoek. Deze richtingen omvatten in vivo tissue engineering, multimateriaal implementaties met omkeerbare shape morphing, snelle respons, microschaalbaarheid, activering op afstand, en de toepassingen van multifysica modellering en machine learning om de structuur-eigenschap en ontwerp-vormverandering relaties van 4D (bio)geprinte constructen te voorspellen.

In **Hoofdstuk 6** zetten we een stap voorwaarts door 4D printen van dynamische microstructuren, zoals meta-biomaterialen, via 2PP van een biocompatibele poly(N-isopropylacrylamide), pNIPAM,-gebaseerde hydrogel. Systematische studies werden eerst uitgevoerd om de correlatie te evalueren tussen de printparameters (*d.w.z.,* laservermogen, scansnelheid en hatching angle) en de dichtheid van pNIPAM componenten (*d.w.z.,* monomeer en crosslinker) in termen van shape morphing en printbaarheid. De thermomechanische eigenschappen van de hydrogels, inclusief de elasticiteitsmodulus, thermische uitzettingscoëfficiënten en hoekafwijking, werden ook gemeten bij verschillende printdoses en activeringstemperaturen. Op basis van deze experimentele karakteriseringen hebben we een thermomechanisch model ontwikkeld om shape morphing in 4D-geprinte zachte microstructuren te voorspellen onder de toepassingen van soft grippers, drug delivery systems en meta-biomaterialen.

Hoofdstuk 7 biedt conclusies en aanbevelingen met betrekking tot de veelbelovende wegen voor toekomstig onderzoek. Ons onderzoek heeft een nieuwe weg geopend in botweefsel engineering, met name bij het ontwikkelen van meta-implantaten. We

concludeerden dat het isoleren van de Poisson's ratio van andere mechanische, morfometrische en massatransporteigenschappen mogelijk is. Ten tweede beïnvloedt de Poisson's ratio significant de respons van botcellen, inclusief metabole activiteit, celadhesie, celmorfologie en celdifferentiatie. Bovendien is het mogelijk om meta-biomaterialen te creëren met shape-morphing capaciteit zodanig dat hun Poisson's ratio in de loop van de tijd verandert.

Table of contents

List of abbreviations (alphabetical order)

2PP - Two-photon polymerization
.gwl - General writing language
.stl - Standard triangle language
AAm-AAc - Acrylamide-acrylic acid
ABS - Acrylonitrile butadiene styrene
AFM - Atomic force microscopy
ALP - Alkaline phosphatase
AM - Additive manufacturing
α-MEM - Alpha minimum essential medium
BMSC - Bone marrow stromal cell
BSA - Bovine serum albumin
CAD - Computer-aided design
CNT - Carbon nanotube
Cu - Copper
DEA - Dielectric elastomer actuator
DE - Dielectric elastomer
DiLL - Dip-in laser lithography
DLP - Digital light processing
DLW - Direct laser writing
DIW - Direct inkjet writing
DOD - Drop-on-demand
EBM - Electron beam melting
ECM - Extracellular matrix
EG - Ethylene glycol
ESC - Embryonic stem cell
FDM - Fused deposition modeling
FEM - Finite element modeling
GelMA - Gelatin methacryloyl
hUVEC - Human umbilical vein endothelial cell
hiPSC - Human induced pluripotent stem cell
HLP - High laser power
IPA - Isopropyl alcohol
LCD - Liquid crystal display
LAP - Lithium phenyl(2,4,6-trimethylbenzoyl)phosphinate
LCEs - Liquid crystalline elastomers
LCST - Lower critical solution temperature
LCP - Liquid crystal polymer
LDH - Lumbar disc herniation
LLP - Low laser power
MAP - Magneto-active polymer

Mbis - N, N-methylenebis(acrylamide)
MEW - Melt electro writing
MN - Micro-needle
MRI - Magnetic resonance imaging
MRE - Magnetorheological elastomer
MRP - Magnetorheological plastomer
MSC - Mesenchymal stem cell
MTT - 3-[4,5-dimethylthiazol-2-yl]-2,5-diphenyl tetrazolium bromide
NPR - Negative Poisson's ratio
NdFeB - Neodymium–iron–boron
NiTi - Nickel-titanium
PBS - Phosphate buffered saline
PCL - Polycaprolactone
PDMS - Polydimethylsiloxane
PEG - Polyethylene glycol
PEGDA - Poly(ethylene glycol) diacrylate
PGDA - Poly(glycerol dodecanoate) acrylate
PGMEA - Propylene glycol monomethyl ether acetate
PLA - Poly-lactic acid
PLMC - Poly(D, L-lactide-co-trimethylene carbonate)
PMMA - Polymethyl methacrylate
PPR - Positive Poisson's ratio
PTFE - Polytetrafluoroethylene
PU - Polyurethane
pNIPAM - Poly(N-isopropylacrylamide)
SLA - Stereolithography
SLM - Selective laser melting
SLS - Selective laser sintering
SMC - Shape memory ceramic
SMA - Shape memory alloy
SME - Shape memory effect
SMP - Shape memory polymer
SOEA - Soybean oil epoxidized acrylate
SD - Standard deviation
TPU - Thermoplastic PU
ZPR - Zero Poisson's ratio
ZrO_2 - Zircon

1

Introduction

"We shall not cease from exploration
and the end of all our exploring
will be to arrive where we started
and know the place for the first time."

Little Gidding, T.S. Eliot

1.1 Background

Orthopedic implants, particularly those used in hip replacements, may suffer from inflammatory responses, osteolysis, and poor osseointegration, especially in older patients, leading to bone-implant interface failures [1]. This challenge stems from the fact that traditional solid or porous implants fail to match the mechanical properties (*e.g.,* elastic modulus) of native bone tissue as well as suboptimal bone-implant interface conditions. Over time, these factors may lead to aseptic loosening and require further surgeries [2]. Moreover, traditional implants are not tailored to individual patients. Therefore, there is no guarantee that they will perform optimally for every patient [3]. Finally, they might be costly and time-consuming in fabrication [3]. As a result, there is a growing need for advanced implant designs that better facilitate osseointegration, ultimately enhancing patients' recovery and quality of life.

One promising way to enhance osseointegration in bone implants, besides biochemical processes, such as coating, is to design implants replicating the microstructural features of (trabecular) bone. These features include fundamental mechanical properties (*e.g.,* effective elastic modulus and loading characteristics), morphometric aspects (*e.g.,* porosity, pore shapes, and surface-to-volume ratios), mass transport properties (*e.g.,* permeability), and design strategies (*e.g.,* combining various unit cell geometries) [4] (Figure 1). Meta-biomaterials are well-suited for this purpose as they offer a wide range of properties, from mechanical to mass transport. These materials can exhibit unique behaviors, such as an NPR (or auxeticity), where they thicken when stretched. Such properties arise from their underlying microstructures and can be adjusted through geometrical design [5].

Research has shown that combining auxetic and non-auxetic meta-biomaterials in the design of bone implants, so-called "*meta-implants*", can improve mechanical fixation, cellular proliferation, and bone cell differentiation more effectively than traditional implants [1] (Figure 1). This is mainly because, in conventional implants, a physical gap may develop between the surrounding bone and the implants under bending [5]. Therefore, the particles released from load-bearing articulating surfaces, such as the acetabular cup and the femoral head, can reach the gap and cause inflammatory infections, particularly osteolysis [5].

To further support the benefits of meta-implants, it is important to assess their cellular interactions with bone cells *in vitro* at the microscale. This is particularly critical given the limited availability of donor tissues and the goal of reducing animal use in experimental studies. As meta-implants are made of different unit cells (*e.g.,* honeycomb or re-entrant microarchitectures), understanding how these unit cell shapes influence cellular response and mechanobiology is important. Particularly, if we consider Poisson's ratio as a key representation of the pore shape, it is still not fully clear how Poisson's ratio regulates the bone cells' fate, despite current studies. For this purpose,

isolating biophysical cues is a critical but challenging task. That is because desired properties often conflict and are interrelated. To elucidate the effects of Poisson's ratio on mechanobiology, we need to isolate Poisson's ratio from other mechanical, morphometric, and mass transport properties. While there are some studies where the effect of Poisson's ratio or pore shapes have been elucidated in meta-biomaterials, they are mainly limited to 2D meta-biomaterials [6, 7] and neglect the importance of isolating Poisson's ratio from other properties [8, 9].

These cellular responses can be examined either under static conditions, where meta-biomaterials are immersed in a physiological medium, or under dynamic conditions using a bioreactor to simulate material deformation or in a microfluidic system with a circulated medium [2]. Most of the research in this field has been done on (bone cells) in a static condition. However, the main drawback is that the pore shape changes under mechanical loading, and therefore, we need to elucidate the effect of Poisson's ratio on mechanobiology under dynamic mechanical loading. Second, the cellular microenvironment is dynamic, which may cause meta-biomaterials to deform. Therefore, the dynamic response of meta-biomaterials should be studied too. Under static conditions, research has demonstrated that auxeticity in meta-biomaterials can enhance osseointegration and cell differentiation [9-11]. Studies have specifically examined the effects of auxetic behavior in promoting bone integration, with auxetic materials outperforming their non-auxetic counterparts. To fabricate dynamic meta-biomaterials for studying the effect of Poisson's ratio on cell response under dynamic cell culture, one promising technique is 4D printing. 4D printing technology integrates time into 3D printing technologies by employing stimuli-responsive (or smart) materials. Meta-biomaterials can, thus, tune their function or shape upon exposure to external stimulus, such as heat or magnetic field [12].

Multiple steps need to be followed to clarify the effects of Poisson's ratio on the mechanobiological responses of meta-biomaterials (Figure 1). *i.* the rational design of meta-biomaterials with isolated Poisson's ratio; *ii.* AM of the designed meta-biomaterials at both micro- and macroscale, particularly via 2PP, *iii.* mechanical characterization of the fabricated meta-biomaterials and comparing experimental observations with computational results; *iv.* Cell culture of the meta-biomaterials with bone cells (*e.g.*, preosteoblasts) under static conditions and their cellular assessments; *v.* 4D printing of meta-biomaterials with dynamic shape morphing and studying their mechanobiological response under dynamic conditions for the future.

1.2 Rational design of meta-biomaterials

There are several techniques to design 3D meta-biomaterials and disentangle their properties rationally. However, each method has pros and cons, and a technique can be chosen depending on the application. For instance, a conventional way is to use direct finite element modeling (FEM) [13], which is a commonly employed method to

predict the mechanical behavior of complex meta-biomaterials, allowing for the evaluation of stress-strain relationships and mechanical properties, such as Poisson's ratio under different loading conditions. This technique mainly uses solid elements, which may not be very efficient regarding simulation time, but it offers more highly accurate data. In this technique, the isolation process is based on trials and errors; therefore, few properties can be tuned [14].

On the other hand, there are techniques, such as homogenization-based FEM [15], in which the simulation time is much lower. The homogenization technique efficiently calculates the elastic properties of heterogenous structures with microarchitectures at the macroscopic level. This technique assumes a perfect bonding between void and solid materials or multiple materials) [16, 17]. The asymptotic homogenization method computes the macroscopic elasticity tensor by integrating the locally varying elasticity tensor, strain field, and prescribed strain field. This approach yields a governing elasticity equation, where the effective elasticity tensor is determined numerically. FEM discretization is applied to solve the equation and obtain the global displacement fields.

Topology optimization is another powerful computational tool for designing meta-biomaterials to optimize the internal structure of materials for specific mechanical and biological functions [18]. By systematically distributing material within a given design space, this technique enables the creation of structures with desired properties, such as tailored Poisson's ratio, effective elastic modulus, and porosity. In tissue engineering, topology optimization helps develop porous architectures that enhance cell proliferation, nutrient transport, and osseointegration by controlling pore size, shape, and connectivity. For example, optimizing scaffold geometry in bone tissue engineering enhanced load-bearing capacity and improved the mimicry of natural bone's mechanical properties [19]. This technique also allows the design of auxetic structures, improving their mechanical adaptability and interaction with surrounding tissues.

Machine learning [20, 21] and multi-objective optimizations [22] are other efficient techniques for isolating Poisson's ratio from all other properties. However, in these techniques, many data points are required beforehand to train the machine or optimize the results. For instance, in a recent study, a machine learning-based approach was employed to design 2D random-network meta-biomaterials with desired mechanical properties (*i.e.,* effective elastic modulus and Poisson's ratio) as inputs [21]. The machine learning model used in that study was trained based on the beams-based FEM data with a very efficient simulation time.

1.3 3D printing of meta-biomaterials

The advancements in 3D printing technology combined with the ever-increasing demand for miniaturization across industries have supercharged the development of micro 3D and 4D printing technologies. Various AM techniques exist to create meta-

biomaterials at different scales, from 2PP to FDM or PolyJet 3D printing [23]. However, one main criterion that the selection of the fabrication technique must meet is the biocompatibility or non-cytotoxicity of the materials, as these meta-biomaterials are used in the context of cell mechanobiology studies and must not hamper the immune system, induce cell mortality, or trigger inflammatory processes. Another criterion is the Young's modulus of the base material. In bone tissue engineering, as the Young's modulus of bone is in the GPa range [24], a biomaterial with a Young's modulus of at least a few GPa is required.

In this dissertation, we aimed to elucidate the cellular interaction with meta-biomaterials by 3D printing them at the microscale. 2PP is one promising AM technique for fabricating complex 3D structures at the microscale.

1.3.1 Two-photon polymerization

Two-photon polymerization is a versatile 3D printing technique used for the fabrication of dynamic structures both at the micro and nanoscale [25]. Unlike conventional light-based photopolymerization techniques that involve the absorption of a single photon to initiate photopolymerization, this novel micro-fabrication technique involves the simultaneous absorption of two near-infrared photons (*i.e.,* two-photon absorption [26]) in a photosensitive material called the photoresist [27]. In this technique, a tightly focused femtosecond pulsated near-infrared (780 nm) laser beam provides the photons that trigger the polymerization process. Ti: sapphire lasers are widely preferred for inducing two-photon absorption as they can produce ultrahigh peak power with a very short pulse width of approximately 100 femtoseconds. In addition to the above, the central wavelength of Ti: sapphire lasers is about 800 nm, roughly equal to half the wavelength of UV photopolymerization. This enables simple control of the threshold energy for polymerization and results in high spatial resolution of the printed structure [28].

In two-photon absorption, two photons are simultaneously absorbed by a photosensitive resin [29]. In single photon absorption, upon illumination of the laser light to a photo-sensitive material, a photon will be absorbed if its energy level is higher or equal to the band gap between the excited electronic state and the ground state. In two-photon absorption, two NIR-photons are simultaneously absorbed so that at the focal point, the absorbed energy is equivalent to that of one UV-photon. The photocurable resin used in 2PP is a liquid-state resin transparent to NIR light but very absorptive in the UV range. In the two-photon absorption process, the photoresist is only polymerized in the desired voxel, and the rest of the resin is not affected by the laser beam. This is one of the primary reasons that enables the 2PP process to create intricate nanostructures with excellent spatial resolution. Generally, a photoresist consists of four main components: the monomer, photoinitiator, cross-linker, and base solvent [30]. The relative proportions of each of these components determine the properties of the structure

printed. Upon exposure to the femtosecond laser, rapid polymerization of the photoresist occurs through three stages. The first stage involves the formation of a radical, which leads to the initiation of chain formation and its propagation (second stage). There is a point during the polymerization process where two radically active polymer chains combine to form a single chain, thus resulting in chain termination (third stage) [31].

1.4 Poisson's ratio and mechanobiology

The effect of Poisson's ratio on mechanobiology has mainly been investigated in 2D [6, 7, 11, 32]. In 2D meta-biomaterials, however, the cells cannot sense 3D unit cell shapes, which can influence cell fate. For instance, in a recent study, three different 2D meta-biomaterials with different pore shapes, including bowtie, brickstone, and honeycomb, representing NPR, ZPR, and PPR, were 2PP fabricated [6]. As the effective elastic modulus of the meta-biomaterials was in the kPa range; therefore, cells could deform them. Such a design was proposed to elucidate the mechanotransductory mechanisms involved in the interactions of mesenchymal stem cells (MSCs) and meta-biomaterials in 2D by converting the cell-induced displacements to forces. In another study, it was concluded that NPR meta-biomaterials provide a better environment for MSCs in terms of cell growth but also affect MSC proliferation and chondrogenic induction [11].

On the other hand, there are only a few studies on the effects of Poisson's ratio on cell response in 3D [8, 9, 33]. These 3D meta-biomaterials provide a better understanding of how cells interact with pores with different shapes. The study showed how cells crawl inside or on the unit cells of the 3D meta-biomaterials, depending on the scale [8]. In another study, three parameters, including Poisson's ratio, effective elastic modulus, and pore size, were considered in the design of meta-biomaterials. The expansion and neural differentiation of pluripotent stem cells on 3D meta-biomaterials with Poisson's ratios ranging from 0 to -0.45 were investigated. They benchmarked the response to their meta-biomaterials with that of regular scaffolds with a Poisson's ratio of +0.30 [9]. It was shown that the auxetic scaffolds promoted the formation of smaller cell aggregate and enhanced the expression of the neuronal marker β-tubulin III upon neural differentiation.

1.5 4D printing of dynamic meta-biomaterials

Incorporating shape-morphing capabilities into 3D printing technology, known as 4D printing, has opened up new solution spaces across research and allowed for the fabrication of structures that are nearly impossible to create using conventional fabrication techniques. Shape morphing in 4D printed structures is initiated when they are exposed to certain external stimuli, including high temperatures, light, moisture, electric or magnetic fields, and a change in pH [12]. The development of smart drug delivery

systems in biomedicine, micro-grippers, and micro-actuators in soft robotics are examples of the promising applications of 4D printing. In biomedical engineering, 4D bioprinting is mainly based on four pillars [12]. *i*. rational mechanical design, *ii*. biocompatibility and stimuli-sensitivity of the material, iii. 3D printing, and *iv*. stimulation setup and configuration. The rational control over these four pillars creates biomedical devices with controlled shape-morphing capabilities, which are also compatible with the body. For instance, considering temperature-responsive biomaterials, they must operate within body temperatures (*i.e.,* 37 °C), such as pNIPAM [34-36]. However, many other materials (*e.g.,* poly-lactic acid (PLA) with a high glass transition temperature [37]) or stimuli are incompatible with the body.

Widely used 4D printing techniques include fused deposition modeling (FDM), stereolithography (SLA), digital light processing (DLP), direct inkjet writing (DIW), selective laser sintering (SLS), electron beam melting (EBM), and 2PP [12]. The selection of the type of 3D printing technology depends on various factors, such as fabrication throughput, accuracy, length scale, mechanical properties of the base material, biocompatibility of the base material, and the suitability of the 3D printing technique [384]. For example, DIW is a promising method in which the cell can be directly added to inks to 3D print relatively large-scale, dynamic tissue-engineered constructs [39].

For fabricating dynamic 3D microstructures, 2PP is a great candidate due to its precision and wide range of biocompatible photoresists [40-43]. In biomedicine, 2PP 4D printing at a microscale has allowed for the development of micro-swimmers capable of acting as drug delivery agents and assisting in the plasmonic heating of cancer cells [44]. The fabrication of micro-grippers and micro-actuators via 2PP 4D printing has also opened new doors for soft robotics applications at the microscale. Geometry also plays a significant role in determining the shape-morphing capabilities of the printed structure. In this regard, mechanical metamaterials, whose properties can be tuned by altering their micro-architectures, have been used to develop structures that exhibit complex shape-morphing characteristics not found in nature. Mechanical metamaterials' unique properties include negative thermal expansion coefficients, negative compressibility, negative stiffness, and auxeticity [45, 46].

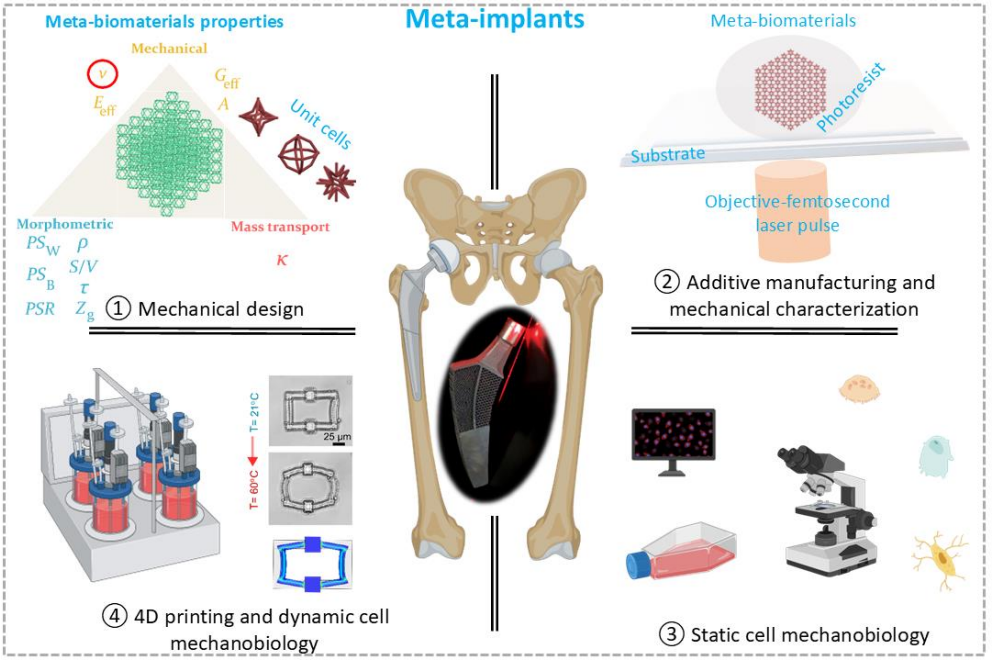

Figure 1. *A schematic illustrating the overall objectives of this dissertation, which is based on four interdisciplinary pillars:* ***i.*** *Mechanical design, in which Poisson's ratio is isolated from all other mechanical, morphometric, and mass transport properties.* ***ii.*** *Additive manufacturing and mechanical characterization of meta-biomaterials.* ***3.*** *Bone cell culture of meta-biomaterials and their mechanobiological assessments.* ***4.*** *4D printing and dynamic cell mechanobiology of meta-biomaterials. Note that the meta-implant image was reproduced from [1].*

1.6 Dissertation aim and outline

This dissertation contains seven chapters addressing the challenges associated with the design of 3D meta-biomaterials with isolated properties, their additive manufacturing, and their bone cellular responses. This fundamental challenge was categorized into two conditions: static and dynamic. Although we mainly focused on the bone cellular response and Poisson's ratio in meta-biomaterials under static conditions, we also provided a solution to create dynamic meta-biomaterials via 4D printing. To tackle these challenges, we had to answer the following sub-questions:

What is the state of the art about the influence of Poisson's ratio on cellular responses in tissue engineering applications?

Chapter 2 presents a literature study on the relationship between mechanobiology and meta-biomaterials. We focus on auxeticity and the effects of Poisson's ratio on the cell response in terms of cell growth, cell differentiation, and focal adhesions. We also briefly review how Poisson's ratio and mechanobiology interact in a dynamic environment. We conclude that a deeper understanding of the isolation of Poisson's ratio

in meta-biomaterials is required to assess its effect on the mechanobiology of cells in tissue engineering.

What are the effects of Poisson's ratio on the preosteoblast cell response in terms of cell growth, metabolic activity, and differentiation?

In the research presented in **Chapter 3**, we report on the development of five different 2PP 3D-printed meta-biomaterials with nearly isolated Poisson's ratio. We conclude that 3D meta-biomaterials with PPRs exhibit higher metabolic activity, cell proliferation, and cell-induced deformation compared to those with NPRs. However, the isolation was not optimal, and therefore, we aimed to fully isolate Poisson's ratio from many other properties, including mechanical, morphometric, and mass transport properties, which led us to Chapter 4.

Is it mechanically possible to isolate Poisson's ratio from most other mechanical, morphometric, and mass transport properties?

In **Chapter 4**, we provide a powerful computational method to isolate Poisson's ratio from many other properties, including elastic modulus, shear modulus, Poisson's ratio, Zener ratio (*i.e.,* mechanical anisotropy level), porosity, pore size, tortuosity, surface-to-volume ratio, connectivity, and permeability. We employ a homogenization-based FEM-based method with a relatively fast response time (< 1 min) to generate 43,000 simulations. We finally isolate the Poisson's ratio via multi-objective optimization method while keeping all other properties as constant as possible with a deviation of less than 9%. As it was unclear how 4D (bio)printing can be used for tissue engineering applications, we also provide a literature review on the biomedical applications of 4D bioprinting. This helps us better understand dynamic microenvironments and how cells react to them.

What are the biomedical applications of 4D printing?

In **Chapter 5**, we review 4D printing and its biomedical applications. It includes biomedical devices, such as stents, implants, occluders, drug delivery systems, and wound healing applications. This review article provides a deeper knowledge of the dynamic behavior of biomedical matters, which led to the following chapter.

Can we 4D print meta-biomaterials at small scales?

In the research presented in **Chapter 6**, we develop a temperature-responsive hydrogel, pNIPAM, with a working temperature around body temperature. The hydrogel can be 3D printed at the microscale via 2PP for soft robotics applications, drug delivery systems, and dynamic meta-biomaterials. We also develop a computational model to predict the shape morphing in the abovementioned applications. The final chapter of this dissertation (**Chapter 7**) discusses the results of the previous chapters and suggests some directions for future research.

Bibliography

[1] H.M. Kolken, S. Janbaz, S.M. Leeflang, K. Lietaert, H.H. Weinans, A.A. Zadpoor, Rationally designed meta-implants: a combination of auxetic and conventional meta-biomaterials, Mater. Horiz. 5(1) (2018) 28-35.
[2] E. Yarali, A.A. Zadpoor, U. Staufer, A. Accardo, M.J. Mirzaali, Auxeticity as a mechanobiological tool to create meta-biomaterials, ACS Applied Bio Materials 6(7) (2023) 2562-2575.
[3] J. Jiao, Q. Hong, D. Zhang, M. Wang, H. Tang, J. Yang, X. Qu, B. Yue, Influence of porosity on osteogenesis, bone growth, and osteointegration in trabecular tantalum scaffolds fabricated by additive manufacturing, Frontiers in Bioengineering and Biotechnology 11 (2023) 1117954.
[4] R. Oftadeh, M. Perez-Viloria, J.C. Villa-Camacho, A. Vaziri, A. Nazarian, Biomechanics and mechanobiology of trabecular bone: a review, Journal of biomechanical engineering 137(1) (2015) 010802.
[5] A.A. Zadpoor, Meta-biomaterials, Biomaterials science 8(1) (2020) 18-38.
[6] N. Munding, M. Fladung, Y. Chen, M. Hippler, A.D. Ho, M. Wegener, M. Bastmeyer, M. Tanaka, Bio-Metamaterials for Mechano-Regulation of Mesenchymal Stem Cells, Advanced Functional Materials (2023) 2301133.
[7] Y. Jin, C. Xie, Q. Gao, X. Zhou, G. Li, J. Du, Y.J.M. He, Design, Fabrication of multi-scale and tunable auxetic scaffolds for tissue engineering, 197 (2021) 109277.
[8] G. Flamourakis, I. Spanos, Z. Vangelatos, P. Manganas, L. Papadimitriou, C. Grigoropoulos, A. Ranella, M. Farsari, Laser-made 3D Auxetic Metamaterial Scaffolds for Tissue Engineering Applications, Macromol Mater Eng 305(7) (2020) 2000238.
[9] Y. Yan, Y. Li, L. Song, C. Zeng, Pluripotent stem cell expansion and neural differentiation in 3-D scaffolds of tunable Poisson's ratio, Acta Biomater. 49 (2017) 192-203.
[10] H.J. Choi, J.J. Lee, J.B. Lee, H.-J. Sung, J.-W. Shin, J.W. Shin, Y. Wu, J.K.J.B.r. Kim, MG-63 cells proliferation following various types of mechanical stimulation on cells by auxetic hybrid scaffolds, 20(1) (2016) 1-8.
[11] A. Tang, J. Ji, J. Li, W. Liu, J. Wang, Q. Sun, Q. Li, Nanocellulose/PEGDA Aerogels with Tunable Poisson's Ratio Fabricated by Stereolithography for Mouse Bone Marrow Mesenchymal Stem Cell Culture, Nanomater. 11(3) (2021) 603.
[12] E. Yarali, M.J. Mirzaali, A. Ghalayaniesfahani, A. Accardo, P.J. Diaz-Payno, A.A. Zadpoor, 4D printing for Biomedical Applications, Advanced Materials (2024) 2402301.
[13] M.J. Mirzaali, H. Pahlavani, E. Yarali, A. Zadpoor, Non-affinity in multi-material mechanical metamaterials, Scientific reports 10(1) (2020) 11488.
[14] E. Yarali, M. Klimopoulou, K. David, P.E. Boukany, U. Staufer, L.E. Fratila-Apachitei, A.A. Zadpoor, A. Accardo, M.J. Mirzaali, Bone cell response to additively manufactured 3D micro-architectures with controlled Poisson's ratio: auxetic vs. non-auxetic meta-biomaterials, Acta Biomaterialia 177 (2024) 228-242.
[15] T. Tancogne-Dejean, D. Mohr, Elastically-isotropic truss lattice materials of reduced plastic anisotropy, International Journal of Solids and Structures 138 (2018) 24-39.
[16] E. Andreassen, C.S. Andreasen, How to determine composite material properties using numerical homogenization, Computational Materials Science 83 (2014) 488-495.
[17] G. Dong, Y. Tang, Y.F. Zhao, A 149 line homogenization code for three-dimensional cellular materials written in matlab, Journal of Engineering Materials and Technology 141(1) (2019) 011005.
[18] Z. Li, Z. Luo, L.-C. Zhang, C.-H. Wang, Topological design of pentamode lattice metamaterials using a ground structure method, Materials & Design 202 (2021) 109523.
[19] A.H. Foroughi, M.J. Razavi, Shape optimization of orthopedic porous scaffolds to enhance mechanical performance, Journal of the Mechanical Behavior of Biomedical Materials 128 (2022) 105098.
[20] S. Kumar, S. Tan, L. Zheng, D.M. Kochmann, Inverse-designed spinodoid metamaterials, npj Computational Materials 6(1) (2020) 73.

[21] H. Pahlavani, K. Tsifoutis-Kazolis, M.C. Saldivar, P. Mody, J. Zhou, M.J. Mirzaali, A.A. Zadpoor, Deep Learning for Size-Agnostic Inverse Design of Random-Network 3D Printed Mechanical Metamaterials, Advanced Materials 36(6) (2024) 2303481.
[22] T. Meier, R. Li, S. Mavrikos, B. Blankenship, Z. Vangelatos, M.E. Yildizdag, C.P. Grigoropoulos, Obtaining auxetic and isotropic metamaterials in counterintuitive design spaces: an automated optimization approach and experimental characterization, npj Computational Materials 10(1) (2024) 3.
[23] M. Askari, D.A. Hutchins, P.J. Thomas, L. Astolfi, R.L. Watson, M. Abdi, M. Ricci, S. Laureti, L. Nie, S. Freear, Additive manufacturing of metamaterials: A review, Additive Manufacturing 36 (2020) 101562.
[24] D. Wu, P. Isaksson, S.J. Ferguson, C. Persson, Young's modulus of trabecular bone at the tissue level: A review, Acta biomaterialia 78 (2018) 1-12.
[25] H. Wang, W. Zhang, D. Ladika, H. Yu, D. Gailevičius, H. Wang, C.F. Pan, P.N.S. Nair, Y. Ke, T. Mori, Two-photon polymerization lithography for optics and photonics: fundamentals, materials, technologies, and applications, Advanced Functional Materials 33(39) (2023) 2214211.
[26] A.K. Nguyen, R.J. Narayan, Two-photon polymerization for biological applications, Materials Today 20(6) (2017) 314-322.
[27] X. Jing, H. Fu, B. Yu, M. Sun, L. Wang, Two-photon polymerization for 3D biomedical scaffolds: Overview and updates, Frontiers in bioengineering and biotechnology 10 (2022) 994355.
[28] S. Maruo, S. Kawata, Two-photon-absorbed near-infrared photopolymerization for three-dimensional microfabrication, Journal of microelectromechanical systems 7(4) (1998) 411-415.
[29] E.D. Lemma, B. Spagnolo, M. De Vittorio, F. Pisanello, Studying cell mechanobiology in 3D: the two-photon lithography approach, Trends in biotechnology 37(4) (2019) 358-372.
[30] R. Infuehr, N. Pucher, C. Heller, H. Lichtenegger, R. Liska, V. Schmidt, L. Kuna, A. Haase, J. Stampfl, Functional polymers by two-photon 3D lithography, Applied Surface Science 254(4) (2007) 836-840.
[31] M. Hippler, 3D Laser Lithography of Stimuli-Responsive Hydrogels, Dissertation, Karlsruhe, Karlsruher Institut für Technologie (KIT), 2020, 2020.
[32] M. Kapnisi, C. Mansfield, C. Marijon, A.G. Guex, F. Perbellini, I. Bardi, E.J. Humphrey, J.L. Puetzer, D. Mawad, D.C.J.A.f.m. Koutsogeorgis, Auxetic cardiac patches with tunable mechanical and conductive properties toward treating myocardial infarction, 28(21) (2018) 1800618.
[33] N.C. Paxton, R. Daley, D.P. Forrestal, M.C. Allenby, M.A.J.M. Woodruff, Design, Auxetic tubular scaffolds via melt electrowriting, 193 (2020) 108787.
[34] L. Chen, M. Liu, L. Lin, T. Zhang, J. Ma, Y. Song, L. Jiang, Thermal-responsive hydrogel surface: tunable wettability and adhesion to oil at the water/solid interface, Soft Matter 6(12) (2010) 2708-2712.
[35] N. Lopez-Larrea, S. Wustoni, M.I. Peñas, J. Uribe, A. Dominguez-Alfaro, A. Gallastegui, S. Inal, D. Mecerreyes, PNIPAM/PEDOT: PSS Hydrogels for Multifunctional Organic Electrochemical Transistors, Advanced Functional Materials (2024) 2403708.
[36] J. Liu, L. Jiang, S. He, J. Zhang, W. Shao, Recent progress in PNIPAM-based multi-responsive actuators: A mini-review, Chemical Engineering Journal 433 (2022) 133496.
[37] M. Mehrpouya, H. Vahabi, S. Janbaz, A. Darafsheh, T.R. Mazur, S. Ramakrishna, 4D printing of shape memory polylactic acid (PLA), Polymer 230 (2021) 124080.
[38] E. Yarali, M. Baniasadi, A. Zolfagharian, M. Chavoshi, F. Arefi, M. Hossain, A. Bastola, M. Ansari, A. Foyouzat, A. Dabbagh, Magneto-/electro-responsive polymers toward manufacturing, characterization, and biomedical/soft robotic applications, Applied Materials Today 26 (2022) 101306.
[39] P.J. Díaz-Payno, M. Kalogeropoulou, I. Muntz, E. Kingma, N. Kops, M. D'Este, G.H. Koenderink, L.E. Fratila-Apachitei, G.J. van Osch, A.A.J.A.H.M. Zadpoor, Swelling-Dependent Shape-Based Transformation of a Human Mesenchymal Stromal Cells-Laden 4D Bioprinted Construct for Cartilage Tissue Engineering, (2022) 2201891.
[40] S. Peng, X. Lei, S. Sun, Y. Zhu, J. Qiu, H. Yang, Magnetic-Driven Micro-Gear Pair Fabricated by Femtosecond Laser Writing, Advanced Engineering Materials 26(10) (2024) 2301960.

[41] L. Tan, Y. Yang, L. Fang, D.J. Cappelleri, Shape-Programmable Adaptive Multi-Material Microswimmers for Biomedical Applications, Advanced Functional Materials (2024) 2401876.
[42] Y. Zhang, H. Yu, X. Zhang, J. Zheng, J. Wang, H. Guo, Y. Qiu, X. Wang, L. Liu, W.J. Li, A Novel Multifunctional Material for Constructing 3D Multi-Response Structures Using Programmable Two-Photon Laser Fabrication, Advanced Functional Materials (2024) 2313922.
[43] J. Zheng, H. Yu, Y. Zhang, J. Wang, H. Guo, H. Luo, X. Wang, Y. Qiu, L. Liu, W.J. Li, 4D Printed Soft Microactuator for Particle Manipulation via Surrounding Medium Variation, Small (2024) 2311951.
[44] C.A. Spiegel, M. Hippler, A. Münchinger, M. Bastmeyer, C. Barner-Kowollik, M. Wegener, E. Blasco, 4D printing at the microscale, Advanced Functional Materials 30(26) (2020) 1907615.
[45] M.J. Mirzaali, A. Ghorbani, K. Nakatani, M. Nouri-Goushki, N. Tümer, S.J. Callens, S. Janbaz, A. Accardo, J. Bico, M. Habibi, Curvature Induced by Deflection in Thick Meta-Plates, Advanced materials 33(30) (2021) 2008082.
[46] Q. Ji, J. Moughames, X. Chen, G. Fang, J.J. Huaroto, V. Laude, J.A.I. Martínez, G. Ulliac, C. Clévy, P.J.C.M. Lutz, 4D Thermomechanical metamaterials for soft microrobotics, 2(1) (2021) 1-6.

2

Auxeticity as a mechanobiological tool to create meta-biomaterials

Yarali, E., Zadpoor, A. A., Staufer, U., Accardo, A., & Mirzaali, M. J. (2023). Auxeticity as a mechanobiological tool to create meta-biomaterials. *ACS Applied Bio Materials*, 6(7), 2562-2575.

Mechanical and morphological design parameters, such as stiffness or porosity, play important roles in creating orthopedic implants and bone substitutes. However, we have only a limited understanding of how the microarchitecture of porous scaffolds contributes to bone regeneration. Meta-biomaterials are increasingly used to precisely engineer the internal geometry of porous scaffolds and independently tailor their mechanical properties (*e.g.,* stiffness and Poisson's ratio). This is motivated by the rare or unprecedented properties of meta-biomaterials, such as auxeticity). It is, however, not clear how these unusual properties can modulate the interactions of meta-biomaterials with living cells and whether they can facilitate bone tissue engineering under static and dynamic cell culture and mechanical loading conditions. Here, we review the recent studies investigating the effects of the Poisson's ratio on the performance of meta-biomaterials with an emphasis on the relevant mechanobiological aspects. We also highlight the state-of-the-art additive manufacturing techniques employed to create meta-biomaterials, particularly at the micrometer scale. Finally, we provide future perspectives, particularly for the design of the next generation of meta-biomaterials featuring dynamic properties (*e.g.,* those made through 4D printing).

2.1 Introduction

3D lattice structures have been widely studied for the design of orthopedic implants that are used for complex bone reconstructions. The success of designing these porous implants relies on several factors, including the mechanical properties of the constituting materials (*e.g.,* stiffness), their geometrical features at the micro-scale (*e.g.,* pore geometry), and their local surface characteristics [1]. All these design factors must be considered simultaneously to adequately mimic (micro-)environment of the (bony) tissue and facilitate the tissue integration process (*i.e.,* osseointegration).

"Stress-shielding" may occur at the bone-implant interfaces if the mechanical properties of the implanted biomaterial (*e.g.,* metal- or ceramic-based materials characterized by high stiffness) do not match those of the host tissue particularly when the implant is stiffer than the surrounding tissue, causing the local deformations of the surrounding tissue to be smaller than they would naturally be. According to the Wolff's law, this phenomenon can result in bone resorption and, eventually, aseptic loosening [2].

From a microstructural viewpoint, implants and scaffolds need to be porous for several reasons: *i.* to effectively mimic the morphology of the bone [3]; *ii.* to facilitate mass transport within the scaffolds/implants, enabling the delivery of nutrients and oxygen to the cells residing in the scaffolds [4]; and *iii.* to replicate the stiffness of the native bone which ranges between 0.2 and 20 GPa [5].

The response of bone cells to biomaterials (*e.g.,* cell adhesion, proliferation, and differentiation) is influenced by the geometry of such porous structures, including pore

shape, pore size, porosity, (local) surface curvatures, and surface nano-patterning. The effects of some of the geometrical parameters, such as porosity [6], surface curvature [7], and surface nano-patterning [8], on the one hand and those of the elastic modulus [9] on the other hand have been extensively studied. However, the effects of some other design parameters, including the Poisson's ratio, on the bone regeneration process in general and bone cell response in particular remain elusive. Any such effects can result either from the mechanical behavior associated with auxeticity or be a direct consequence of the specific shape of the unit cells used for creating auxetic behavior in such architected biomaterials (*e.g.,* the re-entrant unit cell). In both cases, mechanobiological pathways are expected to be responsible for regulating the effects of auxeticity on the bone regeneration process.

To gain a better understanding of how various geometrical and mechanical factors influence the cell response and bone tissue regeneration process, it is important to separate the various effects from each other as much as possible and study them in isolation. One effective approach for tuning, controlling, and decoupling mechanical and morphological properties is the use of a class of engineered architected materials known as mechanical meta-materials. The distinct, unusual properties of these materials at the meso-scale originate from their (geometrical) design at the microscale [2, 10-13]. Among the unusual properties of mechanical meta-materials is auxeticity. Due to their microarchitectural designs, such as the geometry of their unit cells, mechanical metamaterials with NPR expand transversely when stretched longitudinally. In biomedical applications, biocompatible materials can be employed to create multi-physics metamaterials, which are defined as meta-biomaterials [2, 14, 15]. To rationally design meta-biomaterials with controlled mechanical and morphological properties, as well as adequate mechanical strength, various methods, such as (topology) optimization, [11] artificial intelligence (*e.g.,* machine learning) [16,17], analytical models, [18] and finite element analyses [19], have been employed, depending on the specific requirements of the application at hand. These techniques utilize mathematical algorithms to optimize the material's configuration, predict its mechanical properties, and stimulate its behavior under different loading conditions. Combining these methods provides a robust approach to design advanced meta-biomaterials tailored to meet diverse biomedical needs.

Interestingly, auxetic behavior has been frequently observed in biological materials, including hard tissues [20], soft tissues [21], and cells [22], highlighting its importance as a mechanobiological design tool for creating biomimetic meta-biomaterials. Recent studies have also shown that auxeticity in meta-biomaterials can modulate cell differentiation and proliferation [23-26], and may guide the alignment, orientation, and migration of cells (*e.g.,* fibroblast) [24]. Moreover, the rational design of the microarchitecture of meta-biomaterials can enhance the mechanical fixation and longevity of meta-biomaterial-based implants as compared to their conventional counterparts

[27]. On one hand, meta-biomaterials offer a wide range of tunable properties, from mechanical (*e.g.,* stiffness) and geometrical parameters (*e.g.,* porosity) to mass transport properties. On the other hands, these properties are entangled, and it is very challenging to decouple them for studying the individual effects of a specific parameter on the biological response. This gap in the literature underscores the need for further research to assess the true effects of auxeticity on cell response at different length scales.

Furthermore, since the geometry of the unit-cell in meta-biomaterials changes under (mechanical) loading conditions, a better understanding of the role of auxeticity in interactions with living cells is required. This understanding will significantly contribute to the design of meta-biomaterials and their ability to facilitate tissue regeneration. We have, therefore, dedicated a section of this paper to the mechanobiological studies of meta-biomaterials in dynamic cell microenvironments.

This article reviews the currently existing evidence regarding the ways auxetic behavior influences the performance of biomaterials. We critically discuss the potential of auxeticity as a design tool for the development of the next generation of meta-biomaterials and summarize the recent literature on the consequences of (non-)auxetic behavior on the responses of living cells. To this end, we propose novel design approaches and testing methods to incorporate the effects of the Poisson's ratio into the design of meta-biomaterials for future research. Furthermore, we review advanced additive manufacturing and 4D printing techniques that can be used for creating meta-biomaterials with time-dependent properties.

2.2 Auxeticity in biological materials

Auxeticity is found in soft tissues, hard tissues, organs, and cells. Examples of hard tissues exhibiting NPR include trabecular bone [20] and the annulus fibrosus of the intervertebral disc [25, 28, 29]. Soft tissues showing auxetic behavior include cat skin [30], salamander skin, [31] arterial endothelium [32, 33] (under both wall shear stresses and cyclic circumferential strain induced by blood flow), cow teat skin [34], arteries [33, 35], and tendons [21]. In addition, some evidence of auxetic behavior has been found in living cells, such as embryonic epithelia [36, 37] and the nuclei of embryonic stem cells [22].

To measure the auxetic behavior of these biological materials, different techniques, such as imaging, computational modeling, and *in vitro* mechanical testing, have been employed. For example, the auxetic behavior of trabecular bone has been studied by performing *in vitro* experiments on the human tibia under triaxial compressive loading. The auxeticity in the spongy parts of such bones has been demonstrated by calculating the material constants of a transversely isotropic model via computational models [200]. It should, however, be noted that the values of the Poisson's ratio

in biological materials may depend on the level of the applied strains or the aspect ratios of the tested tissue specimens. For example, in cow teat skin, NPR is only reported for specimens with a specific range of length to width ratios (*i.e.,* 1.4-2.45) and under certain levels (35%) of applied strains [34]. *In vivo* and *ex vivo* experiments have been performed on tendon specimens taken from several species, such as human peroneus brevis, human Achilles tendons, and deep flexor tendons (pig and sheep) to study their auxetic behavior (Figures 1a-c) [21]. The Poisson's ratio has been measured using non-destructive medical imaging techniques (*e.g.,* magnetic resonance imaging (MRI)) for *in vivo* conditions and mechanical testing for *ex vivo* [21] conditions (Figure 1c). Regarding the auxeticity in the nuclei of embryonic stem cells during the differentiation process [22], it has been found that the cross-section of the nuclei contracts under compressive loading [22]. Moreover, the stiffness of the nuclei has been found to increase under compressive loading [22] (Figures 1d and e). These observations have been verified using fluorescent optical microscopy and scanning electron microscopy (SEM), as well as by measuring local forces using atomic force microscopy (AFM) [22].

There are also studies employing auxeticity in the design and implementation of medical devices. For example, in *ex vivo* studies, auxetic cardiac patches have been used to mimic the native heart movements against myocardial infraction (Figure 1f) [9]. Furthermore, an auxetic meta-biomaterial has been successfully implemented for the treatment of lumbar disc herniation (LDH) in an *in vivo* rabbit model (Figure 1g) [38]. Further review of such studies is, however, beyond the scope of this review article, as we will be only focusing on the *in vitro* mechanobiological behaviour of meta-biomaterials.

There are several biological substances with nearly zero Poisson's ratio (ZPR). These materials, therefore, exhibit no to little contraction or expansion when subjected to compression or tension. Examples of these biological materials are cartilage, cornea, and brain [39,40]. Poisson's ratio-driven meta-biomaterial designs (*i.e.,* auxetic, zero, or non-auxetic) may, therefore, help in mimicking the properties of native tissues and facilitate the regeneration of tissues *in vitro* [23-25, 41], *ex vivo* [9], and *in vivo* [38].

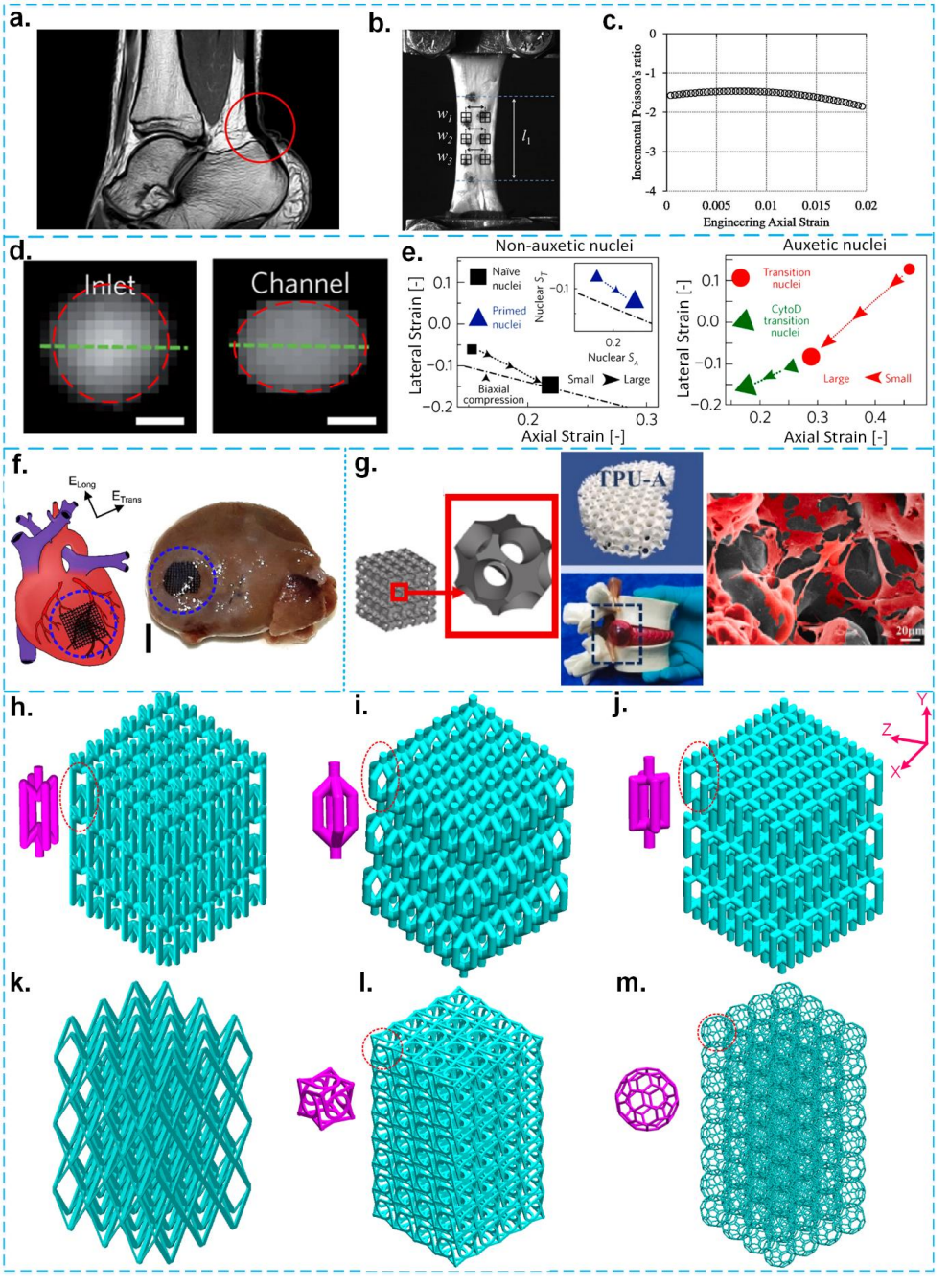

Figure 1. ***a-c.*** *Tendon is an example of a soft tissue showing auxetic behavior. Adapted with permission from ref [21]. Copyright 2015 Elsevier.* ***a.*** *Some MRI images of the human tendon.* ***b.*** *This has been observed in an MRI image of the human tendon that expands under stretching in vivo.* ***c.*** *Some ex vivo results of the uniaxial testing of the human Achilles tendon showing the dependency of the Poisson's ratio on the applied axial strain.* ***d-e.*** *Auxeticity in the nuclei of embryonic stem cells. Adapted with permission from ref [22].*

Copyright 2014 Springer Nature; ***d.*** *Epifluorescence images of a cross-section of the nuclei of a cell before and after entering a microfluidic channel. e. The variation of the lateral strain (i.e., S_T) with the axial strain (i.e., S_A) for both non-auxetic and auxetic nuclei. f. A schematic drawing of an auxetic patch and a representative image of the auxetic patch implemented in a rat after two weeks [9]; the scale bar shows 2 mm.* ***g.*** *The in vivo implementation of an auxetic surface-based meta-scaffold into the LDH of a rabbit [38].* ***g.*** *(left) A schematic drawing of the NPR meta-biomaterial and its constituting unit-cell; (middle) testing the mechanical performance of the NPR meta-biomaterial using a commercially available LDH model; (right) the SEM image of nucleus pulposus cells when adhered to an NPR meta-biomaterial.* ***h-m.*** *Some examples of strut-based meta-biomaterials with* ***h.*** *NPR,* ***i.*** *PPR,* ***j.*** *nearly ZPR, and* ***k.*** *transversely isotropic properties. Reproduced with permission from ref [63]. Copyright 2020 Elsevier,* ***l.*** *Chiral metamaterials (bending-dominated), and* ***m.*** *isotropic buckyball meta-biomaterial.*

2.3 Auxeticity in bone tissue engineering

2.3.1 Poisson's ratio-driven mechanotransduction

The microenvironment experienced by cells is an important factor in bone tissue engineering. Geometry (*e.g.,* surface curvature, pore shape), surface characteristics (roughness, cell-friendly coating), and the cell culture conditions (*i.e.,* static or dynamic) are among the factors determining the microenvironment of cells. They affect cell-cell and cell-extracellular matrix (ECM) interactions, the plasma membrane, the cytoskeleton, and nuclear components through integrin-mediated force-feedback at adhesion sites [7, 42-44]. Cells are constantly exposed to various mechanical stimulations, both extracellular and intracellular, and can respond to changes in these forces through mechanotransductory pathways. These pathways involve the conversion of mechanical signals into biochemical signals that regulate cell behavior [7, 44, 45]. This conversion is mediated by a range of specialized proteins and molecules, including integrins, focal adhesions (vinculin, paxillin), cytoskeletal elements, and signaling molecules. These components work together to orchestrate the formation of complex networks that can activate or inhibit various cellular pathways [7, 46].

Mechanoreceptors, such as integrins, initiate mechano-sensation through physical bonding between the bone cells and loading via the ECM. The connection between mechanotransduction and cellular responses can be studied via both biological assays and computational tools [47]. While there are numerous studies examining these processes in 2D environments, the mechanotransductory mechanisms associated with 3D meta-biomaterials remains largely elusive [48].

Mechanical cues modulate the remodeling rate of the bony tissue and influence its regeneration [42]. Cellular processes, such as adhesion, proliferation, differentiation, and gene expression are, therefore, affected by mechanical forces, in addition to biophysical cues, such as geometry and substrate stiffness. The above-mentioned microenvironmental factors can change the mechanical forces (*e.g.,* stretching, compressive, and shear flow) that can alter the mechanobiology of cells [42] (*e.g.,* bone cells [49],

epithelial cells [50]) through changes in the magnitude or rate of the loads experienced by the cells. For example, bone cells respond to compressive forces and produce biochemical cues, such as prostaglandin, that lead to the formation of new tissue through interactions between biomechanical and biochemical cues [42, 49]. Moreover, it has been shown that auxeticity plays an important role in how mechanotransductory events affect stem cells [22, 26, 51, 52]. Although there has been limited research exploring the role of the Poisson's ratio in mechanotransduction, a recent study has examined its impact on the focal adhesion of embryonic fibroblasts using immunological staining of vinculin. [52] The study compares two different 2D meta-biomaterials with PPR and NPR and finds that both structures exhibit similar patterns of integrin marker expression, indicating that the Poisson's ratio may not significantly impact integrin-mediated adhesions in 2D environments [52]. However, further studies are needed to fully understand how the Poisson's ratio and other mechanical properties of 3D meta-biomaterials affect mechanotransduction and cell behavior.

Understanding the interplay between mechanical properties and cellular behavior is crucial for the development of advanced meta-biomaterials with tailored properties for use in various biomedical applications. Further research in this area could inform the design of these materials and improve their performance in tissue engineering and regenerative medicine.

The rational design of microarchitectures of meta-biomaterials will, thus, allow for tuning the local deformations developed in meta-biomaterials in response to globally applied deformations and enable the on-demand generation of mechanotransductory cues for controlling bone modelling or remodeling processes. The links between physical cues (*e.g.,* materials properties, stiffness) [53], surface (bio-)functionalization [54], and geometry (*e.g.,* curvature [7]) on one hand and biochemical signaling of cells on the other have been extensively studied. Hence, we only focus on the role of auxeticity in the mechanobiological response of meta-biomaterials, particularly for bone tissue engineering purposes.

2.3.2 Meta-biomaterials and their interactions with living cells

The emergence of meta-biomaterials has provided unparalleled opportunities in expanding the design space of biomedical devices. Meta-biomaterials pave the way for establishing optimal architecture-property-functionality relationships so that multifunctional biomedical devices (*e.g.,* orthopedics implants) can be developed.

Mechanical metamaterials are composed of several building blocks or unit cells that can be arranged in an ordered or disordered manner. This makes their effective properties different from those of the base materials from which they are made and directly links them to the design of their microarchitecture. Examples of these unusual properties are ultra-stiff, ultra-lightweight (*i.e.,* the ratio of the elastic modulus to

density) [55], sequential shape-change [56], negative compressibility [57], and NPR (or auxeticity) [58] in which the effective shear modulus is larger than the bulk modulus [59]. Here, we only focus on the auxetic behavior of meta-biomaterials and discuss the methodologies proposed in the past for tuning this specific property.

The rational design of the microarchitectures of meta-biomaterials is the first step in adjusting their auxetic behaviors. In this regard, meta-biomaterials can be divided into two main categories, namely strut-based and sheet-based meta-biomaterials. Although the Poisson's ratio can be tuned from negative to positive in sheet-based meta-biomaterials too [60], there is currently limited information available regarding the interaction of sheet-based auxetic meta-biomaterials with living cells [38]. We will, therefore, focus on strut-based meta-biomaterials and their mechanobiological responses. Moreover, cell culture conditions may play an important role in determining the response of cells to auxetic meta-biomaterials. Therefore, in the following sections, we provide an overview of the response of cells to strut-based meta-biomaterials under both static and dynamic cell culture conditions.

2.3.3 Meta-biomaterials under static conditions

From the viewpoint of mechanical properties, strut-based meta-biomaterials can be divided into two main sub-categories, namely stretch-dominated and bending-dominated [59]. The parameter that determines whether a lattice structure is bending-dominated or stretch-dominated is the Maxwell number which is related to the average number of struts connecting to a specific node [61,62]. In general, the higher the degree of connectivity, the higher the mechanical properties of the structure. From a lateral deformation viewpoint, however, the range of the Poisson's ratio is wider in bending-dominated structures than in stretch-dominated structures. As such, the effects of auxeticity are more central in bending-dominated lattice structures. Figure 1h-m shows several examples of strut-based meta-biomaterials with different properties (*e.g.,* a wide spread of Poisson's ratios from negative to positive values). In such meta-biomaterials, the Poisson's ratio depends on the angle between the struts, the width and height of the unit cells, and the aspect ratio of the struts. The Poisson's ratio of meta-biomaterials can, therefore, be adjusted within the thermodynamically admissible range of the Poisson's ratio for isotropic materials (*i.e.,* -1 to 0.5). Covering such a broad range of Poisson's ratios is impossible within the realm of conventional materials. Moreover, the Poisson's ratio of strut-based meta-biomaterials can be tuned to be either different or the same in various directions. For example, the Poisson's ratio in two specific planes *zy* and *xy* (*i.e.,* v_{xy} and v_{zy}) can be designed to be equal (Figures 1h-j). In the meta-biomaterial depicted in Figure 1k, however, the Poisson's ratios are different in different directions, as this transversely isotropic meta-biomaterial exhibits an NPR in one plane and a PPR in another plane [63]. Living cells may, therefore,

experience different Poisson's ratios or different (global or local) deformation regimes in different planes when interacting with such architected biomaterials.

There are several *in vitro* studies in the literature studying the mechanobiological properties of strut-based meta-biomaterials (either in 2D or 3D) with different Poisson's ratios using different cell types (*e.g.,* fibroblasts, osteoblasts, chondrocytes, and myoblasts) [23, 26, 35, 52, 64]. From the mechanical design viewpoint, however, the effects of the Poisson's ratio are often coupled with those of microarchitectural design and mechanical properties (*e.g.,* stiffness, pore size, porosity, and strut thickness). Given the fact that these properties are inter-related, changing the Poisson's ratio without affecting the other parameters is extremely challenging [26, 64]. There is, therefore, not much evidence yet as to what the isolated effects of auxetic behavior are on cell response, making it difficult to determine whether auxetic materials are superior to non-auxetic biomaterials (*i.e.,* structures with a PPR or a ZPR) in terms of cell differentiation and proliferation.

In addition to the shape of individual unit cells, the dimensions of unit cells play an important role in determining the biological response of meta-biomaterials. There is always a trade-off between the size of living biological cells and the feature size of the meta-biomaterial (*e.g.,* pore size). If the pore size of the meta-biomaterial is significantly smaller than the size of a single cell, the cell growth inside such a microscale meta-biomaterial may be compromised [25]. This is due to potential disturbance in mass transport. In meso-scale meta-biomaterials, however, the feature size of the lattice structure can be larger than the size of a single living cell (*e.g.,* 1000 μm > pore size > 100 μm), allowing cells to easily penetrate into the internal pores of the lattice structure. In such cases, the auxetic behavior can influence cell adhesion, cell proliferation, and cell differentiation. [24] Moreover, in both micro- and meso-scale meta-biomaterials, cell alignment and migration can be influenced by auxeticity [24].

As the mechanical properties of 2D, 2.5D, and 3D lattice structures are different, various mechanobiological responses can be expected. In 2D meta-biomaterials, for example, the in-plane properties are more dominant than the out-of-plane properties. These properties can be employed, for instance, to dominate the auxetic behavior of the lattice structure in one direction [65] or to create hybrid meta-biomaterials [66] by rationally combining unit cells with opposite values (*i.e.,* negative and positive values) of the Poisson's ratio (Figure 2a).

Meta-biomaterials have been assessed for their cytocompatibility. For example, Figures 2b [65] and 2c [66] show the adhesion and viability of fibroblast cells and the viability of human MSCs in contact with meta-biomaterials. Other interactions with cells, such as gene expression, cell morphology, or cell migration are not extensively studied as of yet.

Our knowledge of the role of the Poisson's ratio in guiding cell mechanobiology and cell responses when interacting with meta-biomaterials is limited to a few studies. One example is a study in which three different 2D meta-biomaterials with NPR, ZPR, and PPR were designed and tested in the presence of mouse bone marrow MSCs [23] (Figure 2d, top images). However, other geometrical and mechanical properties at the macro-scale (≥ cm) were not constant in that study. For example, there was a difference of 310 kPa in the compressive elastic modulus of the PPR (2.63 MPa) and NPR (2.94 MPa) meta-biomaterials. Nevertheless, it was argued that the Poisson's ratio influences the proliferation and differentiation of mouse bone marrow MSCs [23] (Figure 2d, bottom images). Moreover, it was reported that NPR meta-biomaterials exhibit a superior performance as compared to their PPR and ZPR counterparts in terms of cell proliferation and cell differentiation [23]. More specifically, the most viable stem cells were observed in the NPR scaffolds, followed by those residing in ZPR structures, while the smallest number of cells were found in the PPR specimens. The proliferation assay 3-[4,5-dimethylthiazol-2-yl]-2,5-diphenyl tetrazolium bromide (MTT) showed that the proliferation was higher in the NPR meta-biomaterials on days 1, 3, and 5. It was observed that NPR meta-biomaterials promote the differentiation of mBMMSCs into chondrocytes, as evidenced by the expressions of proteoglycans and chondrocyte stromal glycosaminoglycan markers [23]. Moreover, stem cells could penetrate through the structures, as shown by a cell viability assay imaged by confocal laser scanning microscopy (Figure 2d, bottom images). It is, however, unclear whether the differences between NPR meta-biomaterials and other experimental groups were due to the difference between their Poisson's ratios or are caused by dissimilarities in the stiffnesses and/or porosity of the meta-biomaterials with different Poisson's ratios or by the fact that NPR scaffold may better mimic the native soft tissue (*i.e.,* cartilage).

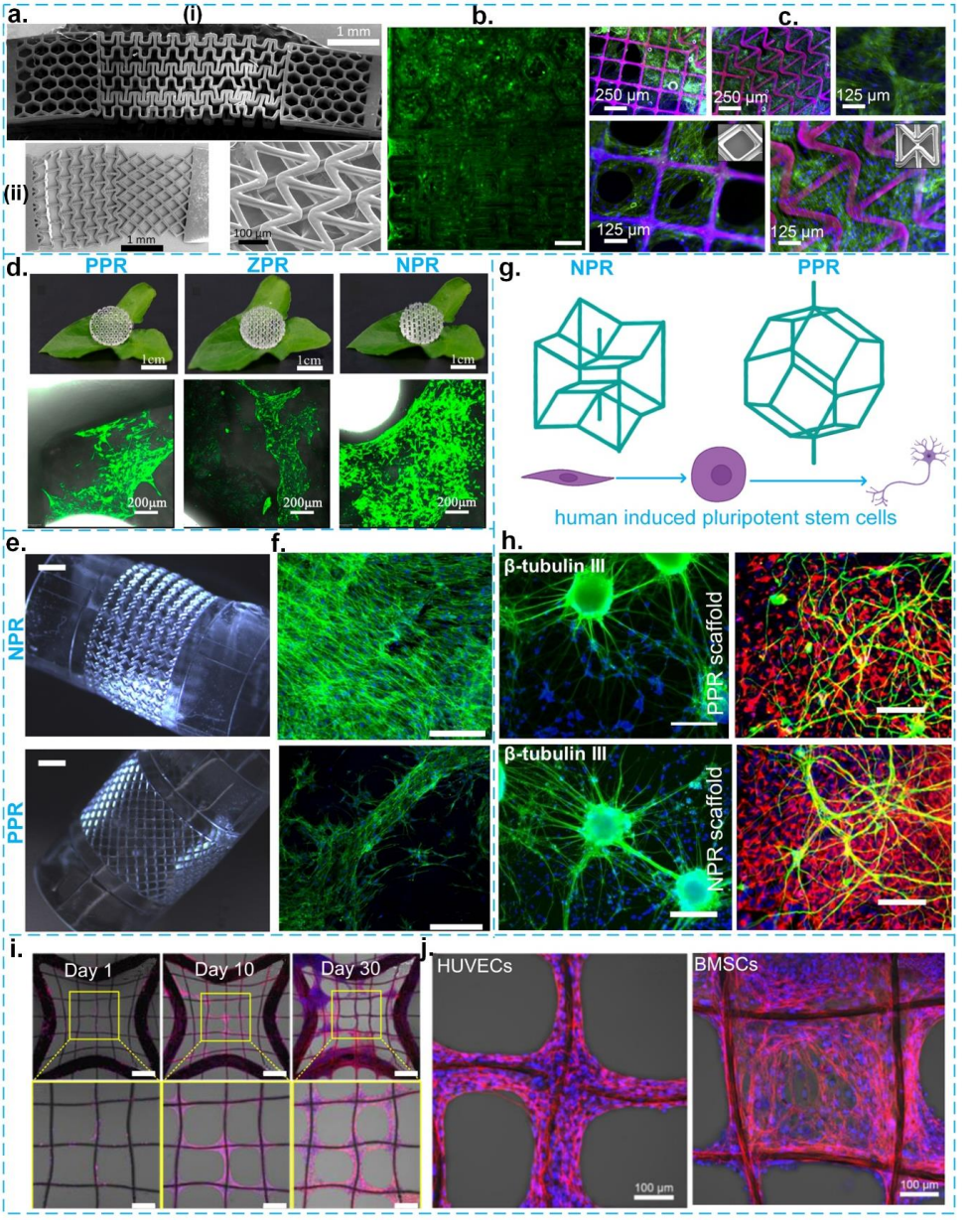

Figure 2. *Some examples of the response of cells to strut-based meta-biomaterials.* ***a.*** *Some examples of two different 2D hybrid meta-biomaterials and their SEM images (**a-i**, of a millimeter-scale 3D printed meta-biomaterial made from polyaliphatic urethane acrylate with isobornyl acrylate fabricated by using an SLA technique (more specifically, dynamic optical projection stereolithography). Adapted with permission from ref [65]. Copyright 2017 Elsevier, and **a-ii**, millimeter-scale 3D printed meta-biomaterials fabricated by a custom-made SLA technique from poly(ethylene glycol) diacrylate (PEGDA). Adapted with permission from ref [66]. Copyright 2012 Elsevier.* ***b.*** *Fluorescent images of PPR and NPR regions of hybrid meta-biomaterials seeded with fibroblast cells after 3 weeks of cell culture. Adapted with permission from ref [65]. Copyright 2017 Elsevier; the scale bar shows 250 µm.* ***c.*** *Fluorescent images showing F-actin and*

nuclei of the hybrid meta-biomaterial seeded with human MSCs. Adapted with permission from ref [66]. Copyright 2012 Elsevier. d. The effects of three types of 2D meta-biomaterials with a PPR, an NPR and a ZPR (top side) on the proliferation of MSCs (bottom side). [23] ***e*** *and* ***f.*** *The interaction of human turbinate MSCs with 2.5D cylindrical meta-biomaterials; [35]* ***e.*** *Some optical microscopy images of NPR and PPR meta-biomaterials, which were 3D printed by SLA from PEGDA polymer.* ***f.*** *Confocal optical microscopy images of F-actin and nuclei of human turbinate MSCs; scale bar shows 300 μm.* ***g*** *and* ***h.*** *The response of mouse embryonic stem cells (ESCs) and human induced pluripotent stem cells (hiPSCs) to 3D strut-based meta-biomaterials made through a multi-step thermo-mechanical fabrication technique from polyurethane foams. Adapted with permission from ref [64]. Copyright 2018 John Wiley and Sons, and Reproduced with permission from ref [26]. Copyright 2017 Elsevier, respectively.* ***g.*** *The configurations of two 3D meta-biomaterials with PPR and NPR while being in contact with hiPSCs. Adapted with permission from ref [64]. Copyright 2018 John Wiley and Sons. h. (left) Fluorescent images of the expression of the β-tubulin III marker of mouse ESCs within both PPR (upper row) and NPR scaffolds (lower row). Reproduced with permission from ref [26]. Copyright 2017 Elsevier; the scale bar shows 200 μm.* ***h.*** *(right) Some fluorescent images of the expression of the neural markers (Hoechst, Nestin and β-tubulin III) of the human iPSK3 cells within both PPR (upper row) and NPR scaffolds (lower row). Reproduced with permission from ref [26]. Copyright 2017 Elsevier; the scale bar is 100 μm. Blue, red, and green show Hoechst, Nestin, and β -tubulin III, respectively. i and j. 2D multi-scale NPR meta-biomaterials made through melt electro writing (MEW). Adapted with permission from ref [68]. Copyright 2021 Elsevier.* ***i.*** *Some fluorescent images of F-actin and nuclei of BMSCs on days 1, 10, and 30, with different magnifications; the scale bar is 200 μm.* ***j.*** *Some magnified fluorescent image of F-actin and nuclei of bone marrow stromal cells (BMSCs) and human umbilical vein endothelial cells (hUVECs) on day 30.*

Tuning the local values of the Poisson's ratio within a 2D meta-biomaterial has been used to control the cellular forces transmitted in regions with different Poisson's ratios when interacting with embryonic fibroblasts (10T1/2) [52]. The focal adhesion measurements of those cells have shown that the deformations applied by the cells to those meta-biomaterials were larger in the NPR regions as compared to the regions with PPR. [52] Both regions in the scaffolds showed high cell proliferation. Different cell division patterns were, however, observed in those two regions with unusual cell division occurring for the cells interacting with NPR zones, which may cause genetic instability and potentially lead to cancer [52].

In addition to 2D (or 2.5D) planar meta-biomaterials, 2.5D cylindrical meta-biomaterials (with an in-plane microarchitecture and an out-of-plane thickness) have shown controllable Poisson's ratios (Figure 2e) [35]. It has been observed that these structures can also tune the mechanobiological response of the human turbinate MSCs [35]. On day 1, no significant differences were observed in cell densities (*i.e.,* proliferation) between the non-auxetic and auxetic scaffolds (Figure 2f) [35]. On days 4, 7, and 11, however, significantly higher cell proliferation was observed in the auxetic scaffolds. From such microscopical observations, it was concluded that, in the non-auxetic grids, the cells only covered a part of the available surface area, whereas, in the auxetic structure, the cells fully covered the entire area of the scaffold and were strongly interconnected (Figure 2f) [35]. This may be attributed to the geometrical design of the scaffolds given that the interspacing between the struts was smaller in the NPR scaffolds as

compared to the PPR ones. Under such conditions, cells may grow and proliferate more easily in the NPR scaffolds.

Although 3D meta-biomaterials can provide a more realistic environment for cells and tissues [67] to grow, only a limited number of studies have assessed their mechanobiological responses [26, 64]. These studies have analyzed the differentiation of pluripotent stem cells (mouse ESCs and hiPSCs) under interactions with 3D meta-biomaterials [26, 64] (Figure 2g). The first example included two types of auxetic and non-auxetic meta-biomaterials with different Poisson's ratios as well as different stiffnesses, porosities, and pore sizes. The values were respectively -0.45, 44 kPa, 90.65%, and 250-300 μm for the auxetic meta-biomaterial and 0.3, 100 kPa, 96.31%, and 300-400 μm for the non-auxetic one [26, 64] (Figure 2g). In another example, however, Poisson's ratios were decoupled from other mechanical properties, including stiffness, resulting in two different auxetic meta-biomaterial designs. The first group had the same Poisson's ratio (-0.45) but different stiffnesses (*i.e.,* 10 and 94 kPa) while the second group had the same stiffness (almost 100 kPa) but different Poisson's ratios (0.3 and -0.45). Various differentiation markers, such as β-tubulin III, alkaline phosphatase (ALP), Oct-4, Nanog, CD31, and VE-cadherin, were assayed for neural [26] and vascular differentiation [64]. From the biological results of the first category (day 16), the vascular markers CD31 and VE-cadherin were assessed by immunohistochemistry and flow cytometry, and respectively showed 56% and 49% for the auxetic scaffolds. For the non-auxetic scaffolds (in the first category), the vascular markers CD31 and VE-cadherin were 16% and 28%, respectively. It can be concluded that there was more vascular differentiation associated with the cells cultured on the auxetic scaffolds. Similarly, the ALP expression, as an indicator of undifferentiated cells, showed that the non-auxetic scaffolds had higher ALP activity than the auxetic ones. Similarly, the expression of Oct-4 and Nanog was higher for the non-auxetic scaffolds [64]. As for neural differentiation, it was observed that the auxetic meta-biomaterials upregulated the expression of β-tubulin III marker as compared to the non-auxetic specimens (Figure 2h) [26]. The neural differentiation of mouse ESCs of the second category (*i.e.,* decoupling of the Poisson's ratio and stiffness) on day 6 showed a similar trend, confirming the role of auxeticity and stiffness in improving neural differentiation (according to the expressions of Nestin, PAX6, and β-tubulin III). This suggests that both NPR scaffolds with higher Poisson's ratio but similar stiffnesses and NPR scaffolds with higher stiffness, but similar Poisson's ratios promoted neural differentiation. [26] It is, however, important to note that the increased vascular differentiation and neural expression associated with the NPR scaffolds as compared to the PPR meta-biomaterials may be due to the differences in the pore sizes (*i.e.,* 200-250 μm vs. 300-400 μm), pore shapes, porosities, or stiffnesses of both groups.

The relationship between the pore size and the unit cell size is of great importance in the design of meta-biomaterials. AM is a promising tool for creating meta-

biomaterials at different length scales, from micro- to meso-scales, and with different pore and unit cell sizes. AM enables the incorporation of more complex features in the design of meta-biomaterials (*e.g.,* Figures 2i and j [68] and Figures 3a-c [24]). This approach helps in better mimicking the microstructural complexity of native (bony) tissue and regulating cell responses at multiple length scales [68, 69].

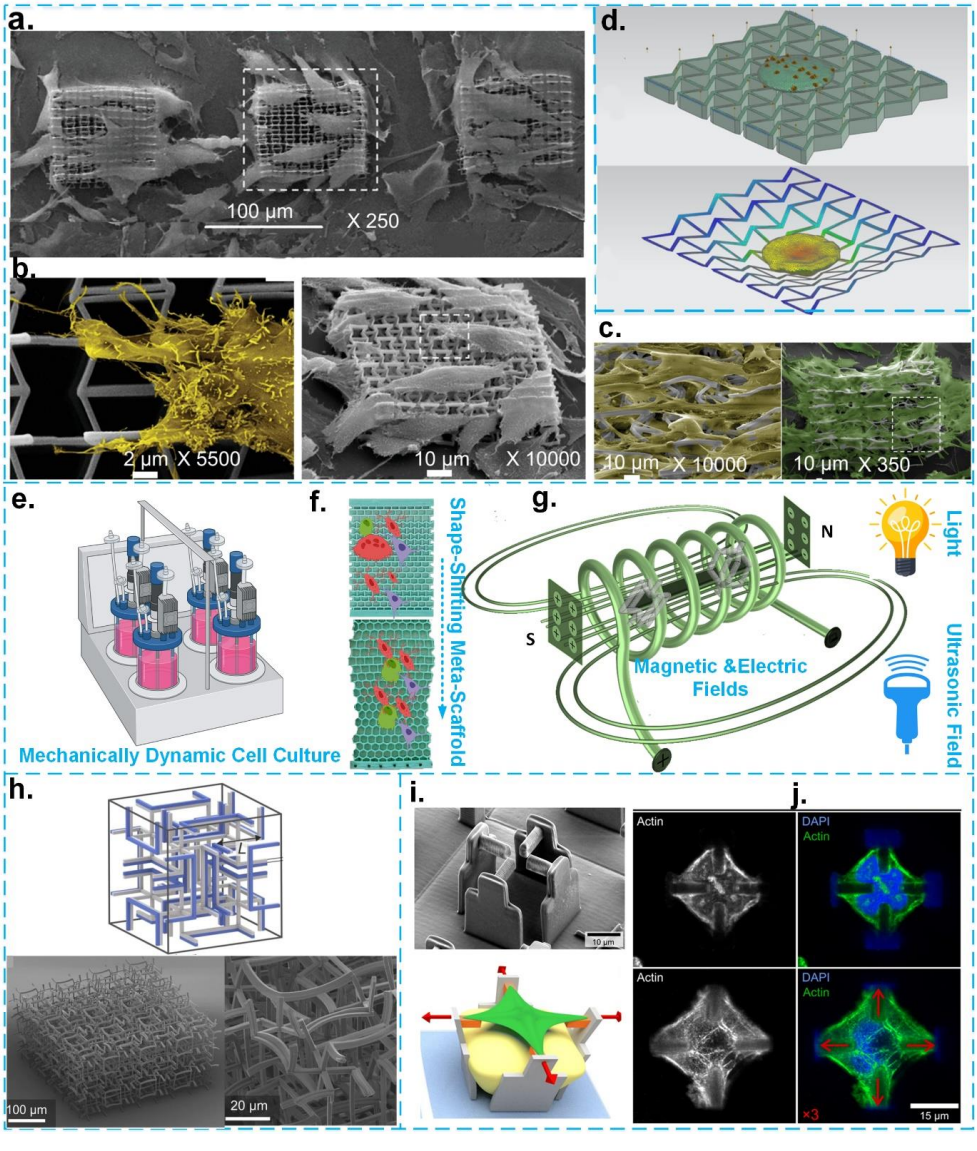

Figure 3. *a-c.* *SEM images of 3D strut-based meta-biomaterials 3D printed by 2PP technique and cultured with fibroblast cell lines. Adapted with permission from ref [24]. Copyright 2020 John Wiley and Sons; at different magnifications. d. The mechanobiological modelling of the interactions of a single eukaryotic cell with an NPR meta-biomaterial in both deformed and undeformed configurations. Adapted with permission from ref [73]. Copyright 2015 IOP Publishing.* ***e-g.*** *A schematic illustration of mechanically* ***(e)*** *and*

*remotely (**g**) dynamic cell culture in meta-biomaterials (**f** [113]). **h.** A 4D printed meta-biomaterial at the microscale. [97] **h.** (top) the initial state of the meta-biomaterial (i.e., initial shape). **h.** (bottom) shows the deformed shape of the meta-biomaterial (i.e., temporary shape) under temperature stimulation with two different magnifications. **i** and **j.** A 2PP 4D printed platform with a reversible actuation capability to mechanically stimulate a single cell. [87] **i.** A SEM image and a schematic drawing of the platform in the presence of a single cell. **j.** Some fluorescent images of the F-actin and nuclei of the stretched and unstretched single cells.*

Porous structures with random microarchitectures can also exhibit an auxetic behavior [41, 70, 71]. These structures can be fabricated using either AM or conventional techniques (*e.g.*, foaming) [41, 70, 71]. The data regarding the biological assessment of meta-biomaterials with random microarchitectures is limited. A rare example is the investigation of the proliferation of an osteoblast-like cell line (MG-63) under static and dynamic loading conditions in the presence of foam-based auxetic scaffolds where the stiffness (via the base material) and degrees of hydrophilicity of the specimens were varied [41]. The auxetic scaffolds made from polyurethane (PU) promoted the proliferation of chondrocytes between days 3 and 5, which was 1.3 times higher than the non-auxetic specimens [71]. After day 5, however, there was no significant difference in the proliferation of the cells interacting with the auxetic and non-auxetic scaffolds, likely because 100% confluence was already reached [71]. Table 1 summarizes the reported biological performance and fabrication techniques of strut-based meta-biomaterials, with 2D meta-biomaterials being the most studied structures for such biological analyses.

Table 1. *An overview of the current literature investigating the biological responses of meta-biomaterials with different values of the Poisson's ratio, scales, material properties, fabrication techniques, and cell types.*

Shape	Unit cell type	Scale	Material	Manufacturing technique	Cell types
2D rectangular	ZPR PPR/NPR	Meso	PEG	pSLA	Human MSCs [114,66]
3D rectangular	NPR	Micro/ Meso	Organic–inorganic hybrid SZ2080	2PP	Mouse fibroblasts [24]
2D rectangular	NPR	Micro/ Meso	PCL	MEW	hUVECs & BMSCs [68]
2D rectangular	PPR/NPR	Meso	Polyaliphatic urethane acrylate blend	pSLA	Fibroblasts [65]
2D rectangular	PPR/NPR	Micro	N.A	DLP	N.A [52]
3D rectangular	PPR/NPR	N.A	PU	A compressed carbon dioxide assisted technique	ESCs & hiPSCs [26,64]

2.5D tubular	NPR	Meso	PCL	MEW	N.A [115]
2D circular	PPR/ZPR/ NPR	Meso	CNF/PEGDA aero-gel	SLA and freeze-drying	Mouse BMSC [23]
2D rectangular	NPR	Micro	Silicon	Deep reactive ion etching	Human MSCs [73]
3D rectangular	NPR	Macro	HA/ PGLA& PU	Solvent cast-ing/salt leaching	MG-63 [41,70,71]
2.5D tubular	PPR/NPR	Micro	PEGDA	pSLA	Human tur-binate MSCs [35]

In addition to *in vitro* studies on meta-biomaterials, several works have focused on computational modeling and optimization of bone scaffolds with respect to their mechanobiological responses [72]. More specifically, in auxetic meta-biomaterials, the interaction between a single eukaryotic cell and a 2D auxetic meta-biomaterial has been modeled [73]. This model has been employed to design a cell-growth sensor to measure the forces applied by cells to the auxetic scaffold (Figure 3d). More interestingly, the presence of the cells can also change the mode shapes of the scaffold and even their orders of appearance [73].

2.3.4 Meta-biomaterials under dynamic conditions

To effectively mimic the microenvironments of tissues and the homogenous distribution of cells within scaffolds, it is important to consider the impact of the dynamic behavior of either meta-biomaterials (*i.e.,* dynamic loading condition) or the environment (*i.e.,* dynamic environments). Indeed, in the body, the dynamic microenvironment surrounding cells continually regulates different cell functions, such as differentiation and proliferation. To better mimic these conditions, dynamic cell cultures need to be employed [74]. There are several factors that can improve cell proliferation and differentiation under dynamic cell culture conditions. Dynamic cell cultures provide mechanical forces that resemble those found in native tissues, thereby enabling a transition between biochemical and biomechanical cues. They also create a uniform cell distribution and establish a dynamic supply of nutrient to cells [75-78]. Another benefit of using dynamic cell cultures is that they allow for guiding cell growth in the scaffolds in a specific (confined) environment. To clearly elucidate the effects of the Poisson's ratio of meta-biomaterials on cell response, dynamic loading conditions must be applied. It is, therefore, important to know how dynamic cell cultures work and to implement this approach in future research to better understand the living cell – meta-biomaterial interactions. Moreover, the biodegradation rate of scaffolds depends on the type of loading and may be different under dynamic loading conditions as compared to static conditions [25]. The biodegradation rate of scaffolds should match the deposition

rate of the newly formed ECM to maintain a balance between the degradation and formation of new tissue [25].

There are generally two methods to operate a dynamic cell culture: mechanically induced loading (*e.g.,* mechanical bioreactors) and remotely induced (*e.g.,* magnetic/electric field or ultrasonic field) actuation [76] (Figures 3e-g). Although auxetic behavior is more dominant under dynamic loading, only a few studies have investigated simultaneous mechanical loading and cell culturing of meta-biomaterials [41, 70]. A foam-based auxetic scaffold is the only example that was tested under dynamic cell culture conditions. The results of that study showed a higher proliferation of MG-63 osteoblast-like cells (i.e., 200% for the stiffer scaffold and 20% for the softer one) under dynamic cell culture conditions. [41] There is, however, no example of a remotely induced dynamic cell culture platform testing the mechanobiological response of meta-biomaterials.

2.4 Micro-AM technology to fabricate meta-biomaterials

Over the past years, AM technology has matured enough to create meta-biomaterials with reliable and reproducible properties that can mimic some of the biological and mechanical characteristics of the native bony tissue. The progress of AM techniques has paved the way for creating meta-biomaterials with complex microarchitectures, thereby enabling the creation of a platform to effectively assess the role of microarchitectural features, such as auxeticity and local curvatures, in (bone) tissue engineering processes.

Light-assisted AM techniques have, so far, been the most widely used 3D printing methods to create meta-biomaterials at the microscale. This is due to the availability of a wide range of materials (*i.e.,* biocompatible polymers) and the ability of these technique to print at very high resolutions with minimum feature sizes in the micron range [67, 79]. Examples of these techniques are SLA [35, 65] and 2PP [24, 80, 81]. Different meta-biomaterials with 3D multi-scale features and sizes down to sub-micron ranges have been 3D printed using 2PP [82-91]. The 2PP AM technique, like other similar light-assisted techniques, can be combined with conventional manufacturing techniques (*e.g.,* molding) in a hybrid fashion to push the boundaries of the existing 3D printing techniques. This approach has been used, for example, to study the curvature-dependent mechanobiology of bone cells at the micro-scale, by integrating molded 2PP 3D printed structures and creating soft elastomeric micro-surfaces [92]. This approach can be further extended to develop meta-biomaterials with tunable morphological and material properties in the future.

One challenge in creating microscale meta-biomaterials is the trade-off between the printing time and print quality, particularly when covering multiple length scales.

A higher degree of geometrical complexity often translates to a longer fabrication time and more complex post-processing steps. In addition, biocompatibility, biodegradability, and printing throughput are the most challenging aspects of micro-fabrication, particularly for 2PP [93]. In future studies, stimuli-responsive materials, such as magneto-responsive materials, can be used to create meta-biomaterials with dynamic and tunable properties [94].

2.5 Future research

Here, we reviewed the current progress of meta-biomaterials, their corresponding biological assessments, and the relevant mechanobiological pathways. We specifically focused on how the different values of the Poisson's ratio (*i.e.,* the degree of auxeticity), which is an indication of the geometrical properties of lattice structures, can influence the biological responses of meta-biomaterials. In addition, we highlighted the importance of dynamic cell culturing and its effects on (bone) tissue engineering using meta-biomaterials. In this section, we discuss the outlook and future directions of this research line and provide several suggestions for follow-up studies.

2.5.1 Outlook and future work

Auxeticity, as a "*mechanobiological tool*" for the development of the next generation of meta-biomaterials, can fine-tune the bone regeneration process. Several studies dealing with the effects of the Poisson's ratio on the mechanobiological response of meta-biomaterials have already appeared in the literature. However, more studies are needed to elucidate the isolated effects of the Poisson's ratio on the cell response. That is because the Poisson's ratio and other geometrical and mechanical properties of meta-biomaterials are highly inter-related. Extreme care, therefore, needs to be taken to ensure these factors are separated from each other to the maximum possible extent.

Another missing aspect in the current body of literature is the effects of the Poisson's ratio on the responses of cells in 3D meta-biomaterials. The variations in the configuration of struts in 2D and 3D structures may cause notable differences in the response of cells interacting with such meta-biomaterials. Therefore, the mechanobiological results of 2D and 2.5D meta-biomaterials cannot necessarily be extrapolated to the 3D ones. To date, only a limited number of studies have addressed the role of the Poisson's ratio in 3D meta-biomaterials [26, 64]. Further investigations are, therefore, required to understand any such differences between 2D and 2.5D structures on the one hand and 3D structures on the other.

From a biological viewpoint, only a few cell types have been so far used to assess the potential of meta-biomaterials in (bone) tissue engineering. Further research with different cell types (*i.e.,* either cell lines or primary cells) is, therefore, required both under mono-culture and co-culture conditions. Moreover, most of the biological assessments performed on meta-biomaterials are limited to the assessment of their

cytocompatibility and cell proliferation. Other biological assays are, thus, required to investigate the effects of meta-biomaterial properties on the differentiation of cells. In addition, *in vivo* experiments are needed to allow for the implementation of meta-biomaterials in clinical settings.

From a manufacturing viewpoint, it remains challenging to create multi-scale meta-biomaterials at different length scales with high throughput. Recent developments in multi-material AM have provided new opportunities for incorporating more complexity in the design of meta-biomaterials through the deposition of soft and hard materials [19]. This may help in decoupling the Poisson's ratio from other mechanical properties, thus providing additional flexibility in the design of meta-biomaterials. Moreover, organic-inorganic hybrid materials [95] can be used to independently tune the elastic modulus and mechanical performance of meta-biomaterials along with their Poisson's ratio. These materials can be 3D printed at the microscale, providing precise control over their microarchitectural features and offering a promising avenue for the development of advanced engineered microenvironments with multifaceted functionalities for various biomedical applications.

In addition, it is still unclear how meta-biomaterials can stimulate cell response under dynamic loading conditions. Meta-biomaterials can show rare properties under external loading, such as local shape-morphing, which can be tuned by varying the Poisson's ratio of individual unit cells (Figure 3h) [96-98]. However, not much is known about how these unique features can influence the cell response. Although it has been shown that external stimuli, such as magnetic or electric fields, light, and ultrasound, may improve new tissue formation [99, 100] or facilitate *in vitro* studies [101], their effects in connection with meta-biomaterials remain elusive. It is also not quite clear how these external stimuli can trigger other biochemical/biological activities in cells and alter their gene expression [76, 87]. One example of such systems is a 4D printed reversible scaffold designed to mechanically stimulate single cells with the aim of altering their gene expressions (*e.g.,* Figures 3i and j, 2PP [87]). More studies are needed to explore the response of cells to the meta-biomaterials stimulated by either mechanical loading or by other types of external stimulus.

4D (bio) printing is a promising AM technology to study the dynamic properties of meta-biomaterials and their cell responses. Creating 4D-printed meta-biomaterials (*i.e.,* structures changing their shape with time [102]) with auxetic properties may be a new research direction to promote tissue formation and influence the response of cells to such types of biomaterials. This approach can provide additional functionality for the design of meta-biomaterials, for example, to create medical devices with integrated drug delivery systems providing certain antimicrobial activities. [103] 4D-printed medical devices have many applications ranging between cardiovascular engineering [75] to orthopedic implants [104] and beyond to create specific biological responses. 877]

One recent example of such applications involves the development of stimuli-responsive deployable metamaterials with dynamic Poisson's ratios (Figure 3h [97, 105, 106]). Moreover, 4D-printed deployable implants can be implanted using minimally invasive surgical techniques. Upon external actuation or stimulation, such deployable meta-implants expand and fit into a cavity or defect zone [107,108]. It is, however, important to gain a better understanding of the interaction between 4D-(bio-)printed structures and living tissues. For example, 4D (bio)printing technology can be used to control the orientation of hMSCs, human embryonic stem cell-derived cardiomyocytes, and endothelial cells in a light-responsive cardiac construct [96]. Finally, to comprehensively understand the dynamic mechanobiology of meta-biomaterials, follow-up studies on implementing 4D-printed meta-biomaterials as micro-robots [97, 98, 109, 110] can be conducted in the future.

The lack of multi-physics computational models for simulating the mechanobiological response of meta-biomaterials and their interactions with living cells is another challenge in this field. Such in silico models represent powerful tools for designing optimal meta-biomaterials with the aim of reducing the cost and time associated with such studies. These models, when coupled with bone modeling approaches [111,112], can serves as an effective tool to predict the mechanical behavior resulting from various microarchitectural designs of meta-biomaterials. They can be also used to better understand the mechanobiological events (*e.g.,* force transmission) occurring within different cell compartments (*e.g.,* nuclei and cytoplasm).

2.6 Conclusions

Although it has been shown that biophysical cues, such as mechanical properties (*e.g.,* stiffness) and geometrical properties (*e.g.,* pore size and porosity), are among the most important parameters to successfully design orthopedic implants, there is a lack of understanding as to how microarchitectures influence the bone tissue regeneration process. One parameter than can widely vary depending on the microarchitectural design is the Poisson's ratio. In particular, it has been shown that the sign of the Poisson's ratio (*i.e.,* negative or positive values) may play a notable role in guiding force transmission across cells, while also affecting the cell response in terms of cell proliferation, adhesion, differentiation, and directionality. Here, we discussed the current state of the art regarding the Poisson's ratio-driven meta-biomaterials and their effects on cell-biomaterial interactions.

Auxetic behavior has been observed in native (soft and hard) tissues and cells, highlighting its importance in designing the next generation of scaffolds and implants. In order to effectively design architected biomaterials inspired by native tissues, it is essential to consider not only the stiffness and microarchitectural parameters of such

biomaterials (*e.g.,* local curvature, porosity, and pore size) but also their Poisson's ratio. There is some evidence in the literature suggesting that NPR meta-biomaterials promote proliferation and differentiation of cells *in vitro*. It is, however, necessary to decouple the effects of the Poisson's ratio from other geometrical and mechanical properties. Moreover, most current studies are limited to 2D meta-biomaterials, and needs to be extended to 3D variants.

The concept of auxeticity assumes an even more interesting role within dynamic loading conditions. Advanced technologies, such as 4D (bio)printing technologies, have shown great promise in creating such meta-biomaterials with dynamic properties. This requires the use of stimuli-responsive biomaterials and a further analysis of the response of living cells to 4D-printed meta-biomaterials. Future studies of such novel effects call for interdisciplinary approaches in which engineers and scientists from various backgrounds, such as mechanical engineering, biology, physics, and materials science, work together to achieve a better understanding of the mechanobiological pathways driving the response of cells to auxetic and non-auxetic meta-biomaterials.

Bibliography

[1] J. Adhikari, A. Roy, A. Chanda, D. Gouripriya, S. Thomas, M. Ghosh, J. Kim, P. Saha, Effects of surface patterning and topography on cellular functions of tissue engineered scaffolds with special reference to 3D bioprinting, Biomaterials Science 11 (2023) 1236-1269.
[2] A.A. Zadpoor, Meta-biomaterials, Biomaterials science 8(1) (2020) 18-38.
[3] M.A. Surmeneva, R.A. Surmenev, E.A. Chudinova, A. Koptioug, M.S. Tkachev, S.N. Gorodzha, L.-E. Rännar, Fabrication of multiple-layered gradient cellular metal scaffold via electron beam melting for segmental bone reconstruction, Materials & Design 133 (2017) 195-204.
[4] S.J. Hollister, Porous scaffold design for tissue engineering, Nature materials 4(7) (2005) 518-524.
[5] D. Wu, P. Isaksson, S.J. Ferguson, C. Persson, Young's modulus of trabecular bone at the tissue level: A review, Acta biomaterialia 78 (2018) 1-12.
[6] C.N. Kelly, T. Wang, J. Crowley, D. Wills, M.H. Pelletier, E.R. Westrick, S.B. Adams, K. Gall, W.R. Walsh, High-strength, porous additively manufactured implants with optimized mechanical osseointegration, Biomaterials 279 (2021) 121206.
[7] S.J. Callens, R.J. Uyttendaele, L.E. Fratila-Apachitei, A.A. Zadpoor, Substrate curvature as a cue to guide spatiotemporal cell and tissue organization, Biomaterials 232 (2020) 119739.
[8] T. van Manen, M. Ganjian, K. Modaresifar, L.E. Fratila-Apachitei, A.A. Zadpoor, Automated Folding of Origami Lattices: From Nanopatterned Sheets to Stiff Meta-Biomaterials, Small 19(3) 2203603.
[9] M. Kapnisi, C. Mansfield, C. Marijon, A.G. Guex, F. Perbellini, I. Bardi, E.J. Humphrey, J.L. Puetzer, D. Mawad, D.C. Koutsogeorgis, Auxetic cardiac patches with tunable mechanical and conductive properties toward treating myocardial infarction, Advanced functional materials 28(21) (2018) 1800618.
[10] Z. Lin, L.S. Novelino, H. Wei, N.A. Alderete, G.H. Paulino, H.D. Espinosa, S. Krishnaswamy, Folding at the microscale: Enabling multifunctional 3D origami-architected metamaterials, Small 16(35) (2020) 2002229.
[11] Z. Vangelatos, H.M. Sheikh, P.S. Marcus, C.P. Grigoropoulos, V.Z. Lopez, G. Flamourakis, M. Farsari, Strength through defects: A novel Bayesian approach for the optimization of architected materials, Science advances 7(41) (2021) eabk2218.
[12] E. Jebellat, M. Baniassadi, A. Moshki, K. Wang, M. Baghani, Numerical investigation of smart auxetic three-dimensional meta-structures based on shape memory polymers via topology optimization, Journal of Intelligent Material Systems and Structures 31(15) (2020) 1838-1852.
[13] M. Mirzaali, N. Shahriari, J. Zhou, A. Zadpoor, Quality of AM implants in biomedical application, Quality Analysis of Additively Manufactured Metals, Elsevier2023, pp. 689-743.
[14] S. Vyavahare, V. Mahesh, V. Mahesh, D. Harursampath, Additively manufactured meta-biomaterials: A state-of-the-art review, Composite Structures (2022) 116491.
[15] S. Ahmadi, R. Hedayati, Y. Li, K. Lietaert, N. Tümer, A. Fatemi, C. Rans, B. Pouran, H. Weinans, A. Zadpoor, Fatigue performance of additively manufactured meta-biomaterials: The effects of topology and material type, Acta biomaterialia 65 (2018) 292-304.
[16] H. Pahlavani, M. Amani, M.C. Saldívar, J. Zhou, M.J. Mirzaali, A.A. Zadpoor, Deep learning for the rare-event rational design of 3D printed multi-material mechanical metamaterials, Communications Materials 3(1) (2022) 46.
[17] H. Pahlavani, K. Tsifoutis-Kazolis, P. Mody, J. Zhou, M.J. Mirzaali, A.A. Zadpoor, Deep learning for size-agnostic inverse design of random-network 3D printed mechanical metamaterials, arXiv preprint arXiv:2212.12047 (2022).
[18] R. Hedayati, M. Sadighi, M. Mohammadi-Aghdam, A. Zadpoor, Mechanical properties of regular porous biomaterials made from truncated cube repeating unit cells: Analytical solutions and computational models, Materials Science and Engineering: C 60 (2016) 163-183.
[19] M. Mirzaali, H. Pahlavani, E. Yarali, A. Zadpoor, Non-affinity in multi-material mechanical metamaterials, Scientific reports 10(1) (2020) 11488.
[20] J. Williams, J. Lewis, Properties and an anisotropic model of cancellous bone from the proximal tibial epiphysis, Journal of Biomechanical Engineering 104(1) (1982) 50-56.

[21] R. Gatt, M.V. Wood, A. Gatt, F. Zarb, C. Formosa, K.M. Azzopardi, A. Casha, T.P. Agius, P. Schembri-Wismayer, L. Attard, Negative Poisson's ratios in tendons: an unexpected mechanical response, Acta biomaterialia 24 (2015) 201-208.
[22] S. Pagliara, K. Franze, C.R. McClain, G.W. Wylde, C.L. Fisher, R.J. Franklin, A.J. Kabla, U.F. Keyser, K.J. Chalut, Auxetic nuclei in embryonic stem cells exiting pluripotency, Nature Materials 13(6) (2014) 638-644.
[23] A. Tang, J. Ji, J. Li, W. Liu, J. Wang, Q. Sun, Q. Li, Nanocellulose/PEGDA Aerogels with Tunable Poisson's Ratio Fabricated by Stereolithography for Mouse Bone Marrow Mesenchymal Stem Cell Culture, Nanomaterials 11(3) (2021) 603.
[24] G. Flamourakis, I. Spanos, Z. Vangelatos, P. Manganas, L. Papadimitriou, C. Grigoropoulos, A. Ranella, M. Farsari, Laser-made 3D Auxetic Metamaterial Scaffolds for Tissue Engineering Applications, Macromolecular Materials
Engineering 305(7) (2020) 2000238.
[25] P. Mardling, A. Alderson, N. Jordan-Mahy, C.L. Le Maitre, The use of auxetic materials in tissue engineering, Biomaterials science 8(8) (2020) 2074-2083.
[26] Y. Yan, Y. Li, L. Song, C. Zeng, Pluripotent stem cell expansion and neural differentiation in 3-D scaffolds of tunable Poisson's ratio, Acta biomaterialia 49 (2017) 192-203.
[27] H.M. Kolken, S. Janbaz, S.M. Leeflang, K. Lietaert, H.H. Weinans, A.A. Zadpoor, Rationally designed meta-implants: a combination of auxetic and conventional meta-biomaterials, Materials Horizons 5(1) (2018) 28-35.
[28] A. Derrouiche, F. Zaïri, F. Zaïri, A chemo-mechanical model for osmo-inelastic effects in the annulus fibrosus, Biomechanics modeling in mechanobiology 18(6) (2019) 1773-1790.
[29] G. Dusfour, S. LeFloc'h, P. Cañadas, D. Ambard, Heterogeneous mechanical hyperelastic behavior in the porcine annulus fibrosus explained by fiber orientation: An experimental and numerical approach, Journal of the mechanical behavior of biomedical materials 104 (2020) 103672.
[30] D. Veronda, R. Westmann, Mechanical characterization of skin—finite deformations, Journal of biomechanics 3(1) (1970) 111-124.
[31] L. Frolich, M. LaBarbera, W. Stevens, Poisson's ratio of a crossed fibre sheath: the skin of aquatic salamanders, Journal of Zoology 232(2) (1994) 231-252.
[32] D.Y. Fozdar, P. Soman, J.W. Lee, L.H. Han, S. Chen, Three-dimensional polymer constructs exhibiting a tunable negative Poisson's ratio, Advanced functional materials 21(14) (2011) 2712-2720.
[33] L.H. Timmins, Q. Wu, A.T. Yeh, J.E. Moore, Jr., S.E. Greenwald, Structural inhomogeneity and fiber orientation in the inner arterial media, American Journal of Physiology-Heart and Circulatory Physiology 298(5) (2010) H1537-45.
[34] C. Lees, J.F. Vincent, J.E. Hillerton, Poisson's ratio in skin, Bio-medical materials and engineering 1(1) (1991) 19-23.
[35] J.W. Lee, P. Soman, J.H. Park, S. Chen, D.-W. Cho, A tubular biomaterial construct exhibiting a negative Poisson's ratio, PLoS One 11(5) (2016) e0155681.
[36] C. Wiebe, G.W. Brodland, Tensile properties of embryonic epithelia measured using a novel instrument, Journal of biomechanics 38(10) (2005) 2087-2094.
[37] X. Chen, G.W. Brodland, Mechanical determinants of epithelium thickness in early-stage embryos, Journal of the mechanical behavior of biomedical materials 2(5) (2009) 494-501.
[38] Y. Jiang, K. Shi, L. Zhou, M. He, C. Zhu, J. Wang, J. Li, Y. Li, L. Liu, D. Sun, 3D-printed auxetic-structured intervertebral disc implant for potential treatment of lumbar herniated disc, Bioactive Materials 20 (2023) 528-538.
[39] J.S. Jurvelin, J.P. Arokoski, E.B. Hunziker, H.J. Helminen, Topographical variation of the elastic properties of articular cartilage in the canine knee, Journal of biomechanics 33(6) (2000) 669-675.
[40] J. Jurvelin, M. Buschmann, E. Hunziker, Optical and mechanical determination of Poisson's ratio of adult bovine humeral articular cartilage, Journal of biomechanics 30(3) (1997) 235-241.
[41] H.J. Choi, J.J. Lee, J.B. Lee, H.-J. Sung, J.-W. Shin, J.W. Shin, Y. Wu, J.K. Kim, MG-63 cells proliferation following various types of mechanical stimulation on cells by auxetic hybrid scaffolds, Biomaterials research 20(1) (2016) 1-8.

[42] K. Haase, A.E. Pelling, Investigating cell mechanics with atomic force microscopy, Journal of The Royal Society Interface 12(104) (2015) 20140970.
[43] M. Babi, R. Riesco, L. Boyer, A. Fatona, A. Accardo, L. Malaquin, J. Moran-Mirabal, Tuning the Nanotopography and Chemical Functionality of 3D Printed Scaffolds through Cellulose Nanocrystal Coatings, ACS Applied Bio Materials 4(12) (2021) 8443-8455.
[44] K.A. Jansen, D.M. Donato, H.E. Balcioglu, T. Schmidt, E.H. Danen, G. Koenderink, A guide to mechanobiology: Where biology and physics meet, Biochimica et Biophysica Acta -Molecular Cell Research 1853(11) (2015) 3043-3052.
[45] K. Modaresifar, M. Ganjian, P.J. Díaz-Payno, M. Klimopoulou, M. Koedam, B.C. van der Eerden, L.E. Fratila-Apachitei, A.A. Zadpoor, Mechanotransduction in high aspect ratio nanostructured meta-biomaterials: The role of cell adhesion, contractility, and transcriptional factors, Materials Today Bio 16 (2022) 100448.
[46] J.D. Humphries, M.R. Chastney, J.A. Askari, M.J. Humphries, Signal transduction via integrin adhesion complexes, Current opinion in cell biology 56 (2019) 14-21.
[47] A. Shuaib, D. Motan, P. Bhattacharya, A. McNabb, T.M. Skerry, D. Lacroix, Heterogeneity in the mechanical properties of integrins determines mechanotransduction dynamics in bone osteoblasts, Scientific reports 9(1) (2019) 1-14.
[48] P. Han, G.A. Gomez, G.N. Duda, S. Ivanovski, P.S. Poh, Scaffold geometry modulation of mechanotransduction and its influence on epigenetics, Acta Biomaterialia (2022).
[49] R. Huiskes, R. Ruimerman, G.H. Van Lenthe, J.D. Janssen, Effects of mechanical forces on maintenance and adaptation of form in trabecular bone, Nature 405(6787) (2000) 704-706.
[50] C.R. White, J.A. Frangos, The shear stress of it all: the cell membrane and mechanochemical transduction, Philosophical Transactions of the Royal Society B: Biological Sciences 362(1484) (2007) 1459-1467.
[51] C. Wang, Z. Vangelatos, C.P. Grigoropoulos, Z. Ma, Micro-engineered architected metamaterials for cell and tissue engineering, Materials Today Advances 13 (2022) 100206.
[52] W. Zhang, P. Soman, K. Meggs, X. Qu, S. Chen, Tuning the poisson's ratio of biomaterials for investigating cellular response, Acta biomaterialia 23(25) (2013) 3226-3232.
[53] B. Yi, Q. Xu, W. Liu, An overview of substrate stiffness guided cellular response and its applications in tissue regeneration, Bioactive Materials (2021).
[54] N.I.S. Murizan, N.S. Mustafa, N.H.A. Ngadiman, N. Mohd Yusof, A. Idris, Review on nanocrystalline cellulose in bone tissue engineering applications, Polymers 12(12) (2020) 2818.
[55] H. Zhang, J. Paik, Kirigami Design and Modeling for Strong, Lightweight Metamaterials, Advanced Functional Materials 32(21) (2022) 2107401.
[56] C. Coulais, A. Sabbadini, F. Vink, M. van Hecke, Multi-step self-guided pathways for shape-changing metamaterials, Nature 561(7724) (2018) 512-515.
[57] Y. Yao, Y. Ni, L. He, Rutile-mimic 3D metamaterials with simultaneously negative Poisson's ratio and negative compressibility, Materials & Design 200 (2021) 109440.
[58] M.J. Mirzaali, A. Ghorbani, K. Nakatani, M. Nouri-Goushki, N. Tümer, S.J. Callens, S. Janbaz, A. Accardo, J. Bico, M. Habibi, Curvature Induced by Deflection in Thick Meta-Plates, Advanced materials 33(30) (2021) 2008082.
[59] X. Yu, J. Zhou, H. Liang, Z. Jiang, L. Wu, Mechanical metamaterials associated with stiffness, rigidity and compressibility: A brief review, Progress in Materials Science 94 (2018) 114-173.
[60] L. Zhou, X. Zheng, K. Du, X. Guo, Q. Yin, A. Lu, Y. Yi, Parametric and experiment studies of 3D auxetic lattices based on hollow shell cuboctahedron, Smart Materials & Structures 30(2) (2021) 025042.
[61] J. Bauer, L.R. Meza, T.A. Schaedler, R. Schwaiger, X. Zheng, L. Valdevit, Nanolattices: an emerging class of mechanical metamaterials, Advanced Materials 29(40) (2017) 1701850.
[62] M. Scheffler, P. Colombo, Cellular ceramics: structure, manufacturing, properties and applications, John Wiley & Sons2006.
[63] M. Eynbeygui, J. Arghavani, A. Akbarzadeh, R. Naghdabadi, Anisotropic elastic-plastic behavior of architected pyramidal lattice materials, Acta Materialia 183 (2020) 118-136.
[64] L. Song, M.F. Ahmed, Y. Li, C. Zeng, Y. Li, Vascular differentiation from pluripotent stem cells in 3-D auxetic scaffolds, Journal of tissue engineering and

regenerative medicine 12(7) (2018) 1679-1689.
[65] J.J. Warner, A.R. Gillies, H.H. Hwang, H. Zhang, R.L. Lieber, S. Chen, 3D-printed biomaterials with regional auxetic properties, Journal of the mechanical behavior of biomedical materials 76 (2017) 145-152.
[66] P. Soman, J.W. Lee, A. Phadke, S. Varghese, S. Chen, Spatial tuning of negative and positive Poisson's ratio in a multi-layer scaffold, Acta biomaterialia 8(7) (2012) 2587-2594.
[67] A. Accardo, M.-C. Blatché, R. Courson, I. Loubinoux, C. Vieu, L. Malaquin, Direct laser fabrication of free-standing PEGDA-hydrogel scaffolds for neuronal cell growth, Materials Today 21(3) (2018) 315-316.
[68] Y. Jin, C. Xie, Q. Gao, X. Zhou, G. Li, J. Du, Y. He, Fabrication of multi-scale and tunable auxetic scaffolds for tissue engineering, Materials & Design 197 (2021) 109277.
[69] Q. Gao, C. Xie, P. Wang, M. Xie, H. Li, A. Sun, J. Fu, Y. He, 3D printed multi-scale scaffolds with ultrafine fibers for providing excellent biocompatibility, Materials Science Engineering: C 107 (2020) 110269.
[70] H.J. Choi, J.J. Lee, Y.J. Park, J.-W. Shin, H.-J. Sung, J.W. Shin, Y. Wu, J.K. Kim, MG-63 osteoblast-like cell proliferation on auxetic PLGA scaffold with mechanical stimulation for bone tissue regeneration, Biomaterials research 20(1) (2016) 1-8.
[71] Y.J. Park, J.K. Kim, The effect of negative Poisson's ratio polyurethane scaffolds for articular cartilage tissue engineering applications, Advances in Materials Science and Engineering 2013 (2013).
[72] Ó.L. Rodríguez-Montaño, C.J. Cortés-Rodríguez, A.E. Uva, M. Fiorentino, M. Gattullo, G. Monno, A. Boccaccio, Comparison of the mechanobiological performance of bone tissue scaffolds based on different unit cell geometries, Journal of the mechanical behavior of biomedical materials 83 (2018) 28-45.
[73] A.D. Lantada, A. Muslija, J.P. García-Ruíz, Auxetic tissue engineering scaffolds with nanometric features and resonances in the megahertz range, Smart Materials & Structures 24(5) (2015) 055013.
[74] M. Isomäki, C. Fedele, L. Kääriäinen, E. Mäntylä, S. Nymark, T.O. Ihalainen, A. Priimagi, Light-Responsive Bilayer Cell Culture Platform for Reversible Cell Guidance, Small Science (2021) 2100099.
[75] H. Shi, C. Wang, Z. Ma, Stimuli-responsive biomaterials for cardiac tissue engineering and dynamic mechanobiology, APL bioengineering 5(1) (2021) 011506.
[76] N. Castro, S. Ribeiro, M. Fernandes, C. Ribeiro, V. Cardoso, V. Correia, R. Minguez, S. Lanceros-Mendez, Physically active bioreactors for tissue engineering applications, Advanced Biosystems 4(10) (2020) 2000125.
[77] J. Melke, F. Zhao, K. Ito, S. Hofmann, Orbital seeding of mesenchymal stromal cells increases osteogenic differentiation and bone-like tissue formation, Journal of Orthopaedic Research® 38(6) (2020) 1228-1237.
[78] G.N. Schädli, J.R. Vetsch, R.P. Baumann, A.M. de Leeuw, E. Wehrle, M. Rubert, R. Müller, Time-lapsed imaging of nanocomposite scaffolds reveals increased bone formation in dynamic compression bioreactors, Communications biology 4(1) (2021) 1-14.
[79] C.A. Spiegel, M. Hippler, A. Münchinger, M. Bastmeyer, C. Barner-Kowollik, M. Wegener, E. Blasco, 4D printing at the microscale, Advanced Functional Materials 30(26) (2020) 1907615.
[80] P. Pip, C. Donnelly, M. Döbeli, C. Gunderson, L.J. Heyderman, L. Philippe, Electroless deposition of Ni–Fe alloys on scaffolds for 3D nanomagnetism, Small 16(44) (2020) 2004099.
[81] X. Tan, J.A.I. Martínez, G. Ulliac, B. Wang, L. Wu, J. Moughames, M. Raschetti, V. Laude, M. Kadic, Single-Step-Lithography Micro-Stepper Based on Frictional Contact and Chiral Metamaterial, Small 18(28) (2022) 2202128.
[82] J. Song, C. Michas, C.S. Chen, A.E. White, M.W. Grinstaff, From Simple to Architecturally Complex Hydrogel Scaffolds for Cell and Tissue Engineering Applications: Opportunities Presented by Two-Photon Polymerization, Advanced healthcare materials 9(1) (2020) 1901217.
[83] L. Bourdon, J.-C. Maurin, K. Gritsch, A. Brioude, V. Salles, Improvements in resolution of additive manufacturing: advances in two-photon polymerization and direct-writing electrospinning techniques, CS Biomaterials Science & Engineering 4(12) (2018) 3927-3938.

[84] I. Spanos, Z. Vangelatos, C. Grigoropoulos, M. Farsari, Design and Characterization of Microscale Auxetic and Anisotropic Structures Fabricated by Multiphoton Lithography, Nanomaterials 11(2) (2021) 446.
[85] Z. Vangelatos, C. Li, C. Grigoropoulos, K. Komvopoulos, Comparison of the mechanical performance of architected three-dimensional intertwined lattices at the macro/microscale, Extreme Mechanics Letters 40 (2020) 100930.
[86] T. Frenzel, M. Kadic, M. Wegener, Three-dimensional mechanical metamaterials with a twist, Science 358(6366) (2017) 1072-1074.
[87] M. Hippler, K. Weißenbruch, K. Richler, E.D. Lemma, M. Nakahata, B. Richter, C. Barner-Kowollik, Y. Takashima, A. Harada, E. Blasco, Mechanical stimulation of single cells by reversible host-guest interactions in 3D microscaffolds, Science advances 6(39) (2020) eabc2648.
[88] V. Parodi, E. Jacchetti, A. Bresci, B. Talone, C.M. Valensise, R. Osellame, G. Cerullo, D. Polli, M.T. Raimondi, Characterization of mesenchymal stem cell differentiation within miniaturized 3D scaffolds through advanced microscopy techniques, International Journal of Molecular Sciences 21(22) (2020) 8498.
[89] T. Zandrini, O. Shan, V. Parodi, G. Cerullo, M.T. Raimondi, R. Osellame, Multi-foci laser microfabrication of 3D polymeric scaffolds for stem cell expansion in regenerative medicine, Scientific reports 9(1) (2019) 1-9.
[90] G. Weisgrab, O. Guillaume, Z. Guo, P. Heimel, P. Slezak, A. Poot, D. Grijpma, A. Ovsianikov, 3D Printing of large-scale and highly porous biodegradable tissue engineering scaffolds from poly (trimethylene-carbonate) using two-photon-polymerization, Biofabrication 12(4) (2020) 045036.
[91] M. Hippler, E.D. Lemma, S. Bertels, E. Blasco, C. Barner-Kowollik, M. Wegener, M. Bastmeyer, 3D scaffolds to study basic cell biology, Advanced Materials 31(26) (2019) 1808110.
[92] S.J. Callens, D. Fan, I.A. van Hengel, M. Minneboo, L.E. Fratila-Apachitei, A.A. Zadpoor, Emergent collective organization of bone cells in complex curvature fields, Nature Communications 14 (2020).
[93] A. Arslan, W. Steiger, P. Roose, H. Van den Bergen, P. Gruber, E. Zerobin, F. Gantner, O. Guillaume, A. Ovsianikov, S. Van Vlierberghe, Polymer architecture as key to unprecedented high-resolution 3D-printing performance: The case of biodegradable hexa-functional telechelic urethane-based poly-ε-caprolactone, Materials Today 44 (2021) 25-39.
[94] Z. Liu, M. Li, X. Dong, Z. Ren, W. Hu, M. Sitti, Creating three-dimensional magnetic functional microdevices via molding-integrated direct laser writing, Nature communications 13(1) (2022) 1-11.
[95] G. Merkininkaitė, E. Aleksandravičius, M. Malinauskas, D. Gailevičius, S. Šakirzanovas, Laser additive manufacturing of Si/ZrO2 tunable crystalline phase 3D nanostructures, Opto-electronic advances 5(5) (2022) 1-11.
[96] Y. Wang, H. Cui, Y. Wang, C. Xu, T.J. Esworthy, S.Y. Hann, M. Boehm, Y.-L. Shen, D. Mei, L.G. Zhang, 4D Printed Cardiac Construct with Aligned Myofibers and Adjustable Curvature for Myocardial Regeneration, ACS Applied Materials &
Interfaces 13(11) (2021) 12746-12758.
[97] J. Qu, M. Kadic, A. Naber, M. Wegener, Micro-structured two-component 3D metamaterials with negative thermal-expansion coefficient from positive constituents, Scientific reports 7(1) (2017) 1-8.
[98] Q. Ji, J. Moughames, X. Chen, G. Fang, J.J. Huaroto, V. Laude, J.A.I. Martínez, G. Ulliac, C. Clévy, P. Lutz, 4D Thermomechanical metamaterials for soft microrobotics, Communications Materials 2(1) (2021) 1-6.
[99] S. Camarero-Espinosa, L. Moroni, Janus 3D printed dynamic scaffolds for nanovibration-driven bone regeneration, Nature communications 12(1) (2021) 1-12.
[100] S. Ribeiro, C. Ribeiro, E.O. Carvalho, C.R. Tubio, N. Castro, N. Pereira, V. Correia, A.C. Gomes, S. Lanceros-Méndez, Magnetically activated electroactive microenvironments for skeletal muscle tissue regeneration, ACS Applied Bio Materials 3(7) (2020) 4239-4252.
[101] E. Türker, N. Demirçak, A. Arslan-Yildiz, Scaffold-free three-dimensional cell culturing using magnetic levitation, Biomaterials science 6(7) (2018) 1745-1753.

[102] Y. Zheng, M.K.L. Han, Q. Jiang, B. Li, J. Feng, A. del Campo, 4D hydrogel for dynamic cell culture with orthogonal, wavelength-dependent mechanical and biochemical cues, Materials Horizons 7(1) (2020) 111-116.
[103] M.M. Fernandes, P. Martins, D.M. Correia, E.O. Carvalho, F.M. Gama, M. Vazquez, C. Bran, S. Lanceros-Mendez, Magnetoelectric Polymer-Based Nanocomposites with Magnetically Controlled Antimicrobial Activity, ACS Applied Bio Materials 4(1) (2021) 559-570.
[104] X. Chen, S. Han, W. Wu, Z. Wu, Y. Yuan, J. Wu, C. Liu, Harnessing 4D Printing Bioscaffolds for Advanced Orthopedics, Small 18(36) (2022) 2106824.
[105] Z. Meng, M. Liu, H. Yan, G.M. Genin, C.Q. Chen, Deployable mechanical metamaterials with multistep programmable transformation, Science Advances 8(23) (2022) eabn5460.
[106] R. Galea, K.K. Dudek, P.-S. Farrugia, L.Z. Mangion, J.N. Grima, R. Gatt, Reconfigurable magneto-mechanical metamaterials guided by magnetic fields, Composite Structures 280 (2022) 114921.
[107] F. Bobbert, S. Janbaz, A. Zadpoor, Towards deployable meta-implants, Journal of Materials Chemistry B 6(21) (2018) 3449-3455.
[108] W. Zhao, Z. Huang, L. Liu, W. Wang, J. Leng, Y. Liu, Porous bone tissue scaffold concept based on shape memory PLA/Fe3O4, Composites Science &
Technology 203 (2021) 108563.
[109] W. Zhang, H. Wang, H. Wang, J.Y.E. Chan, H. Liu, B. Zhang, Y.-F. Zhang, K. Agarwal, X. Yang, A.S. Ranganath, Structural multi-colour invisible inks with submicron 4D printing of shape memory polymers, Nature Communications 12(1) (2021) 1-8.
[110] M. Hippler, E. Blasco, J. Qu, M. Tanaka, C. Barner-Kowollik, M. Wegener, M. Bastmeyer, Controlling the shape of 3D microstructures by temperature and light, Nature communications 10(1) (2019) 1-8.
[111] E.N. Marieb, K. Hoehn, Human anatomy & physiology, Pearson education2007.
[112] B.D. Ratner, A.S. Hoffman, F.J. Schoen, J.E. Lemons, Biomaterials science: an introduction to materials in medicine, Elsevier2004.
[113] M. Mirzaali, S. Janbaz, M. Strano, L. Vergani, A.A. Zadpoor, Shape-matching soft mechanical metamaterials, Scientific reports 8(1) (2018) 965.
[114] P. Soman, D.Y. Fozdar, J.W. Lee, A. Phadke, S. Varghese, S. Chen, A three-dimensional polymer scaffolding material exhibiting a zero Poisson's ratio, Soft Matter 8(18) (2012) 4946-4951.
[115] N.C. Paxton, R. Daley, D.P. Forrestal, M.C. Allenby, M.A. Woodruff, Auxetic tubular scaffolds via melt electrowriting, Materials & Design 193 (2020) 108787.

3

Bone cell response to additively manufactured 3D micro-architectures with controlled Poisson's ratio: auxetic *vs.* non-auxetic meta-biomaterials

Yarali, E., Klimopoulou, M., David, K., Boukany, P. E., Staufer, U., FratilaApachitei, L. E., ... & Mirzaali, M. J. (2024). Bone cell response to additivelymanufactured 3D micro-architectures with controlled Poisson's ratio: Auxetic vs. non-auxetic meta-biomaterials. *Acta Biomaterialia*, 177, 228-242.

The Poisson's ratio and elastic modulus are two parameters determining the elastic behavior of biomaterials. While the effect of elastic modulus on the cell response is widely studied, very little is known regarding the effects of the Poisson's ratio. The micro-architecture of meta-biomaterials determines not only the Poisson's ratio but also several other parameters that also influence cell response, such as porosity, pore size, and effective elastic modulus. It is, therefore, very challenging to isolate the effects of the Poisson's ratio from those of other micro-architectural parameters. Here, we computationally design meta-biomaterials with controlled Poisson's ratios, ranging between -0.74 and +0.74, while maintaining consistent porosity, pore size, and effective elastic modulus. The 3D meta-biomaterials were additively manufactured at the micro-scale using 2PP, and were mechanically evaluated at the meso-scale. The response of murine preosteoblasts to these meta-biomaterials was then studied using *in vitro* cell culture models. PPR meta-biomaterials resulted in higher metabolic activity than those with NPRs. The cells could attach and infiltrate all meta-biomaterials from the bottom to the top, fully covering the scaffolds after 17 days of culture. Interestingly, the meta-biomaterials exhibited different cell-induced deformations (*e.g.,* shrinkage or local bending) as observed via scanning electron microscopy. The outcomes of osteogenic differentiation (*i.e.,* Runx2 immunofluorescence staining) and matrix mineralization (*i.e.,* Alizarin red staining) assays indicated the significant potential impact of these meta-biomaterials in the field of bone tissue engineering, paving the way for the development of advanced bone meta-implants.

3.1 Introduction

Both the effective elastic modulus of scaffolds (~stiffness) and the biomaterial's Young's modulus may modulate cell fate and subsequent tissue development through mechanotransduction pathways involving cytoskeletal reorganization, and changes in gene expression and protein synthesis [1-4]. It is, therefore, necessary to consider the elastic modulus of the target tissue in the design of biomaterials and scaffolds, which can vary greatly from soft tissues (*e.g.,* brain with an elastic modulus of approximately 1-4 kPa [5-7]) to hard tissues (*e.g.,* cancellous bone with an elastic modulus of around 0.04-1 GPa [6, 8]).

Several strategies can be employed to modulate the effective elastic modulus of scaffolds depending on the targeted tissue, biochemical properties, and manufacturing techniques. These strategies encompass a variety of factors, including the base material, coating, external stimuli, and geometrical cues [9-11]. For instance, in porous scaffolds or implants, the micro-architectural design determines the effective elastic modulus with porosity and pore size serving as critical morphological parameters that need to be tailored to mimic native tissues [12, 13].

In addition to the effective elastic modulus, the Poisson's ratio is a crucial factor in biomaterial design and is known to play a significant role in regulating cell behavior

[9, 14-17]. The Poisson's ratio of architected biomaterials with repetitive unit cells is a function of the kinematic design of their underlying mechanisms. This ratio can be varied from negative to positive values by rationally adjusting the geometrical designs of the repetitive unit cells [18, 19]. Mechanical metamaterials offer a promising approach to control the Poisson's ratio while keeping the effective elastic modulus unaffected. These materials are a class of advanced engineered materials featuring unconventional properties owing to their micro-architectural design [20-27].

One example of the unusual properties of mechanical metamaterials is the auxetic property. Auxetic metamaterials expand transversely when stretched longitudinally and contract transversely when compressed longitudinally, which is the opposite of the behavior shown by conventional materials [20, 28-31]. This unique property can make auxetic materials ideal for use in hybrid hip implants, as they can expand on the side of the implant experiencing tension under bending [32]. This can solve the current challenges in traditional hip implants which exhibit shrinkage on the tension side and expansion on the compression side under such loading conditions. Expansion on the compression side is beneficial as it promotes adherence to the surrounding bone and prevents aseptic loosening. However, the shrinkage on the tension side may eventually lead to the creation of a gap between the bone and the implant, increasing the risk of implant loosening. Auxetic meta-biomaterials could address this problem by offering an NPR on the tension side of such implants, which has been already demonstrated as a conceptual design and early prototype [32]. Such a design, therefore, can prevent implant loosening and improve the connection between the implant and the surrounding bone [32, 33]. Therefore, auxetic meta-biomaterials have the potential to offer unique solutions to the challenges faced in the design of implantable medical devices [34].

To better understand the effects of mechanical cues on cell-scaffold interactions, both effective elastic modulus and Poisson's ratio must be considered. However, the maximum values of both the Poisson's ratio and effective elastic modulus are coupled with each other (Hashin–Shtrikman bounds [35-37]). The effective elastic modulus is coupled with micro-architectural parameters, which makes it challenging to change either the morphology or the elastic behavior without affecting the other. However, rational design techniques could be used to decouple the Poisson's ratio of meta-biomaterials from their effective elastic modulus and morphological properties.

Recent studies have highlighted the significance of the Poisson's ratio in regulating cell behavior [9, 13, 17, 38-40]. For example, NPR meta-biomaterials have been shown to differently affect cell proliferation [17], differentiation [9], alignment, and directionality, as compared to PPRs [16]. However, most research has focused on the effect of the Poisson's ratio in 2D (and 2.5D) meta-biomaterials, with only a few studies investigating the impact of the Poisson's ratio in 3D biomaterials [9, 16, 40]. In those studies, however, the interdependence between micro-architectural parameters, Poisson's

ratio, and effective elastic modulus, has not been sufficiently addressed. Here, we aim at elucidating the independent effects of the Poisson's ratio in 3D micro-environments on the response of preosteoblast cells.

Advanced micro-AM techniques, such as 2PP, have emerged as a valuable tool for exploring the influence of the Poisson's ratio on cell response in 3D micro-/meso-scale structures [41-44]. The 2PP technique creates high-resolution, complex meso-scale structures with micro-metric or sub-micrometric features [45-50], enabling the creation of 3D scaffolds with varying Poisson's ratios and allowing the study of the impact of these properties on the cell behavior in 3D. Moreover, the availability of chemically cytocompatible photoresists makes the 2PP technique a potential tool in cell biology studies [42].

In this study, we first used computational mechanics and the FEM to rationally design meta-biomaterials with different values of the Poisson's ratio (range of - 0.74 to + 0.74) while maintaining similar values of the effective elastic modulus, porosity, pore size, and strut diameter. Then, we employed the 2PP technique to fabricate these complex meta-biomaterials at the meso-scale (*i.e.,* 1356.0×1356.0×1800.0 μm3 with a strut diameter of 36.0 μm) using a methacrylate photosensitive polymer (called IP-Q™). Subsequently, we measured the mechanical properties of IP-Q at the micro-scale (*i.e.,* a cylinder with equal diameter and height of 30.0 μm) for our FEM models using micro-compression, and similarly, characterized the mechanical properties of the meta-biomaterials at the meso-scale to validate our rational design approach. Finally, we evaluated the response of mouse preosteoblasts seeded onto the meta-biomaterials by assessing their viability, metabolic activity, spatiotemporal organization, as well as the osteogenic differentiation and matrix mineralization.

Our study provides new insights into the importance of the Poisson's ratio, as a mechanical cue in the design of meta-biomaterials. This offers new opportunities for developing innovative 3D-engineered micro-environments that can be customized for specific tissue engineering and regenerative medicine applications.

3.2 Results

3.2.1 Design of the meta-biomaterials

Five distinct structures with controlled Poisson's ratios, namely negative (NPR), zero (ZPR and Hybrid), and positive (PPR_p and PPR_s), were designed based on the results of the computational models (Figure 1.b-d). The NPR, PPR_s and Hybrid (a combination of NPR and PPR) designs were created with the same porosity, longitudinal effective elastic modulus (= E_L, Figure 1.d.i), pore size, strut diameter, and overall dimensions. The PPR_p exhibited almost identical porosities but different values of the effective longitudinal elastic modulus as compared to the NPR meta-biomaterial. The ZPR

meta-biomaterial featured a near-zero Poisson's ratio (Figure 1.d.iii), but a different pore shape as compared to the Hybrid one. The designed structures exhibited different mechanical behaviors when loaded in different directions (x or y), as they were transversely isotropic structures. We, therefore, reported the transverse effective elastic modulus (= E_T, Figure 1.d.i) and its ratio to the longitudinal effective elastic modulus (Figure 1.d.iii and Table 1).

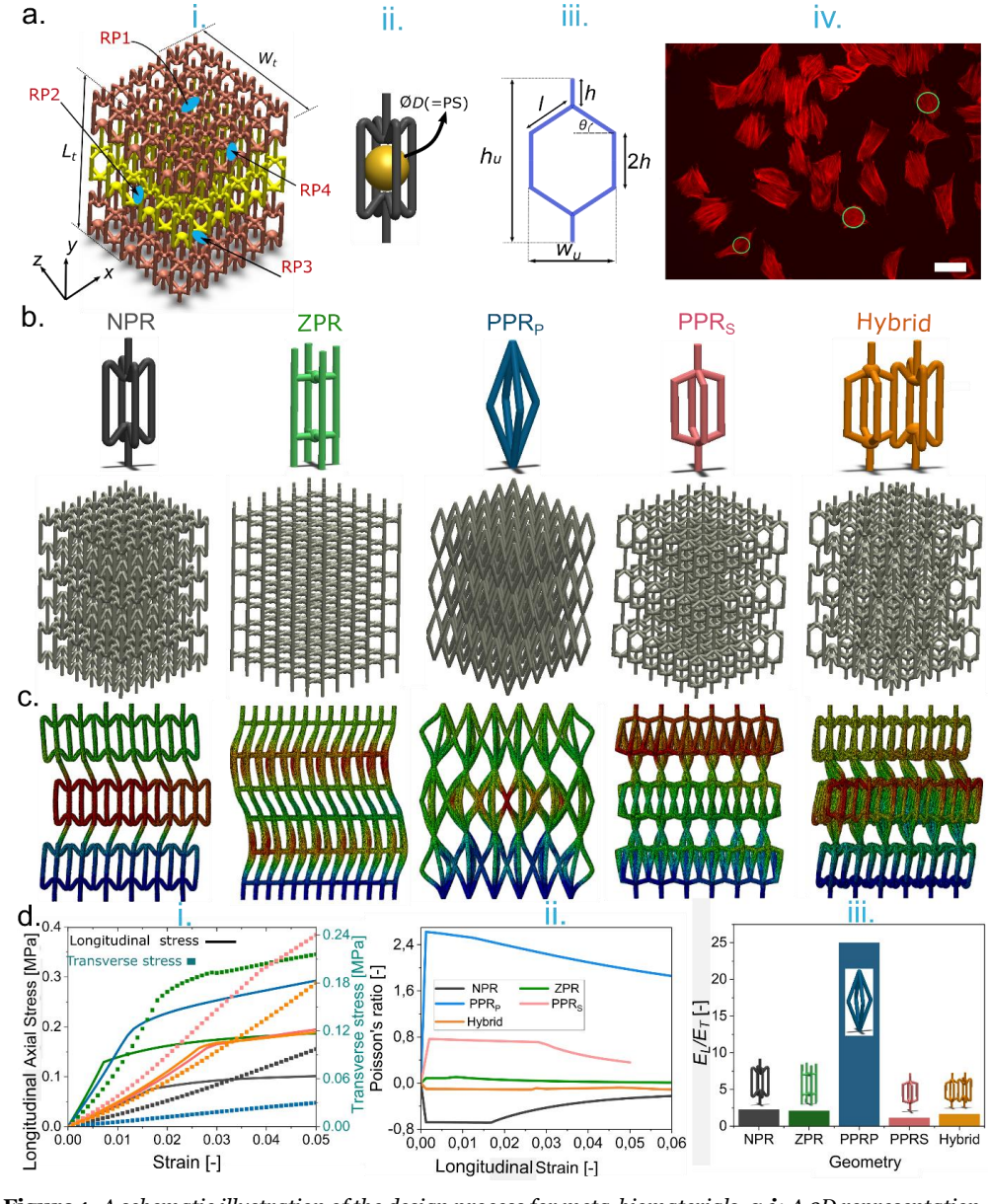

Figure 1. *A schematic illustration of the design process for meta-biomaterials.* ***a.i:*** *A 3D representation of the meta-biomaterials, displaying the corresponding geometrical parameters, a global coordinate system*

$(x - y - z)$, and reference points (i.e., RP1-RP4). L_t and W_t represent the overall height and width of the meta-biomaterials, respectively. ***a.ii:*** *A depiction of a unit cell of the meta-biomaterials, highlighting the pore size (PS) and the diameter (D) of the yellow sphere.* ***a.iii:*** *A 2D schematic representation of a unit cell of the meta-biomaterials with corresponding geometrical parameters. h_u and w_u, h, l , and θ represent the overall height and width of a unit cell, length of vertical struts, length of tilted struts, and the angle between two struts, respectively.* ***a.iv.*** *The preosteoblast cells after 1 day of culture (immunofluorescence staining of actin). The scale bar represents 100 µm.* ***b.*** *A schematic illustration of the final design of the meta-biomaterials and their corresponding unit cells.* ***c.*** *The deformation pattern of the meta-biomaterials modelled using FEM at 6% longitudinal strain under quasi-static loading. The contour qualitatively displays the magnitude of the measured displacement in the specified units (blue represents the lowest magnitude while red indicates the highest one).* ***d.*** *The final numerical results of the meta-biomaterials in terms of the longitudinal stresses/strains (**i.**), Poisson's ratio (i.e., v_{yz}) (**ii.**) and the ratio of the longitudinal effective elastic modulus to the transverse one (**iii.**).*

Table 2. *Geometrical and mechanical properties of the final design of the meta-biomaterials with their corresponding mean and standard deviations. PS and d_s respectively stand for pore size and strut diameter. Note that the numbers in the table without standard deviations are obtained from computational simulations and computer-aided design (CAD) for which no standard deviations are available.*

Type	2D unit cell	Porosity [%]	E_L Exp [MPa]	E_L FEM [MPa]	E_T FEM [MPa]	E_L / E_T [-]	ν_{yz} [-]	ν_{xz} [-]	ν_{xy} [-]	d_s [µm]	PS [µm]
NPR		92.64	9.67±0.40	4.50	2.00	2.25	-0.74	-0.22	-0.22	36.0	184.0
ZPR		92.64	20.00±0.80	18.00	8.60	2.09	0.08	0.05	0.03	36.0	184.0
PPR_p		92.64	16.11±1.10	15.00	0.60	25.00	2.24	-0.59	0.11	36.0	174.7
PPR_s		94.47	10.15±0.40	5.64	5.00	1.13	0.74	-0.22	0.33	36.0	184.0
Hybrid		92.64	13.30±0.60	5.89	3.60	1.64	-0.10	0.00	-0.07	36.0	174.0

We also assessed the deformation pattern of the meta-biomaterials under a certain compression strain (= 6%) (Figure 1.c). The designs with NPRs and ZPRs exhibited different modes of deformation (lateral sliding), unlike those with a PPR (*i.e.,* v_{yz}). The mechanical and morphological parameters of the final design of the meta-biomaterials are presented in Table 1. It is worth mentioning that the PPR designs (*i.e.,* PPR_p and PPR_s) exhibited NPR in one direction (*i.e.,* v_{xz}, Table 1). We believe that this can be improved in further studies by considering three symmetric planes in the design of the meta-biomaterials.

3.2.2 3D Printing and mechanical characterization of the meta-biomaterials

We used 2PP to fabricate the designed meta-biomaterials at the micro-scale (Video 1 of the supplementary material and Figure 2.a). However, printing complex micro-structures via 2PP requires finding refined printing parameters (*e.g.,* laser power, scanning speed, slicing distance (the z-distance between two adjacent layers), and hatching distance (the x-, and y- distance between two adjacent polymerized lines)), stitching parameters (*e.g.,* block size, shear angle and connection between blocks), scanning mode (piezo or z-drive), and acceleration and movement of the stage. Structures that needed to be supported during the printing process, such as NPR and Hybrid, required careful attention to ensure high-quality prints. The detailed printing parameters are described in the experimental section.

We measured the mechanical properties of IP-Q at the micro-scale and found that its engineering stress-strain curves are highly nonlinear (Figure 2.b.i and Video 2 of the supplementary material). We considered such nonlinearity (hyperelastic behavior) in the modeling of the meta-biomaterials through the third-order reduced polynomial hyperelastic model. Based on the material's behavior at smaller strain (below 5% in Figure 2.b.i), the Young's modulus of the IP-Q was found to be 823.00± 23 MPa (mean value ± SD).

To characterize the macro-mechanical properties of the 3D printed specimens (Figure 2.c), we obtained the engineering stress-strain variation (Figure 2.b.ii). The stress values, represented by the mean values with their corresponding standard deviations as shaded regions, display significant fluctuations, which can be attributed to the densification and possible damage (at higher strains) in the studied lattice structures. We focused on the initial linear part of the stress/strain graph (*i.e.,* < 2% axial strain) to determine the effective elastic modulus of our specimens (Figure 2.b.ii, and Table 1).

It is worth noting that we included a solid pedestal (1400×1400×200 μm^3) beneath each scaffold (Figure 2.c). The addition of the solid pedestal was required to prevent the specimens from moving and ensure their stability during cell culture, thus facilitating subsequent handling and processing steps. This modification is expected to be

particularly helpful in the development of complex and delicate biofabricated structures with low relative densities (< 10%), where maintaining their stability and avoiding potential disruptions during cell culture is of utmost importance.

The deformation patterns of meta-biomaterials following compression tests were captured using an optical microscope (Figure 2.d). In these tests, the structures, particularly in the middle part, were observed to deform laterally, either to the right or left, under large deformation at 50% longitudinal strain.

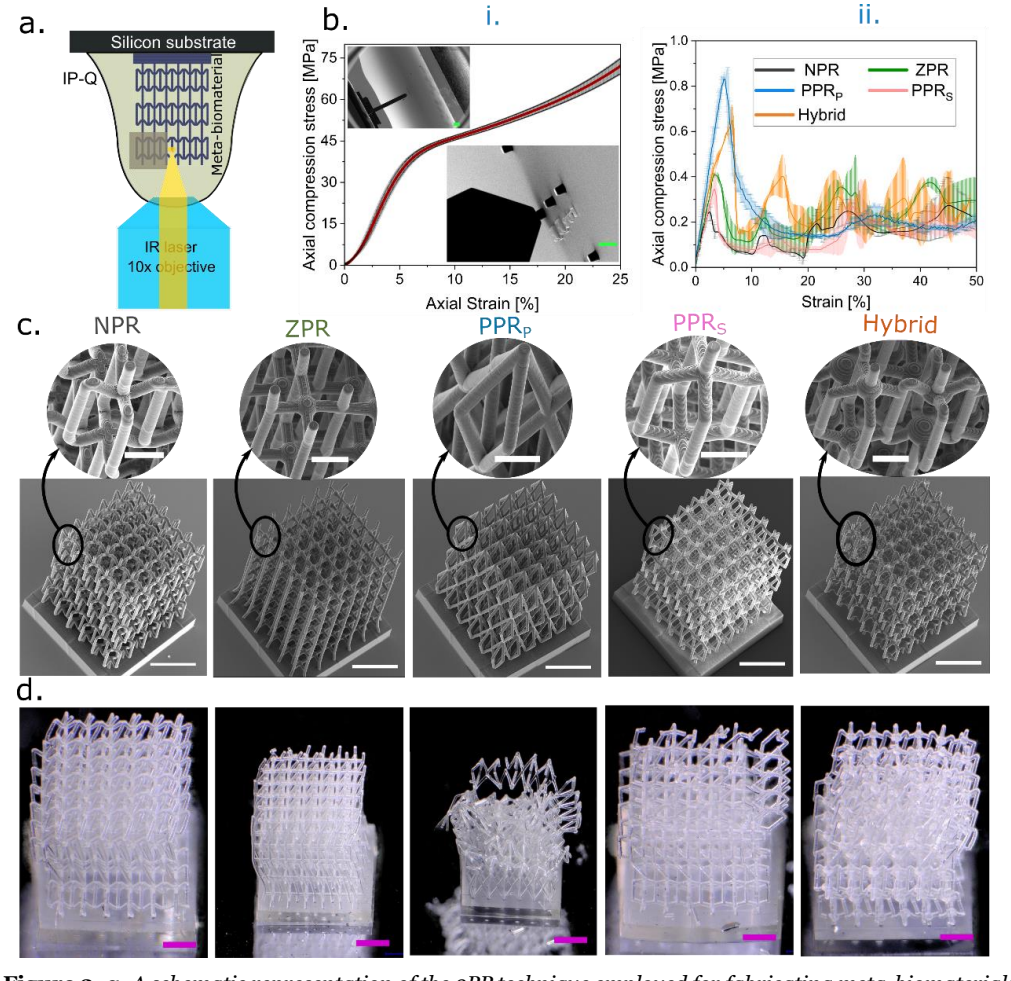

Figure 2. ***a.*** *A schematic representation of the 2PP technique employed for fabricating meta-biomaterials from IP-Q photoresist on a silicon substrate using a laser (10× objective).* ***b.*** *The mechanical evaluation of IP-Q cylinders (**i**) and meta-biomaterials (**ii**);* ***i.*** *The engineering stress-strain curves measured for IP-Q-based specimens at the micro-scale under 25% strain and a strain rate of 0.25 µm s⁻¹. The scale bars in the upper and lower images correspond to 50 and 500 µm, respectively. The red and black lines represent mean and standard deviation, respectively.* ***ii.*** *The compression testing of the meta-biomaterials at 50% strain (1 mm displacement) performed with a displacement rate of 10 µm s⁻¹.* ***c.*** *The SEM images of meta-biomaterials 3D printed using 2PP, showcasing their respective unit cells at higher magnifications. The*

scale bars for the overall structures and unit cells measure 500 and 100 μm, respectively. ***d.*** *The optical microscopy of compressed meta-biomaterials at 50% strain (1 mm displacement) when tested using a displacement rate of 10 μm s^{-1}. The scale bar represents 300 μm.*

3.2.3 Attachment and growth of the preosteoblast cells

The polymerized IP-Q resin employed for the creation of the meta-biomaterials was found to be cytocompatible, following viability tests conducted on the MC3T3-E1 preosteoblasts (Figure S1 of the supplementary material). The cells were able to attach, grow, and migrate upwards to the top surfaces of the structures in about 6 days, as confirmed by SEM imaging after various culturing times (Figure 3). This was supported by the seeding along the *y*-direction (Figure 1.a.i), which facilitated cell growth through the pores and onto the flat pedestal. The micro-architectures of the unit cells promoted the upward growth of the cells. After 17 days, the cells had already covered the entire meta-biomaterials. However, it was observed that the NPR scaffolds had fewer cells as compared to the other structures (Figures 3, 4; days 6 and 10).

Interestingly, increasing the cell culture time revealed local bending of the struts in the cell-laden meta-biomaterials (Figures 3, 4, and S2 of the supplementary material). As cells grew upward, they appeared to crawl along the struts, stretching them until the entire meta-biomaterial was covered. This resulted in local bending, which was more pronounced in the NPR group than in the other groups.

Cell growth together with the shrinkage of the cells as well as the meta-biomaterials over time induce 3D deformation in meta-biomaterials (see Figures 3 and 4.b, with statistical data reported in Table S1 in the supplementary material). This effect was particularly prominent in the PPR_p group, where the shape of the structure transitioned from a cuboid to a pyramid.

To determine whether the observed substantial deformation is a result of living cells interacting with the meta-biomaterials, a control group without cells on day 17 was also examined. This group underwent the same culture, fixation, and dehydration conditions as the cell culture specimens with cells (first column of Figure 3). To quantify the deformation of these meta-biomaterials, the shrinkage of their top surface was measured (Table 2). It should be noted that the shrinkage was calculated based on a comparison between the initial configuration immediately after fabrication and the current surface area.

The induced deformation in the cell-free meta-biomaterials was negligible for the NPR, ZPR, PPR_s and Hybrid groups on day 10, except for the PPR_p group. The PPR_p group exhibited an average shrinkage of 29.1% on day 17, which warrants consideration when evaluating the final deformation attributed to the cells (Figure 3, first column).

Furthermore, to ascertain whether the deformation observed in the meta-biomaterials was attributable to living cells interacting with the structures or cell shrinkage during SEM imaging processes, we quantified the shrinkage of the meta-biomaterials before fixation and dehydration on day 17 (Figure 3, last column, control with cells before fixation and dehydration). The optical images of the meta-biomaterials (top surfaces) revealed that PPR_p group had experienced the highest degree of shrinkage as compared to the other meta-biomaterials (46.1% vs. 21.1%). This finding suggests that the final deformation depicted in the SEM images resulted from both the forces exerted by the cells and the shrinkage caused by cell dehydration and specimen processing.

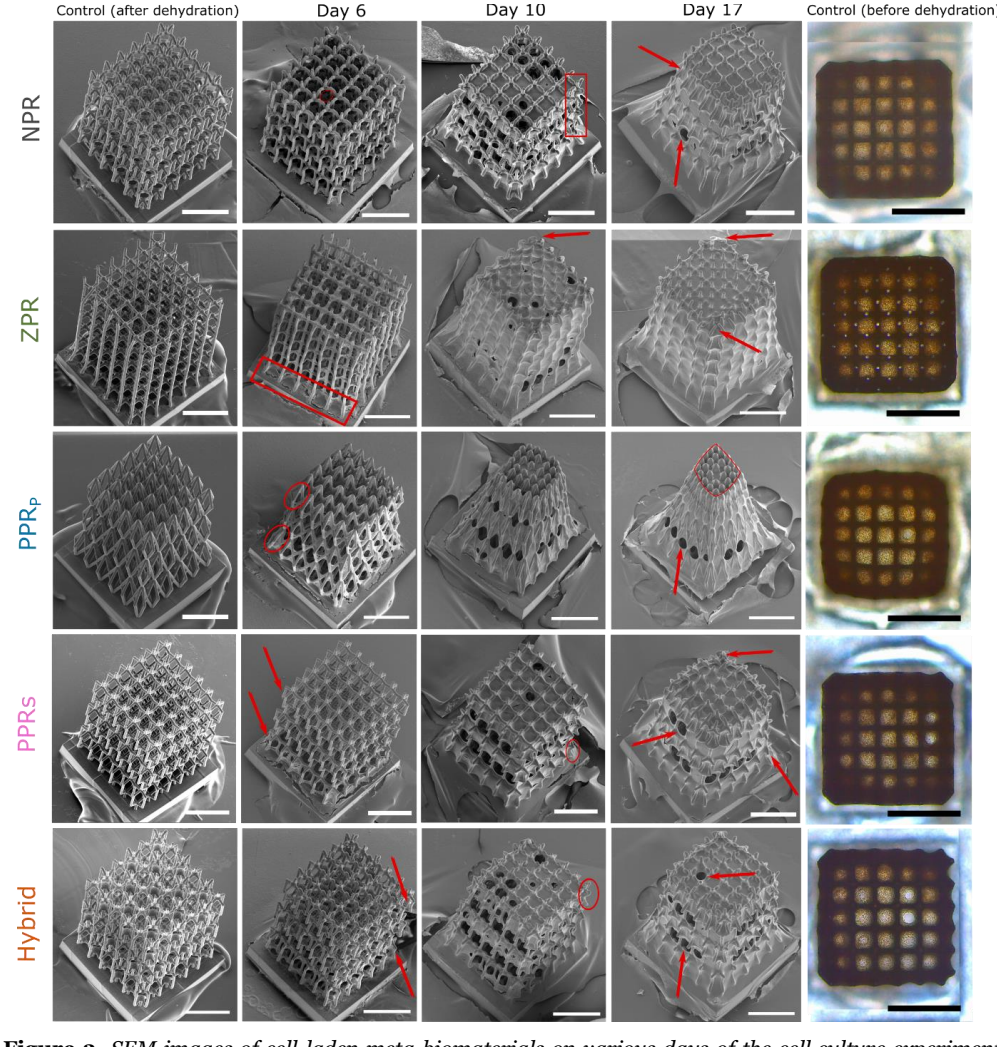

Figure 3. *SEM images of cell-laden meta-biomaterials on various days of the cell culture experiments. Included are optical microscopy images of control specimens without cells post-fixation and dehydration (day 17, first column), and control specimens with cells pre-fixation and dehydration after a 17-day culture*

period. Scale bars for all the SEM and optical microscopy images measure 500 and 700 μm, respectively. Red annotations highlight local deformations resulting from cellular growth.

Table 2. *The shrinkage ratio of the top surface of the cell-free meta-biomaterials (after dehydration) and cell-laden meta-biomaterials (before dehydration).*

Type	NPR [%]	ZPR [%]	PPR_p [%]	PPR_s [%]	Hybrid [%]
Control (no cell after dehydration), day 17	5.9±0.5	9.3±1.1	29.1±2.1	7.0±0.6	12.7±0.9
Control (with cells before dehydration), day 17	21.1±1.0	24.1±2.4	46.1±3.1	22.2±2.0	21.6±1.1

3.2.4 Metabolic activity and osteogenic response of the preosteoblast cells

The metabolic activity of the cells seeded on the different meta-biomaterials increased with time (Figure 4.c, with statistical data reported in Table S2 of the supplementary material), indicating that the cells could proliferate and grow within the microporous structures. It is important to note that, to account for the effects of the metabolic activity of the initial cell population, the metabolic activities were normalized by dividing them by their corresponding day 1 value. This adjustment was made because most cells were situated on the pedestal during the early stages of cell culture (Figure 3 and 4). The PPR_p and PPR_s groups displayed the highest metabolic activity at later time points, while the NPR group had the lowest (Figure 4.c).

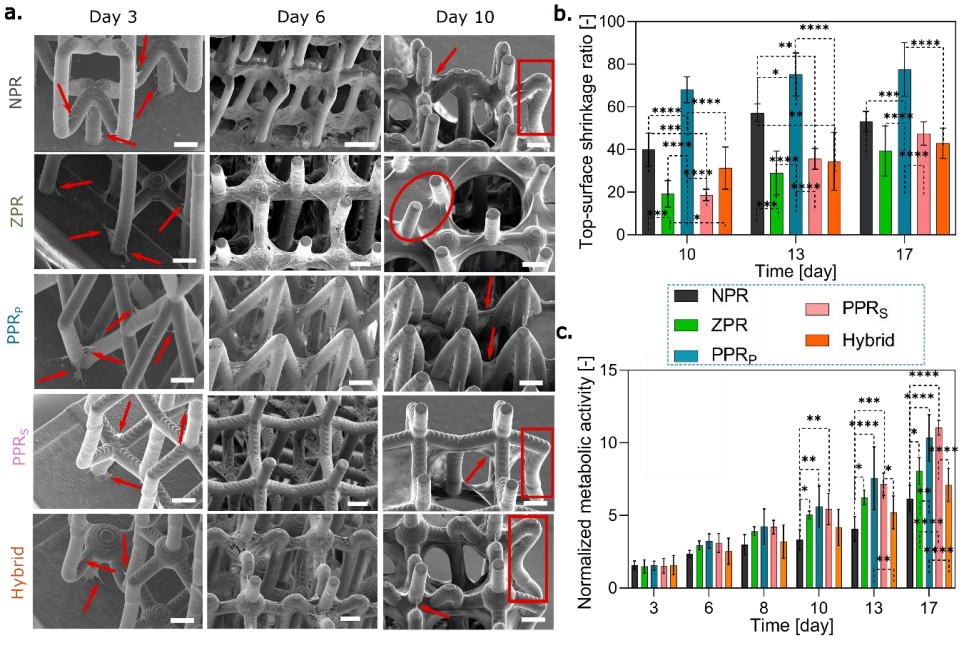

Figure 4. ***a.*** *High-magnification SEM images of meta-biomaterials exhibiting local deformation (bending) induced by cellular activity. Red arrows indicate cell presence, while ellipses and rectangles highlight cell-induced deformation (bending). The scale bar measures 50 µm, except for the NPR image at day 6, which has a 100 µm scale bar.* ***b.*** *A quantitative analysis of the SEM-measured deformations, represented as the shrinkage ratio of the top-surface of the meta-biomaterial specimens, with* $(p - value = < 0.0001,\ F\ (4, 23) = 48.19,\ \eta^2 = 0.8934)$, $(p - value = < 0.0001,\ F\ (4, 25) = 26.09,\ \eta^2 = 0.8068)$ *and* $(p - value = < 0.0001,\ F\ (4, 25) = 17.30,\ \eta^2 = 0.7346)$ *on days 10, 13 and 17, respectively. Note that the number of independent samples per each group was 6 except for the NPR on day 10, which was 5.* ***c.*** *The normalized metabolic activity of the cells across a 17-day culture period (relative to day 1), with* $(p - value,\ F\ (DFn = 4, DFd = 32),\ \eta^2)$ *of (0.0009, 6.150, 0.4346), (< 0.0001, 10.07, 0.5573) and (< 0.0001, 29.15, 0.7846) on days 10, 13 and 17, respectively. Note that the number of independent samples per each group at each timepoint was 7, except for PPRs and Hybrid groups, which was 8. Statistical significance is denoted by *, **, ***, **** corresponding to* $p < 0.05$, $p < 0.01$, $p < 0.001$, *and* $p < 0.0001$, *respectively. The non-asterisks groups indicate that the differences between the groups are not statistically significant (i.e.,* $p > 0.05$*).*

To evaluate the osteogenic response of the preosteoblast cells, three groups were selected, namely NPR, PPR_p, and Hybrid. The NPR group comprised meta-biomaterials with an extreme NPR, the PPR_p represented meta-biomaterials with an extreme PPR (*i.e.*, v_{yz}) as a counterpoint to the NPR group, and the Hybrid group served as a control group possessing almost the same effective elastic moduli and porosity as the NPR group but with a near-zero Poisson's ratio. The osteogenic differentiation of the cells was assessed by measuring the expression of Runx2 after 10 days of culture (Figure 5.a.i and 5.b.i and Video 3-8 of the supplementary material) whereas matrix mineralization was assessed by Alizarin red staining of the matrix after 17 days of culture

(Figure 5.a.ii and 5.b.ii and Video 9-14 of the supplementary material). Both assessments were representative of the top surface of the scaffolds and not the entire 3D structures.

After 17 days of culture, a mineralized matrix was detected in all the three different meta-biomaterials (Figure 5.a.ii and 5.b.ii). Interestingly, the mineralized matrix presents on the surface of the NPR specimens, which exhibited less cell coverage, presented a relatively ordered pattern (predominantly within the pores).

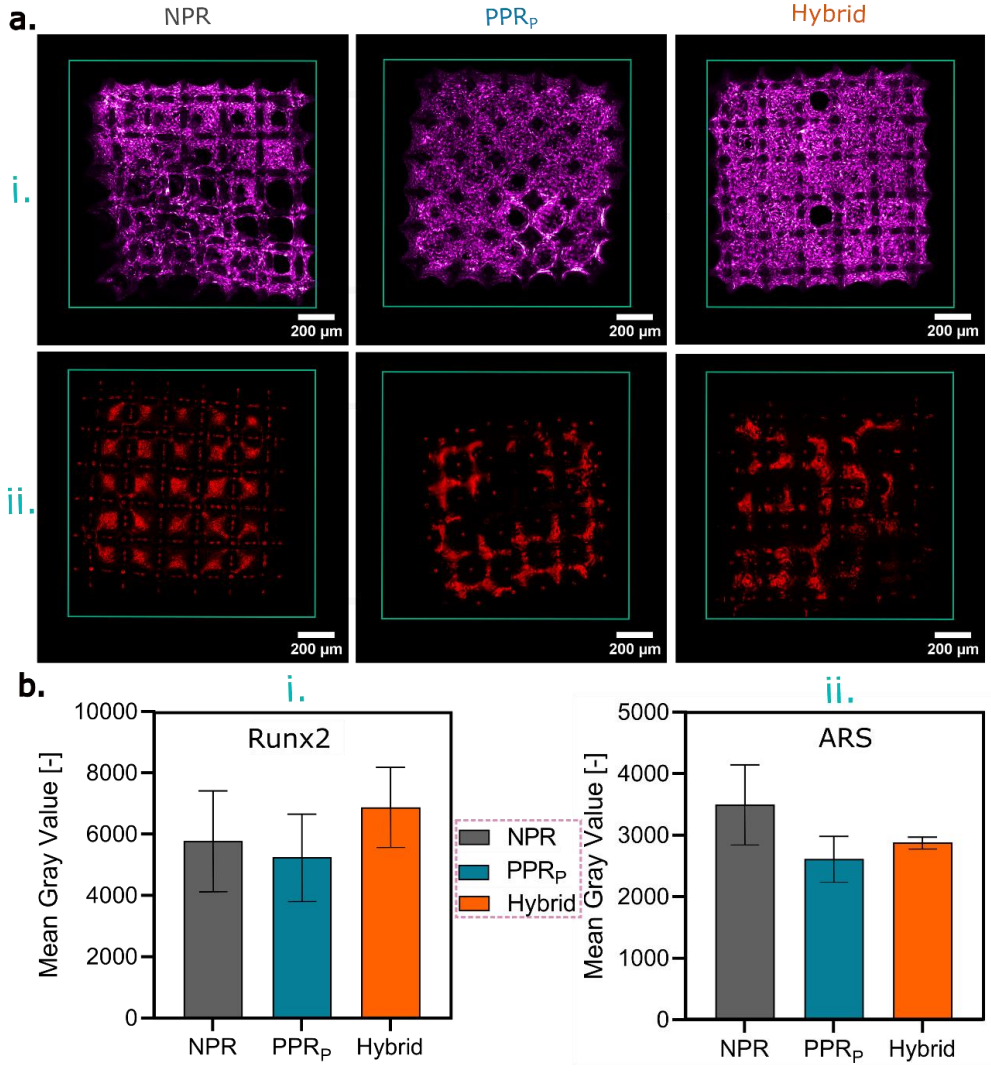

Figure 5. *The osteogenic responses of preosteoblasts-laden meta-biomaterials.* ***a.*** *The confocal microscopy images of Runx2 (**a.i**) and mineralized matrix (**a.ii**) on days 10 and 17, respectively. The green rectangle represents the initial cross-section of the meta-biomaterials post-fabrication.* ***b.*** *A quantitative*

*analysis of Runx2 (**b.i**) and mineralized matrix (**b.ii**). No statistically significant differences were detected ($p > 0.05$) for the Runx2 and ARS assays.*

3.3 Discussion

3.3.1 Rational design and fabrication of the meta-biomaterials

The developed meta-biomaterials with controlled Poisson's ratio were found to influence the response of preosteoblast cells. To design the meta-biomaterials studied here, several physical parameters, including, porosity, pore size, strut diameter, and effective elastic modulus (~stiffness), were considered, so as to mimic the properties of the trabecular bone as much as possible. Nevertheless, the effective elastic modulus of the developed meta-biomaterials was not still in the range of the trabecular bone (0.04-1 GPa [6,8]). This point can be addressed either by adjusting the micro-architecture of the meta-biomaterials or by changing the base material from which the meta-biomaterials are made. Geometry-based adjustment of the effective elastic modulus of the meta-materials can be achieved by changing the strut diameter, changing the angle between the struts (θ), and modifying the ratio of the height of the unit cells to their width (*i.e.*, h_u/w_u in Figure 1.a.iii). As such, increasing strut diameter leads to increased values of the effective elastic modulus while also drastically decreasing the Poisson's ratio. Changing the angle between the struts (θ) can disrupt the compatibility between the pore sizes of the designs and affect the effective elastic modulus. The h_u/w_u value affects the pore size, effective elastic modulus, and porosity such that a lower ratio leads to better consistency for pore size, considering the cell size and the similarity of pore sizes in both PPR and NPR meta-biomaterials.

Another approach for manipulating the effective elastic modulus of meta-biomaterials is to modify the additive manufacturing parameters. For example, the Young's modulus of the base material (IP-Q) varies during the 2PP process as the delivered dose of energy (*i.e.,* laser power × scanning speed^{-1}) increases [56], or as the slicing distance and hatching distance [56] decrease. Modifying some other printing parameters (*e.g.*, by switching between alternate and non-alternate hatch lines) may also have similar effects. However, decreasing the scanning speed, slicing distance, or hatching distance drastically increases the printing time for such complex meta-biomaterials. We optimized the final designs and printing parameters considering the complexity of the designs, printing quality, printing time, while also decoupling their Poisson's ratio from other properties. More details of the optimization process used to adjust the parameters of the manufacturing process can be found in the experimental section.

The meta-biomaterials in this study exhibited transversely isotropic behavior, meaning that they had two planes of symmetry. This resulted in two effective elastic

moduli (*i.e.,* E_{xx}, and E_{yy}) and three Poisson's ratios (*i.e.,* ν_{yz}, ν_{xz}, and ν_{xy}). In the longitudinal direction (*i.e., y*-direction), the Poisson's ratio was decoupled from other mechanical and morphological parameters in some designs, particularly, the NPR and PPRs. However, it is yet not decoupled from effective elastic modulus in the transverse direction (*i.e.,* E_{yy}), Table 1. One way to overcome this is to design a fully isotropic meta-biomaterials with three symmetrical planes (*i.e., xy*, *zy*, and *xz*). In this case, only one effective elastic modulus and one Poisson's ratio would be enough to characterize the meta-biomaterials, and therefore, the decoupling procedure may become less challenging.

We used 2PP and IP-Q photoresist for fabricating the meta-biomaterials studied here because our primary objective in the current study was to understand the response of bone cells (*e.g.,* cell growth and differentiation) to meta-biomaterials with micro-architectural dimensions that are of the same order of magnitude as the size of individual cells. While it is important to study the effects of the fabrication technique and the constituting material on the response of cells to such meta-biomaterials, the options for such types of studies are currently limited because 2PP is the only 3D printing technique capable of generating free-form architected biomaterials with such small dimensions and with precisely controlled architectures. Moreover, changing the fabrication technique can influence the surface properties of the produced meta-biomaterials, which might subsequently affect cell responses. All these potential effects need to be studied in the future.

While the overall quality of the printed meta-biomaterials was assessed using SEM, the quality of the 3D printed meta-biomaterials can be further analyzed in future via other imaging techniques, such as micro-computed tomography (μ-CT) or confocal microscopy.

3.3.2 Mechanical characterization

The experimental and numerical values of the longitudinal effective elastic modulus were in good agreement (Table 1, ZPR and PPR_p groups). We attribute the slight discrepancies between the experimental and numerical values to errors in the micro-mechanical compression tests, the inaccuracies of the macro-mechanical uniaxial test machine, the print quality, and the post-development shrinkage of the structures.

Regarding the pattern transformation of the meta-biomaterials under compression test, the specimens with PPRs were unable to withstand such large deformations while those with ZPRs or NPR deformed without failure up to 50% longitudinal strain. This was attributed to the much larger E_L/E_T value of the PPR_p group as compared to the other experimental groups. The NPR, PPR_s, and Hybrid specimens had the same values of the effective elastic modulus but highly different ultimate strengths (Figure 2.a.ii). For the structures with the same effective elastic modulus, Hybrid and NPR

specimens had the highest and lowest ultimate strength, respectively. Moreover, the Hybrid specimens showed a higher plateau stress after yielding as compared to the PPR_s and NPR specimens. This capability was more highlighted when the cellular forces largely deformed the structures. Such post-yield fluctuations of the stress-strain were mainly due to structural densifications caused by excessive deformation. In PPR_p, however, there was only a negligible degree of densification (Figure 2.a.ii and c). The maximum principal stress in all the structures occurred near the corners of the struts but with different distributions and magnitudes depending on the type of the structure. For instance, the maximum principal stress of PPR_p was higher in the middle layer, unlike the NPR for which the maximum values occurred in the top and bottom layers. The distribution of the maximum principal stress in PPR_s was more homogeneous than in the other groups.

Following the experimental and numerical results (Figure 2.d), the PPR structures, which are characterized by maximal effective elastic modulus ratios (PPR_p) and minimal effective elastic modulus ratios (PPR_s), experienced collapse under large deformation. The discrepancy between the experimental and FEM patterns for the PPR_p and PPR_s groups can be attributed to the inability of our FEM model to detect damage (or failure [57]) and collapse in the struts.

3.3.3 Cell-induced deformation of the meta-biomaterials

The fact that the local bending was more pronounced in the NPR meta-biomaterials can be attributed to the larger length of the struts (h) in this group, resulting in increased bending deformation. In contrast, the ZPR group, consisting of straight struts, demonstrated greater resistance to local bending. This may explain the fewer number of cells observed in the NPR group as compared to the ZPR and PPR_p groups.

Furthermore, from a geometrical perspective, the NPR meta-biomaterial exhibits a negative and acute angle between the struts (*i.e.,* $\theta<0$), whereas the ZPR and PPR_p structures are characterized by zero or positive angles (*i.e.,* $\theta \geq 0$). Such sharp and negative angles in the unit cell of the NPR group may decrease cell growth as compared to the other groups. However, this requires further experiments and dedicated data analysis. Additionally, a noticeable graded bending of the struts was observed, specifically in the NPR group on day 8 (Figure S2 of the supplementary material). This suggests that prior to day 17, when the meta-biomaterial was not yet entirely covered by the cells, the first layer of the meta-biomaterial (particularly in the NPR group) was subjected to bending, resulting in the top surface deforming less (*i.e.*, smaller localized bending) (Figure S2 of the supplementary material).

The higher shrinkage in the PPR_p group can be attributed to the increased E_L/E_T value in the PPR_p group. A higher E_L/E_T value implies that while the PPR_p group exhibited a greater longitudinal effective elastic modulus, it possessed a substantially lower

effective elastic modulus in the transverse direction than the longitudinal one, leading to diminished mechanical strength in the transverse direction (Figure 1.d.ii and Table 1). Consequently, cells can more readily deform these structures (Figure 3). Therefore, the volumetric contraction was more pronounced in the PPR_p group, as compared to local bending.

The cell-induced shrinkage of the meta-biomaterials can be used to study some aspects of mechanotransduction in bone cells. The force transmitted from the cell nuclei to focal adhesion and then to the meta-biomaterials can be back-calculated using computational models [58]. This type of analysis, which is based on computational modeling of some aspects of the relevant mechanobiological processes, can offer a tool for indirect measurement of cellular forces [59,60].

The shrinkage of the non-seeded specimens (Figure 3, first column) was attributed to the properties of the IP-Q material and the micro-architectures of the designed meta-biomaterials. Capillary forces during the fixation and dehydration of the specimens caused them to shrink. In the case of the PPR_p group, higher shrinkage was observed due to the greater differences in its longitudinal and transverse effective elastic moduli (Figure 1.d.ii).

3.3.4 Metabolic activity and osteogenic response of the preosteoblast cells

The reduced metabolic activity in the NPR group is likely due to the sharp angles in the NPR specimens as compared to the PPR structures, which probably hindered cellular adaptation to this micro-architecture, as suggested by the SEM images (Figure 3, day 10 and S2 of the supplementary material, days 8, 13). This may have adversely affected cell growth. Surprisingly, our findings contrast with the reports available in the literature suggesting that auxeticity provides a more favorable environment for mesenchymal stem cells growth [17]. Such contradictory results warrant further investigation for clarification. These discrepancies may be due to the improved isolation of the Poisson's ratio from other micro-architectural parameters in this study as compared to other studies, as well as due to the different cell types, unit cell types and material used. Furthermore, although cells managed to reach and cover most of the meta-biomaterials after 17 days of culture, cell-free spaces remained visible. This observation was supported by the increasing metabolic activity measured until day 17 and higher magnification SEM images (Figure 4 and S2 of the supplementary material).

Regarding the osteogenic response of the preosteoblast cells in the meta-biomaterials, no significant differences in the expression of Runx2 were detected among the various groups (Figure 5.b.i). However, the expressions of both Runx2 and ARS were non-significantly higher in the NPR group as compared to the PPR one (Figure 5.b.i and ii). Previous studies have shown that the neural differentiation of pluripotent

stem cells may be higher in PPR scaffolds as compared to auxetic scaffolds [9]. These findings confirm that the scaffolds were able to support the osteogenic differentiation of preosteoblasts and matrix mineralization. Further research is required to fully understand the effects of the Poisson's ratio on these cellular functions. However, the unit cell geometry appears to influence cell growth in these structures, warranting additional exploration.

It is worth mentioning that different types of ordered or disordered (*i.e.,* random) meta-biomaterials [61] can be designed with the same Poisson's ratios. It is entirely possible and, indeed, likely that cells respond differently to distinct unit cell designs, even if the structures maintain an identical Poisson's ratio. This aspect was a central focus of our study, where we observed different cell behaviors with the ZPR and Hybrid meta-biomaterials, despite both exhibiting almost similar values of the Poisson's ratio.

It should be also noted that while we studied the response of cells to the designed meta-biomaterials under static culture conditions, the cells themselves deformed the meta-biomaterials significantly over a 17-day culture duration (Figure 3). It is, however, important to study the effects of external, dynamic loading on the cell response of meta-biomaterials. Introducing dynamic loading conditions can add complexities, such as changes in the movement of the medium, temporal changes in the pore size, differences in the structure of the unit cell, and local cellular deformations. These factors might influence the cell behavior and need to be further studied in the future. Here we used the cell seeding along the y-direction. We believe that the direction of cell seeding might also influence the cell responses (*e.g.,* cell proliferation and differentiation) due to variations in the unit cell configurations and their mechanical properties.

3.4 Materials and methods

3.4.1 Rational design of the meta-biomaterials

To determine the optimal parameters for the 3D design of meta-biomaterials, we started off with 2D structures to initially guess the mechanical properties. This approach was advantageous as computational modeling of 2D structures is more straightforward than that of 3D structures. Moreover, there is an explicit analytical relationship describing the relationship between the design parameters of hexagonal unit cells and the Poisson's ratio (v) of the resulting 2D meta-biomaterial [51]:

$$v = -\varepsilon_T/\varepsilon_L;\ v_{yz} = ((h/l + sin\,\theta)\,sin\,\theta))\,/\,cos^2\,\theta\,; \quad (1)$$

where ε_T and ε_L denote the transverse and longitudinal strains, respectively. The geometrical parameters h, l and θ are illustrated in Figure 1.a.iii. The porosity of such meta-biomaterials is defined as:

$$Porosity = (1 - V_{scaffold}/V_{solid}) \times 100; \quad (2)$$

where $V_{scaffold}$ and V_{solid} respectively refer to the volumes of the meta-biomaterial calculated from a CAD software and the volume of a solid cube encompassing the entire meta-biomaterial structure ($L_t \times W_t \times W_t$ in Figure 1.a.i).

Furthermore, we defined pore size as the diameter of the largest sphere that can fit within a unit cell of the meta-biomaterials (*i.e.*, the yellow sphere in Figure 1.a.ii).

To rationally design the meta-biomaterials studied here, we employed a combination of a customized Matlab (R2022b) code (Mathworks, US), SolidWorks (2022, Dassault Systèmes, France), and computational models created using a commercial nonlinear FEM code (Abaqus, 2022, Dassault Systèmes, France) for modeling the meta-biomaterials and expediting the process. We applied Equation 1 to obtain a rough approximation of v_{yz} and study the effects of geometrical parameters (*e.g.*, h and l, and θ) on it, which is valid for 2D structures. First, we designed a 2D auxetic meta-biomaterial with a large absolute value of the (negative) Poisson's ratio (= -1) to serve as a reference in our mechanical design. Subsequently, we adjusted the geometrical parameters to match the mechanical and morphological properties of the auxetic structure for other designs. Multiple iterations were performed to calculate the longitudinal effective elastic modulus, porosity, pore size, and strut diameter in 2D structures.

Using the initial approximation of these parameters (*e.g.*, unit cells size, pore size and porosity) in 2D and the cell size constraint, we determined the final 3D designs along with their corresponding unit cells (Figure 1.b) via 3D FEM. We assumed the meta-biomaterials are comprised of 6×6×3 unit cells with an overall dimension of 1356.0×1356.0×1800.0 μm^3 (in x, z, and y, Figure 1.a.i) with a particular definition of the pore size (Figure 1.a.ii) and parametrized unit cells (Figure 1.a.iii). We first applied two constraints to limit the permitted porosity and pore size. We limited the porosity to the values found for the trabecular bone (*i.e.*, 50-95%) [52] while the pore sizes were limited to values exceeding 100.0 μm to allow for easy penetration of preosteoblast cells into the meta-biomaterials and to facilitate mass transport. The latter constraint was based on our measurement of the size of the preosteoblast cells (MC3T3-E1) via visualizing their cytoskeleton morphologies, which indicated that the cells were in the approximate range of 50-100 μm (Figure 1.a.iv). The unit cell parameters (*e.g.*, h or l), were, therefore, adjusted to have a similar effective elastic modulus but different Poisson's ratio values. This resulted in a pore size of 180.1 ± 5.3 μm and a strut diameter of 36.0 μm.

It is noted that both effective elastic moduli and Poisson's ratios reported in Figure 1.d and Table 1 were calculated at small strains (= 1 %) to minimize the effects of plasticity and damage on the calculation. It is worth noting that to calculate the mechanical

and morphological properties of the meta-biomaterials, we used 3D solid elements (instead of beam elements). We merged the struts of meta-biomaterials to create a uniform, single-solid structure. Therefore, no concerns of struts overlapping and multiple mass counting [53] exist.

3.4.2 FEM analysis

The .step (the standard for the exchange of product data) files of the designs were imported from SolidWorks into Abaqus. To model the constitutive behavior of the base material (IP-Q), which exhibited a highly nonlinear behavior (Figure 2.b.i), we used hyperelastic models, allowing IP-Q to be compressible but assuming it to be isotropic. Different hyperelastic models, including Neo-Hookean ($\Psi = C_{10}(\bar{I}_1 - 3) + \frac{1}{D}(J-1)^2$), Mooney-Rivlin ($\Psi = C_{10}(\bar{I}_1 - 3) + C_{01}(\bar{I}_2 - 3) + \frac{1}{D}(J-1)^2$), and third-ordered reduced polynomial ($\Psi = \sum_{i=1}^{3} C_{i0}(\bar{I}_1 - 3)^i + \frac{1}{D_i}(J-1)^{2i}$) were examined. Ψ, $\bar{I}_i$, C_{ij}, D , and J represent strain energy density function, the invariants of the modified Cauchy-Green tensors, distortional response-related coefficients, volumetric response-related coefficients, and total volume ratio, respectively. We calibrated the models based on the uniaxial engineering stress/strain of the polymerized IP-Q under compression loading (Figure 2.b.i), considering strains < 6%, and calculated the material constants. For this purpose, the engineering stress (**P**, first Piola–Kirchhoff stress tensor) was derived from the strain energy density function as $\mathbf{P} = \partial\Psi / \partial\mathbf{F}$, where **F** is the deformation gradient tensor. In uniaxial compression test, considering λ_x, λ_y and λ_z, as stretches in x, y and z directions, $\mathbf{F}_{3\times3} = [\lambda_x, 0, 0; 0, \lambda_y, 0; 0, 0, \lambda_z]$ with $\lambda_x = \lambda_y$. We found the best curve that fitted on the above-mentioned constitutive models and our experimental data in Matlab (R2022b) (Mathworks, US) to calibrate the material constants. The third-order reduced polynomial model provided the best fit between the modeling and experimental results, ensuring enhanced computational stability with a coefficient of determination (R^2) of 0.9910. The material coefficients for the model were determined as $C_{10} = 52.80$ MPa, $C_{20} = 11521.43$ MPa, $C_{30} = -603444.78$ MPa, $D_1 = 0.0003$ MPa^{-1} and $D_2 = D_3 = 0$. The very small values of the volumetric response-related coefficients (D_i) indicated that IP-Q is nearly incompressible.

To apply the boundary conditions to the meta-biomaterials, all the degrees of freedom of the reference points (RPs) were kinematically coupled to the corresponding node sets in the model (Figure 1.a.i). RP1, RP2, RP3, and RP4 were respectively located on the top surface of the structures in the xz plane, the left side of the structures in the yz plane, the bottom surface of the structures in the xz plane, and the right side of the structures in the yz plane. In addition, the sets of RP1-RP3 and RP2-RP4 were respectively used to model the meta-biomaterials along the longitudinal and transverse directions. It is worth mentioning that no RP was considered in the xy plane as the meta-

biomaterials were transversely isotropic. The nonlinear static solver of Abaqus was used for all the simulations, which were assumed to be quasistatic in nature. Geometric nonlinearities were also considered due to the micro-architectural complexity of the meta-biomaterials. To measure the longitudinal effective elastic modulus (E_L) and Poisson's ratio (v_{yz} or v_{yx}), the structures were loaded along the y-direction (loading I) under displacement-controlled conditions. For the transverse effective elastic modulus (E_T), the structures were loaded along the x- or z-direction (loading II) under displacement-controlled conditions. The boundary conditions for the loadings I and II were ($u_{y,RP_3} = 0, u_{y,RP_1} = 0.05 \times L_t$) and ($u_{x,RP_2} = 0, u_{x,RP_4} = 0.05 \times W_t$), respectively, where u is the displacement. The meta-biomaterials were discretized with 3D quadratic tetrahedral elements of type C3D10. To ensure the robustness of our numerical analyses and achieve mesh-independent results, we performed a mesh sensitivity analysis with varying element sizes. The results of this study demonstrated the values calculated for the effective elastic modulus converge within 4% when 450000 elements are used.

The engineering stresses of the simulations were calculated by taking the reaction force derived from the FEM modeling and dividing it by the initial projected cross-sectional area of the meta-biomaterials ($W_t \times W_t$ in loading I and $L_t \times W_t$ in loading II). The engineering strain was calculated by taking the displacement of the relevant RP (RP1 in loading I and RP2 in loading II) and dividing it by the initial height (L_t in loading I) or initial width of the meta-biomaterials (W_t in loading II). Ultimately, the longitudinal and transverse effective elastic moduli were computed using the reaction force of the RPs and the projected cross-sectional areas as:

$$E_L = (F_{RP1}/(W_t \times W_t))/\varepsilon_L;\ E_T = (F_{RP2}/(L_t \times W_t))/\varepsilon_T; \tag{3}$$

where F_{RP1}, and F_{RP2}, respectively represent the longitudinal reaction force of RP1 (in loading I), and the longitudinal reaction force of RP2 (in loading II).

The Poisson's ratios in two orthogonal planes (*i.e.*, v_{yz} (= v_{yx}), v_{xy} (= v_{zy}), and v_{xz} (= v_{zx})) were calculated using the following equations:

$$\begin{aligned} v_{yz} &= -(\bar{u}_{z-right} - \bar{u}_{z-left})/(W_t \times \varepsilon_{y,L})\text{: loading in the } y\text{-direction;} \\ v_{xy} &= -(\bar{u}_{y-bottom} - \bar{u}_{y-top})/(L_t \times \varepsilon_{x,L})\text{: loading in the } x\text{-direction;} \\ v_{xz} &= -(\bar{u}_{z-right} - \bar{u}_{z-left})/(W_t \times \varepsilon_{x,L})\text{: loading in the } x\text{-direction;} \end{aligned} \tag{4}$$

where $\bar{u}$ indicates the average displacements of the nodes on the corresponding surfaces. For example, $\bar{u}_{z-right}$ shows the average displacement of the nodes in the z-direction that are placed on the right side of the meta-biomaterial in Figure 1.a.i. Also, $\varepsilon_{x,L}$ and $\varepsilon_{y,L}$ correspond to the applied longitudinal strains in the x- and y-directions, respectively.

3.4.3 2PP-based fabrication of the meta-biomaterial specimens

The meta-biomaterials were fabricated using 2PP. Their designs were created using a commercial CAD software, SolidWorks (Dassault Systèmes, France), and was exported as a .stl (standard triangle language) file. These .stl files were then imported into the DeScribe software (Nanoscribe, Germany) to generate General Writing Language (.gwl) files. The .gwl files were subsequently imported into Nanowrite (printing software, Nanoscribe, Germany) for connection to the 2PP 3D printer, facilitating the fabrication of the final meta- biomaterials. The specimens were then printed using a Photonic Professional GT+ (Nanoscribe, Germany) 3D printer.

The dip-in laser lithography (DiLL) configuration was employed, with a 10× objective featuring a numerical aperture (N.A) of 0.30. The lens was chosen based on the size of the specimens and solid/void features that needed to be reproduced. A negative tone-methacrylate-based photoresist known as IP-Q (Nanoscribe, Germany) with a refractive index of 1.49 was used as the photoresist. The specimens were printed on silicon substrates (25×25×0.7 mm^3 in dimensions, Nanoscribe, Germany) featuring a refractive index of 3.71.

Furthermore, as the 3D meta-biomaterials exceeded the writing field and working distance of the 10× objective (707.10×707.10 μm^2 and 700 µm, respectively), we divided them into smaller blocks (Figure 2.a). We also conducted multiple printing trials to refine the printing parameters, particularly for the NPR and Hybrid groups. These two groups theoretically had some features that need supports, which were practically challenging to print. To overcome this challenge, we employed a piezo scanning mode instead of *z*-drive for the stage movement. This approach was chosen because *z*-drive movement can cause mechanical stage movement and photoresists instability, potentially leading to micro-movement and print imperfection. Another technique to avoid photoresist instability immediately after the print starts is to decelerate the mechanical movement of the stage in printing blocks that likely require support. This was achieved by reducing the acceleration and velocity of the stage to 5 mm s^{-2} and 100 mm s^{-1}, respectively.

To improve print quality in solid structures, we considered the integration of a shear angle (the angle between the stitched designs) with a specific overlap. Since the meta-biomaterials consisted of tilted struts, it is noticeable to consider the effects of the tilted struts' angles (*i.e.,* θ) and shear angle at the same time. A proper shear angle is recommended be selected so that the stitching planes create an angle between the material and themselves. In this case, a shear angle close to zero is favorable for NPR, PPR_p, PPR_s, and Hybrid groups, as these structures had already tilted struts. For the ZPR group, however, a shear angle of 20^o was chosen, as there are no tilted struts.

Additionally, overlaps between the segments and the number of contours as well as their distances were adjusted to optimize the print quality of the NPR and Hybrid groups. This was accomplished by conducting several tests on a unit cell of the NPR group (without stitching) to determine the optimal conditions for these parameters.

Before printing the meta-biomaterials, the silicon substrates were cleaned with acetone and isopropyl alcohol (IPA; both from Sigma-Aldrich, Germany) using a lint-free wipe and were subsequently blow dried with nitrogen. To further clean and activate the surface of the substrates, an oxygen plasma cleaner (Diener electronic GmbH, Germany) was employed at 80 W with a gas flow rate of 5 cm^3 min^{-1}, and a pressure of 0.12 bar for 15 min. To enhance the adhesion between the specimens and substrates, silanization with 3–(Trimethoxysilyl) propyl methacrylate (Sigma-Aldrich, Germany) for 1 hour. Silanization facilitates effective chemical bonding by rendering the substrate surface hydrophobic. A suitable concentration of 3-(Trimethoxysilyl) propyl methacrylate was established at 2.67% v/v by diluting it with ethanol. Following silanization, the specimens were washed with acetone, distilled water, and were then air-dried.

After exposing the specimens, the samples were immersed in propylene glycol monomethyl ether acetate (PGMEA, Sigma-Aldrich, Germany) for 1 hour in a borosilicate Petri dish to dissolve the unpolymerized photoresist. Subsequently, the specimens were rinsed with IPA for 5 min in a Petri dish to eliminate the PGMEA. To further reduce capillary force-induced deformation in the structures and to provide stronger bonding between the specimens and silicon substrates, Novec 7100 engineered fluid (Sigma-Aldrich, Germany) was applied for 30 s, as this solvent exhibits a lower surface tension than IPA.

3.4.4 Micro-mechanical test experiment

To measure the mechanical properties of the polymerized IP-Q at the micro-scale and integrate them into our FEM models, a compression test was performed on standard micro-cylindrical specimens with equal diameter and height of 30.0 µm using the FT-NMT03 nano-mechanical testing system (FemtoTools, FT-NMT03, Switzerland). The specimens were 3D printed using 2PP with the same parameters as the actual meta-biomaterials, which included a laser power of 50 mW, a scanning speed of 100000 µm/s, a slicing distance of 5 µm, and a hatching distance of 1 µm. We assumed that the IP-Q possessed isotropic elastic properties. A 200 mN silicon probe with a tip cross-section of 50×50 $µm^2$ was employed to compress the specimens. To visualize the interface between the probe and the specimens, the FT-NMT03 machine was integrated into a scanning electron microscope (JSM-6010LA, LEOL, Japan). To account for the stiffness of the silicon substrate and the adhesive used between the substrate and sample holder, the substrate's stiffness was initially measured at a 0.25 µm s^{-1} displacement rate with a 3 µm displacement. Following this, the compression experiment was conducted at the same displacement rate but at a 25% strain, after establishing

contact between the probe and specimen. The final engineering (nominal) stress and strain were obtained by dividing the derived force and loading displacement to the initial cross-section area and initial length, respectively.

3.4.5 Macro-mechanical compression test

To measure the mechanical properties of the meta-biomaterials at the macro-scale, a mechanical uniaxial test machine (LLOYD instrument LR5K, UK) with a 5 N load cell was employed. All the experiments were conducted in the compression mode at a stroke rate of 10 μm s^{-1} until 50% strain. The acquired force-displacement data was used to calculate the engineering stress and engineering strain of the specimens by dividing them by the initial projected cross-section and by the height of the specimens, respectively. The effective elastic modulus of the meta-biomaterials was then determined from the linear portion of the engineering stress-strain curve.

3.4.6 Preosteoblast cell culture

Mouse preosteoblast cells (MC3T3-E1, Sigma Aldrich, Germany) were pre-cultured in alpha minimum essential medium (α-MEM without nucleoside) supplemented with 10% (v/v) fetal bovine serum and 1% (v/v) penicillin-streptomycin (all from Thermo Fisher Scientific, US) for one week at 37 °C and 5% CO_2. The culture medium was refreshed every 2 days. To sterilize the specimens, they were first immersed in 70% ethanol for 10 min, followed by twice submersion in 1× phosphate buffered saline (PBS) (Sigma Aldrich, Germany). Subsequently, the specimens were exposed to UV light for 20 min. For all biological assessments except for the PrestoBlue assay, the specimens were glued to a transparent polymethyl methacrylate (PMMA) substrate (9 mm in diameter and 2 mm in thickness) using a biocompatible silicone adhesive and were placed in a 24-well plate. The cells were seeded on the specimens along the y-direction (1×10^5 cells per sample) in a 24-well plate. After 4 hours of incubation, the specimens were transferred to new well plates (Greiner, Bio-One, The Netherlands). From day 2, the cells were supplied with osteogenic medium containing 50 μg mL^{-1} ascorbic acid (1:1000) and 4 mM β-glycerophosphate (1:500) (both from Sigma Aldrich, Germany). All the cell culture experiments were conducted with at least three replicates per group, and two independent experiments were carried out for each assay.

3.4.7 Immunofluorescence staining of the cytoskeleton

The cells were fixated by washing the specimens with 1× PBS twice, followed by immersion in 4% (v/v) formaldehyde solution (Sigma Aldrich, Germany) for 10 min. After washing the cells with 1× PBS twice, they were permeabilized by immersion in 0.5% Triton X-100/PBS solution (Sigma Aldrich, Germany) at 4 °C for 5 min, followed by incubation in 1% BSA/PBS (Sigma Aldrich, Germany) at 37 °C for 5 min. Anti-vinculin mouse monoclonal primary antibody (1:100 in 1% bovine serum albumin (BSA)/PBS, Sigma Aldrich, Germany) and rhodamine-conjugated phalloidin (1:1000

in 1% BSA/PBS, Thermo Fisher Scientific, US) as a primary antibody were added followed by incubation for 1 hour at 37 °C. This was followed by washing the cells in 0.5% Tween-20/PBS (Sigma Aldrich, Germany) three times for 5 min each. The specimens were then incubated again in Alexa Fluor 488, donkey antimouse polyclonal secondary antibody (1:200 in 1% BSA/PBS, Thermo Fisher Scientific, US) at room temperature for 1 h. Finally, the specimens were washed with 0.5% Tween-20/PBS three times for 5 min each, followed by 5 min washing with 1× PBS.

3.4.8 PrestoBlue assay

This assay was used to measure the metabolic activity of the cell-laden meta-biomaterials after 1, 3, 6, 8, 10, 13, and 17 days of culture. Accordingly, the specimens ($n = 4$) were placed in a 96-well plate without the PMMA substrates (with 300 µL of α-MEM). α-MEM with 10% PrestoBlue (300 µL, Thermo Fisher Scientific, US) was added and the specimens were incubated for one hour at 37 °C and 5% CO_2. Subsequently, 100 µL of the incubated medium was transferred to a 96-well plate (Greiner, Bio-One, The Netherlands) in duplicate. Finally, the metabolic activity of the specimens was measured by using a Victor X3 micro-plate reader (PerkinElmer, Groningen, The Netherlands) at a 530 nm excitation wavelength and 595 nm emission wavelength.

3.4.9 SEM imaging

To conduct SEM imaging, the specimens were washed and fixated following the same steps as for cytoskeleton staining. After washing the specimens with 1× PBS, followed by distilled water for 5 min (twice each step), the specimens were dehydrated in 50%, 70%, and 96% ethanol for 15, 20, and 20 min, respectively. Subsequently, the specimens were dried in air overnight at room temperature. Prior to SEM imaging, gold sputtering was performed on all the specimens at 20 mA for 20 s twice in ±45° tilted configurations to ensure a homogeneous distribution of the gold layer with a thickness of ~12 nm. An SEM (JEOL JSM-IT100, Japan) was used to image the specimens.

3.4.10 Runx2 staining

First, the specimens were fixated and permeabilized following a similar procedure as for F-actin. The specimens were then incubated in a dilution of primary and secondary antibodies, including Runx2 rabbit monoclonal primary antibody (1:250 in 1% BSA/PBS, Abcam, UK), and Alexa Fluor 488, donkey anti-rabbit polyclonal secondary antibody (1:200 in 1% BSA/PBS, Thermo Fisher Scientific, US), respectively.

3.4.11 Alizarin red staining (ARS)

Initially, the specimens were fixated using the same fixation procedure. The specimens were then incubated in 2% (w/v) ARS solution (Sigma Aldrich, Germany) for 30 min in the dark, followed by washing them five times with distilled water.

3.4.12 Fluorescence microscopy

A fluorescent microscope (ZOE fluorescent cell imager, Bio-Rad, The Netherlands) was employed to visualize the cytoskeleton of the stained cells (20× objective featuring 0.4 NA).

3.4.13 Live/dead assay

After washing the meta-biomaterials with 1× PBS twice, a solution of 2 µM calcein and 3 µM ethidium homodimer-1 (both from Thermo Fisher Scientific, Waltham, MA, USA) in 1 ml 1× PBS was added to the specimens, which were then stored in dark for 30 min at room temperature.

3.4.14 Confocal imaging

A confocal microscope (Zeiss LSM 710, USA) with a 10× objective and 0.25 NA (air configuration) was used to image the Runx2 and ARS. The confocal microscope covered 263 µm (25 slices of z-stack). A laser with 50% power at a wavelength of 543 nm was used. For ARS, only one channel with excitation and emission wavelengths of 543 and 562 nm, respectively, was used. For Runx2, a laser with a wavelength of 488 nm and 60% power with two channels (488 nm and 540 nm) and (543 nm and 562 nm) was employed for the excitation and emission wavelengths, respectively.

3.4.15 Image Analysis

To quantitatively compare the expression levels of Runx2 and ARS, Fiji (ImageJ, National Institutes of Health, USA) was utilized. The .czi images from the confocal were imported into fiji prior to the measurement. To measure the maximum intensity and modification of the images, a macro code (.ijm) was written. The contrast of all the images were enhanced by 0.35 saturated pixels and the final images were derived based on the maximum intensity of each layer.

3.4.16 Statistical Analysis

Origin (2022, USA) was used for the micro- and macro-mechanical tests for the calculation of the means and standard deviations. Prism (9.4.1, GraphPad, US) was also utilized for biological results, including metabolic activity, shrinkage of the meta-biomaterials, and osteogenic responses (*i.e.,* Runx2 and ARS) to calculate the mean and standard deviations, adjusted p-value, and effect size (*i.e.,* eta-squared (η^2) and Cohen's d values). All the experiments were performed with at least three replicates, and two independent sets of biological experiments for the statistical analyses. We performed a normality test using the Shapiro–Wilk test with alpha= 0.05, to confirm the normal distribution of the data in each group. Moreover, the repeatability of the second independent set of the biological experiments were assessed via the Student's T-test. We also performed ordinary one-way ANOVA test, followed by post-hoc analysis using the

Tukey's multiple comparison test for considering the interaction effect between groups. It is noted that for all the experiments and graphs, a $p < 0.05$ was considered as statistically significant. Moreover, η^2 was calculated based on the ratio of the sum of squares between groups and the total sum of squares [54]. For pairwise analysis, the Cohen's d value was calculated based on the ratio of the mean differences between two groups and the total pooled standard deviation of the same two groups as follows [55]:

$$\text{Cohens}'d \text{ value} = \frac{(M_1 - M_2)}{SD_{pooled}};\ SD_{pooled} = \sqrt{\frac{(n_1-1)\times {SD_1}^2 + (n_2-1)\times {SD_2}^2}{n_1+n_2-2}}; \quad (5)$$

where M, SD, n, and SD_{pooled} indicate the mean of each group, the standard deviation of each group, the sample size of each group, and the pooled standard deviation of two groups 1 and 2, respectively. The subscripts 1 and 2 represent groups 1 and 2, respectively. Moreover, $F\ (DFn, DFd)$ ratio shows the distribution of degrees of freedom in the numerator (DFn) and the dominator (DFd), and was defined as the ratio of the mean square between groups and within groups. We reported the η^2 and $F\ (DFn, DFd)$ values for the comparison groups in which a statistically significant difference at each timepoint was observed.

3.5 Conclusions

We studied the influence of the Poisson's ratio of 3D meta-biomaterials on the behavior of preosteoblast cells. Therefore, we initially used computational models to rationally design 3D meta-biomaterials. In this design, the Poisson's ratio was isolated from other micro-architectural parameters and mechanical properties, such as the effective elastic modulus, porosity, and pore size. For the fabrication of these complex meta-biomaterials at the meso-scale, we used an advanced micro-AM technique (*i.e.,* 2PP) and IP-Q as the base material. Both the micro- and meso-mechanical characterizations of the IP-Q and meta-biomaterials showed a high degree of material nonlinearity (*i.e.,* hyperelastic behavior). The hyperelastic behavior of the polymerized IP-Q photoresist was modeled using the third-order reduced polynomial model. We designed the final meta-biomaterials using an FEM approach, considering the hyperelastic properties of the polymerized IP-Q, porosity of the trabecular bone, and the size of preosteoblasts. The cell-laden meta-biomaterials exhibited differences in terms of cell infiltration along the struts, (lateral) structural deformation over time, and metabolic activity of the cells. The cells seeded on the meta-biomaterials with PPRs (*i.e.,* v_{yz}) demonstrated significantly higher levels of metabolic activity and induced more deformation of the structures as compared to those seeded on the auxetic meta-biomaterials. This difference in the cell responses is likely due to the unit cell geometry and anisotropy in the effective elastic modulus, with the PPR_P having the most pronounced anisotropy, leading to increased deformation.

Furthermore, all the meta-biomaterials considered here supported the osteogenic differentiation of preosteoblasts as well as matrix mineralization. However, there were no significant differences between the various groups. This study presents a new platform for the design, fabrication, and assessment of meso-scale meta-biomaterials with controlled Poisson's ratios. The presented design approach also holds considerable promise for the development of bone implants and may contribute toward expanding our understanding of how physical cues impact cell responses, both individually and in combination

3.6 Supplementary material

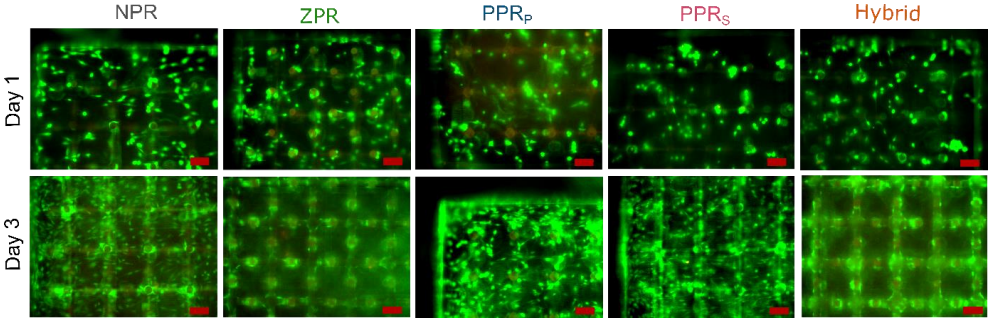

Figure S1. *Fluorescent microscopy images illustrating the viability of the MC3T3-E1 preosteoblast cells seeded on the different meta-biomaterials for 1 and 3 days, as determined by live/dead assay (scale bar = 100 μm). The results indicated that the IP-Q material is not cytotoxic for these cells and that the cells could grow on all the meta-biomaterials.*

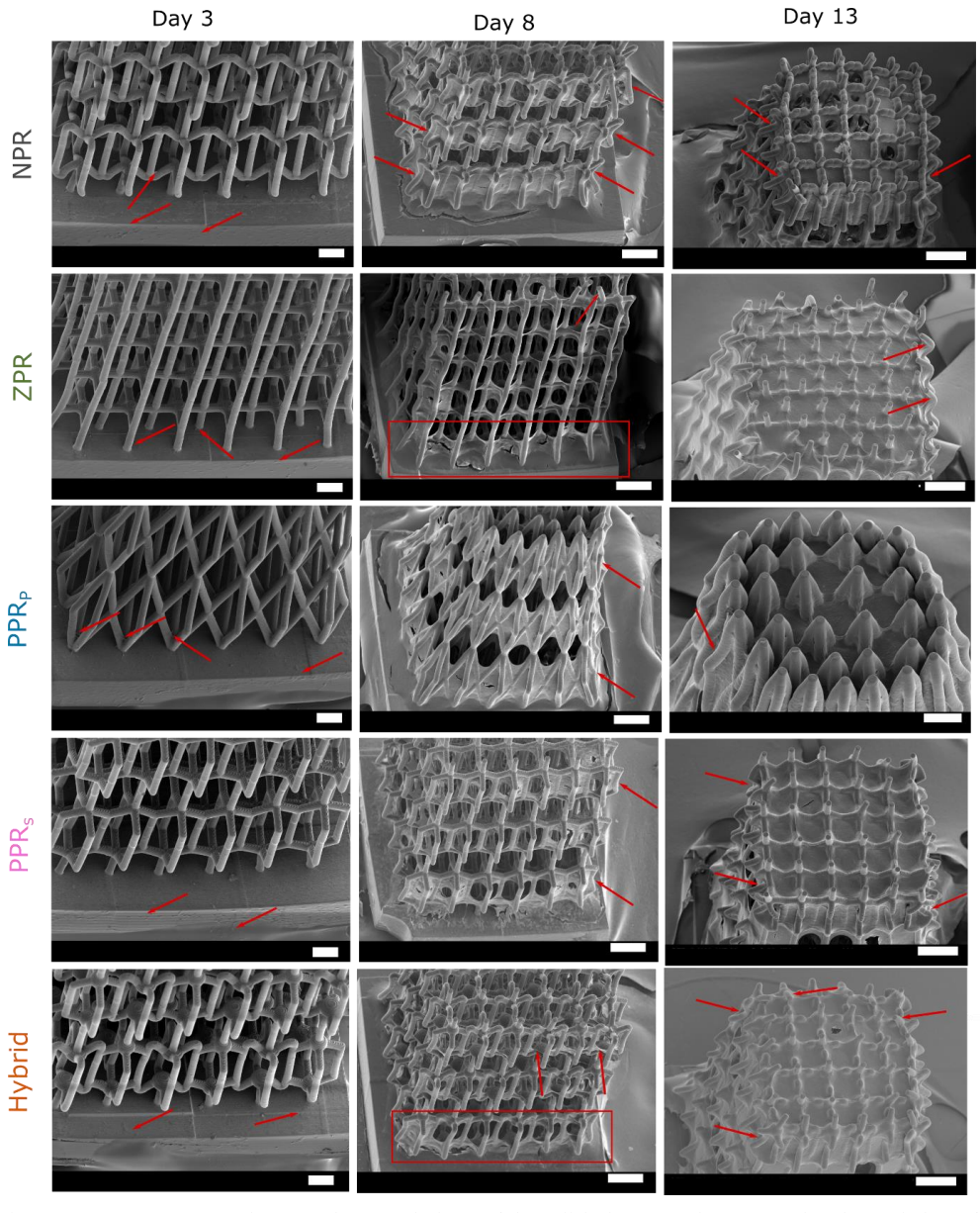

Figure S2. *SEM images showing the morphology of the cell-laden meta-biomaterials. The scale bars for the images of day 3 is 100 µm and for days 8 and 13 is 200 µm, except for the PPR_p on day 13, which is 100 µm.*

Table S1. *The Cohen's d absolute values obtained from the Tukey's multiple comparison test for the shrinkage ratio of the top surface of the cell-laden meta-biomaterials on days 10, 13 and 17. The effect sizes are only reported for the comparison groups with an adjusted p-value < 0.05.*

Cohen's *d* absolute values of the top-surface shrinkage ratio			
Group	Day 10	Day 13	Day 17
NPR *vs.* ZPR	3.0	3.6	-
NPR *vs.* PPRp	4.0	2.3	2.6
NPR *vs.* PPRs	3.7	4.7	-
NPR *vs.* Hybrid	-	2.3	-
ZPR *vs.* PPRp	7.9	4.5	3.1
ZPR *vs.* Hybrid	1.5	-	-
PPRp *vs.* PPRs	10.1	5.0	3.1
PPRp *vs.* Hybrid	4.5	3.4	3.4

Table S2. *The Cohen's d absolute values obtained from the Tukey's multiple comparison test for the normalized metabolic activity of the preosteoblast cells seeded on the meta-biomaterials, on days 10, 13 and 17. The data presented here correspond to the comparison groups with an adjusted p-value < 0.05.*

Cohen's *d* absolute values of the normalized metabolic activity			
Group	Day 10	Day 13	Day 17
NPR *vs.* ZPR	3.2	3.1	2.1
NPR *vs.* PPRp	2.0	2.1	3.2
NPR *vs.* PPRs	2.3	3.8	6.8
ZPR *vs.* PPRp	-	-	1.8
ZPR *vs.* PPRs	-	-	4.1
PPRp *vs.* Hybrid	-	1.4	2.4
PPRs *vs.* Hybrid	-	2.0	4.5

Bibliography

[1] B. Yi, Q. Xu, W. Liu, An overview of substrate stiffness guided cellular response and its applications in tissue regeneration, Bioact. Mater (2021).
[2] A. Maggi, H. Li, J.R. Greer, Three-dimensional nano-architected scaffolds with tunable stiffness for efficient bone tissue growth, Acta Biomater. 63 (2017) 294-305.
[3] T. Jiang, X.-Y. Tang, Y. Mao, Y.-Q. Zhou, J.-J. Wang, R.-M. Li, X.-R. Xie, H.-M. Zhang, B. Fang, N.-J. Ouyang, Matrix mechanics regulate the polarization state of bone marrow-derived neutrophils through the JAK1/STAT3 signaling pathway, Acta Biomater. (2023).
[4] A. Vilar, M. Hodgson-Garms, G.D. Kusuma, I. Donderwinkel, J. Carthew, J.L. Tan, R. Lim, J.E. Frith, Substrate mechanical properties bias MSC paracrine activity and therapeutic potential, Acta Biomater. (2023).
[5] A. Bizanti, P. Chandrashekar, R. Steward Jr, Culturing astrocytes on substrates that mimic brain tumors promotes enhanced mechanical forces, Exp. Cell Res. 406(2) (2021) 112751.
[6] L.C. Ransanz, P.F. Van Altena, V.M. Heine, A. Accardo, Engineered cell culture microenvironments for mechanobiology studies of brain neural cells, Front. Bioeng. Biotechnol. 10 (2022) 1096054.
[7] A. Accardo, C. Cirillo, S. Lionnet, C. Vieu, I. Loubinoux, Interfacing cells with microengineered scaffolds for neural tissue reconstruction, Brain Research Bulletin 152 (2019) 202-211.
[8] M. Niinomi, M. Nakai, Titanium-based biomaterials for preventing stress shielding between implant devices and bone, Int. J. Biomater. 2011 (2011).
[9] Y. Yan, Y. Li, L. Song, C. Zeng, Pluripotent stem cell expansion and neural differentiation in 3-D scaffolds of tunable Poisson's ratio, Acta Biomater. 49 (2017) 192-203.
[10] B. Zou, Z. Liang, D. Zhong, Z. Cui, K. Xiao, S. Shao, J. Ju, Magneto-Thermomechanically Reprogrammable Mechanical Metamaterials, Adv Mater 35(8) (2023) 2207349.
[11] M.E. Pallarès, I. Pi-Jaumà, I.C. Fortunato, V. Grazu, M. Gómez-González, P. Roca-Cusachs, J.M. de la Fuente, R. Alert, R. Sunyer, J. Casademunt, Stiffness-dependent active wetting enables optimal collective cell durotaxis, Nat. Phys. 19(2) (2023) 279-289.
[12] P. Chansoria, J. Blackwell, E.L. Etter, E.E. Bonacquisti, N. Jasiewicz, T. Neal, S.A. Kamal, J. Hoque, S. Varghese, T. Egan, Rationally Designed Anisotropic and Auxetic Hydrogel Patches for Adaptation to Dynamic Organs, Adv. Funct. Mater. 32(43) (2022) 2207590.
[13] E. Yarali, A.A. Zadpoor, U. Staufer, A. Accardo, M.J. Mirzaali, Auxeticity as a Mechanobiological Tool to Create Meta-Biomaterials, ACS Appl. Bio Mater 6(7) (2023) 2562-2575.
[14] H. Haag, P.D. Dalton, V. Bloemen, The Synergy of Biomimetic Design Strategies for Tissue Constructs, Adv. Funct. Mater. (2022) 2201414.
[15] N. Munding, M. Fladung, Y. Chen, M. Hippler, A.D. Ho, M. Wegener, M. Bastmeyer, M. Tanaka, Bio-Metamaterials for Mechano-Regulation of Mesenchymal Stem Cells, Advanced Functional Materials (2023) 2301133.
[16] G. Flamourakis, I. Spanos, Z. Vangelatos, P. Manganas, L. Papadimitriou, C. Grigoropoulos, A. Ranella, M. Farsari, Laser-made 3D Auxetic Metamaterial Scaffolds for Tissue Engineering Applications, Macromol Mater Eng 305(7) (2020) 2000238.
[17] A. Tang, J. Ji, J. Li, W. Liu, J. Wang, Q. Sun, Q. Li, Nanocellulose/PEGDA Aerogels with Tunable Poisson's Ratio Fabricated by Stereolithography for Mouse Bone Marrow Mesenchymal Stem Cell Culture, Nanomater. 11(3) (2021) 603.
[18] W. Lv, L. Dong, D. Li, A novel metamaterial with individually adjustable and sign-switchable Poisson's ratio, European Journal of Mechanics-A/Solids 97 (2023) 104851.
[19] D. Li, J. Yin, L. Dong, R.S. Lakes, Strong re-entrant cellular structures with negative Poisson's ratio, Journal of materials science 53(5) (2018) 3493-3499.
[20] K.K. Dudek, J.A.I. Martínez, G. Ulliac, M. Kadic, Micro-Scale Auxetic Hierarchical Mechanical Metamaterials for Shape Morphing, Adv Mater 34(14) (2022) 2110115.

[21] X. Xin, L. Liu, Y. Liu, J. Leng, 4D printing auxetic metamaterials with tunable, programmable, and reconfigurable mechanical properties, Adv. Funct. Mater. 30(43) (2020) 2004226.
[22] B. Jang, S. Won, J. Kim, J. Kim, M. Oh, H.J. Lee, J.H. Kim, Auxetic meta-display: Stretchable display without image distortion, Adv. Funct. Mater. 32(22) (2022) 2113299.
[23] D. Chen, D. Li, K. Pan, S. Gao, B. Wang, M. Sun, C. Zhao, X. Liu, N. Li, Strength enhancement and modulus modulation in auxetic meta-biomaterials produced by selective laser melting, Acta Biomater. 153 (2022) 596-613.
[24] Y. Zhu, S. Jiang, Q. Zhang, J. Li, C. Yu, C. Zhang, A novel monoclinic auxetic metamaterial with tunable mechanical properties, International Journal of Mechanical Sciences 236 (2022) 107750.
[25] A. Sorrentino, D. Castagnetti, Novel polyhedral mechanical metamaterial exhibiting negative Poisson's ratio, Smart Materials and Structures 32(3) (2023) 035008.
[26] Y. Zhu, S. Jiang, J. Li, D.K. Pokkalla, Q. Wang, C. Zhang, Novel isotropic anti-tri-missing rib auxetics with prescribed in-plane mechanical properties over large deformations, International Journal of Applied Mechanics 13(10) (2021) 2150115.
[27] W. Lv, D. Li, L. Dong, Study on blast resistance of a composite sandwich panel with isotropic foam core with negative Poisson's ratio, International Journal of Mechanical Sciences 191 (2021) 106105.
[28] M.J. Mirzaali, A. Ghorbani, K. Nakatani, M. Nouri-Goushki, N. Tümer, S.J. Callens, S. Janbaz, A. Accardo, J. Bico, M. Habibi, A.A. Zadpoor, Curvature Induced by Deflection in Thick Meta-Plates, Adv Mater 33(30) (2021) 2008082.
[29] Y. Zhu, Y. Luo, D. Gao, C. Yu, X. Ren, C. Zhang, In-plane elastic properties of a novel re-entrant auxetic honeycomb with zigzag inclined ligaments, Engineering Structures 268 (2022) 114788.
[30] M. Mirzaali, H. Pahlavani, E. Yarali, A. Zadpoor, Non-affinity in multi-material mechanical metamaterials, Scientific reports 10(1) (2020) 11488.
[31] A. Sorrentino, D. Castagnetti, L. Mizzi, A. Spaggiari, Bio-inspired auxetic mechanical metamaterials evolved from rotating squares unit, Mechanics of Materials 173 (2022) 104421.
[32] H.M. Kolken, S. Janbaz, S.M. Leeflang, K. Lietaert, H.H. Weinans, A.A. Zadpoor, Rationally designed meta-implants: a combination of auxetic and conventional meta-biomaterials, Mater. Horiz. 5(1) (2018) 28-35.
[33] A. Sorrentino, D. Castagnetti, Negative Poisson's ratio lattice for designing vertebral biomaterials, Mechanics of Advanced Materials and Structures 29(27) (2022) 6626-6633.
[34] A.A. Zadpoor, M.J. Mirzaali, L. Valdevit, J.B. Hopkins, Design, material, function, and fabrication of metamaterials, APL Materials 11(2) (2023).
[35] I. Ostanin, G. Ovchinnikov, D.C. Tozoni, D. Zorin, A parametric class of composites with a large achievable range of effective elastic properties, J Mech Phys Solids 118 (2018) 204-217.
[36] Z. Hashin, The elastic moduli of heterogeneous materials, US Department of Commerce, Office of Technical Services1960.
[37] Z. Hashin, S. Shtrikman, A variational approach to the theory of the elastic behaviour of multiphase materials, J Mech Phys Solids 11(2) (1963) 127-140.
[38] W. Zhang, P. Soman, K. Meggs, X. Qu, S. Chen, Tuning the poisson's ratio of biomaterials for investigating cellular response, Adv. Funct. Mater. 23(25) (2013) 3226-3232.
[39] J.W. Lee, P. Soman, J.H. Park, S. Chen, D.-W. Cho, A tubular biomaterial construct exhibiting a negative Poisson's ratio, PLoS One 11(5) (2016) e0155681.
[40] L. Song, M.F. Ahmed, Y. Li, C. Zeng, Y. Li, Vascular differentiation from pluripotent stem cells in 3-D auxetic scaffolds, Tissue Eng Regen Med. 12(7) (2018) 1679-1689.
[41] A. Accardo, M.-C. Blatché, R. Courson, I. Loubinoux, C. Vieu, L. Malaquin, Direct laser fabrication of free-standing PEGDA-hydrogel scaffolds for neuronal cell growth, Mater Today 21(3) (2018) 315-316.
[42] T. Abele, T. Messer, K. Jahnke, M. Hippler, M. Bastmeyer, M. Wegener, K. Göpfrich, Two-Photon 3D Laser Printing Inside Synthetic Cells, Adv Mater 34(6) (2022) 2106709.
[43] C. Wang, Z. Vangelatos, C.P. Grigoropoulos, Z. Ma, Micro-engineered architected metamaterials for cell and tissue engineering, Mater. Today Adv. 13 (2022) 100206.

[44] J. Im, Y. Liu, Q. Hu, G.F. Trindade, C. Parmenter, M. Fay, Y. He, D.J. Irvine, C. Tuck, R.D. Wildman, Strategies for Integrating Metal Nanoparticles with Two-Photon Polymerization Process: Toward High Resolution Functional Additive Manufacturing, Adv. Funct. Mater. (2023) 2211920.
[45] V. Harinarayana, Y. Shin, Two-photon lithography for three-dimensional fabrication in micro/nanoscale regime: A comprehensive review, Opt Laser Technol 142 (2021) 107180.
[46] N. Barin, H.E. Balcioglu, I. de Heer, M. de Wit, M.L. Lamfers, M.E. van Royen, P.J. French, A. Accardo, 3D-Engineered scaffolds to study microtubes and localization of epidermal growth factor receptor in patient-derived glioma cells, Small (2022) 2204485.
[47] A. Sharaf, B. Roos, R. Timmerman, G.-J. Kremers, J.J. Bajramovic, A. Accardo, Two-photon polymerization of 2.5 D and 3D microstructures fostering a ramified resting phenotype in primary microglia, Front. Bioeng. Biotechnol. 10 (2022) 926642.
[48] Q. Akolawala, M. Rovituso, H.H. Versteeg, A.M. Rondon, A. Accardo, Evaluation of proton-induced DNA damage in 3D-engineered glioblastoma microenvironments, ACS Appl. Mater. Interfaces 14(18) (2022) 20778-20789.
[49] T. Wang, H. Ugurlu, Y. Yan, M. Li, M. Li, A.-M. Wild, E. Yildiz, M. Schneider, D. Sheehan, W. Hu, Adaptive wireless millirobotic locomotion into distal vasculature, Nat. Commun. 13(1) (2022) 4465.
[50] S. Chen, Z. Tan, P. Liao, Y. Li, Y. Qu, Q. Zhang, M. Yang, K.W.Y. Chan, L. Zhang, K. Man, Biodegradable Microrobots for DNA Vaccine Delivery, Adv. Healthc. Mater (2023) 2202921.
[51] I.J. Gibson, M.F. Ashby, The mechanics of three-dimensional cellular materials, Proc. Math. Phys. Eng. Sci. 382(1782) (1982) 43-59.
[52] V. Karageorgiou, D. Kaplan, Porosity of 3D biomaterial scaffolds and osteogenesis, Biomater. 26(27) (2005) 5474-5491.
[53] R. Hedayati, M. Sadighi, M. Mohammadi-Aghdam, A. Zadpoor, Effect of mass multiple counting on the elastic properties of open-cell regular porous biomaterials, Materials & Design 89 (2016) 9-20.
[54] J. Cohen, Eta-squared and partial eta-squared in fixed factor ANOVA designs, Educational and psychological measurement 33(1) (1973) 107-112.
[55] J. Cohen, Statistical power analysis for the behavioral sciences, Academic press2013.
[56] Q. Hu, G.A. Rance, G.F. Trindade, D. Pervan, L. Jiang, A. Foerster, L. Turyanska, C. Tuck, D.J. Irvine, R. Hague, The influence of printing parameters on multi-material two-photon polymerisation based micro additive manufacturing, Addit. Manuf. 51 (2022) 102575.
[57] J. Fortin-Smith, J. Sherwood, P. Drane, D. Kretschmann, Characterization of maple and ash material properties for the finite element modeling of wood baseball bats, Applied Sciences 8(11) (2018) 2256.
[58] J. Barrasa-Fano, A. Shapeti, A. Jorge-Penas, M. Barzegari, J.A. Sanz-Herrera, H. Van Oosterwyck, TFMLAB: A MATLAB toolbox for 4D traction force microscopy, SoftwareX 15 (2021) 100723.
[59] A.D. Lantada, A. Muslija, J.P. García-Ruíz, Auxetic tissue engineering scaffolds with nanometric features and resonances in the megahertz range, Smart Mater Struct 24(5) (2015) 055013.
[60] D.O. Sohutskay, A.B. Tepole, S.L. Voytik-Harbin, Mechanobiological wound model for improved design and evaluation of collagen dermal replacement scaffolds, Acta Biomater. 135 (2021) 368-382.
[61] M.J. Mirzaali, V. Moosabeiki, S.M. Rajaai, J. Zhou, A.A. Zadpoor, Additive manufacturing of biomaterials—Design principles and their implementation, Materials 15(15) (2022) 5457.

4

Decoupling mechanical and morphometric properties in meta-biomaterials

Yarali, E., Urs S., Fratila-Apachitei L. E., Mahdavi R., Zadpoor, A., Accardo, A., & Mirzaali, M. J. (2024). Decoupling mechanical and morphometric properties in meta-biomaterials. *Nature Communications*, revised.

Meta-biomaterials are engineered biomaterials with unprecedented properties derived from their microscale design, positioning them as promising candidates for developing medical devices (*e.g.,* meta-implants). A significant challenge in developing meta-biomaterials lies in effectively decoupling their intertwined mechanical properties (*e.g.*, elastic and shear moduli, Poisson's ratio) and morphometric properties (*e.g.*, porosity, connectivity, surface area) properties. To address this challenge, we introduced non-stochastic unit cells featuring cubic and isotropic properties with three orthotropic planes of symmetry. We explicitly derived the geometrical relationships necessary to explore our design spaces and calculate the morphometric properties (*e.g.,* pore sizes). We employed a numerical homogenization method based on a 3D voxelization approach to model the unit cells of the meta-biomaterials within our design space, representing the empty and solid phases in a binary format. Through an extensive number of simulations (*i.e.,* 43,000) and a multi-objective optimization technique, we successfully isolated the Poisson's ratio while maintaining other mechanical properties (*i.e.*, effective elastic and shear moduli, and mechanical anisotropy level), morphological properties (*i.e.* relative density, pore size, tortuosity, surface-to-volume ratio and connectivity) and mass transport parameters (*i.e.,* permeability) as constant as possible, with an average deviation below 10.9%. The resultant meta-biomaterials were additively manufactured using PolyJet 3D printing and two-photon polymerization techniques, respectively at the macro- and microscales. Mechanical testing was conducted on these fabricated meta-biomaterials to validate the predictions of our computational models. The established computational model and fabricated meta-biomaterials provide promising avenues for advancing tissue engineering and facilitating studies in cell mechanobiology, enabling precise exploration of the isolated effects of mechanical and morphometric properties.

4.1 Introduction

Meta-biomaterials are engineered, biocompatible materials whose unique properties arise from the architecture of their artificial microstructure. These materials open a wide design space for real-world applications, particularly in biomedical engineering, where they enable the creation of structures with unprecedented properties, such as auxeticity that surpass those of conventional materials [1-4]. Meta-biomaterials are made from stochastic or non-stochastic building blocks, such as strut-based [5-7] or surface-based [8, 9] unit cells. The specific arrangement and the geometric design of these repetitive unit cells offer extensive design freedom, enabling designers to customize the properties of meta-biomaterials [3].

The design flexibility of meta-biomaterials extends beyond mechanical properties (*e.g.,* elastic modulus, shear modulus, Poisson's ratio, and mechanical anisotropy level). It includes morphometric (*e.g.,* porosity, pore size, tortuosity, surface/volume ratio, and connectivity) and mass transport (*i.e.,* permeability and diffusivity)

properties. However, mechanical, morphometric, and mass transport properties are often interdependent, meaning adjusting one parameter (*e.g.,* increasing the effective elastic modulus) can lead to changes in others (*e.g.,* Poisson's ratio). Furthermore, these properties are intertwined, and in certain applications, such as mimicking tissue microenvironments, it is crucial to decouple them to achieve specific mechanical and morphometric properties [10]. This challenge is magnified when seeking extreme properties, such as high values of PPR or NPR [1].

There are certain known facts regarding the mechanical, morphological, and mass transport properties of meta-biomaterials. For instance, the relationship between the relative mass density and the elastic modulus is known to be of a power-law nature [11], with the effective elastic modulus of any microarchitectural design being constrained by the Hashin–Shtrikman bound [12], for any given relative mass density. Another example is the relationship between porosity and permeability [11], which depends on the pore shape, and is correlated with other properties, such as the Poisson's ratio. Theoretical limits exist also for the Poisson's ratio, v, of 3D isotropic solid materials, where it can range between -1.0 (*i.e.,* extremely high shear modulus and low bulk modulus) to 0.5 (*i.e.,* extremely high bulk modulus and low shear modulus) according to $B/G = (v+1)/3(0.5-v)$, assuming positive values for both B (*i.e.,* bulk modulus) and G (*i.e.,* shear modulus) [11]. In the context of meta-biomaterials, penta-mode meta-biomaterials and auxetic meta-biomaterials can exhibit Poisson's ratios of 0.5 [13], and -1 [14, 15], respectively. However, in the context of meta-biomaterials, achieving simultaneous control over several mechanical parameters, such as Poisson's ratio, shear modulus, and bulk modulus is highly challenging and has yet to be fully realized.

To decouple these properties more effectively, it is advantageous for meta-biomaterials to be as more mechanically isotropic as possible. However, 3D meta-biomaterials often exhibit inherent anisotropy due to the spatial arrangement of their struts, particularly in non-stochastic unit cells [16]. The degree of anisotropy in lattice-based meta-biomaterials depends on factors, such as the symmetry of the unit cells (*e.g.,* the number of mirror planes), and unit cell parameters (*e.g.,* strut diameter, strut length, strut angle). Consequently, the microarchitecture of the unit cell as well as its geometric parameters need to be rationally designed. In addition to mechanical anisotropy, geometrical symmetry (*e.g.,* two [1], or three planes of symmetry [17]) is crucial for certain applications, such as studying the effects of directionality in the mechanobiology of cells [18]. Therefore, there is a demand for developing meta-biomaterials with minimal mechanical anisotropy, such as isotropic or cubic properties, characterized by the fewest possible elasticity coefficients.

The ability to independently tune the Poisson's ratio is particularly important in the design of biomedical devices and in the study of cellular mechanobiology. Isolating the Poisson's ratio from other mechanical and morphometric properties is an area that

remains unexplored. The Poisson's ratio can serve as a powerful design tool in creating the next generation of implants, known as meta-implants [19], where local tailoring of this property can lead to a better match in deformation characteristics with the surrounding bone tissues [19]. Moreover, in mechanobiological studies, Poisson's ratio has been shown to influence the proliferation and differentiation of bone cells (preosteoblasts) [1], fibroblasts [18], and human mesenchymal stem cells [20]. However, tuning the Poisson's ratio without affecting other properties remains a significant challenge. Existing studies have primarily focused on limited aspects, such as nearly zero values [17], 2D structures [20, 21], and asymmetric values across three orthogonal directions [1, 20].

To design meta-biomaterials with multiple desired properties simultaneously, particularly, to isolate their Poisson's ratio, various methodologies can be employed. They include direct FEMs [22], numerical homogenization [23], inverse design using physics-informed deep learning approaches [3, 24, 25], multi-objective optimization [17] and trials and errors [26]. Each technique has its advantages and drawbacks in terms of computational costs, simplicity, accuracy, and versatility. For instance, the direct FEM using solid elements yields accurate results but is computationally expensive. One efficient method may involve using FEM methods (*e.g.,* homogenization-based [27]) to perform extensive number of simulations rapidly, followed by multi-objective optimization to isolate Poisson's ratio in meta-biomaterials.

In this study, we propose a new design of 3D meta-biomaterials and characterize their mechanical, morphometric, and mass transport properties. The goal is to isolate the Poisson's ratio from other properties of the meta-biomaterial, achieving both extreme negative and positive values. The properties we targeted include the Poisson's ratio v, the effective elastic modulus E_{eff}, the effective shear modulus G_{eff}, the Zener ratio A, the relative mass density ρ, the pore size PS, the permeability k, the tortuosity τ, the surface-to-volume ratio S/V, and the connectivity Z_g. The designed meta-biomaterials exhibited either isotropic properties (*i.e.,* with only two independent elastic coefficients) or cubic symmetry (*i.e.,* with three independent elastic coefficients). We conducted extensive numerical simulations using FEM-based numerical homogenization to calculate the elastic properties. Critical values within the design space were determined through explicit geometrical analysis of the meta-biomaterials. To isolate the Poisson's ratio from all other properties, we employed a multi-objective optimization technique with a high throughput. Finally, we 3D printed the designed meta-biomaterials at different length scales using PolyJet and 2PP technologies and experimentally characterized their mechanical properties at the macroscale.

4.2 Results and discussion

4.2.1 Mechanical properties of the meta-biomaterials

We investigated the correlation between the mechanical properties of 3D meta-biomaterials proposed in Figure 1, in terms of θ and normalized L (*i.e.*, L/H, Figure 2a). This analysis provided a comprehensive understanding of the design space of our meta-biomaterials in terms of v, E_{eff}/E_0, G_{eff}/G_0, and A. It should be also noted that the results we report here are based on the categories that are defined in the Materials and Method section (*i.e.*, Category I ($\theta_{\min} < \theta \leq 90.0^{o}$), Category II ($90.0^{o} < \theta \leq 135.0^{o}$), and Category III ($135.0^{o} < \theta < \theta_{\max}$)).

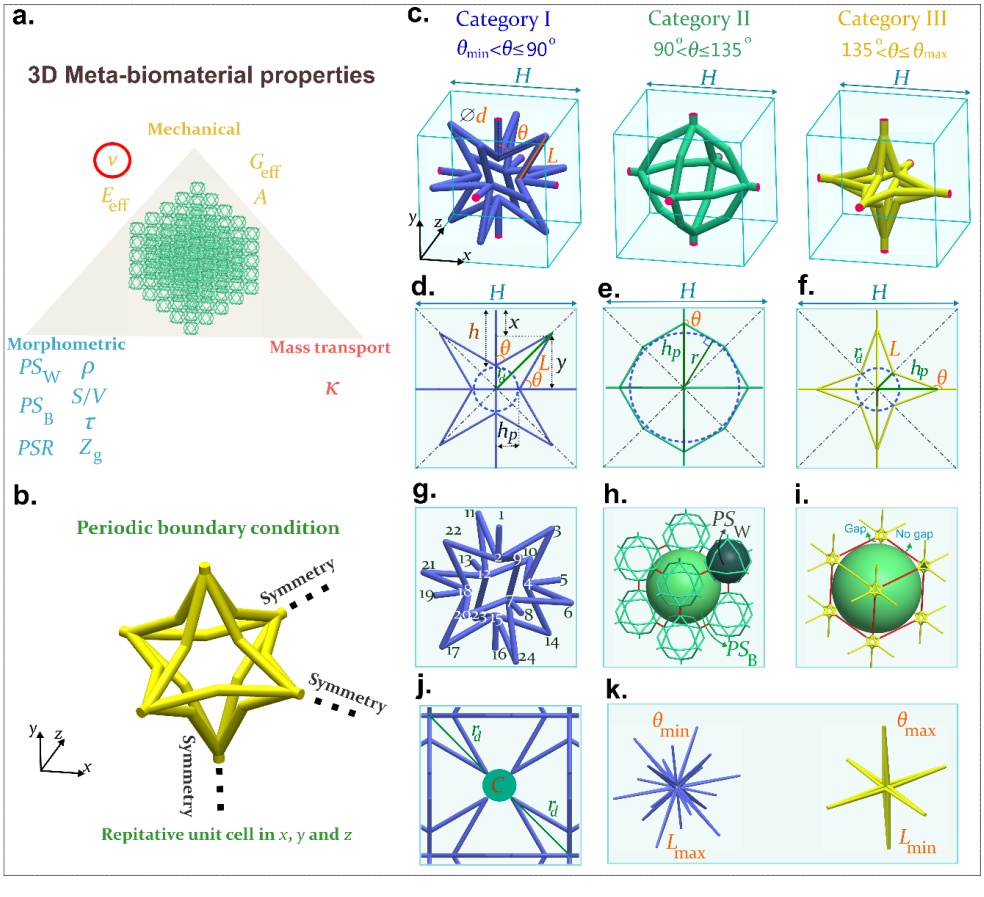

Figure 1. ***a.*** *A general illustration of the objective of this study, showing a 3D symmetric meta-biomaterial with isolated Poisson's ratio alongside its mechanical, morphometric and mass transport properties.* ***b.*** *A schematic drawing of a 3D unit cell of the meta-biomaterial in a Cartesian coordinate system, with three planes of geometrical symmetry and periodic boundary conditions.* ***c.*** *The classification of unit cells into three distinct categories: Category I ($\theta_{min} < \theta \leq 90.0^{o}$, shown in blue), Category II ($90.0^{o} < \theta \leq 135.0^{o}$, shown in green), and Category III ($135.0^{o} < \theta < \theta_{max}$,shown in yellow). Here, θ, L and d are the three input parameters, while H represents the overall size of the unit cell.* ***d.*** *A 2D schematic drawing of a unit cell*

from Category I, used to calculate parameters h, h_p, and PS_W. ***e.*** *A 2D schematic drawing of a Category II unit cell, illustrating the calculation of PS_W.* ***f.*** *A 2D schematic drawing of a Category III unit cell, also used to calculate PS_W.* ***g.*** *A 3D schematic showing a unit cell with labeled nodes. These labels are necessary for reporting their coordinates and morphometric properties. h. A 3D schematic drawing of $2 \times 2 \times 2$ unit cells (from Category II) demonstrating PS_W and PS_B i. A 3D schematic showing PS_B when L is small enough that the green sphere does not touch the non-boundary struts but touches the red struts (boundary ones).* ***j.*** *A 2D schematic drawing for deriving an explicit formula for the maximum L in Category I unit cells.* ***k.*** *The critical values of θ and L in our meta-biomaterial design. The blue unit cell has the minimum θ (46.6^o), maximum L (200.9/300), and $d = 8.0/300$. In contrast, the yellow unit cell features the maximum θ (177.7^o), and the minimum and maximum L (140.5/300), with $d = 8.0/300$.*

In Category I, the Poisson's ratio ranged between -0.59 and 0.26, with a notable sign change from negative to positive occurring around $\theta = 68.0^o$ (Figure 1a, and b). This early transition in sign, as compared to the typical 90.0^o transition seen in 1D or 2.5D metamaterials, results from the 3D design and geometrical symmetry (*i.e.,* geometrical constraints) of the unit cells. For small values of normalized L (until $L/H < 65.0/300$), the Poisson's ratio remained positive, but it increased further as L increased (indicated by the blue color contour in Figure 2a). For Category II, the Poisson's ratio ranged between 0.01 and 0.34. Within this category, increasing θ up to 120.0^o led to an increase in the Poisson's ratio, which then decreased again as θ approached 135.0^o. Similarly, the Poisson's ratio increased with L until $L/H = 100.0/300$, but decreased beyond this point. In Category III, the Poisson's ratio ranged between 0.01 and 0.33, with increasing of both θ and L resulting in a decrease of the magnitude of ν. It should also be noted that Categories I, II, and III contained 38.63%, 36.89%, and 24.49% of the data, respectively in terms of the number of simulations conducted per Category.

The 3D distribution of E_{eff}/E_0 indicated that its variation with θ was generally smooth, except for a number of critical angles (*i.e.,* $\theta > \sim 170.0^o$ and $\theta < \sim 60.0^o$, Figure 2a and Figure S2a-i of the supplementary material). The higher values of E_{eff}/E_0 at these angles are likely due to the strut overlapping effects. In this case, a much higher number of voxels is required to capture the elastic moduli accuracy, which, in general, increases the computational cost. In Category II, the variation of E_{eff}/E_0 vs. θ was relatively constant when considering the effect of L. Across Categories I, II, and III, E_{eff}/E_0 ranged between 2.054×10^{-6} and 0.014 (mean ± *SD*: 0.001 ± 0.001), between 3.223×10^{-6} and 0.018 (0.002 ± 0.002) and between 9.483×10^{-6} and 0.011 (0.002 ± 0.002), respectively.

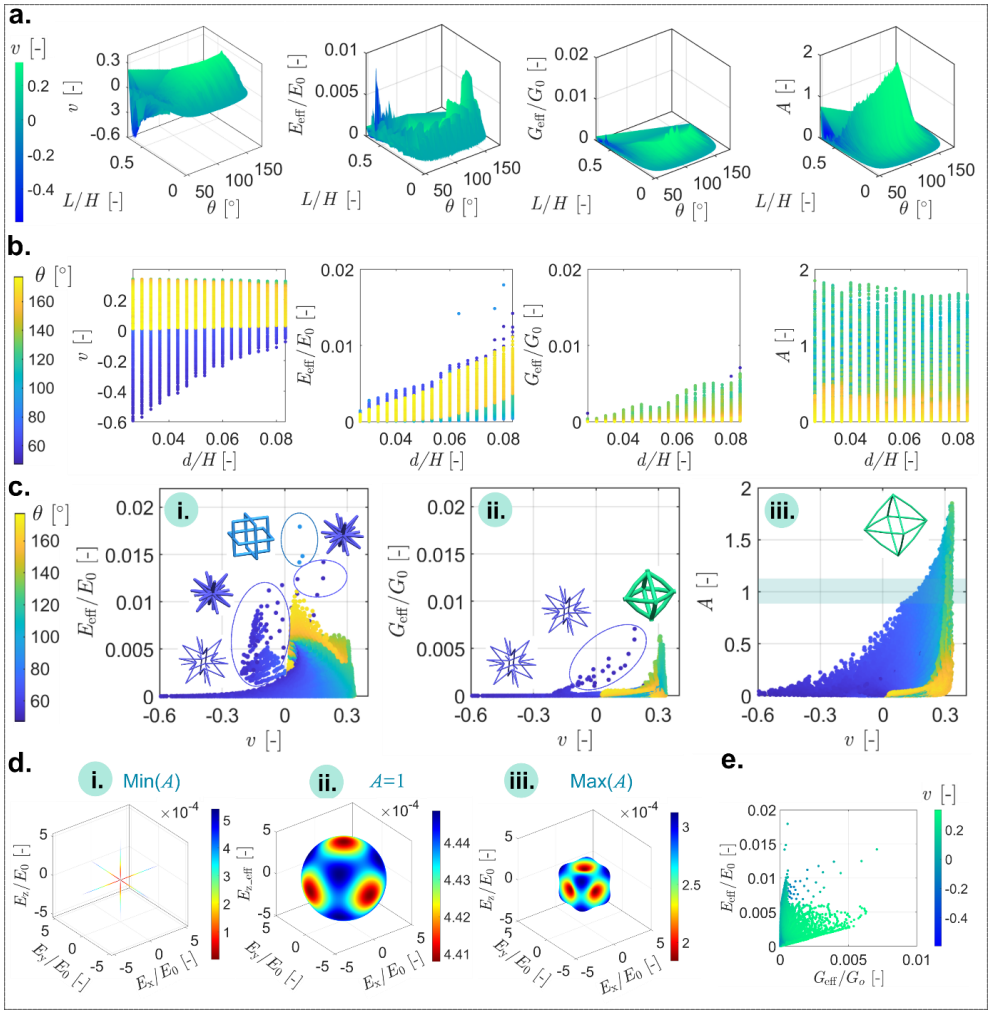

Figure 2. *The mechanical properties of the meta-biomaterials.* ***a.*** *3D surface plots of the mechanical properties as functions of θ and L, with a color bar representing the Poisson's ratio (v).* ***b.*** *The effects of the strut diameter (d) on v, E_{eff}/E_0, G_{eff}/G_0 and A. The color bar corresponds to the changes in θ.* ***c.*** *The evaluation of the elastic properties, including the normalized E_{eff} (E_{eff}/E_0, i.), G_{eff} (G_{eff}/G_0, ii.) and A (iii.) in relation to the Poisson's ratio (v). The light blue highlight in the plot A (iii) marks the range between 0.95 and 1.05 for A (i.e., fully isotropic unit cells).* ***d.*** *The stiffness maps of the unit cells with minimum (A_{min} = 9.20×10^{-4}, i.), unity (A = 1.0, ii.) and maximum Zener ratio (A_{max} = 1.90, iii.). The input parameters for these unit cells respectively were θ = 99.0°, L = 7.9/300 and d = 8.0/300, θ = 86.9°, L = 121.9/300 and d = 22.0/300 and θ = 131.0°, L = 103.5/300 and d = 8.0/300 .* ***e.*** *The variation of E_{eff}/E_0 vs. G_{eff}/G_0 in relation to the v (color bar).*

The 3D distribution of G_{eff}/G_0 as a function of θ and L showed a normal-like distribution with a maximum peak, indicating that G_{eff}/G_0 increased to a maximum at certain values of θ (*i.e.*, $\theta = 135.0^{\circ}$) and L (*i.e.*, $L/H = 100.0/300$), before decreasing

(Figure 2a and Figure S2a-i of the supplementary material). In Categories I and II, G_{eff}/G_0 increased with θ, but it decreased in Category III as θ increased. Similar to the distribution of E_{eff}/E_0, G_{eff}/G_0 showed an unexpected increase at the critical values of L (*i.e.,* $L/H > 160.0/300$) when θ was very small (*i.e.,* $\theta < 60.0^{\circ}$). The ranges of G_{eff}/G_0 for Categories I, II, and III were 6.003×10^{-7} to 0.007 ($6.834 \times 10^{-5} \pm 1.491 \times 10^{-4}$), 6.90×10^{-7} to 0.006 ($2.564 \times 10^{-4} \pm 5.497 \times 10^{-4}$), and 7.186×10^{-7} to 0.005 ($1.352 \times 10^{-4} \pm 2.704 \times 10^{-4}$), respectively.

The distribution of A was similar to that of G_{eff}/G_0, with peaks occurring at similar values of θ (*i.e.,* $\theta = 135.0^{\circ}$) and L (*i.e.,* $L/H = 100.0/300$, Figure 2a and Figure S2a-i of the supplementary material). The level of anisotropy, A, in Categories I, II, and III ranged from 9.56×10^{-4} to 1.26 (0.17 ± 0.27), 9.21×10^{-4} to 1.85 (0.32 ± 0.47), and 9.33×10^{-4} to 0.83 (0.0574 ± 0.09), respectively. All the categories could generate anisotropic meta-biomaterials with $A < 1.00$, but only Category II produced meta-biomaterials with $A > 1.00$, indicating that Category II structures are generally more isotropic as compared to those from Categories I and III (especially for very small or large values of θ).

Another key input parameter that significantly affected the mechanical properties of meta-biomaterials was the strut diameter, d, in addition to the spatial rearrangement of the struts (*i.e.,* θ and L). Varying d from 8.0/300 to 25.0/300 had a pronounced effect on v, E_{eff}/E_0, G_{eff}/G_0, and A (Figure 2b). In particular, changes in the strut diameter not only altered the magnitude of v but also switched its sign from negative to positive when $d > 25.0/300$. Moreover, increasing d led to a nonlinear decrease in v for the unit cells in Category I. However, the effects of changes in d on other mechanical properties could be compensated by adjusting θ and L. While increasing d significantly boosted E_{eff}/E_0 and G_{eff}/G_0, it had a minimal impact on A.

To further explore the correlation between the mechanical properties (*i.e.,* effective elastic and shear moduli and Zener ratio) and Poisson's ratio, we examined their 2D distributions (Figure 2c). The variation of E_{eff}/E_0 vs. v in Category I showed that higher values of Poisson's ratio could only be achieved by decreasing E_{eff}/E_0, making it challenging to expand the design space for auxetic meta-biomaterials with higher E_{eff}/E_0 [28, 29].

The meta-biomaterials from Category III exhibited the highest E_{eff}/E_0 as compared to Category I, but their Poisson's ratio tended towards zero. The maximum E_{eff}/E_0 was observed in unit cells with approximately right angles and negligible h (*i.e.,* $\theta = 90.2^{\circ}$, $L = 137.0/300$ and $d = 24.0/300$; Figure 2c-i, marked by a cyan ellipse). Figure 2c indicates that as the Poisson's ratio becomes more negative, the design space tightens in terms of the effective elastic modulus. Nonetheless, some of our meta-biomaterials achieved a similar range of E_{eff}/E_0 in Category I and III, which the Poisson's

ratios ranged between −0.30 and 0, and 0.30 and 0, respectively. Moreover, Poisson's ratio values in our 3D symmetric meta-biomaterials covered a wide range from −0.59 to 0.34, which is rare in 3D meta-biomaterials with symmetric properties. It should be noted that the blue data points in Figure 2c-i, encircled in purple, belong to the unit cells from Category I with a very large L (*e.g.,* $\theta = 50.8^{o}$, $L = 177.2/300$ and $d = 24.0/300$).

A similar trend was observed for the effective shear modulus, G_{eff}/G_0, but with a tighter distribution (in terms of area, Figure 2c-ii). As shown in Figure 2a-ii, the meta-biomaterials with PPRs (Categories II and III) exhibit higher G_{eff}/G_0, which is opposite to pentamode meta-materials [13]. Comparing the variations of E_{eff}/E_0 and G_{eff}/G_0 we found that: *i.* while meta-biomaterials with right angles (the blue unit cell in Figure 2c-i) exhibited the highest E_{eff}/E_0, they showed relatively low G_{eff}/G_0, and *ii.* meta-biomaterials with maximum G_{eff}/G_0 exhibited nearly maximum v, whereas those with maximum E_{eff}/E_0, showed nearly zero v. The maximum G_{eff}/G_0 occurred when θ approached 135.0^{o} (*i.e.,* $\theta = 129.3^{o}$, $L = 96.1/300$, and $d = 25.0/300$, Figure 2c-ii).

The level of mechanical anisotropy, A (Figure 2c-iii), however, provided a broader design space than E_{eff}/E_0 and G_{eff}/G_0, particularly in regions with NPRs. The meta-biomaterials with a high A (*i.e.,* $A > 1.50$), belonged to those from Category II with a θ ranging from 101.2^{o} to 131.0^{o}. More specifically, the unit cell with $\theta = 131.0^{o}$, $L = 103.5/300$ and $d = 8.0/300$ possessed the highest level of anisotropy (*i.e.,* $A = 1.85$, Figure 2c-iii). Moreover, similar to G_{eff}/G_0, the maximum A occurred at maximum v.

To visually illustrate the level of anisotropy of the unit cells, we plotted their stiffness maps for respectively minimum, unity, and maximum A (Figure 2d). For unit cells with $A < 1.00$, the homogenized stiffness tensor surfaces were much thinner, but the stiffness values in the x, y, and z directions) remained the same. For example, the minimum A belonged to unit cells with θ between 99.0^{o} and 107.0^{o}, $L = 7.7/300$ and $d = 8.0/300$. This means that these meta-biomaterials exhibited similar Poisson's ratios and effective elastic and shear moduli along three orthogonal directions (*i.e.,* x, y, or z), but significantly different properties in other directions (*e.g.,* 45.0^{o} respect to x). Meta-biomaterials with A values around 1 (*i.e.,* $0.95 < A < 1.05$, shown in the blue shadow in Figure 2c-iii), all exhibited PPRs (*i.e.,* $v_{\text{avg}} = 0.25$). We also presented a histogram of the data at this region (Figure S2a-ii of the supplementary material), confirming that auxetic meta-biomaterials predominantly exhibit higher levels of anisotropy than non-auxetic ones, as observed in previous studies [17].

Regarding the correlations between E_{eff}/E_0, G_{eff}/G_0, and A, let us consider Figure 2e. First, depending on the Poisson's ratio, meta-biomaterials exhibited either a high G_{eff}/G_0 but lower E_{eff}/E_0 (PPRs) or a low G_{eff}/G_0 but high E_{eff}/E_0 (nearly ZPRs and NPRs). For meta-biomaterials with A around unity (*i.e.,* $0.95 < A < 1.05$), the

correlation between E_{eff}/E_0 and G_{eff}/G_0 was linear, similar to isotropic materials (subplot in Figure S2a-ii of the supplementary material). It should, however, be noted that this linearity only applied to meta-biomaterials with PPRs.

4.2.2 Morphometric properties of the meta-biomaterials

We determined the morphometric properties of the meta-biomaterials, including PS_{W}, PS_{B} and PSR (see Section "Materials and methods) for different values of the input parameters (*i.e.,* θ, L and d), according to our derived geometrical relationships (Table 1), Figure 3. The variation of PS_{W} with θ indicated that increasing θ led to an increase in PS_{W} until θ reached 120.0^{o}, after which PS_{W} decreased as θ continued to increase towards its maximum value. However, this relationship depended on the magnitude of L. At small values of L (*i.e.,* $L/H < 0.1$), PS_{W} was almost independent of θ, as the unit cell size became very small. For unit cells with $0.1 < L/H < 0.4$, the variation of PS_{W} with θ exhibited symmetry, meaning that the same PS_{W} could be achieved in both Categories I and III. However, since larger values of L (*i.e.,* $L/H > 0.4$) primarily occurred in Category I, isolating the Poisson's ratio became challenging for such unit cells. PS_{W} in Categories I, II, and III ranged between 0.03 and 0.91 (0.29± 0.19), 0.03 and 0.94 (0.43± 0.22), and 0.03 and 0.63 (0.22± 0.13), respectively.

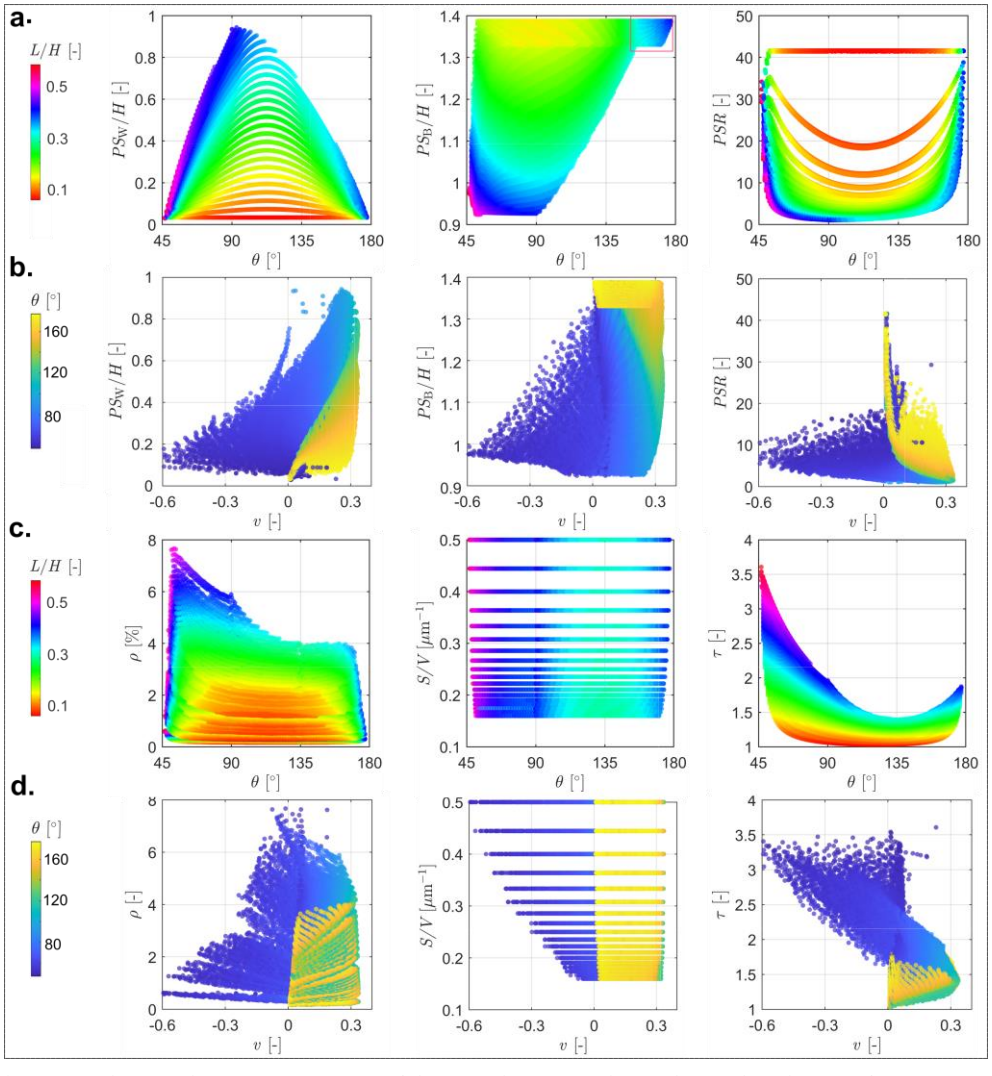

Figure 3. *The morphometric properties of the meta-biomaterials.* ***a.*** *The 2D distribution of PS_W, PS_B and PSR vs. θ. The color bar indicates the variation of L/H.* ***b.*** *The evaluation of the PS_W, PS_B and PSR in terms of v. The color bar represents the changes in θ.* ***c.*** *The 2D correlation between ρ, S/V and τ as a function of θ, with the color bar corresponding to the changes in L/H. d. The evaluation of ρ, S/V and τ in terms of v. The color bar indicates the changes in θ.*

Table 1. *A summary of the final form of the geometrical relationships in Categories I, II and III of our meta-biomaterials.*

Category	Category I	Category II	Category III
$\boldsymbol{\theta}$	$\theta_{min}<\theta\leq 90^{o}$	$90^{o}<\theta\leq 135^{o}$	$135^{o}<\theta<\theta_{max}$
$\boldsymbol{L}$	$0 < L \leq L_{max}$	$0<L\leq 0.36H$	$0<L\leq 0.36H$
$\boldsymbol{PS_W}$	$2L(\sin\theta - \cos\theta)-d$	$2L(\sin^2\theta - \sin\theta\cos\theta)-d$	$2L\sqrt{\sin^2\theta - \cos^2\theta +1}-d$
$\boldsymbol{PS_B}$	$\min\left(\sqrt{2}H-d\ \&\ \sqrt{3H^2+8L^2\sin^2\theta-8HL\sin\theta}-d\right)$	$\min\left(\sqrt{2}H-d\ \&\ \sqrt{3H^2+8L^2\sin^2\theta-8HL\sin\theta}\right)$	$\min\left(\sqrt{2}H-d\ \&\ \sqrt{3H^2+8L^2\sin^2\theta-8HL\sin\theta}-d\right)$
$\boldsymbol{PS_{min}}$	d	d	d
$\boldsymbol{L_{min}}$	$PS_W=PS_{min}$	$PS_W=PS_{min}$	$PS_W=PS_{min}$
$\boldsymbol{L_{min}}$	$\frac{2d}{2(\sin\theta-\cos\theta)}$	$\frac{2d}{2(\sin^2\theta-\sin\theta\cos\theta)}$	$\frac{2d}{2\sqrt{sin^2\theta-cos^2\theta+1}}$
$\boldsymbol{L_{max}}$	$\sqrt{2}H=2r+d+C$	$h=h_{min}=d/2$	$h=h_{min}=d/2$
$\boldsymbol{L_{max}}$	$\frac{\sqrt{2}(H-d)}{2\sqrt{\sin^2\theta-\cos^2\theta+1}}$	$\frac{H/2-d/2}{\lvert\sin\theta-\cos\theta\rvert}$	$\frac{H/2-d/2}{\lvert\sin\theta-\cos\theta\rvert}$
$\boldsymbol{\theta_{critical}}$	$L_{min}=L_{max}$	–	$L_{min}=L_{max}$
$\boldsymbol{\theta_{min}}$	$(d+PS_{min})\left(2\sqrt{\sin^2\theta_{min}-\cos^2\theta_{min}+1}\right)-\sqrt{2}(H-d)\left(2(\sin\theta_{min}-\cos\theta_{min})\right)=0$	–	–
$\boldsymbol{\theta_{max}}$	–	–	$\left(\frac{H}{2}-\frac{d}{2}\right)\left(2\sqrt{\sin^2\theta_{max}-\cos^2\theta_{max}+1}\right)\cdot(d+PS_{min})(\lvert\sin\theta_{max}-\cos\theta_{max}\rvert)=0$

On the other hand, the variation of PS_W with v did not follow a consistent pattern (Figure 3b). In Category I, sharper angles resulted in a smaller (tighter) PS_W, consistent with the behavior predicted by Eq. 5. This behavior is similar to the variation of the effective elastic and shear moduli vs. Poisson's ratio (Figure 2a). This means that to achieve auxetic meta-biomaterials with larger Poisson's ratios, one has to deal with a narrower design space in terms of PS_W, requiring sharper (smaller) angles.

Conversely, the variation of PS_B behaved oppositely to PS_W, with respect to the input parameters θ and L (Figure 3a). In Category III, PS_B reached a plateau around $\theta = 155.0^{o}$, remaining unchanged with further changes in θ (highlighted by the red rectangle in Figure 3a). This plateau occurred at the maximum value, where PS_B was equal to the face diagonal of the cube, $\sqrt{2}H - d$ (Figure 1e). The slight variation in PS_B within this plateau region was due to the differences in the strut diameter. The normalized L/H in this plateau region ranged from approximately 0.30 to 0.45. Overall, PS_B in Category III ranged between 1.18 and 1.39 (1.35± 0.03). In Category I, PS_B decreased when θ increased, ranging from 0.92 to 1.39 (1.14± 0.15). In Category II, increasing θ led to an increase in PS_B, ranging from 0.93 to 1.39 (1.24± 0.12). Similar to PS_W, PS_B exhibited

a random distribution with respect to v, further complicating the isolation of Poisson's ratio (Figure 3b).

The design space in terms of PSR displayed a smooth distribution across Categories I to III, indicating that similar PSR values could be generated (Figure 3a). This aspect is crucial for the subsequent optimization of the meta-biomaterials. For the unit cells with very small L/H (*i.e.,* $L/H < 0.1$), where PS_W was minimal, PSR was very large (*i.e.,* $PSR > 10.0$), which does not facilitate the optimization. Similar to PS_W, SR showed a symmetric variation with respect to unit cells at $\theta = 120.0^o$. PSR in Categories I, II, and III ranged from 1.07 to 41.63 (6.85 ± 6.42), 1.04 to 41.63 (4.85± 5.19), and 1.92 to 41.63 (9.36± 7.01), respectively. Considering the distribution of PSR vs. v (Figure 3b), the unit cells with the largest PSR typically exhibited nearly zero Poisson's ratios, as their L/H was very small.

The variation of the relative mass density with the input parameters indicated that increasing θ results in decreased relative mass density, until $\theta = 135.0^o$ (in Categories I and II). This trend is due to the variation of h with θ (Eq.2 and Figure S1a of the supplementary material). In Category III, however, increasing θ, resulted in a slight increase in the relative mass density, following the same trend as h. As for L, larger values of L resulted in a higher relative mass density, as more material is required. For very small values of L, the unit cells did not significantly contribute to the overall properties of the meta-biomaterials, making the variation of the relative mass density with θ almost negligible (Figure 3c). The relative mass density in Categories I, II and III ranged from 0.17 to 7.67 (2.03± 1.39), 0.16 to 5.77 (1.51± 0.99), 0.16 to 3.99 (1.33± 0.86), respectively. The relationship between Poisson's ratio and relative mass density followed an irregular pattern, making the optimization challenging.

According to Eq.S22, S/V is only dependent on the strut diameter d. Figures 3c and 3d also indicated that the distribution of S/V is not dependent on the other two input parameters θ and L. In our designed meta-biomaterials, S/V ranged from 0.16 to 0.5, as we changed the normalized strut diameter from 8.0/300 to 25.0/300. Moreover, the relationship between S/V and Poisson's ratio followed an irregular pattern, particularly in Category I (Figure 3d).

The distribution of tortuosity (see Section "Materials and method) followed an ordered trend concerning the input parameters θ and L (Figure 3c). However, there was no clear pattern regarding the variation of tortuosity with Poisson's ratio, making decoupling more challenging (Figure 3c). The effect of θ on the tortuosity was such that meta-biomaterials from Category I exhibited higher tortuosity values, while those from Categories II and III, particularly Category II, showed lower tortuosity. This is because the meta-biomaterials from Category II featured minimum h (Figure S1a of the supplementary material), leading to minimum L_{short} and, consequently, minimum tortuosity.

In Categories I and II, increasing θ resulted in decreased tortuosity particularly in Category I, indicating that increasing θ from its minimum value to 135.0^{o} results in a smoother path or shorter L_{short} (as per Eq. 24). Regarding the effect of L, increasing L led to an increase in L_{short} and, consequently, increased tortuosity, regardless of the unit cells category. Overall, Eq.24 demonstrated a correlation between tortuosity and the input parameters.

In Category I, tortuosity ranged from 1.06 to 3.61, with a mean of 1.90 and a standard deviation of 0.47. The minimum and maximum tortuosity values belonged to meta-biomaterials with $\theta = 89.0^{o}$, $L = 9.2/300$, and $d = 8.0/300$ and $\theta = 46.8^{o}$, $L = 200.0/300$, and $d = 8.0/300$, respectively. In Category II, tortuosity ranged from 1.03 to 1.96 with a mean of 1.32 and a SD of 0.18. The minimum and maximum tortuosity values belonged to meta-biomaterials with $\theta = 123.0^{o}$, $L = 7.8/300$, and $d = 8.0/300$ and $\theta = 90.2^{o}$, $L = 144.5/300$ and $d = 9.0/300$, respectively. In Category III, tortuosity ranged from 1.03 to 1.87 with a mean of 1.32 and an SD of 0.15. The minimum and maximum tortuosity values in Category III belonged to meta-biomaterials with $\theta = 135.0^{o}$, $L = 9.0/300$ and $d = 8.0/300$, and $\theta = 177.0^{o}$, $L = 138.0/300$, and $d = 8.0/300$, respectively.

The three plots in Figure 3c illustrate that relative mass density, S/V, and tortuosity followed a similar pattern in our meta-biomaterial designs, described as $A - B(\sin\theta - \cos\theta - C)$, in which A, B, and C are constants that primarily depend on L. This pattern suggests that auxetic meta-biomaterials (Category I) have the potential to exhibit higher values of relative mass density, S/V, and tortuosity as compared to non-auxetic ones (*i.e.,* Category III and II). This trend of relative mass density has also been shown in other studies [1].

4.2.3 Multi-objective Optimization of the meta-biomaterials

To isolate the Poisson's ratio from other properties, a systematic multi-objective optimization approach was necessary. We aimed to find two meta-biomaterials (or a pair) featuring maximum difference in Poisson's ratio and minimum difference in other parameters, including mechanical and morphometric parameters. This means that one meta-biomaterial exhibits an extreme NPR, and the other one exhibits an extreme PPR; while the other mechanical and morphometric properties remain as constant as possible. Nevertheless, due to the complexity of our optimization, we only considered the mechanical properties in the objection function as Eq.3. We first calculated the objective function for all the possible pairs (*i.e., i, j*) of the 43,000 number of simulations, which was equal to 1,848,957,000 numbers of pairs. We established the histogram of the calculated values of the objective function, which was Gaussian-like (Figure S3a-i of the supplementary material). Based on this normality, we only focused on data

whose objective function values fell within 0 and $2SD$ range to avoid high computational costs (Figure 4a).

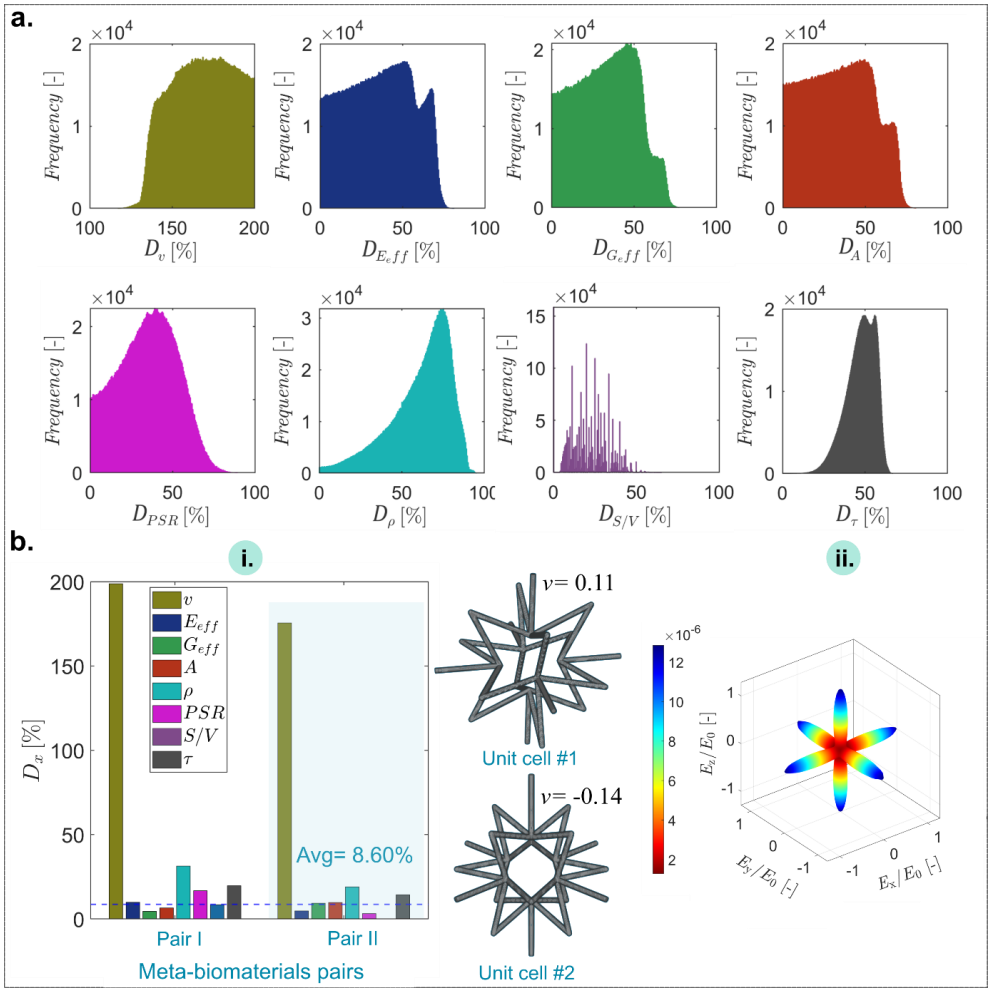

Figure 4. *The results of the multi-objective optimization.* ***a.*** *The histogram of the deviation in all mechanical and morphometric properties for each pair comparison.* ***b.i.*** *The final optimized meta-biomaterials with isolated Poisson's ratio at 10%, 15%, 20% and 32% deviations. Only two pairs were achieved (pairs I and II), one with maximum deviation of 31.37% (pair I) and the other one with 18.93% (pair II). The horizontal blue line indicates the average of all mechanical and morphometric properties (excluding Poisson's ratio) in the pair II. The final unit cells #1 and #2 with isolated Poisson's ratio are shown.* ***b.ii.*** *The stiffness map of the unit cell #1, which is similar to unit cell #2 showing their level of anisotropy.*

We then computed the deviation (or difference) of each mechanical and morphometric properties in each pair (between two unit-cells) using Eq.4 (Figure 4a). We computed the deviation of each property for all the possible pairs to calculate the (total) average deviation, as a criterion to find the optimal pairs It is important to note that

the high deviations (> 100%) for the Poisson's ratio were due to the differences in the sign of the Poisson's ratios (negative *vs.* positive) in each pair comparison. Following the histogram of the deviations (Figure 4a), fewer pairs exhibited lower deviations, which is expected. Particularly, this was more highlighted for the deviations of the morphometric properties, as they were not directly involved in the objective function. It is also shown that the relative mass density, and tortuosity are the most challenging ones in our optimization method (Figure 4a).

However, we set three different levels for the maximum deviation of each parameter: 10%, 15%, 20%, and 32%. The results of our optimization showed that it is not possible to find a pair of meta-biomaterials with the maximum deviation of less than 18.93%. For the deviation of less than 31.37%, we found two pairs as presented in Figure 4b-i. Two pair comparisons were notable: one with a maximum deviation of 31.37% (pair I, Figure 4b-i) and another with 18.93% (pair II, Figure 4b-i). In pair I (two unit cells from Category I), the maximum deviation of 31.37% belongs to the relative mass density, highlighting its challenging impact on our optimization process. We selected pair II, with a maximum variation of 18.93%, where the average variation across all properties (except for Poisson's ratio) was 8.60%. The two corresponding unit cells in pair II, labeled as unit cell # 1 and unit cell # 2 are illustrated in Figure 4b. Interestingly, although both unit cells belong to Category I (*i.e.,* $\theta < 90.0^{o}$), the first unit cell exhibited an NPR (*i.e.,* $\nu = -0.14$), while the second had a PPR (*i.e.,* $\nu = 0.11$).

To assess the anisotropy level of these two unit cells, we also plotted their stiffness maps (Figure 4b-ii). These maps revealed that both unit cells exhibit cubic symmetry with normalized elastic moduli of $E_{\text{eff}}/E_0 = 0.017$ and $G_{\text{eff}}/G_0 = 6.245 \times 10^{-4}$. Previously, this meant that these two meta-biomaterials are not only geometrically symmetric, but also exhibit similar mechanical properties in the three orthogonal directions of x, y and z. All mechanical and morphometric properties of these two unit cells are reported in Table 2. These two meta-biomaterials exhibit very similar mechanical properties (deviations of less than 10%) but are slightly different in their morphometric properties (deviations of 18.93%, 16.22%, and 14.24%, respectively for the relative mass density, surface-to-volume ratio, and tortuosity).

Table 2. *The mechanical and morphometric parameters of the meta-biomaterials with isolated Poisson's ratio* (*i.e.*, $\theta_1 = 64.0^o, L_1 = 104.5/300$ *and* $\theta_2 = 71.0^o, L_2 = 84.5/300$).

Properties	Simplified model		Deviation [%]
Parameter	design #1	design #2	-
v [−]	-0.14	0.11	178.57
E [MPa]	0.016	0.017	4.82
G [MPa]	6.55×10^{-4}	5.94×10^{-4}	9.32
A [−]	0.07	0.08	9.68
PSR [−]	3.75	3.63	3.18
ρ [−]	0.40	0.32	18.93
S/V [μm^{-1}]	0.5	0.5	0
τ [−]	2.07	1.78	14.24
Z_g [−]	2.42	2.42	0
k [m^2]	3.10×10^{-9}	4.07×10^{-9}	23.83

To validate the tortuosity calculated from Eq.S24 (supplementary material) in our modeling, we compared it with values obtained from a 3D voxel-based model using a customized plugin in ImageJ [30]. To achieve this, we used $n = 300$ for the voxelization to achieve a highly detailed 3D model. The distribution and the mean of the tortuosity were calculated (Figure S3b of the supplementary material). The tortuosity values derived from Eq.S24 for designs #1 and #2 were 2.07 and 1.89, respectively, while the values from the 3D solid model were 2.27 and 1.93, respectively. The comparison between these results showed a high level of agreement, validating our approach.

Regarding the connectivity of the meta-biomaterials, it should be noted that all the generated structures (with arbitrary L and θ input parameters) had the same connectivity. This uniformity arises from the total number of elements and the local connectivity of each node in these meta-biomaterials (Figure 1). Given the local connectivity of 2 for the marginal nodes of the unit cells (*i.e.,* nodes P1, P5, P8, P19, P13, and P16 in Figure 1g), and using Eq.S20 from the supplementary material, the calculated connectivity of the meta-biomaterials was 2.42.

The permeability of the Poisson's ratio-isolated meta-biomaterials calculated using FEM (Figure S3c of the supplementary material), showed a strong correlation with the variation in tortuosity and relative mass density. The final deviation of the permeability between unit cells #1 and 2 was about 23.83% (Table 3). The distribution of the Elucident line (L_e) vs. straight line (L_g) indicated a higher fluctuation for design #1 as compared to design #2 (Figure S3b from the supplementary material). This is because design #1 has a sharper angle than design #2. The pressure distribution and the flow speed contours are also presented in Figure S3c of the supplementary material. The similarity in permeability variation to that of the tortuosity and relative mass density can be attributed to the interrelated nature of these properties, which often have

nonlinear relationships [31]. Therefore, controlling one parameter can provide partial control over the others.

It is worth mentioning that the most challenging property to control in our model was the relative mass density (Figure 4). One potential solution is to use hollow struts instead of solid ones. This approach would allow for simultaneous tuning of mechanical and morphometric properties with greater flexibility. However, fabricating such micro meta-biomaterials with hollow struts poses significant challenges. For instance, although 2PP can theoretically 3D print these structures, removing the resin trapped within the hollows is very challenging.

4.2.4 3D Printing and mechanical characterization of the meta-biomaterials

To validate the results of our computational model, we 3D-printed six different meta-biomaterials and characterized their effective compressive modulus. To normalize the effective elastic modulus of the meta-biomaterials, it was necessary to first measure the Young's modulus of the base photoresist (IP-Q) (Figure 5a). From the linear region of the stress/strain curve in Figure 5a, Young's modulus was calculated to be 1008.2 ±7.5 MPa.

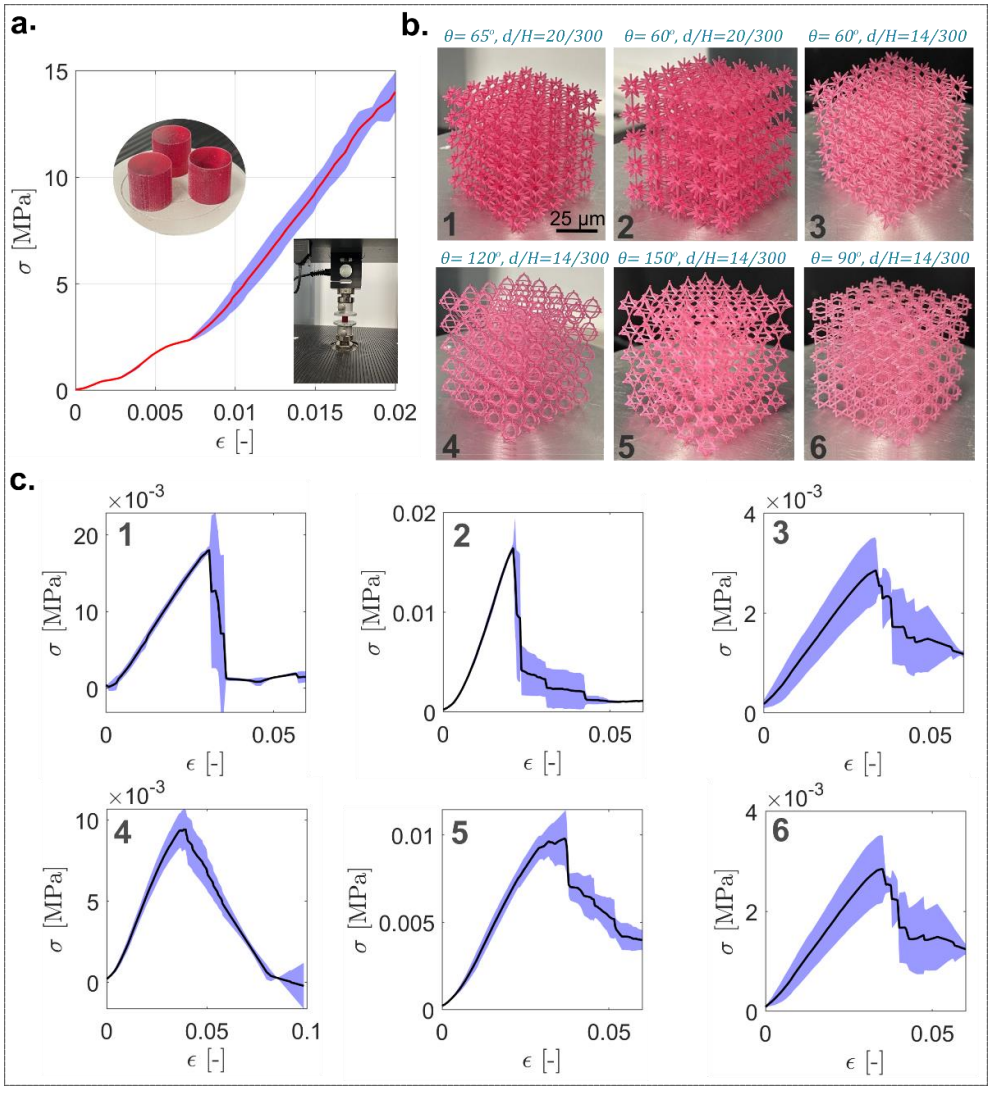

Figure 5. *The mechanical characterization of the meta-biomaterials at the macroscale.* ***a.*** *The uniaxial compression stress (σ) of the polymerized resin vs. strain (ε) at a displacement rate of 5 mm/s. The red solid line represents the mean, and the blue shadow indicates the standard deviation.* ***b.*** *Images of six PolyJet 3D printed meta-biomaterials with different geometrical parameters.* ***c.*** *The stress/strain response of the six meta-biomaterials under a uniaxial compression test with a 5 mm/s displacement rate. The black solid line and the blue shadow indicate the mean and the upper/lower bounds.*

The six meta-biomaterials, selected from different categories with varying input parameters, were 3D printed using an inkjet printing combined with UV curing, PolyJet, (Figure 5b). We then characterized the compression behavior of these meta-biomaterials under uniaxial loading at a displacement rate of 5 mm/s. The results are displayed in Figure 5c and Table 3, with additional details provided in Supplementary

videos S6-11. The experimentally measured effective elastic modulus showed strong agreement with our computational model. The minor discrepancies observed between the computational model and experimental results are likely due to 3D printing imperfections, assumptions in the computational models, potential sliding of the specimens on the bottom and top surfaces during testing, and the voxel resolution in our model.

Table 3. *The comparison between the results derived from the numerical homogenization method and the 3D solid elements.*

Meta-bio-material	**Unit cell**	**Homogenization method**			**3D solid elements**		**Experiment**	**Solid-Works**
L [× 1 /300], θ [°], d [× 1/300]		E_{eff}/E_0 [× 10^{-4}	υ [−]	ρ [%]	E_{eff}/E_0 [× 10^{-4}	υ [−]	E_{eff}/E_0 [× 10^{-4}	ρ [%]
110, 65, 20		6.400	0.05	3.55	5.680	0.00	6.799	3.43
110, 60, 20		9.840	0.02	3.57	8.320	-0.06	9.642	3.46
140, 60, 14		0.800	-0.17	2.02	0.800	-0.22	0.897	0.90
90, 120, 14		4.800	0.32	1.22	4.640	0.30	3.010	3.01
100, 150, 14		4.640	0.32	1.26	4.720	0.30	3.728	3.73
100, 90, 14		0.960	0.24	1.38	0.960	0.24	0.906	0.91

Furthermore, we 3D printed the meta-biomaterials at the microscale using the 2PP technique, which enables micrometric feature resolution (Figure S4 of the supplementary material). This included fabricating final structures with a normalized strut diameter of $8.0/300$ (Figure S4a-iv and S4a.v of the supplementary material), indicating the scalability of our developed meta-biomaterials. We also performed a compression test on a meta-biomaterial with $\theta = 65.0^{o},\ L = 110.0/300$, and $d = 20.0/300$, capturing an optical image of the deformed specimen (Figure S4b of the supplementary material).

4.3 Summary and conclusions

We introduced 3D geometrically symmetric meta-biomaterials with fully isotropic (*i.e.,* characterized by elastic modulus and Poisson's ratio) and cubic properties (*i.e.,* characterizing by elastic and shear moduli and Poisson's ratio), defined by 9 planes of symmetry. To explore the design space of these proposed meta-biomaterials in terms of mechanical and morphometric properties, we developed all necessary geometrical relationships in terms of input parameters (*i.e.,* strut angle, strut length, and strut diameter). By determining critical values in these relationships, we explored a broad design space for optimizing the proposed meta-biomaterials.

We employed an effective computational method combining homogenization techniques and FEM based on the 3D voxelization of the non-stochastic unit cells to calculate their mechanical, morphometric, and mass transport properties. We concluded that this method allowed achieving a broad spectrum of symmetric Poisson's ratios, ranging from -0.59 (Category I) to 0.34 (Category II), which is rare in 3D meta-biomaterials. Furthermore, we fine-tuned the level of anisotropy in our meta-biomaterials based on input parameters, resulting in high and low Zener ratios for unit cells from Categories I and II, respectively. We also concluded that meta-biomaterials from Category II exhibited a higher level of mechanical isotropy than other categories.

Through extensive simulations and a multi-objective optimization technique, which minimized an objective function incorporating elastic properties (*i.e.,* Poisson's ratio, effective elastic and shear moduli, and Zener ratio) while constraining morphometric properties, we successfully isolated Poisson's ratio from other mechanical and morphometric characteristics. The analyses of many designs allowed identifying two with highly different Poisson's ratio (*i.e.,* one negative and one positive) while all the other mechanical and morphometric parameters differed by less than 11%. This will enable studying the isolated influence of the Poisson's ratio on cell-growth and differentiation.

We also fabricated our proposed meta-biomaterials using PolyJet and 2PP techniques, achieving precise control over feature resolution at both macro- and microscales, respectively. We mechanically characterized the compression behavior of our

3D printed meta-biomaterials to validate our predicted computational results. The experimental results confirmed the high accuracy of our computational predictions, validating the robustness of our computational model and fabrication approach.

We believe that our methodology for designing 3D symmetric meta-biomaterials and effectively isolating Poisson's ratio not only advances the understanding of the mechanical design of meta-biomaterials but also opens new avenues for future mechano-biological studies, particularly when focusing on the effect of a single parameter. These advancements have significant implications for real-world applications, particularly in the development of meta-implants that can be tailored to optimize cellular responses and enhance bone tissue regeneration.

4.4 Material and methods

4.4.1 Geometrical design of the meta-biomaterials

The detailed derivation of the equations related to the geometrical design of our meta-biomaterials is provided in the supplementary material, with a summary of all the geometrical formulas presented in Table 1. It should be noted that we categorized our designs into three categories, namely Category I, Category II, and Category III, based on the parameters θ and L (Figure 1c). Specifically:

Category I: $\theta_{\min} < \theta \leq 90.0^{o}$ and $0 < L \leq L_{\max}$,

Category II: $90.0^{o} < \theta \leq 135.0^{o}$ and $0 < L \leq 0.36H$

Category III: $135.0^{o} < \theta < \theta_{\max}$ and $0 < L \leq 0.36H$.

In our designs, two distinct pore sizes were defined, given that the proposed meta-biomaterials are composed of repetitively arranged monolithic unit cells. The first pore size refers to the internal pore shape within the unit cell, termed as the "pore size within" (PS_{W}, represented by the dark green sphere in Figure 1h). The second pore size is defined by the voids created between adjacent unit cells, referred to as the "pore size between" (PS_{B}, represented by the light green sphere in Figure 1h). These pore sizes have direct and explicit relationships with θ and L, the actual form of which depends on the Category. As these two pore sizes play a role in both unit cells and the meta-biomaterials, we considered their ratio, named pore size ratio (PSR) as $PSR = PS_{\mathrm{B}}/PS_{\mathrm{W}}$, in our final optimization process.

After extracting all the geometrical correlations for the critical values of the input parameters, we generated a large number of unit cells within the design space defined by our model (*i.e.,* $\theta_{\min}$, $\theta_{\max}$, $L_{\min}$, and $L_{\max}$, as shown in Figure 1k). The generation process is further illustrated in the supplementary video S1.

4.4.2 Voxelization of the meta-biomaterials

To voxelize the meta-biomaterials, we considered a single unit cell as a representative structure, which is encapsulated within a 3D cube of side-length H, as previously mentioned. We assumed H to be identically unity in the three orthogonal directions. Let n represent the number of voxels along each orthogonal direction (*i.e.,* x, y, and z), resulting in each voxel being cubic as well and having a size of H/n. The voxel matrix was a binary matrix composed of zeros and ones, where each value indicated the absence (zero) or presence (one) of materials within the unit cell. The overall size of the unit cell is equal to the matrix of $n \times n \times n$. The criterion for determining the presence of the material was whether the minimum distance from the voxel's center to the line segment of the strut was less than the strut diameter. The detailed information on the calculation of the minimum distance can be found in [27].

To generate the voxel representation of the unit cells, we first parametrically formulated the coordinate systems of all the vertices of the unit cells (Figure 1g), as detailed in Table S1 of the supplementary material. We assumed that the coordinate system originated at the corner of the cube (Figure 1c).

The overall size of the unit cell and the quality of the voxelated unit cell depend on the number of voxels, n, along the orthogonal directions. Figure S1b of the supplementary material illustrates unit cells in 2D and 3D. It is worth noting that the relative mass density of the unit cells was also calculated through the voxelization process. This was done by taking the ratio of the volume of voxels with material (*i.e.,* with entries of 1) to the total volume of the unit cell.

4.4.3 Measuring the connectivity, tortuosity, and permeability of the meta-biomaterials

The connectivity of the meta-biomaterials was calculated as the ratio of the sum of the connectivity at each node in the unit cell to the total number of nodes in the unit cell [32]. The corresponding formula for the connectivity is provided in Section S2 of the supplementary material. The surface-to-volume ratio (S/V) was calculated as the ratio of the total surface area of the struts in a unit cell to the total volume of the unit cell. The empirical equation for this calculation is also detailed in Section S2 of the supplementary material.

We defined the geometrical tortuosity (*i.e.,* τ), as the ratio of the shortest path length from the inlet to the output of the flow (from the top to the bottom of the unit cell, specifically between nodes P1 and P16 as shown in Figure 1g) to the end-to-end length of the unit cell, referred to as Euclidean length (L_e). The formula for calculating tortuosity is presented in Section S2 of the supplementary material. For greater precision, tortuosity was also calculated using a 3D model based on the voxelization of the

3D unit cells, using a customized plugin in ImageJ [30]. This purpose involved first voxelizing the unit cells and then generating all the 2D image slices (z-stacks), as shown in the supplementary videos S2-S4. We merged all the z-stacks in ImageJ to create a 3D voxelized unit cell and then applied the Tortuosity plugin from [30] to compute the tortuosity.

To calculate the permeability of the meta-biomaterials, we employed a commercial FEM code, COMSOL Multiphysics (6.1, COMSOL Inc, Sweden). Considering the overall size of the unit cells, we modeled a cavity within a cube with the dimensions $300 \times 300 \times 300\ \mu m^3$. The model was set up using the creeping flow regime to solve the continuity and Navier Stokes equations. At the inlet boundary, the pressure was set to 10^{-3}Pa, while atmospheric pressure was set to zero at the outlet. The boundaries that correspond to the solid-fluid interface were defined as walls, with a no-slip boundary condition applied. Symmetry boundary conditions were used for the outer boundaries. The mass density and flow viscosity were respectively set to 1000 kg/m^3 and 0.001 Pa. s. The permeability of the meta-biomaterials was then calculated using Eq. 25 from Section S2 of the supplementary material.

4.4.4 Numerical homogenization modeling of the meta-biomaterials

To model the meta-biomaterials in this study, we applied periodic boundary conditions (Figure 1b) to significantly reduce the computational time. This approach is particularly useful because the real meta-biomaterials have complex microarchitectures composed of multiple unit cells oriented in different directions (*i.e.*, x, y, and z). Moreover, we employed a computational homogenization technique to calculate the effective mechanical properties, including the effective elastic modulus (E_{eff}), shear modulus (G_{eff}), and anisotropy ratio (A) [27]. The use of this homogenization method was motivated by the high computational cost associated with finite element modeling of such complex meta-biomaterials.

The homogenization technique is an efficient method for calculating the macroscopic mechanical properties of heterogenous structures with microarchitectures, assuming perfect bonding between different phases in the material (*e.g.,* between void and solid material or between two different materials) [27, 33]. In the asymptotic homogenization method, the macroscopic elasticity tensor is derived from the locally varying elasticity tensor, strain field, and prescribed strain field (Eqs.S26-29 of the supplementary material). This process results in a governing elasticity equation, in which the effective elasticity tensor is solved numerically by discretizing the equation using FEM to calculate the global displacement fields. Detailed descriptions of the implementation of this method can be found in [33] and [27] for 2D and 3D boundary value problems. Here, we used the customized MATLAB function provided by [27].

4.4.5 3D solid FEM of the meta-biomaterials

To validate the numerical homogenization results of the 3D meta-biomaterials, we analyzed 3D solid elements of the meta-biomaterial designs using FEM via the commercial nonlinear FEM code, Abaqus, (2022, Dassault Systèmes, France). The meta-biomaterials were simulated using a quasi-static solver, accounting for geometrical nonlinearity due to the complexity of the structures. Specifically, the ".step" (the standard for the exchange of product data) files of the designs, consisting of $5 \times 5 \times 5$ unit cells, were imported from SolidWorks (2022, Dassault Systèmes, France) into Abaqus. The same material properties used in the homogenization method were applied here, specifically a linear isotropic material with $E_0 = 1250$ MPa and $v = 0.45$.

Two reference points were defined and kinematically coupled to all the nodes on the top and bottom surfaces of the meta-biomaterials. As a boundary condition, all the degrees of freedom at the bottom reference point were fixed (*i.e.,* $U = U_R = 0$). The meta-biomaterials were subjected to mechanical loading by applying a uniaxial compression displacement with 1% strain. It is important to note that, due to the symmetry of the meta-biomaterials in three orthogonal directions, we only loaded the specimens along one direction, y, in all the 3D solid elements simulations and experiments.

The meta-biomaterials were meshed using 3D quadratic tetrahedral elements (10 nodes), known as C3D10 as shown in Figure S1c of the supplementary material. To ensure the reliability of our numerical investigations and obtain consistent outcomes regardless of the mesh size, we conducted a mesh convergence analysis. The results indicated that the effective elastic modulus values converged within a 4% range when using 1.4 million elements, with an hour-long simulation time.

The engineering stress of the meta-biomaterials was calculated by dividing the reaction force derived from the FEM modeling by the initial projected cross-sectional area of the meta-biomaterials. The engineering strain (ε) was calculated by dividing the displacement of the top reference point by the initial height of the meta-biomaterials. Ultimately, the effective elastic modulus was computed using the reaction force at the top reference point (*i.e.,* $F_{RP_{\text{top}}}$) and the projected cross-sectional area as follows:

$$E_{\text{eff}} = \frac{F_{RP_{\text{top}}}}{H^2 N_z N_x} \times \frac{1}{\varepsilon} \tag{1}$$

The Poisson's ratio was calculated by considering the lateral deformations of either the middle nodes or all nodes. Depending on the approach, the values of the Poisson's ratios may differ slightly. Here, we assumed that the middle layers were sufficiently far from the boundary conditions (top for loading and bottom for fixed constraints) and calculated the Poisson's ratio based on this assumption as follows:

$$v = \frac{-\varepsilon_x}{\varepsilon_y} = \frac{-\left(U_{x_{\text{left}}} - U_{x_{\text{right}}}\right)}{\varepsilon H N_x}; \tag{2}$$

where $U_{x_{\text{left}}}$ and $U_{x_{\text{right}}}$ are the average displacements (along x) of the middle nodes on the highlighted blue and green planes in Figure 1b.

4.4.6 Multi-objective optimization process for the meta-biomaterials

Multi-objective optimization was employed to isolate Poisson's ratio from the mechanical and morphometric properties of the meta-biomaterials. To achieve this, we first considered mechanical properties, including E_{eff}, G_{eff}, A, and v in the objective function (OF), defined as follows:

$$OF = \frac{|v_i + v_j|}{|v_i| + |v_j|} + \frac{\left|E_{\text{eff}_i} - E_{\text{eff}_j}\right|}{\left|E_{\text{eff}_i}\right| + \left|E_{\text{eff}_j}\right|} + \frac{\left|G_{\text{eff}_i} - G_{\text{eff}_j}\right|}{\left|G_{\text{eff}_i}\right| + \left|G_{\text{eff}_j}\right|} + \frac{|A_i - A_j|}{|A_i| + |A_j|} \tag{3}$$

The positive sign in the Poisson's ratio term helps identify pairs of meta-biomaterials with different signs (one positive and one negative). We aimed at minimizing the objective function values to achieve a pair of meta-biomaterials with extremely different Poisson's ratio (one negative one positive) but similar other properties. To normalize the contribution of each parameter in the objective function (Eq.3), we divided each difference by its corresponding magnitude (*i.e.,* $|Parameter1_i| + |Parameter1_j|$), in which i and j stand for unit cell 1 and unit cell 2 in each pair, respectively.

To find the optimal pair with the maximum similarity in E_{eff}, G_{eff} and A but with opposite signs of v, we sorted the values of the objective function. To accelerate the optimization process, we filtered the data by assuming a normal-like distribution, only those values within 0 and $2SD$ range were considered. All other properties were similarly sorted for the data within this range. The deviation between all pairs (D) was also calculated as follows:

$$D_x = \frac{\left|parameter_i - parameter_j\right|}{\max\left(|parameter_i| \text{ and } \left|parameter_j\right|\right)} \times 100 \tag{4}$$

4.4.7 PolyJet 3D printing of the meta-biomaterials

We used a multi-material 3D printer, the Polyjet J5 (MediJet®, Stratasys® Ltd., USA), which is a spray-based inkjet printer, to fabricate our meta-biomaterials. Polyject printing works based on the spray inkjet method, in which the droplets of a photoresist are polymerized via UV. The commercially available photoresist VeroMagentaTM (RGD841, Stratasys® Ltd., USA), a relatively hard material, was used. Due to the

complexity of our meta-biomaterials, particularly those from Category 1 (re-entrant unit cells) that require supports, we used a water-soluble photoresist, WSS™150 (Stratasys® Ltd., USA), as the support material. The specimens were soaked in tap water overnight to remove the support material, followed by air drying in a fume hood overnight. The .stl files of the meta-biomaterials were imported into the printer's compatible software (GrabCAD Print) for the fabrication.

4.4.8 2PP-based fabrication of the meta-biomaterial specimens

The meta-biomaterials at the micro-level were fabricated using 2PP. 2PP is an advanced 3D printing technique capable of fabricating very small features, from a few hundred nanometers to larger scales (centimeters) by two-photon absorption of a femtosecond laser [34, 35]. The initial designs were created using SolidWorks (2022, Dassault Systèmes, France), and then exported as .stl files. These files were imported into DeScribe software (Nanoscribe, Germany) to generate .gwl files, which were subsequently used in Nanowrite software (printing software, Nanoscribe, Germany) to interface with the 2PP 3D printer for the fabrication process. The printing was carried out using a Photonic Professional GT+ 3D printer from Nanoscribe.

The DiLL configuration was employed, using a 10× objective featuring a N.A of 0.30. This lens was chosen based on the size of the specimens and solid/void features that needed to be accurately reproduced. A negative tone, methacrylate-based resin known as IP-Q (Nanoscribe, Germany) with a refractive index of 1.49 was used as the photoresist. The specimens were printed on silicon substrates (25×25×0.7 mm3, Nanoscribe, Germany) with a refractive index of 3.71 @ 780 nm.

For the stage movement during the print, we employed the piezo modality instead of the *z*-drive one. That is because the *z*-drive movement can induce micro-mechanical instability in the stage and the photoresists, potentially leading to imperfections. Given the maximum 300 μm range for the piezo mode, the overall size of the meta-biomaterials (*i.e.,* 1.5 × 1.5 × 1.5 mm^3), and the writing field of the 10× objective (707.10×707.10 μm2), we stitched the meta-biomaterials into smaller blocks. To further avoid photoresist instability at the start of the printer, we decelerated the mechanical movement of the stage to 5 mm/s2 with a maximum velocity of 100 mm/s. After conducting multiple printing trials to optimize the printing parameters, we finalized the following settings: 100% laser power (*i.e.,* 50 mW), 30000 μm/s scanning speed, and 1 μm for both slicing and hatching distances.

To improve print quality in solid structures, we integrated a block shear angle (the angle between the stitched designs) with a specific overlap. Since the meta-biomaterials contain tilted struts, it was crucial to consider the effects of both the tilted struts and the block shear angle at the same time. A block shear angle of 40° was selected for all

types of the meta-biomaterials to achieve better printing quality, along with 5 μm overlaps in both vertical and longitudinal directions.

Additionally, overlaps between the segments and the number of contours, as well as their spacing, were optimized to enhance the printing quality. This optimization was achieved by conducting several tests on a unit cell of the meta-biomaterials (without stitching) to determine the best settings for these parameters. Based on the quality of the prints, five contours with a spacing of 1 μm were selected.

Before printing, the silicon substrates were cleaned with acetone and IPA (both from Sigma-Aldrich, Germany) using a lint-free wipe, followed by blow drying with nitrogen. To further clean and activate the surface of the substrates, an oxygen plasma cleaner (Diener Electronic GmbH, Germany) was used at 80 W with a gas flow rate of 5 cm3/min and a pressure of 0.12 bar for 15 minutes. To enhance the adhesion between the specimens and substrates, silanization was performed by submersing the substrates into pure 3–(Trimethoxysilyl) propyl methacrylate (Sigma-Aldrich, Germany) for 1 hour. Silanization facilitates effective chemical bonding by making the substrate surface hydrophobic. After silanization, the specimens were washed with IPA and distilled water, followed by air-drying.

After exposing the specimens, they were immersed in PGMEA (Sigma-Aldrich, Germany) for 1 hour in a borosilicate petri dish to dissolve the unpolymerized resin. The specimens were then rinsed with IPA for 5 minutes to remove residual PGMEA. To further reduce capillary force-induced deformation in the structures and to enhance bonding between the specimens and silicon substrates, Novec 7100 engineered fluid (Sigma-Aldrich, Germany) was applied for 30 seconds, as this solvent has a lower surface tension than IPA.

4.4.9 Macro-mechanical compression test

To measure the mechanical properties of the meta-biomaterials at the macroscale, we employed a mechanical uniaxial test machine (LLOYD instrument LR5K, UK) equipped with load cells for 5kN (to calculate the Young's modulus of the bulk material using cylindrical specimens), 100 N (for the specimen numbers 1, 2, 4, and 5 from Figure 5b) and 50 N (for the specimen numbers 3 and 6 from Figure 5b), respectively. All the experiments were conducted in the quasi-static compression mode at a stroke rate of 5 mm/s. The force displacement data acquired during testing was used to calculate the engineering stress and engineering strain of the specimens by dividing the force by the initial projected cross-sectional area and the displacement by the height of the specimens, respectively. The effective elastic modulus of the meta-biomaterials was then determined from the linear portion of the engineering stress-strain curve.

4.4.10 Meso-mechanical compression test

For uniaxial compression of the 2PP 3D printed meta-biomaterials, we used a dynamic mechanical testing machine (MechanoCulture TX, CellScale, Canada). For this purpose, we used a 10 N load cell to compress the specimens under load-controlled mode (with a maximum force of 1 N) over a 10 second period.

4.4.11 SEM and optical imaging

Prior to SEM, all the specimens were sputter-coated with gold at 20 mA for 20 seconds twice, using ±45° tilted configurations to ensure a homogeneous distribution of the gold layer, which was approximately ~12 nm. SEM imaging was performed using a JEOL JSM-IT100 (Japan). For optical imaging of our specimens, we used a Keyence Digital Microscope VHX-6000 (Keyence, Japan).

4.5 Supplementary material

4.5.1 Geometrical design of the meta-biomaterials

The meta-biomaterials proposed here were geometrically symmetric (Figure 1b). They possess 9 planes of symmetry, particularly in three orthogonal planes xy, xz and yz. To design the meta-biomaterials, we assumed that their unit cell was encapsulated within a cube with a fixed size of H (Figure 1c). The six tails of the unit cell (*i.e.,* the red dots in Figure 1c) were fixed on the six faces of the cube. This means that those boundary nodes are always attached to those faces while all other geometrical parameters vary (*i.e.,* θ and L). By changing the geometrical input parameters, the non-boundary nodes move along the face diagonal of the cube.

The dimension H serves as a scale factor for the overall size of the meta-biomaterials and does not change their mechanical properties. Therefore, it was not considered as an input parameter in our computational model. To avoid the effect of the overall size (*i.e.,* H) on the mechanical and morphometric results, we normalized the dimensions, such as L, d and pore sizes by dividing them to H.

To parametrically design our meta-biomaterials, we derived all the relationships between the geometrical and morphometric parameters (*e.g.,* pore sizes). The parameter h, referred to as the tail length (Figure 1d), had to be explicitly derived first. To achieve this, we extracted the following geometrical constraints (Figure 1d).

$$h_{\mathrm{p}} = \frac{H}{2} - h; x = Lcos\theta - h; \tag{S1}$$

Therefore, by ensuring consistency along the y direction (*i.e.,* $x + y = H/2$), the parameter h was derived as follows:

$$h = \frac{H}{2} - L(\sin\theta - \cos\theta) \quad \text{(S2)}$$

The parameter h/H, therefore, depends on L/H and θ. To further clarify the relationship between h and L and θ, we plotted the normalized h (h/H) *vs.* θ for different values of L/H (Figure S1a). The maximum value of h/H (= 0.5) occurs at the minimum θ, which is 45°, and remains constant at this value regardless the values of L/H. Conversely, the minimum h/H is observed at $\theta = 135°$. However, considering the constraint $h/H \geq 0$, the point where $h/H = 0$ varies with L/H, particularly when $L/H \geq 0.35$. For instance, when $L/H = 0.5$, h/H reaches zero at $\theta = 90°$ (Figure S1a). Note that the critical value of L/H at which $h/H = 0$ at $\theta = 135°$ is obtained by considering Eq.S2 as follows::

$$L = \frac{H}{2(\sin\theta_h - \cos\theta_h)} = 0.35H \quad \text{(S3)}$$

Therefore, based on this dependence of geometrical parameters (θ and L), we classified the unit cells into three categories; Category I, when $\theta_{min} < \theta \leq 90°$ and $0.0 < L \leq L_{max}$, Category II, when $90° < \theta \leq 135°$ and $0.0 < L \leq 0.35H$ and Category III when $135° < \theta < \theta_{max}$ and $0.0 < L \leq 0.35H$ (Figure 1c). Note that the L_{max} can theoretically be infinite, but its practical limit will be determined by the minimum overlap constraint when patterning the unit cells.

The critical values of θ and L (*i.e.,* θ_{min}, θ_{max}, L_{min} and L_{max}) define the design space of our meta-biomaterials, making their accurate calculation essential. These critical values are determined differently, depending on the type of the unit cell (the ranges of θ). To begin, we first need to calculate the pore sizes.

In Categories I, II and III, the pore size within is equal to the diameter of the blue circle encapsulated within the unit cell as shown in Figure 1d, 1e and 1f, respectively (*i.e.,* $PS_W = 2r_d - d$). In case of Category I, PS_W is therefore as follows, considering Eq.S1:

$$PS_W = 2h_p - d = H - 2h - d; \quad \text{(S4)}$$

where d corresponds to the strut diameter. The final form of PS_W was derived as follows, considering Eq. S2:

$$PS_W = 2L(\sin\theta - \cos\theta) - d \quad \text{(S5)}$$

In Category II, similarly, PS_W is equal to following formula (Figure 1e):

$$PS_W = 2h_p \sin(\pi - \theta) - d \quad \text{(S6)}$$

Eventually, PS_W in Category II is formulated as follows, considering Eq.S1:

$$PS_{\mathrm{W}} = 2L(\sin^2\theta - \sin\theta\cos\theta) - d \tag{S7}$$

In Category III, r_d is formulated as follows (Figure 1f):

$$r_d = \sqrt{L^2 + h_{\mathrm{p}}^2 - 2h_{\mathrm{p}}Lcos(\pi - \theta)} = L\sqrt{\sin^2\theta - \cos^2\theta + 1} \tag{S8}$$

Therefore, considering $PS_{\mathrm{W}} = 2r_{\mathrm{d}} - d$, the final form of PS_{W} is as follows:

$$PS_{\mathrm{W}} = 2L\sqrt{\sin^2\theta - \cos^2\theta + 1} - d \tag{S9}$$

The pore size between, PS_{B}, on the other hand, is three dimensionally calculated by considering at least $2 \times 2 \times 2$ unit cells, as illustrated in Figure 1h, the light green sphere. To calculate PS_{B}, let's consider the cube created by $2 \times 2 \times 2$ unit cells. To create such a cube, we linearly pattern a unit cell eight times. The pore size between is equal to the distance between two unit cells on the body diameter of the cube (*e.g.,* the distance between the unit cells at the corner top and the one at the corner bottom). Considering node P20 (Figure 2g) of the top unit cell and node $P10_{\mathrm{transfer}}$ (Figure 2g) of the bottom unit cell, the coordinate of node $P10_{\mathrm{transfer}}$ was calculated by transforming the top unit cell by $(H, H, -H)$. Therefore, PS_{B} was derived as follows:

$$PS_{\mathrm{B}} = \sqrt{3H^2 + 8L^2\sin^2\theta - 8HLsin\theta} - d \tag{S10}$$

However, at a certain condition, for instance, when L is small, PS_{B} is equal to the face diagonal of the 3D red cube (Figure 1i) as $\sqrt{2}H$, regardless of strut diameter. Therefore, in this case PS_{B} is as follows:

$$PS_{\mathrm{B}} = \sqrt{2}H - d \tag{S11}$$

To determine which equation applies, one approach is to compare Eqs. S10 and S11 and solve for critical values of L at each θ, where the two expressions are equal. Alternatively, a simpler and more practical method is to calculate PS_{B} as the minimum of the two values (*i.e.,* $PS_{\mathrm{B}} = min({PS_{\mathrm{B}}}^{S10}, {PS_{\mathrm{B}}}^{S11})$.

Here, to calculate the minimum of L, PS_{W} should also be minimum. Considering PS_{min} as the minimum of the PS_{W}, and Eq.S5 for Category I, the minimum of L is explicitly formulated as follows:

$$L_{\mathrm{min}} = \frac{d + PS_{\mathrm{min}}}{2(\sin\theta - \cos\theta)} \tag{S12}$$

Similarly, for Category II, considering Eq.S7, the minimum of L is equal to:

$$L_{\mathrm{min}} = \frac{d + PS_{\mathrm{min}}}{2(\sin^2\theta - \sin\theta\cos\theta)} \tag{S13}$$

For Category III, by considering Eq.S9, the minimum of the L is calculated as follows:

$$L_{\min} = \frac{d+PS_{\min}}{2\sqrt{\sin^2\theta-\cos^2\theta+1}} \quad \text{(S14)}$$

It should be notated that $PS_{\min}$ must not be smaller than strut diameter d, as values below this threshold lead to overlapping struts. Such overlaps complicate the voxelization process, particularly for unit cells in Categories I and III with very sharp angles, by increasing computational cost and reducing model accuracy. We here set $PS_{\min} = d$, but to further avoid these problematic configurations, greater $PS_{\min}$ can be chosen (*e.g.*, $PS_{\min} = 2d$).

On the other hand, the maximum of L is achieved for different conditions, depending on the Category. In Category I, it is achieved when r (Figure 1j) is equal to the half of the face diagonal of the unit cell. However, we should also consider the strut diameter and a clearance between two tips of adjacent struts (*i.e.*, C, the diameter of the green circle in Figure 1j). Therefore, considering $r = L\sqrt{\sin^2\theta - \cos^2\theta + 1}$, $L_{\max}$ is explicitly formulated as follows:

$$L_{\max} = \frac{\sqrt{2}H - d - C}{2\sqrt{\sin^2\theta - \cos^2\theta + 1}} \quad \text{(S15)}$$

To calculate the clearance C, the value of $L_{\max}$ should be the same for Categories I and II when $\theta = 90^{\circ}$. But we need to calculate $L_{\max}$ in Categories II and III first.

In Categories II and III, $L_{\max}$ is achieved when h is minimum. However, we considered a minimum for h (*i.e.*, $h_{\min} = d/2$), because of the strut diameter. Therefore, considering Eq.S2 and $h_{\min}$, $L_{\max}$ is as follows:

$$L_{\max} = \frac{H/2-h_{\min}}{|\sin\theta-\cos\theta|}; \quad \text{(S16)}$$

The constant C, considering same value for both Eqs.S15 and 16 when $\theta = 90.0^{\circ}$, is equal to $\sqrt{2}d - d$ and therefore the final form of Eq.S15 is as follows:

$$L_{\max} = \frac{\sqrt{2}(H - d)}{2\sqrt{\sin^2\theta - \cos^2\theta + 1}} \quad \text{(S17)}$$

The critical values of θ (*i.e.*, $\theta_{\min}$ in Category I and $\theta_{\max}$ in Category III) are achieved when the maxima and minima of L are equal (*i.e.*, $L_{\min} = L_{\max}$). Therefore, in Category I, $\theta_{\min}$ is calculated through the following equation using fsolve function in Matlab.

$$(d + PS_{\min})\left(2\sqrt{\sin^2\theta_{\min} - \cos^2\theta_{\min} + 1}\right) - \sqrt{2}(H - d)\left(2(\sin\theta_{\min} - \cos\theta_{\min})\right) = 0 \quad \text{(S18)}$$

Similarly, $\theta_{\max}$ (in Category III) was calculated by considering Eqs.S14 and 16, through the following equations (via fsolve function in Matlab):

$$\left(\frac{H}{2} - \frac{d}{2}\right)\left(2\sqrt{\sin^2\theta_{\max} - \cos^2\theta_{\max} + 1}\right) - (d + PS_{\min})(|\sin\theta_{\max} - \cos\theta_{\max}|) = 0 \quad \text{(S19)}$$

Table S1. *The parametrized coordinates of the nodes of a unit cell. These coordinates were used to systematically voxelize the unit cells when changing the input parameters (i.e., θ, L and d).*

node	x	y	z
P1	$H/2$	H	$H/2$
P2	$H/2$	$H/2 + L(sin\theta - cos\theta)$	$H/2$
P3	$H/2 + Lsin\theta$	$H/2 + Lsin\theta$	$H/2$
P4	$H/2 + L(sin\theta - cos\theta)$	$H/2$	$H/2$
P5	H	$H/2$	$H/2$
P6	$H/2 + Lsin\theta$	$H/2$	$H/2 + Lsin\theta$
node	x	y	z
P7	$H/2$	$H/2$	$H/2 + L(sin\theta - cos\theta)$
P8	$H/2$	$H/2$	H
P9	$H/2$	$H/2 + Lsin\theta$	$H/2 + Lsin\theta$
P10	$H/2 + Lsin\theta$	$H/2$	$H/2 - Lsin\theta$
P11	$H/2$	$H/2 + Lsin\theta$	$H/2 - Lsin\theta$
P12	$H/2$	$H/2$	$H/2 - L(sin\theta - cos\theta)$
P13	$H/2$	$H/2$	0
P14	$H/2 + Lsin\theta$	$H/2 - Lsin\theta$	$H/2$
P15	$H/2$	$H/2 - L(sin\theta - cos\theta)$	$H/2$
P16	$H/2$	0	$H/2$
P17	$H/2 - Lsin\theta$	$H/2 - Lsin\theta$	$H/2$
P18	$H/2 - L(sin\theta - cos\theta)$	$H/2$	$H/2$
P19	0	$H/2$	$H/2$
P20	$H/2 - Lsin\theta$	$H/2$	$H/2 + Lsin\theta$
P21	$H/2 - Lsin\theta$	$H/2$	$H/2 - Lsin\theta$
P22	$H/2 - Lsin\theta$	$H/2 + Lsin\theta$	$H/2$
P23	$H/2$	$H/2 - Lsin\theta$	$H/2 - Lsin\theta$
P24	$H/2$	$H/2 - Lsin\theta$	$H/2 + Lsin\theta$

4.5.2 Measuring the connectivity, tortuosity, and permeability of the meta-biomaterials

The connectivity of the meta-biomaterials was calculated as follows [32]:

$$Z_g = \frac{\sum_{i=1}^{m} Z_i}{m}; \tag{S20}$$

where m is the total number of nodes in the unit cell (here, $m = 24$), as shown in Figure 1g. Moreover, the connectivity in each node (*i.e.*, Z_i) was calculated based on the number of struts connected to each node.

The surface-to-volume ratio (S/V) was simply calculated as the ratio of the total surface of the struts in a unit cell to the total volume of the struts as follows:

$$\frac{S}{V} = \frac{\pi d(6h + 24L)}{\pi\left(\frac{d}{2}\right)^2 (6h + 24L)}; \tag{S21}$$

where the simplified form of Eq.S21 is as follows:

$$S/V = 4/d \tag{S22}$$

The geometrical tortuosity (*i.e.*, τ) was calculated as follows:

$$\tau = \frac{L_{\text{short}}}{L_e} = \frac{2h + 4L}{H}; \tag{S23}$$

where L_{short} and L_e are the shortest path through the pores and the straight-line distance (or Euclidean distance) across the unit cell, respectively. Considering Eq.S2 for h, the final relationship for τ will be as follows:

$$\tau = 1 - \frac{2L}{H}(sin\theta - cos\theta - 2) \tag{S24}$$

To calculate the permeability, k, the following relationship from Darcy's law of media flow in the porous medium was employed:

$$k = u_{\text{out}}\mu\frac{H}{\Delta P}; \tag{S25}$$

where u_{out}, μ, H and ΔP correspond to the flow velocity of the outlet, dynamic viscosity of the fluid, the length of the unit cell and the pressure difference between the outlet and inlet, respectively.

4.5.3 Numerical homogenization modeling of the meta-biomaterials

The macroscopic elasticity tensor, E^H_{ijkl}, of a periodic structure according to the homogenization theory is as follows [33]:

$$E^H_{ijkl} = \frac{1}{|V|}\sum_{e=1}^{M}\int_V E_{pqrs}(\varepsilon^{0(ij)}_{pq} - \varepsilon^{(ij)}_{pq})(\varepsilon^{0(ij)}_{rs} - \varepsilon^{(ij)}_{rs})dV \tag{S26}$$

where V, E_{pqrs}, $\varepsilon_{pq}^{0(ij)}$, $\varepsilon_{pq}^{(ij)}$ are respectively describe the volume of the unit cell, the locally varying stiffness tensor, macroscopic strain fields (unit strains in six directions for 3D problems), and locally varying strain fields, which is described as follows:

$$\varepsilon_{pq}^{(ij)} = \varepsilon_{pq}(\chi^{ij}) = 1/2\left(\chi^{ij}{}_{p,q} + \chi^{ij}{}_{q,p}\right); \tag{S27}$$

wherein χ^{ml} is the displacement field and can be solved through the elasticity equations with prescribed macroscopic (unit) strains as follows:

$$\int_V E_{ijpq}\varepsilon_{ij}(w)\varepsilon_{pq}(\chi^{ml})dV = \int_V E_{ijpq}\varepsilon_{ij}(w)\varepsilon_{pq}^{0(ml)}dV \tag{S28}$$

where w is a virtual displacement field. According to homogenization technique, the final stiffness matrix is derived by discretizing Eq.S28 based on FEM. By skipping the FEM details, the final form of the homogenized constitutive matrix (C^H), assuming isotropy and linear elastic property for the base material (*i.e.,* only two parameters of Poisson's ratio and Young's modulus), is finally described as follows [33,27]:

$$\mathrm{C}_{\mathrm{ij}}^{\mathrm{H}} = \frac{1}{|V|}\sum_{(e)}\int_{V^{(e)}}\left(\chi_{(\mathrm{e})}{}^{0(i)} - \chi_{(\mathrm{e})}{}^{(i)}\right)^T k_{\mathrm{e}}\left(\chi_{(\mathrm{e})}{}^{0(i)} - \chi_{(\mathrm{e})}{}^{(i)}\right)dV^{(e)} \tag{S29}$$

where $\chi_{(\mathrm{e})}{}^{0(i)}$ is the unit displacement and $\chi_{(\mathrm{e})}{}^{(i)}$ is the global displacement field which is calculated from the global stiffness from the FEM. It should be noted that the C^H is the constitutive matrix for the elements which depends on the Young's modulus and Poisson's ratio of the based isotropic material and is a 6×6 symmetric matrix in Voigt notation [36].

The effective elastic moduli from the homogenized constitutive matrix (C^{H}) can be determined as follows:

$$E_{\mathrm{x}} = \frac{1}{S_{11}};\ E_{\mathrm{y}} = \frac{1}{S_{22}};\ E_z = \frac{1}{S_{33}}; \tag{S30}$$

where, S is the homogenized compliance matrix and obtained as $\frac{1}{\mathrm{C}^{\mathrm{H}}}$.

Similarly, the effective shear moduli can be obtained from the other three diagonal entries of the C^{H} matrix as follows:

$$G_{\mathrm{yz}} = \frac{1}{S_{44}};\ G_{\mathrm{zx}} = \frac{1}{S_{55}};\ G_{\mathrm{xy}} = \frac{1}{S_{66}} \tag{S31}$$

The Poisson's ratios in different planes are as follows based on the generalized Hooke's law:

$$v_{xy} = -\frac{S_{21}}{S_{11}};\ v_{yx} = -\frac{S_{12}}{S_{22}};\ v_{xz} = -\frac{S_{31}}{S_{11}};\ v_{zx} = -\frac{S_{13}}{S_{33}};\ v_{yz} = -\frac{S_{32}}{S_{22}};\ v_{zy} = -\frac{S_{23}}{S_{33}} \quad \text{(S32)}$$

It should be noted that the v_{xy} can also be calculated in terms of the homogenized constitutive matrix (C^H) as follows [36, 37]:

$$v_{xy} = \frac{C_{12}^H}{C_{11}^H + C_{12}^H}; \quad \text{(S33)}$$

Depending on the magnitude of the entries of the matrix C^H or S^H, the meta-biomaterials behave differently, ranging from anisotropic to fully isotropic. The fully isotropic meta-biomaterials are identified with only two mechanical parameters named elastic modulus and Poisson's ratio in which the shear modulus is dependent on these two parameters. On the other hand, however, if the meta-biomaterial is identified with three properties namely elastic modulus, shear modulus and Poisson's ratio, it is called cubic meta-biomaterials. In this case, it possess 9 planes of mirror symmetry, although they have the same effective moduli and same effective shear moduli along the three orthogonal directions [38]. As such, depending on the number of the independent properties, different mechanical properties can be assigned to the meta-biomaterials. One parameter to determine the level of anisotropy is called Zener ratio, which is calculated in terms of the entries of the matrix C^H as follows [39]:

$$A = \frac{2C_{44}^H}{C_{11}^H - C_{12}^H}; \quad \text{(S34)}$$

If the A is equal or close to 1, means that the meta-biomaterial is isotropic.

4.5.4 Effects of voxels number on the elastic properties of the meta-biomaterials

We parametrically analyzed the effect of the number of voxels along each axis, n, on the mechanical properties and relative density of the meta-biomaterials. This parameter indicates the resolution of voxelization of the meta-biomaterials. Finer voxelization results in more precise results; however, it also significantly increases the computational costs. Therefore, a trade-off between computational costs and the precision of the results was necessary to determine the optimal number of voxels. To achieve this, n was varied from 35 to 185, and the resultant mechanical properties (*i.e.,* v, E_{eff}, G_{eff} and A), relative density and simulation time were calculated (Figure S1d of the supplementary material). The convergence of all properties achieved after voxel number of 160, resulting in significant computational costs (*e.g.,* over 500 s per each simulation, see Figure S1d of the supplementary material). However, to perform relatively large number of simulations (~43,000), we selected $n = 75$ as a relatively optimal number

of voxels. Moreover, the voxelized unit cells of the meta-biomaterials were visualized to represent the fineness of the voxelization (Figure S1e of the supplementary material). Following this illustration for the effect of n, the voxelized unit cell with $n = 75$ exhibited a desirable fineness compared to those with $n < 75$. It should be noted that the convergence study of the voxel numbers in our meta-biomaterials was performed on a single unit cell (Figure S1 of the supplementary material). However, since different meta-biomaterials may require varying voxel numbers for convergence, additional studies, particularly on Category I unit cells with a high degree of overlap, may be necessary to improve precision.

4.5.5 Validation of the homogenization results

The homogenization method that we employed here is an in-house numerical package based on the voxelization of unit cells and the application of periodic boundary conditions. To make sure the validity of our results, we compared them with those derived from the 3D solid elements using commercial FEM code (*i.e.,* Abaqus). Six different unit cells with varying input parameters were analyzed through both the homogenization method and the 3D solid elements, with the corresponding results presented in Table 1. We also measured the actual relative density via 3D solid elements using SolidWorks, as reported in Table 1. The results demonstrated that our in-house computational tool is highly reliable for simulating meta-biomaterials.

It is important to note that the discrepancies between the values of v, E_{eff}/E_0, and ρ derived from the numerical homogenization and the 3D solid elements due to the following reasons: *i.* The middle layers were exclusively considered for calculating the Poisson's ratio of the 3D meta-biomaterials in the solid elements. This approach resulted in slightly different v values comparing to considering the entire nodes. For instance, for a meta-biomaterial with $\theta = 60.0^{\circ}, L = 140.0/300$, and $d = 14/300$ (as listed in Table 1), the value of v considering the nodes on the middle unit cells featured 22.72% variation with the solid elements, however, the variation was 13.63% if all side nodes (Figure 1b) is considered. *ii.* We employed the periodic boundary conditions for the homogenization method, while, in the 3D solid elements, we only considered $5 \times 5 \times 5$ unit cells due to computational costs considerations. It is noted that the reason that we chose $5 \times 5 \times 5$ unit cells for the 3D solid elements was because the results of the 3D solid element and the homogenization converged for $5 \times 5 \times 5$ unit cells. Based on our preliminary study, the Poisson's ratio did not reach a plateau as early as the effective elastic modulus. Consequently, the absolute values of the Poisson's ratio and effective elastic modulus derived from the 3D solid models were slightly larger and smaller, respectively, than those from the homogenization method making them more sensitive to the number of the unit cells considered. *iii.* The results of the homogenization method depend on the number of voxels along each axis, n. For example, with $n = 120$ (instead of 75), the variation of the Poisson's ratio with the 3D solid element for a

meta-biomaterial with $\theta = 60.0^{o}, L = 140.0/300$, and $d = 14.0/300$ was 13.63% instead of 22.72% (when $n = 75$).

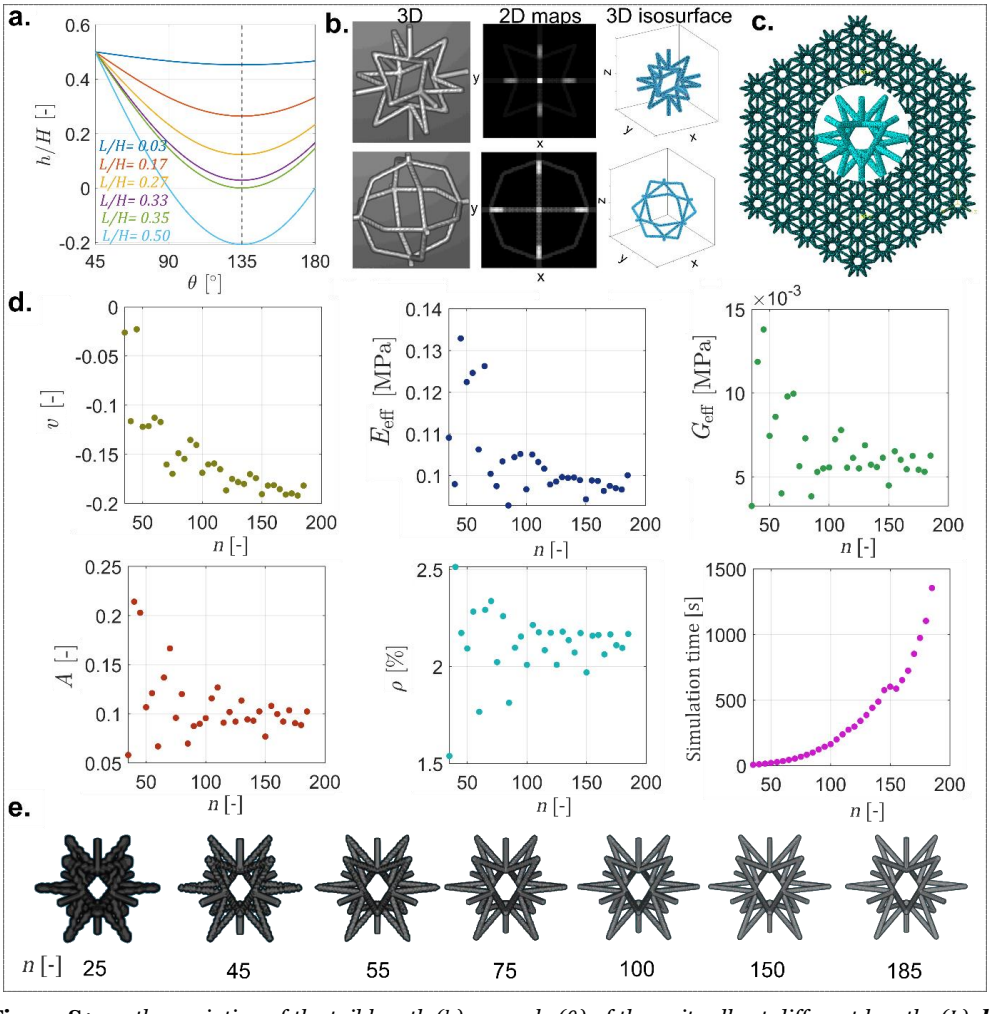

Figure S1. ***a.*** *the variation of the tail length (h) vs angle (θ) of the unit cells at different lengths (L).* ***b.*** *Schematics showing two 3D voxelized unit cells, their 2D maps, and their 3D isosurface plot.* ***c.*** *The discretized 3D meta-biomaterials with a proper mesh type and number of elements for the 3D solid element analysis. d. The results of the effect of the n on the convergency of elastic properties including v, E_{eff}, G_{eff}, and A , and ρ and simulation time.* ***e.*** *A schematic showing the accuracy of the voxelization in terms of number of voxels varying from 25 to 185 for a certain unit cell with ,* $\theta = 60.0^{o}$, $L = 140.0/300$ *and* $d = 14.0/300$.

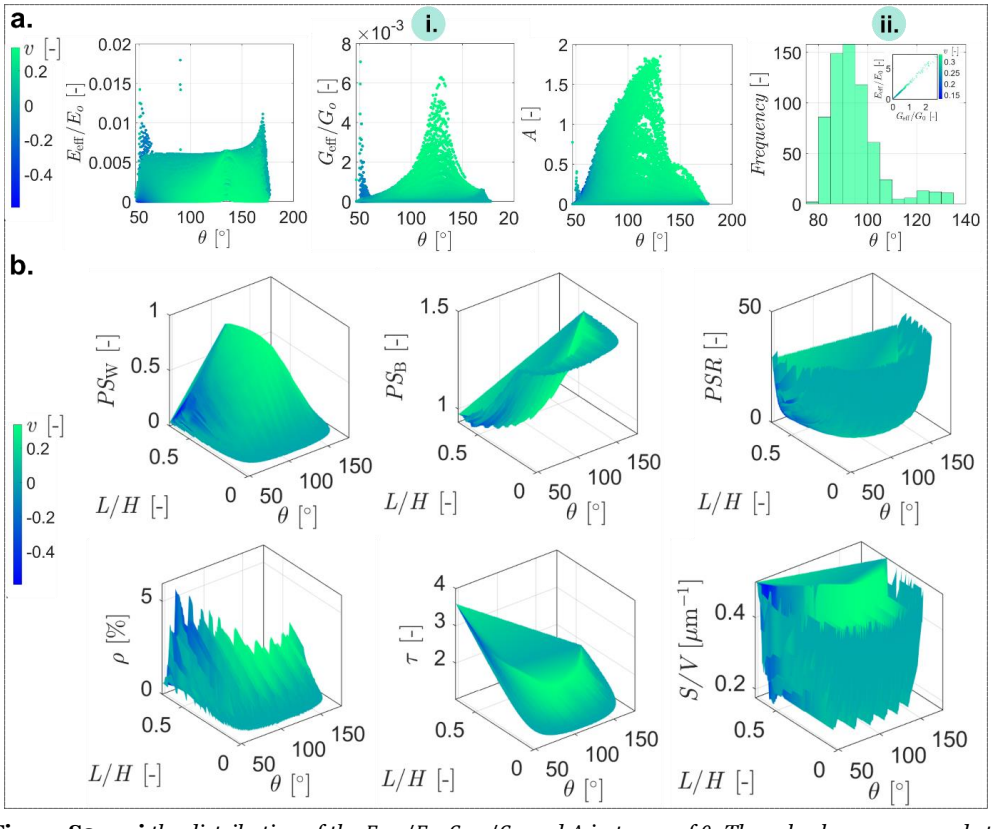

Figure S2. ***a.i*** *the distribution of the* E_{eff}/E_0, G_{eff}/G_0 *and* A *in terms of* θ. *The color bar corresponds to the Poisson's ratio values.* ***a.ii.*** *The histogram plot of the Zener ratio in terms of* θ *when* $0.95 < A < 1.05$, *meaning the fully isotropic meta-biomaterials.* ***b.*** *the dependency of the morphometric properties on the input parameters of the unit cells (*θ *and* L*).*

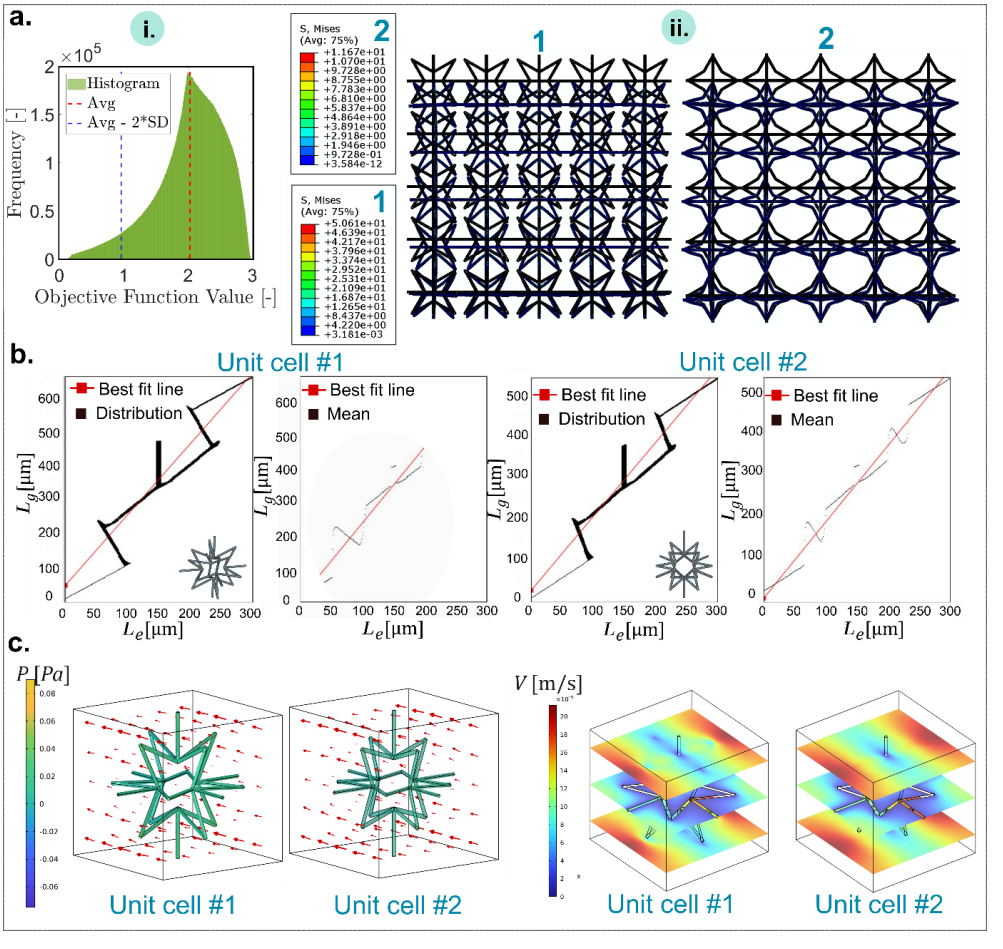

Figure S3. ***a.i.*** *the histogram of the objective function value defined in Eq.S33, which shows a normal-like distribution.* ***a.ii.*** *the distribution of the Von Misses stress within two 3D meta-biomaterials (category I and III) under 1% strain through 3D solid elements FEM. Note that a magnification of 10 was used here to magnify the deformation.* ***b.*** *The correlation between the Elucident (L_e) and straight path lines (L_g) within the isolated meta-biomaterials with respect to the Poisson's ratio (unit cells #1 and 2).* ***c.*** *the result of the permeability study on the isolated meta-biomaterials with respect to the distributions of the pressure and speed of the flow.*

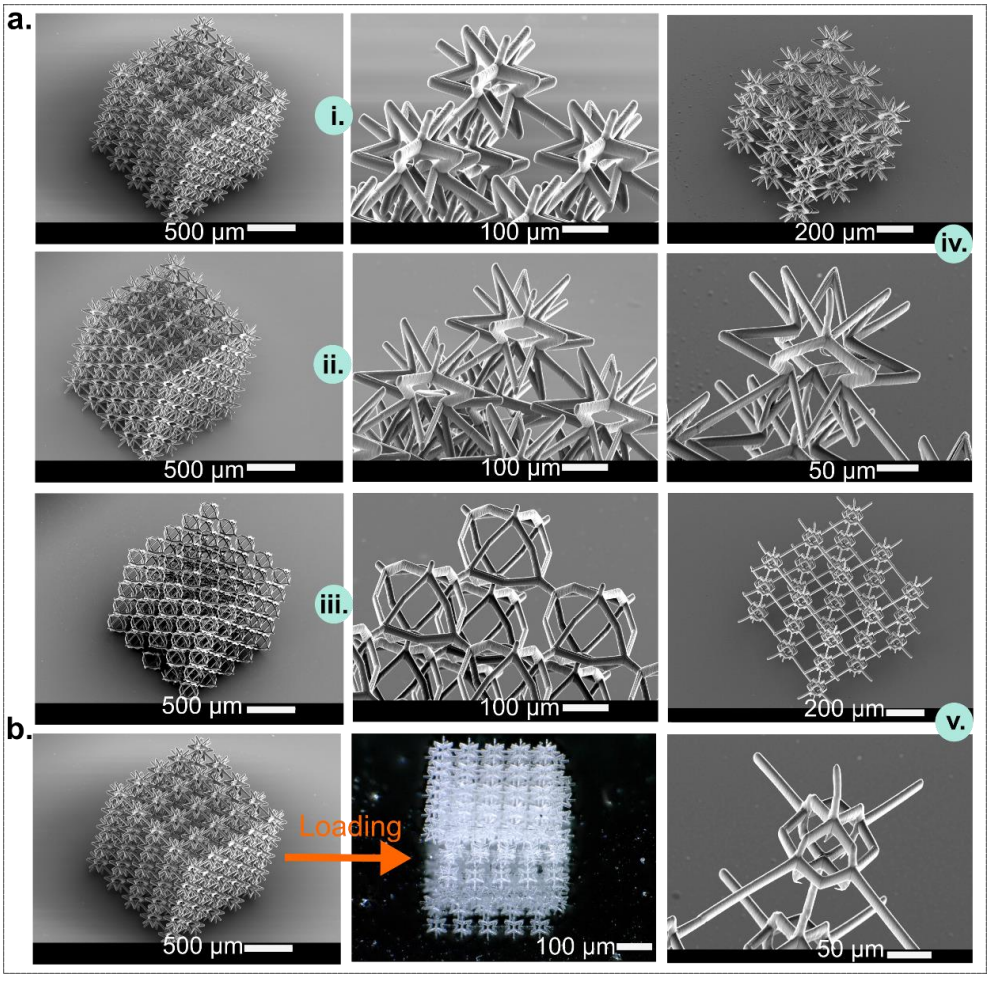

Figure S4. *2PP 3D printing of a selected set of meta-biomaterials with input parameters, including* ***a. i.*** $\theta = 65.0^o$, $L = 110.0/300$ *and* $d = 20.0/300$. ***ii.*** $\theta = 60.0^o$, $L = 140.0/300$ *and* $d = 14.0/300$, ***iii.*** $\theta = 120^o$, $L = 90.0/300$ *and* $d = 14.0/300$, ***iv.*** $\theta = 64^o$, $L = 104.5/300$ *and* $d = 8.0/300$, ***v.*** $\theta = 100.0^o$, $L = 42.9/300$ *and* $d = 8.0/300$. ***b.*** *an optical image of a meta-biomaterial featuring* $\theta = 65.0^o$, $L = 110.0/300$ *and* $d = 20.0/300$ *(the SEM illustrated in* ***a.i****) deformed within 10 s loading and 1000 mN force.*

Bibliography

[1] E. Yarali, M. Klimopoulou, K. David, P.E. Boukany, U. Staufer, L.E. Fratila-Apachitei, A.A. Zadpoor, A. Accardo, M.J. Mirzaali, Bone cell response to additively manufactured 3D micro-architectures with controlled Poisson's ratio: auxetic vs. non-auxetic meta-biomaterials, Acta Biomaterialia 177 (2024): 228-242.
[2] P. Jiao, J. Mueller, J.R. Raney, X. Zheng, A.H. Alavi, Mechanical metamaterials and beyond, Nature communications 14(1) (2023) 6004.
[3] H. Pahlavani, K. Tsifoutis-Kazolis, M.C. Saldivar, P. Mody, J. Zhou, M.J. Mirzaali, A.A. Zadpoor, Deep Learning for Size-Agnostic Inverse Design of Random-Network 3D Printed Mechanical Metamaterials, Advanced Materials 36(6) (2024) 2303481.
[4] Y. Lee, B. Jang, H. Song, S. Kim, Y.W. Kwon, H.S. Kang, M.S. Kim, I. Park, T.-S. Kim, J. Jang, A seamless auxetic substrate with a negative Poisson's ratio of– 1, Nature Communications 15(1) (2024) 7146.
[5] Z. Gao, X. Zhang, Y. Wu, M.-S. Pham, Y. Lu, C. Xia, H. Wang, H. Wang, Damage-programmable design of metamaterials achieving crack-resisting mechanisms seen in nature, Nature Communications 15(1) (2024) 7373.
[6] C.S. Ha, D. Yao, Z. Xu, C. Liu, H. Liu, D. Elkins, M. Kile, V. Deshpande, Z. Kong, M. Bauchy, Rapid inverse design of metamaterials based on prescribed mechanical behavior through machine learning, Nature Communications 14(1) (2023) 5765.
[7] J. Park, J. Noh, J. Shin, G.X. Gu, J. Rho, Investigating Static and Dynamic Behaviors in 3D Chiral Mechanical Metamaterials by Disentangled Generative Models, Advanced Functional Materials (2024) 2412901.
[8] S.J. Callens, C.H. Arns, A. Kuliesh, A.A. Zadpoor, Decoupling minimal surface metamaterial properties through multi-material hyperbolic tilings, Advanced Functional Materials 31(30) (2021) 2101373.
[9] Y. Guo, M.I.N. Rosa, M. Gupta, B.E. Dolan, B. Fields, L. Valdevit, M. Ruzzene, Minimal Surface-Based Materials for Topological Elastic Wave Guiding, Advanced Functional Materials 32(30) (2022) 2204122.
[10] E. Yarali, A.A. Zadpoor, U. Staufer, A. Accardo, M.J. Mirzaali, Auxeticity as a mechanobiological tool to create meta-biomaterials, ACS Applied Bio Materials 6(7) (2023) 2562-2575.
[11] A.A. Zadpoor, Additively manufactured porous metallic biomaterials, Journal of Materials Chemistry B 7(26) (2019) 4088-4117.
[12] Z. Hashin, S. Shtrikman, A variational approach to the theory of the elastic behaviour of multiphase materials, Journal of the Mechanics and Physics of Solids 11(2) (1963) 127-140.
[13] S. Wu, Z. Luo, Z. Li, S. Liu, L.-C. Zhang, Topological design of pentamode metamaterials with additive manufacturing, Computer Methods in Applied Mechanics and Engineering 377 (2021) 113708.
[14] X. Hu, T. Tan, B. Wang, Z. Yan, A reprogrammable mechanical metamaterial with origami functional-group transformation and ring reconfiguration, Nature Communications 14(1) (2023) 6709.
[15] T. Li, Y. Li, 3D Tiled Auxetic Metamaterial: A New Family of Mechanical Metamaterial with High Resilience and Mechanical Hysteresis, Advanced Materials 36(15) (2024) 2309604.
[16] Q.T. Do, C.H.P. Nguyen, Y. Choi, Homogenization-based optimum design of additively manufactured Voronoi cellular structures, Additive Manufacturing 45 (2021) 102057.
[17] T. Meier, R. Li, S. Mavrikos, B. Blankenship, Z. Vangelatos, M.E. Yildizdag, C.P. Grigoropoulos, Obtaining auxetic and isotropic metamaterials in counterintuitive design spaces: an automated optimization approach and experimental characterization, npj Computational Materials 10(1) (2024) 3.
[18] G. Flamourakis, I. Spanos, Z. Vangelatos, P. Manganas, L. Papadimitriou, C. Grigoropoulos, A. Ranella, M. Farsari, Laser-made 3D Auxetic Metamaterial Scaffolds for Tissue Engineering Applications, Macromol Mater Eng 305(7) (2020) 2000238.

[19] H.M. Kolken, S. Janbaz, S.M. Leeflang, K. Lietaert, H.H. Weinans, A.A. Zadpoor, Rationally designed meta-implants: a combination of auxetic and conventional meta-biomaterials, Mater. Horiz. 5(1) (2018) 28-35.
[20] N. Munding, M. Fladung, Y. Chen, M. Hippler, A.D. Ho, M. Wegener, M. Bastmeyer, M. Tanaka, Bio-Metamaterials for Mechano-Regulation of Mesenchymal Stem Cells, Advanced Functional Materials (2023) 2301133.
[21] K.K. Dudek, J.A. Iglesias Martínez, G. Ulliac, L. Hirsinger, L. Wang, V. Laude, M. Kadic, Micro-Scale Mechanical Metamaterial with a Controllable Transition in the Poisson's Ratio and Band Gap Formation, Advanced Materials (2023) 2210993.
[22] M.J. Mirzaali, H. Pahlavani, E. Yarali, A. Zadpoor, Non-affinity in multi-material mechanical metamaterials, Scientific reports 10(1) (2020) 11488.
[23] T. Tancogne-Dejean, D. Mohr, Elastically-isotropic truss lattice materials of reduced plastic anisotropy, International Journal of Solids and Structures 138 (2018) 24-39.
[24] X. Zheng, X. Zhang, T.T. Chen, I. Watanabe, Deep learning in mechanical metamaterials: from prediction and generation to inverse design, Advanced Materials 35(45) (2023) 2302530.
[25] M. Abu-Mualla, J. Huang, Inverse design of 3D cellular materials with physics-guided machine learning, Materials & Design 232 (2023) 112103.
[26] T. Li, Y. Li, 3D Tiled Auxetic Metamaterial: A New Family of Mechanical Metamaterial with High Resilience and Mechanical Hysteresis, Advanced Materials (2024) 2309604.
[27] G. Dong, Y. Tang, Y.F. Zhao, A 149 line homogenization code for three-dimensional cellular materials written in matlab, Journal of Engineering Materials and Technology 141(1) (2019) 011005.
[28] H. Kolken, K. Lietaert, T. van der Sloten, B. Pouran, A. Meynen, G. Van Loock, H. Weinans, L. Scheys, A.A. Zadpoor, Mechanical performance of auxetic meta-biomaterials, journal of the mechanical behavior of biomedical materials 104 (2020) 103658.
[29] I. Ostanin, G. Ovchinnikov, D.C. Tozoni, D. Zorin, A parametric class of composites with a large achievable range of effective elastic properties, Journal of the Mechanics and Physics of Solids 118 (2018) 204-217.
[30] W.L. Roque, R.R. Costa, A plugin for computing the pore/grain network tortuosity of a porous medium from 2D/3D MicroCT image, Applied Computing and Geosciences 5 (2020) 100019.
[31] K.M. Graczyk, M. Matyka, Predicting porosity, permeability, and tortuosity of porous media from images by deep learning, Scientific reports 10(1) (2020) 21488.
[32] M.J. Mirzaali, H. Pahlavani, A. Zadpoor, Auxeticity and stiffness of random networks: Lessons for the rational design of 3D printed mechanical metamaterials, Applied Physics Letters 115(2) (2019).
[33] E. Andreassen, C.S. Andreasen, How to determine composite material properties using numerical homogenization, Computational Materials Science 83 (2014) 488-495.
[34] W. Wang, Z.-Q. Chen, B. Lin, M.-C. Liu, Y. Zhang, S.-J. Liu, Y. Li, Q. Zhao, Two-photon polymerization-based 3D micro-scaffolds toward biomedical devices, Chemical Engineering Journal (2024) 152469.
[35] X. Lyu, Z. Zheng, A. Shiva, M. Han, C.B. Dayan, M. Zhang, M. Sitti, Capillary trapping of various nanomaterials on additively manufactured scaffolds for 3D micro-/nanofabrication, Nature Communications 15(1) (2024) 6693.
[36] X. Chen, J. Moughames, Q. Ji, J.A.I. Martínez, H. Tan, S. Adrar, N. Laforge, J.-M. Cote, S. Euphrasie, G. Ulliac, Optimal isotropic, reusable truss lattice material with near-zero Poisson's ratio, Extreme Mechanics Letters 41 (2020) 101048.
[37] A.F. Bower, Applied mechanics of solids, CRC press, 2009.
[38] S.C. Cowin, Continuum mechanics of anisotropic materials, Springer Science & Business Media, 2013.
[39] C.M. Zener, S. Siegel, Elasticity and Anelasticity of Metals, The Journal of Physical Chemistry 53(9) (1949) 1468-1468.

5

4D bioprinting for biomedical applications

Yarali, E., Mirzaali, M. J., Ghalayaniesfahani, A., Accardo, A., Diaz-Payno, P. J., & Zadpoor, A. A. (2024). 4D printing for Biomedical Applications. *Advanced Materials*, 2402301.

4D bioprinting endows 3D printed (bio-)materials with multiple functionalities and dynamic properties. 4D printed materials have been recently used in biomedical engineering for the design and fabrication of biomedical devices, such as stents, occluders, micro-needles, smart 3D-cell engineered micro-environments, drug delivery systems, wound closures, and implantable medical devices. However, the success of 4D printing relies on the rational design of 4D printed objects, the selection of smart materials, and the availability of appropriate types of external (multi-)stimuli. Here, we first highlight the different types of smart materials, external stimuli, and design strategies used in 4D bioprinting. Then, we present a critical review of the biomedical applications of 4D printing and discuss the future directions of biomedical research in this exciting area, including *in vivo* tissue regeneration studies, the implementation of multiple materials with reversible shape memory behaviors, the creation of fast shape-transformation responses, the ability to operate at the microscale, untethered activation and control, and the application of (machine learning-based) modeling approaches to predict the structure-property and design-shape transformation relationships of 4D (bio)printed constructs.

5.1 Introduction

AM processes, also known as 3D printing techniques, enable the fabrication of 3D objects with complex geometries and tailored mechanical properties [1-5]. This technology, however, has hitherto been largely constrained to the creation of static objects that exhibit constant properties over time [6, 7]. This limitation has been mitigated by the advent of 4D printing, a disruptive technology that introduces a temporal component to the traditionally static 3D printed constructs, thereby enabling the fabrication of dynamic structures that respond to external stimuli.

The implications of 4D printing are profound. These dynamic structures can undergo controlled transformation between multiple states, thereby exhibiting advanced functionalities, such as shape adaptation and environmental responsiveness [8]. Unlike 3D printing objects, which feature static applications, 4D printed constructs have found applications in a variety of fields including, but not limited to, self-assembly [9], self-healing [10, 11], shape-morphing (*e.g.,* self-folding) [12, 13], and multi-functionality [14]. This range of applications extends from wearable and medical devices to robotic systems, sensors, and actuators [7].

In regenerative medicine, 4D bioprinting has the potential to revolutionize tissue engineering by enabling the creation of functional tissues and organs [15]. Moreover, the technology's scalability across various length scales (*i.e.*, from micro to macro [16, 17]) opens the door for the production of miniaturized soft robots and sensors [16, 17] as well as micro-scaffolds for *in vitro* cell studies [18, 19].

The cornerstone of 4D printing is the rational selection of stimuli-responsive materials, such as shape memory polymers (SMPs), hydrogels, and liquid crystal polymers (LCPs), among others [16]. The successful integration of these materials is dependent on a well-designed interaction mechanism, a compatible 3D printing technique, and the precise application of external stimuli. Particularly in biomedical applications, the materials selected must also meet biocompatibility criteria to be considered for *in vivo* use.

Various 3D printing technologies serve as the foundational methods for 4D printing processes. These include DIW [15], FDM [20], vat photo-polymerization [21] (*e.g.,* SLA or DLP [22]), direct laser writing (DLW) (*e.g.,* 2PP [23, 24]), SLS [25], and selective laser melting (SLM) [26]). Moreover, hybrid techniques that combine 3D printing with conventional manufacturing processes have also been developed, including molding-integrated [27] and electroless metallic plating-integrated 4D printing [28]. The choice of a specific 4D printing process depends on various factors, including the intended application, the length scale, the mechanical and biological properties of the relevant materials, as well as the production method (*e.g.,* batch or mass productions) [6].

Design strategies, often inspired by origami/ kirigami-based principles [29-32]), are integrated into 4D printing processes to create multi-functional structures that challenge the boundaries of conventional manufacturing techniques. These strategies operate at various lengths and time scales, potentially transforming how materials and devices are conceptualized and fabricated.

Given the growing interest in personalized healthcare solutions, 4D printing has attracted considerable attention for its role in pioneering advanced biomedical devices, including stents, occlusion devices, micro-needles (MNs), implants, and scaffolds, among others [33]. Nevertheless, the practical implementation of 4D printed biomedical devices requires a comprehensive understanding of the underlying principles and mechanisms that govern the 4D bioprinting process. This review, therefore, aims to elucidate these principles by offering a detailed explanation of the 4D printing process, an overview of the range of smart (bio-)materials, and a comprehensive analysis of relevant applications in biomedicine.

5.2 4D printing process

The dynamism inherent in 4D printed constructs stems from their ability to undergo temporal transformations between multiple states (*i.e.*, commonly a shift from a temporary to a permanent configuration) upon exposure to external stimuli [19, 34]. This introduces an additional layer of complexity to the design process, necessitating careful consideration of three fundamental parameters: *i.* the selection of stimuli-

responsive materials, *ii*. the types of external stimuli to be employed, and *iii*. the rational design of the geometry and/or topology of the 4D printed construct [35].

Among stimuli-responsive materials, SMPs and hydrogels have received a great deal of attention, owing to their wide applicability and responsiveness to a diverse range of stimuli (*e.g.*, physical, chemical, or biological stimuli [36, 37]). For example, SMPs can return to a pre-determined shape upon thermal activation, while hydrogels may swell or contract in response to changes in pH or temperature. This broad array of activation mechanisms provides designers with a range of possibilities for engineering tailored responses in 4D printed constructs.

Moreover, the mechanics of design cannot be underestimated as it plays a pivotal role in the predictability and controllability of self-morphing behaviors. Devising a suitable geometry is essential for channeling the intrinsic material properties and stimuli-responsiveness into the desired mechanical performance. As such, there is a growing emphasis on the necessity to develop complex algorithms and computational tools for the geometrical and topological optimization of 4D printed constructs.

The stimulus itself, acting as a trigger for the dynamic change, requires careful selection and calibration. Stimuli can range from light, heat, and humidity to more specialized triggers, such as electric or magnetic fields, and even biological molecules, such as enzymes. The type of stimulus chosen has direct implications for the application at hand. For instance, in the biomedical context, the use of bio-responsive stimuli is a key to the development of smart drug delivery systems or tissue scaffolds that adapt to the physiological environment.

To elucidate, consider the application of 4D printing in drug delivery systems. In such a scenario, the geometric design should facilitate controlled substance release, while material selection should ensure biocompatibility and responsiveness to physiological stimuli (*e.g.*, pH changes in the digestive tract). Furthermore, the external stimulus (*e.g.*, a bio-responsive element) should be carefully aligned with the specific medical requirements, whether they relate to time-release mechanisms or targeted drug delivery.

This section, therefore, aims to provide a comprehensive review of the critical elements underpinning the 4D printing process, including an analysis of the most promising stimulus-responsive materials, a classification and evaluation of applicable external stimuli, and a discussion on the advancements in geometrical design methodologies for 4D constructs.

5.2.1 Materials

The smart materials used in 4D printing for biomedical applications must meet a triad of crucial criteria: *i*. biocompatibility, to ensure physiological safety, *ii*. functional

responsiveness under physiological conditions, such as body temperature or pH levels, and *iii*. mechanical robustness during and after shape transformation [38, 39]. For example, temperature-sensitive 4D printed biomedical constructs should not only be biocompatible but also operational at body-compatible temperatures (~37 °C). As another example, the magnetic fields actuating magneto-responsive 4D printed biomedical devices must exhibit non-cytotoxic properties to ensure cellular safety [40].

Stimuli-responsive or "*smart*" materials manifest characteristics, such as shape transformation or shape memory effect (SME), upon exposure to specific external stimuli [16, 41]. While shape transformation entails an immediate shift from a temporary to a permanent state, SME materials possess the ability to "memorize" and revert to their original shape upon re-exposure to an activating stimulus. The kinetics of these transformations – specifically, the rate of shape change – is an aspect of paramount significance in specific sectors, such as soft robotics [42]. Despite significant progress in the creation of fast-response 4D printed objects, the field remains in its early stages and requires further studies.

In the ever-evolving landscape of 4D printing research, the continuous exploration and integration of novel materials and design methodologies serve as catalysts for advancements in biomedical applications. A plethora of smart materials, such as SMPs, hydrogels, LCPs, shape memory alloys (SMAs), dielectric elastomers (DEs), piezoelectric materials, magneto-active materials, and bioactive particles or fillers, meet the aforementioned criteria. Notably, SMPs and hydrogels emerge as the forerunners in the domain of 4D bioprinting, owing to their superior printability, biocompatibility, and capacity for complex shape transformation [36, 43-45].

5.2.1.1 Types of 4D-printing materials

5.2.1.1.1 *SMPs*

SMPs are smart polymers that are renowned for their stimuli-responsive properties. Upon exposure to specific external stimuli, such as temperature, light, or pH, these polymers can transition between their temporary and permanent shapes [41, 46]. Such morphological changes can range from simple bending to more complex forms, such as helixing or topographical modifications, depending on the mechanical properties of the SMPs [47]. In the domain of biomedicine, the versatile properties of SMPs (*i.e.*, biocompatibility, mechanical robustness, tunability (*i.e.,* tailored stiffness), and processability [48]) have facilitated their deployment in various applications, such as bone repair tools [49], drug delivery systems [50, 51], occlusion devices [52, 53], scaffolds [54, 55], and embolization devices [56].

Two distinct methodologies can be employed for programming the SME in SMPs: manual and AM-based processes [57]. The latter, albeit more challenging, is often more effective in achieving complex shape transformations but requires a comprehensive

understanding of printing parameters and geometrical complexities for effective shape morphing. In contrast, the manual method provides a less precise and sophisticated but more straightforward programming options.

SMPs may be characterized as being one-way, two-way, or multi-way SMEs depending on their cyclic behavior and the number of stored shapes, which can be chemically manipulated [58, 59]. To quantify the SME in SMPs, such parameters as the strain recovery ratio (R_r) and the strain fixity ratio (R_f), are widely used [60] (Figure 1.a.i). These parameters quantify the capability of SMPs to recover to their original shape and to maintain a temporary shape, respectively [60]. Ideally, both R_r and R_f should approach 100% for an SMP to be considered highly effective.

To schematically illustrate the programming and recovery steps in SMPs, Figure 1.a.i illustrates a 3D thermo-mechanical cycle of SMPs to demonstrate their programming and recovery steps at the macroscale. The cycle includes four steps: *i*. loading (path AB), *ii*. cooling (path BC), *iii*. unloading (path CD), and *iv*. heating or recovery (path DA or DE). The first three steps are collectively referred to as the "*programming*" process. During the loading stage, one (or multiple) temporary shape(s) are formed. The cooling stage stabilizes the temporary shapes, which result from the solidification phenomenon. External loads are removed during the unloading stage. The permanent shape is retrieved in the heating stage. The heating stage comprises two recovery processes: *stress-free-strain-recovery* and *fixed-strain-stress-recovery* processes. In the stress-free-strain-recovery process, shape or strain is recovered under stress-controlled conditions (the green hashed line or blue solid line in Figure 1.a.i). In the fixed-strain-stress-recovery process, force is retrieved under strain-controlled conditions (the red dashed line in Figure 1.a.i). It is worth noting that the loading stage does not necessarily require temperatures higher than T_{trans} (known as cold programming) [61].

SMPs can be made from either natural polymers, such as polypeptides, polysaccharides, or from synthetic ones, such as PLA and polycaprolactone (PCL) [62, 63]. While synthetic polymers usually offer superior mechanical strength as compared to the natural ones, they might pose toxicity risks [64]. Biodegradable SMPs can be synthesized using synthetic monomers, such as ε-caprolactone and p-dioxanone [65].

Temperature-responsive SMPs are commonly used due to their broad range of glass transition temperatures, which can vary from -70 to 150 °C [66]. SMPs with higher glass transition temperatures are preferred for extreme conditions. For instance, a high-temperature responsive SMP based on polyamide/diacrylate has been 4D printed using a light-assisted AM technique called liquid crystal display (LCD) 3D printing [67] (Figure 1.a.ii**)**. The glass transition temperatures of SMPs can be adjusted to achieve body-friendly temperatures by modifying the involved chemical reagents or manufacturing processes. In the first method, the composition of the base SMP is

altered through copolymerization and adjusting the concentration of cross-linkers [68, 69]. In the second method, the glass transition temperature is controlled by creating composite SMPs through multi-material 4D printing [57, 59, 70] or by adding nano-/micro-particles to SMPs [71]. In addition, 3D printing parameters, such as printing speed, can influence the glass transition temperature.

5.2.1.1.2 Hydrogels

Hydrogels constitute a fascinating subset of smart soft polymers due to their unique hydrophilic characteristics and versatile mechanical properties. Composed of a 3D network that encompasses both swelling and non-swelling polymeric components [72], hydrogels can absorb substantial amounts of water, leading to transitions between distinct states: sol-gel, gel-gel, and gel-sol-gel [45]. These transitions are dependent on environmental parameters, such as water content, temperature, pH levels, and ionic concentrations [45].

Molecularly, hydrogels can be stabilized through either chemical bonding (*e.g.,* irreversible, covalent bonds) or physical bonding (*e.g.,* reversible, hydrogen, and van der Waals' bonds) [73]. Striking a balance between swelling ratio and mechanical strength represents a central challenge in hydrogel research. This trade-off becomes particularly pivotal in the domain of 3D printing, where sufficient stiffness is necessary for the construction of freestanding structures. The crosslinking density is a crucial factor in this regard, as a higher crosslinking density leads to increased stiffness of the hydrogel [74].

Owing to their inherent biocompatibility and bioprintability, hydrogels have been intensively researched for their applicability in 4D printing within biomedical settings. They have demonstrated the capability for complex and controllable deformations, even in the presence of living cells [15]. Various 3D printing techniques, such as extrusion-based printing [75, 76], laser-assisted bioprinting [77, 78], and the drop-on-demand (DOD) technique [79], have been employed to fabricate hydrogel-based structures. Each method comes with its unique set of challenges, including the quest for high resolutions in 4D printed structures. DOD, for example, is a promising technique that addresses this challenge by accurately controlling the deposition of hydrogel droplets and the timing between them to achieve the required resolution [80].

In the rapidly expanding field of 4D printing, hydrogels have been deployed as shape-morphing agents in many applications, such as sensors, soft actuators [81], controlled drug delivery systems [44], and *in vitro* studies on cellular differentiation [18]. For example, temperature-responsive hydrogels offer exciting possibilities in soft robotics and actuators by allowing the formation of reversible shape-morphing structures [82]. However, achieving complex shape morphing with hydrogels for advanced applications requires rational mechanical design, including non-homogeneous geometries,

multi-material constructs, and carefully engineered mechanisms for the application of external stimuli [15, 83, 84].

Electro-active hydrogels add another layer of functionality by enabling both negative and positive curvatures within a single construct. This is achieved through rational design of electrode patterns and the modulation of electric fields [85-87] (Figure 1.b.i [87]), opening up new avenues for applications, such as tissue engineering. Such capability of achieving complex shape morphing in hydrogels, and their printability has opened up new avenues for applications such as tissue engineering (*e.g.*, 4D bioprinting of engineered cartilage with tailored shape-morphing behavior [15], Figure 1.b.ii).

Furthermore, hydrogels have demonstrated significant potential in the domain of controlled drug delivery. They provide an optimized platform for controlled drug release and ensure biocompatibility with both the encapsulated drugs and the surrounding biological tissues. This encapsulation also affords a protective mechanism against environmental contaminants, thereby enhancing the stability and efficacy of the carried drugs [88-90].

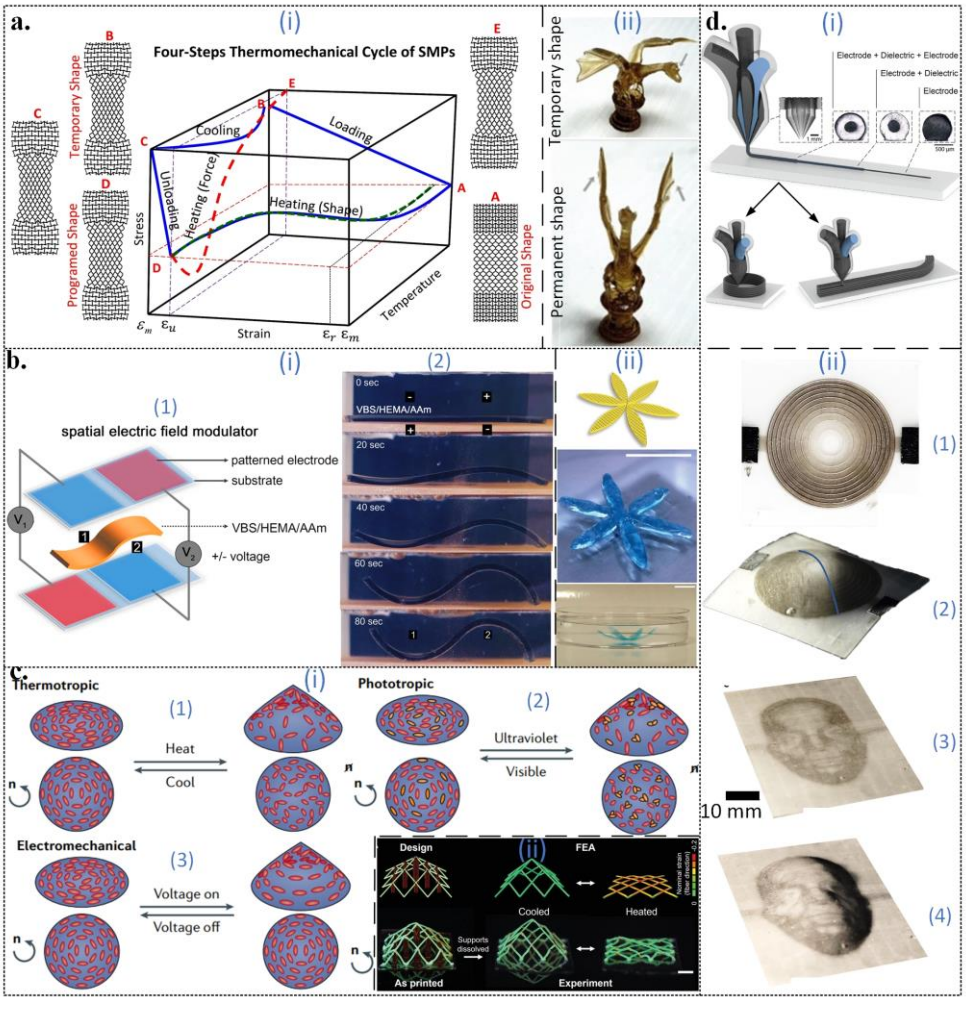

Figure 1. *Examples of different stimulus-responsive materials.* ***a.i.*** *A 3D schematic drawing of programming and recovery thermomechanical cycles in the 4D printing process is presented for typical temperature-responsive SMPs. It includes four steps, namely loading, cooling, unloading, and heating, with their corresponding shapes.* ***a.ii.*** *An illustration demonstrating the permanent and temporary shapes of a 4D printed structure made by LCD. Reproduced with permission. [67]. Copyright 2022, Elsevier.* ***b.i.*** *Electroactive hydrogel actuation under a multipolar spatial electric field for inducing negative and positive mean radii of curvatures [87] (**i.1**). This implementation creates a sequential actuation process within 80 s in an electroactive hydrogel-based actuator (**i.2**).* ***ii.*** *A 4D bioprinted water-responsive hydrogel made through DIW [15]. The top, middle, and bottom sub-figures show the initial design, the initial shape of the 4D printed hydrogel, and the transformed shape. The scale bars represent 10 mm.* ***c.i.*** *The micro-configurations of LCPs, showing the disruption of orders in the presence of heat (**1**), light (**2**), and an electric field (**3**). Reproduced with permission [94]. Copyright 2022, Springer Nature.* ***c.ii.*** *A 4D printed LCP is depicted, exhibiting a shape-morphing behavior upon exposure to temperature changes Reproduced with permission [95]. Copyright 2022, Wiley-VCH. The scale bar represents 10 mm.* ***d.i.*** *A schematic drawing illustrating inkjet-based multi-material 4D printing of DEs. Reproduced with permission [157]. Copyright 2021, Wiley-VCH.*

d.ii. *4D printing of multi-layer DEs with different configurations and their topological shape-morphing to mimic a simple semi-spherical out-of-plane deformation (**1** and **2**) as well as a human face (**3** and **4**) [146].*

5.2.1.1.3 Liquid crystal materials

LCPs and liquid crystalline elastomers (LCEs) are distinct classes of liquid crystalline materials [91, 92] that offer unique mechanical and functional characteristics, owing to their specialized molecular structures. LCPs are thermoplastic polymers renowned for their superior mechanical strength, excellent chemical resistance, high-temperature stability and biocompatibility [93]. These properties make them suitable candidates for a range of biomedical applications, such as such as surgical instruments, dental devices, orthopedic implants, and controlled drug delivery systems [94].

Conversely, LCEs fall under the category of soft smart polymers and are capable of large, reversible, and rapid actuations. They consist of liquid crystals (or mesogens) integrated within an elastomeric matrix, demonstrating molecular anisotropy and entropic elasticity [95]. The actuation behavior in LCEs depends on the alignment of the mesogens, which can be triggered through mechanical stretching, shearing, or external stimuli, such as temperature changes. Mesogens can be incorporated into an elastomeric matrix either as a side chain or main chain [96]. The exposure to external stimuli causes a nematic–isotropic phase transition, leading to SME in LCPs [95, 97, 98]. Figure 1.c.i illustrates the micro-mechanism of three different LCEs in the presence of heat, light, and electric field [94]. LCEs find application in areas, such as soft robotics (*e.g.*, robotic surgical tools), artificial muscles, actuators, and controlled drug delivery systems [99].

Advanced AM techniques have been employed to fabricate structures from both LCPs and LCEs, with each method presenting specific advantages and limitations [100]. For example, DIW is a technique that permits mesogen alignment along the printing direction [96]. Although it lacks precision and complex shape-morphing capabilities, DIW enables the creation of functionally graded LCE-based structures by modulating the printing parameters. In contrast, DLP offers high-precision fabrication but faces challenges in mesogens alignment, resulting in simpler structures [101]. Hybrid AM techniques combine the advantages of DIW with those of DLP to facilitate the fabrication of complex LCE-based constructs (Figure 1.c.ii) [95].

While the potential of LCPs and LCEs in the realm of 4D printing and soft robotic is undeniable, significant challenges remain. For instance, in electro-active LCP-based actuators, there is a risk of undesirable increases in electrical conductivity. Furthermore, the high-temperature sintering process involved in 4D printing can lead to unintended deformations. Additionally, the curing times for LCP actuators, which can span from a few minutes to several hours, limit rapid fabrication capabilities [102-104].

To address these challenges, innovative approaches are being investigated. One such approach involves the use of UV-assisted printing to produce LCE-based soft actuators with biphasic liquid metal conductors [105]. This technique enables the realization of multifaceted shape-changing patterns through the employment of different LCE double-layer cross structures. By modulating the sequence and path of the printing process for these double layers, diverse deformation modes can be achieved [105].

5.2.1.1.4 SMAs

SMAs are metal-based smart materials that exhibit remarkable shape recovery capabilities in response to certain types of stimuli, such as temperature changes or magnetic fields. Generally composed of two main phases (*i.e.*, martensite (at lower temperatures) and austenite phase (at higher temperatures)), SMAs can undergo transformations between various shapes [26]. Depending on the cyclic behavior of SMAs, they can be categorized into three groups: one-way, two-way, and pseudoelastic SMAs [106]. The first two categories exhibit SME and can be programmed. However, pseudoelastic SMAs can completely recover their shapes without any additional recovery processes (without SME). Therefore, pseudoelastic SMAs behave similar to elastic materials and are, thus, less desirable for 4D printing applications [106]. Nickel-Titanium (NiTi) alloy can be an example of these three categories, depending on the thermomechanical cycling [106].

The behavior of SMAs is dependent on their chemical compositions and microstructures. An archetypal example is NiTi alloy. At temperatures below the martensite finish temperature, the alloy can be deformed and adopts a different shape. However, upon heating above the austenite start temperature, it reverts to its original form, thereby demonstrating one-way SME. This behavior is closely related to the nickel content and the microstructure of the alloy. Conversely, two-way SME, where the alloy "remembers" distinct shapes at varying temperatures, is facilitated through mechanical training of the material. Moreover, an increment in the nickel content usually correlates with elevated transformation temperatures in SMAs.

The fabrication of SMA structures typically employs NiTi and Ni-Mn-Ga alloys. These can be manufactured using various AM techniques, such as powder bed-based methods (*e.g.,* SLM [26, 107-109], directed energy deposition, electron beam melting [110], powder bed binder jetting [108, 111]), or extrusion-based techniques (*e.g.,* inject 3D printing) [112]. However, the 4D printing of SMAs remain relatively less studied as compared to smart polymers, such as SMPs and hydrogels. This can be attributed to several factors, including their low stretchability, challenges in their 3D printing processes, prolonged manufacturing timelines, and higher costs [26]. Each of the AM techniques used for the fabrication of SMA specimens has certain advantages and disadvantages. The SLM technique offers high resolution and the ability to create complex geometries from SMA. However, these benefits come at the cost of high energy

consumption and the necessity for specialized equipment and extensive parameter optimization. The high-temperature gradients involved in SLM processes can also affect the phase transitions in SMAs, impacting their shape memory properties [113, 114]. Directed energy deposition is well known for its ability to manufacture large-scale components. However, the deposition process may induce internal stresses that affect the mechanical properties of the SMA [115]. Electron beam melting offers high precision but is generally more expensive and requires a high-vacuum environment, which can be restrictive [116]. Powder bed binder jetting provides an option with lower thermal impact. However, the binder materials can interfere with the properties of SMAs [108, 117]. Finally, extrusion-based techniques, such as inkjet 3D printing, have the advantage of low material waste but often face limitations in resolution and speed, making them less suitable for complex SMA components [118].

As an alternative to Nickel-based alloys, copper (Cu) alloys have recently been used as other types of SMAs, next to high temperature β-Ti alloys. Cu alloys present distinctive advantages, such as significantly lower costs as compared to Nickel-based SMAs. Cu alloys (*e.g.*, Cu-Al-Ni [26]), also offer versatility in tailoring thermal and mechanical properties through alloying [26]. These alloys are also capable of demonstrating both one-way and two-way SMEs. The use of Cu alloys allows for a broader range of activation temperatures and may enhance electrical conductivity, offering new avenues for stimulus-response in 4D printing applications [26]. However, the transition to Cu-based SMAs requires extensive evaluation for biomedical applications, particularly focusing on issues, such as biocompatibility and corrosion resistance [26]. Furthermore, β-Ti SMAs (*e.g.,* Ti–Nb) exhibit high transition temperature, large theoretical shape morphing and low costs [119].

Despite these challenges, 4D printed SMAs have distinct advantage over other smart materials, such as SMPs and hydrogels, in terms of their superior mechanical strength. This characteristic makes them increasingly attractive for specialized applications that require robust mechanical performance.

5.2.1.1.5 Ceramic-based materials

The utilization of shape memory ceramics (SMCs) in biomedical and 4D printing applications is an emerging domain that necessitates further investigation to better understand their potential applications. Zirconia ceramics [120], notably, have demonstrated shape memory and superelastic properties. This can be attributed to their ability to undergo a martensitic phase transformation, a mechanism that effectively converts thermal energy (*i.e.*, heat) into mechanical strain or the other way around [121]. The brittle nature of these ceramics, which typically results in failure at low strains after a few cycles, can be mitigated by providing a fine-scale structure with few crystal grains. These oligocrystalline structures reduce internal mismatch stresses during the

martensitic transformation, leading to robust SMCs that can endure many superelastic cycles up to large strains [122].

Moreover, zirconia ceramics can exhibit superior shape memory properties when deformed at a temperature between their martensite and austenite transition temperatures. This can be accomplished through a stress-induced transformation from austenite to martensite, which, when the load is removed, retains the new shape. Subsequent heating above the austenite transition temperature causes the martensite to revert to austenite, returning the material to its original shape [120].

Advancements in 4D printing technologies have enabled the fabrication of complex ceramic structures through the use of zirconia (ZrO_2) inks with varying solid contents [123,124]. This method allows for the sintering of 3D printed lattices and bilayer ceramic architectures that can undergo pre-programmed shape transformations [125]. The development of this technology holds promise for generating complex ceramic structures with specific functionalities.

An alternative approach for shaping ceramics draws inspiration from nature, specifically the self-folding behavior seen in plant seed dispersal units that occur due to differential swelling behaviors [126]. This technique involves manipulating the microstructure of the material to undergo local anisotropic shrinkage during heat treatments. The methodology involves magnetically aligning functionalized ceramic platelets in a liquid ceramic suspension, which is then consolidated through an enzyme-catalyzed reaction. This process can be used to create alumina compacts with bio-inspired bilayer architectures, allowing for controlled shape change during the sintering step. Different complex shapes, such as bending, twisting, or combinations of these movements, could be programmed [126].

Furthermore, recent research has synthesized a reconfigurable and shape memory preceramic suitable for 4D printing, composed of liquid silicone (polydimethylsiloxane, PDMS), shape memory epoxy, and ceramic nanoparticles (ZrB2 NPs) [127]. For this purpose, the initial shape is printed through DIW and is then reshaped into the desired complex geometry through a two-step curing process at different temperatures. The shape memory capability of the precursor allows it to be programmed into temporary shapes and revert to the original state under heat stimulus.

Another innovative strategy merges 4D printing and origami techniques to fabricate ceramic structures [128]. This entails the use of specialized inks made from elastomers and ceramic precursors. After printing, these structures are subjected to pyrolysis, transforming them into ceramics. The ability to program these structures for specific deformations during pyrolysis expands the design space for ceramics, offering a new paradigm for constructing lightweight and strong ceramic components [128].

5.2.1.2 Properties of types of 4D-printable materials

5.2.1.2.1 Temperature-responsive materials

Temperature-responsive materials, commonly referred to as thermo-responsive polymers, are recognized by their intrinsic capacity to undergo changes in physical or chemical properties in response to external temperature stimuli. The ability to exhibit such changes, coupled with inherent biocompatibility and adjustable phase transition characteristics, makes these materials particularly advantageous for advanced biomedical and 4D printing applications [129].

pNIPAM, serves as an example in this category and has gained considerable attention in the biomedical field. The important feature of this polymer is its lower critical solution temperature, which is close to the human body temperature. This unique characteristic enables its use in a plethora of biomedical applications, such as controlled drug delivery, tissue engineering, and bioseparation [130]. Specifically, hydrogels synthesized from PNIPAM can encapsulate pharmaceutical agents and modulate their release kinetics in a temperature-dependent manner [131]. Such materials offer the potential for targeted and timed drug delivery systems that can be manipulated via external thermal stimuli [132].

In addition to PNIPAM, Pluronic F-127 and polyethylene glycol (PEG)-based polymers also constitute notable examples of temperature-responsive materials. Pluronic F-127 has been successfully employed in thermal-ablation therapies targeting malignant cells, thereby displaying its potential for use in oncological applications [133]. Similarly, PEG-based polymers have found applications in wound healing, where temperature-responsive behavior can facilitate the timely release of a healing agent or cytokines to accelerate tissue repair [134].

5.2.1.2.2 Electroactive materials

Electroactive materials represent another class of smart materials that manifest a change in dimensional or functional properties upon exposure to an electric field. Such materials are composites, comprising a base substrate and an electrically responsive conductive filler. While metals can serve as the base material, polymers have gained greater importance in the context of 4D printing [135, 136].

Electroactive materials find their primary applications in sensors, actuators, and energy-harvesting devices due to their intrinsic stimuli-responsive properties [137]. The most frequently used electroactive materials used in 4D printing include piezoelectric materials and DEs.

Piezoelectric materials

Piezoelectric materials offer a unique suite of characteristics that are tailored for smart structures. These materials, comprising either metal-based ceramics or

polymers, exhibit the capacity to generate electrical charges when subjected to mechanical deformation such as pressure, strain, vibrations, and sound [138]. Metal-based ceramics (*e.g.*, lead zirconate titanate and barium titanate [138]) are prevalently used in transducer applications. Polymeric examples include polyvinylidene difluoride (PVDF), known for its high flexibility.

Innovative fabrication methods have emerged in the domain of piezoelectric materials, enabled by advanced 4D printing techniques. FDM, for instance, facilitates the fabrication of thermoplastic-based piezoelectric materials, such as polypropylene, acrylonitrile butadiene styrene (ABS), and polytetrafluoroethylene (PTFE), overcoming the limitations inherent to traditional ceramic processing techniques [138, 139, 140]. These materials are selected due to their relatively low dielectric and elastic properties [140-142].

Furthermore, piezoelectric materials offer new horizons in biomedical engineering. The fabrication of smart (porous) biomedical implants utilizing these materials brings forth a host of advantages, including but not limited to mechanical strength, high mass transport properties, and tunable biodegradation rates [143-145].

Dielectric elastomers (DEs)

DEs constitute another category of electroactive materials that are predominantly utilized in soft robotics [146]. Dielectric elastomer actuators (DEAs), functioning as deformable capacitors, exhibit large strains under electric fields. These materials are structured with an elastomer sheet sandwiched between two compliant electrodes, resulting in deformation upon electric stimulation.

Two prevalent types of DEs are based on acrylic and silicone elastomers. The fabrication methods for DEAs generally employ pre-stretching of the elastomer material, which is subsequently framed to enhance its electric field-induced deformation and breakdown strength [147]. Conventional (and planar) manufacturing techniques, such as spin coating [147-149] and sequential mechanical assembly [150], have been used to fabricate DEAs. While these methods yield primarily planar shape morphing, additional processes can transform such in-plane deformations into out-of-plane deformations (*e.g.*, bending, rolling) [149, 151].

Recent innovations have presented multi-layer techniques, which allow DEAs to deform without the necessity for pre-stretching [152]. Examples include bio-inspired mechanisms, such as the jumping features observed in click beetle [147].

From an AM viewpoint, 4D printing of most of the current silicone-based DEs is still in its infancy due to the low viscosity and long curing time of silicone [153]. However, some AM techniques, such as FDM [1545], SLA [155], and DOD inkjet 3D printing [156], have been successfully used for DE fabrication. In particular, multi-material

inkjet 3D printing can be appealing to print multi-material DEs to achieve more complex shape-morphing **[**157**]** (Figure 1.d.i). Furthermore, FDM and SLA require long curing times and cannot achieve the same level of consistency in the layer thickness found in pre-fabricated elastomeric films [158]. In some cases, it is also possible to combine AM techniques with conventional techniques, such as spin coating, to fabricate certain sophisticated multi-layer DEs (Figure 1.d.ii) [149]. 4D printing of DEs aiming at complex shape morphing remains an active area of research and extensive research is being conducted currently [137, 159-161].

5.2.1.2.3 Magneto-active materials

Magneto-active polymers (MAPs) form a specialized category of smart materials whose properties (*e.g.,* elasto-plastic properties and stiffness) change upon the application of an external magnetic field. The interaction between magnetic fields and these polymers lead to a magnetic field-dependent torque until the magnetic domain within the material achieve alignment with the applied field [162, 163]. These materials are mainly composed of a soft base polymer, typically silicone-based, infused with magneto-active fillers. These fillers exhibit ferromagnetic or paramagnetic properties, and encompass a range of materials including carbon black, carbon nanotubes (CNTs), carbon nanofibers, and metallic particles (*e.g.*, gold NPs, neodymium–iron–boron (NdFeB), or Fe_3O_4) [6]. Iron oxide particles are often used as magneto-active fillers due to their unique combination of chemical stability, high heating efficiency, and biocompatibility [164].

MAPs can be classified into “soft” and “hard” categories based on the magnetic saturation levels of the fillers used. Soft magnetic MAPs incorporate low-saturation materials such as iron oxides, whereas hard magnetic MAPs utilize fillers with high magnetic saturation, such as NdFeB [163, 165]. The implication of this classification on the functional characteristics of MAPs requires more comprehensive investigation.

A further classification of MAPs can be done based on the types of base polymer used, resulting in magnetorheological elastomers (MREs) and magnetorheological plastomers (MRPs) [166]. MREs are distinguished by their high sensitivity to applied magnetic fields and their capability for reversible deformation [167, 168]. In contrast, MRPs demonstrate a more plastic nature, maintaining their deformed state even after the removal of stress. The inherent difference in properties makes MREs more suitable for dynamic systems requiring quick and reversible changes in mechanical characteristics. On the other hand, MRPs are tailored for applications requiring permanent deformations, thus offering strong plasticity and damping characteristics. Most MRP matrices are thermosets (*i.e.*, cross-linked polymers, such as PUs and poly(vinyl alcohol) (PVA). The versatility of these materials is exemplified by multi-functional MRPs, particularly 3D printed structures using PCL/thermoplastic PU (TPU) polymers that showcase shape memory and self-healing capacities [166].

The topology of the magneto-active fillers within the polymer matrix can be engineered to create complex shape-morphing and anisotropic properties in both MREs and MRPs. However, the mechanisms through which varying the distributions of various fillers can impact the overall performance of the material, and the type of the optimization strategies still need to be explored.

Manufacturing techniques for MAPs are broadly classified into two categories: conventional methods (*e.g.*, molding or templating) and AM techniques [6,168]. Each category presents its own set of challenges and advantages. For instance, conventional methods are often constrained by limitations in the creation of complex geometries and less control over filler dispersion [169]. FDM, SLA, inkjet (including electrohydrodynamic inkjet [170]), and DLW are common AM techniques to make MAPs structures [6]. Alternatively, 4D printing allows for more complex designs and the capability to create MAPs without the need to external magnetic fields [169].

Interestingly, hybrid manufacturing techniques are emerging to circumvent the limitations of each method [27]. In these techniques, high concentrations of magnetic particles (~20-70wt%) preclude the use of advanced micro-AM techniques, such as 2PP [27]. Therefore, micro-molds are fabricated using 2PP, and the final MAP structures are created through molding. Such hybrid methods may also involve the encapsulation of MR fluids within elastomers, allowing the 3D printing of soft structures with tunable elastic properties. After creating hybrid MREs, a laser-assisted technique can be used to magnetize them. In this approach, local magnetization profiles are created by locally heating the magneto-active polymer with a laser, which enables complex shape-morphing [163] (Figure 2.a). This process is similar to multi-material 3D printing [169]. Examples of such MREs include acrylate-based polymers containing Fe_3O_4 particles, which can be used to tune the mechanical and magnetic properties of 3D printed composites [21].

Biocompatibility remains a crucial consideration for MAPs, especially in biomedical applications. While iron oxide NPs are generally considered biocompatible, other ferromagnetic particles such as iron, and its alloys may introduce toxicity risks. Therefore, a comprehensive evaluation of not only the type of filles and based polymers but also their concentration and the nature of the magnetic fields applied is necessary for assessing cellular viability [163].

5.3 Stimulation

Stimulation stands as a pivotal element in the efficacy of 4D printed structures within the context of biomedical applications. The core of 4D printing in biomedicine lies not just in its ability to fabricate structures capable of functioning *in vivo* without cytotoxic effects, but also in its requirement for external stimuli to trigger specific actions or changes. Stimulation used in 4D printing can, in general, be divided into three

main categories: physical, chemical, and biological. Specific 4D printed structures can respond to multiple stimuli based on the composition of the smart structure, which can be a smart composite or a smart material with different fillers [171]. We will only focus on physical and chemical stimulation, as little information is available regarding the 4D printing of biologically responsive materials.

5.3.1 Physical stimulation

Physical stimuli, such as temperature and magnetic fields, are widely used to trigger 4D printed medical devices. Owing to their ease of manipulation and reliable outcomes, these stimuli induce changes at the molecular level, affecting the conformation of polymeric chains or the internal arrangement of the material. These changes result in shape morphing and the creation of dynamic behavior in the printed objects, enabling them to adapt to environmental conditions such as fluctuating body temperatures. The integration of physical stimuli into 4D printing offers a pathway for evolving more complex, adaptive medical devices.

5.3.1.1 Temperature

Temperature stands as a sub-category of physical stimulation, pivotal for actuating 4D printed structures. SMPs emerge as the material of choice for temperature-induced responses, prominently for their SMEs. It is also worth mentioning that temperature-responsive 4D printed objects possess the capability for multifunctional recovery, including morphological changes and even changes in optical properties such as color. For instance, Figure 2.b shows a 4D printed temperature-responsive chameleon, which changes its color upon exposure to different temperatures [172].

The mechanism for SME requires a designated transition temperature, either the glass transition temperature (T_g) or the crystal-melt transition temperature (T_m), depending on the structure of the polymer (*i.e.,* amorphous or crystalline, respectively) [59]. SME results from a thermally-induced phase transition between two rubbery or glassy (*i.e.,* active and frozen, respectively) states. The molecular architecture generally consists of two key components: *i.* a chemical cross-link that dictates the permanent shape (*i.e.,* hard phases), and *ii.* temperature-sensitive segments (*i.e.,* soft phases), that facilitate temporary shape changes when the temperature crosses a threshold temperature, T_{trans} [173, 174].

For biomedical applications, the direct method of temperature stimulation (*e.g.*, immersing the 4D printed object in hot water or heating with hot air) is often impractical due to the *in vivo* environment's inaccessibility. Hence, alternative strategies for internal heat generation have been proposed, exploiting external stimuli such as focused ultrasound [175], IR light [55], microwaves [176], laser light [177], or even magnetic or electric fields [178].

5.3.1.2 Magnetic field

Magnetic fields stand as another prominent form of physical stimulation in the domain of 4D printing, particularly well-suited for untethered actuation in miniaturized soft robotics and biocompatible applications [179,180]. Similar to temperature-sensitive mechanisms, magnetic fields induce what is termed a "magnetic memory effect", allowing the material to revert to its pre-designed form upon exposure to a magnetic field.

A typical example illustrating the magnetic memory effect is the fabrication of magneto-active SMP composites. These composites consist of a stable elastomeric matrix and a MR fluid that serves as the programmable phase [181]. When subjected to a magnetic field, these composites exhibit specific stages of programming and recovery (Figure 2.c.i and 2.c.ii). Initially, in the absence of a magnetic field, the elastomeric components of the composite bear the mechanical stress, while the MR fluid remains in a liquid state. Upon the application of a magnetic field, the MR fluid transitions to a more rigid phase, effectively bearing the stress and causing the elastomeric components to relax. Once the magnetic field is removed, the composite reverts to its original shape, illustrating its magnetic memory capabilities.

The mechanism of heat generation induced by magnetic fields is predicated on the principles of induction [6]. In such scenarios, the magnetic fillers within the magneto-active materials undergo rearrangement when subjected to an alternating magnetic field. This rearrangement leads to energy dissipation and subsequent heat generation [182]. Such a mechanism is advantageous over other remote stimulation methods, such as light or electric fields, both in terms of speed of transition and the capacity for temperature control through a feedback mechanism based on magnetic hysteresis loss [183, 184]. There is also no need for the connection of power transmission lines to the 4D printed devices, thus reducing the risk of failure. Furthermore, it is possible to induce selective heating by locally patterning the structure with magneto-active particles.

In biological applications, stringent constraints must be considered to so as not to adversely impact biological tissues. The safe frequency range for magnetic fields in biological contexts is generally considered to be between 50 and 100 kHz [185]. Another determinant factor is the size of the magneto-active particles, which must be optimized to ensure cell compatibility while achieving the desired magnetic memory effect [163].

Careful consideration is also required to achieve a balanced interplay among various parameters such as the type of magnetic field (alternating *vs.* direct), the type of magneto-active fillers, their particle sizes, concentration levels, and the base polymer. These factors collectively influence the efficiency, safety, and efficacy of magnetic field-induced actuation in 4D printed structures.

5.3.1.3 Electric field

Electric fields constitute another important modality for the activation of 4D printed structures. These structures incorporate electro-active fillers that become responsive when exposed to an electric field, resulting in shape-morphing behavior through various mechanisms, such as Joule heating [135, 136].

Joule heating serves as a prominent means to induce shape changes and presents several merits, including rapid activation, uniformity, remote controllability, and convenience [135, 186]. For instance, gold electrodes have been employed to initiate the shape recovery of nano-composites at a relatively low voltage of 13.4 V [135, 186]. This low voltage threshold enables simultaneous actuation and monitoring of 4D printed structures.

Electric fields have been widely used to activate SMEs in DEs, hydrogels, and SMPs. Various materials have been explored for these applications, including hydrogels made of acrylamide crosslinked with N, N'-Ethylene Bisacrylamide [187], chitosan-based hydrogels [85], and alginate-based hydrogel grafts [188]. For instance, a chitosan-based hydrogel was employed in an electric field and pH-responsive antibacterial drug delivery system [85]. Poly (D, L-lactide-co-trimethylene carbonate) (PLMCs) reinforced with CNTs have been 3D printed via DIW to function at high voltages up to 25 V [189].

Various applications have originated from these advancements, including the creation of stent-like structures through FDM of CNT-reinforced PLA [190]. These structures demonstrated shape recovery within 60 seconds at a voltage of 20 V (Figure 2.d). Moreover, smart drug delivery systems employing methacrylate-based hydrogels have been designed to operate at voltages less than 2V [191]. On the microscale, 2PP has been utilized for the precision 3D printing of electro-active hydrogels, paving the way for biocompatible drug delivery systems [192].

5.3.1.4 Water/solvent

Water or moisture can serve as a physical stimulus to trigger hygroscopic materials, which tend to absorb moisture, to deform into a desired shape [193, 194]. The Self-Assembly Lab at the Massachusetts Institute of Technology, a pioneer in 4D printing [193], has developed a 3D printed hydrophilic polymer with up to 150% stretchability when exposed to moisture. This expansion is strategically guided by placing stiffer parts in the desirable direction to reach the final desired shapes. Utilizing a combination of rigid and hygroscopic materials to construct hinges, only the hygroscopic sections become active when exposed to water. By strategically placing these hinges on a 1D line or 2D plane, different shapes can be obtained upon stimulation. This technique can also be applied to 3D-to-3D or 3D-to-2D shape transformations. In this way, it is possible

to 3D print multiple hydrophilic polymers that may react differently when immersed in water to create complex self-morphing behaviors [195].

Hydrogels have emerged as the material of choice for water-responsive materials applications, especially given their high biomimetic potential [196]. Naturally-driven hydrogels, such as gelatin, collagen, silk fibroin, and chitosan with hydrophilic natures, offer promising applications in 4D bioprinting [197]. Complex, dynamic shape-morphing can be achieved based on the concepts of multi-materials and rational design in a composite ink made of stiff cellulose fibrils and a soft acrylamide matrix [83]. For example, a water-responsive multi-material structure was 4D printed via extrusion-based printing of hydrogels and elastomers. Different shape-morphing behaviors could be achieved that are inspired by the movement of the octopus's tentacles when immersed in distilled water [198] (Figure 2.e.i). Water-responsive hydrogels also have the potential to be 4D printed at different length scales from the microscale [199] to the macroscale with programmed shape-morphing behaviors.

In tissue engineering applications, water-sensitive 4D printed scaffolds change their shapes in a spatiotemporally dependent manner at different levels of water absorption. An example is a two-layered construct made of photo-patterned polyethylene glycol (PEG) layers with varying molecular weights, which demonstrates that differential swelling ratios could give rise to anatomically-relevant shapes [200]. These biocompatible scaffolds have been observed to exhibit an impressive cell viability rate of 90% over an eight-week culture period [200]. In cartilage tissue engineering, water-responsive 4D printed constructs have been used to fabricate MSCs-laden scaffolds featuring shape-morphing properties [15]. The bi-layered hydrogel scaffold was made from hyaluronan and alginate with different swelling ratios *via* an extrusion-based 4D bioprinting technique.

Beyond water, solvents such as ethyl acetate and isopropyl alcohol can also trigger reversible dynamic deformation in 4D printed structures [9]. These solvent-responsive materials, often referred to as capillary force-responsive materials, can undergo swelling or shrinkage as the solvent evaporates. The 4D printed constructs can even be manufactured at the microscale through 2PP [9, 23, 201]. As an example, Figure 2.e.ii and iii show two 4D printed self-assembly microstructures inspired by a butterfly [9] and a gecko [23], respectively.

The use of solvent-responsive materials is further augmented by their reversible dynamics. For instance, chitosan cross-linked with citric acid can undergo one-way shape morphing when immersed in a chemical solvent. This process creates a concentration gradient as the solvent diffuses through hydrophilic chitosan and hydrophobic materials. In contrast, immersing the material in water can restore the original shape by minimizing this gradient [202].

5.3.1.5 Light

Light offers a unique medium for the actuation of 4D printed structures due to its various advantageous properties: it is a clean energy source, available ubiquitously, triggers rapid response, and can be controlled remotely without physical contact [203, 204]. Consequently, light not only has the capability to heat 4D printed objects remotely but also serves as a vital stimulus for inducing shape-morphing behaviors, particularly in biomedical applications [205, 206].

Materials responsive to light can generally be classified into two categories: photochemical-responsive and photothermal-responsive [204, 207]. Photochemical-responsive materials inherently convert light energy to mechanical energy through photochemical processes. For instance, UV-responsive SMPs such as densely-branched polycoumarate derivatives have been developed to demonstrate multi-stimuli-responsive characteristics [208]. Conversely, photothermal-responsive materials contain additional photothermal reagent, such as gold nanoparticles or carbon-based nanoparticles to form a thermally-responsive matrix [204, 209-211]. These agents absorb light and convert it into internal heat, which in turn actuates the base material. For example, azobenzene-containing SMPs are widely used in photothermal-responsive 4D structures, owing to their trans–cis photo-isomerization properties [212].

To manufacture photo-responsive materials, photo-polymerization 3D printing technologies are in the presence of specific wavelengths, typically UV (or IR light) [213]. Alternatively, the FDM method can be used for photothermal-responsive materials without the need for UV light exposure [214-216]. In addition, photo-responsive fillers, such as carbon black, can be added to thermoplastic polymers, such as TPU for 3D printing applications [215]. Figure 2.f shows a photo-responsive poly(ether ether ketone)-based SMP inspired by the opening of an umbrella and the flying of a butterfly, which exhibits shape-shifting behavior when exposed to UV light **[**217**]**.

However, the use of light as stimulus is not without of challenges [218]. Firstly, photo-activated reagents may induce cytotoxic effects, particularly detrimental in biomedical applications [204]. Secondly, the process of photo-thermal conversion can lead to overheating of the samples [219]. Lastly, the efficiency of light-activation is highly dependent on specific wavelengths, which imposes a constraint on the materials and wavelengths used during the printing process to avoid undesired structural changes. The power and wavelength of the light should not only be sufficient for activating 4D printed structures but must also not damage the body [218].

To mitigate some of these limitations, alternative light sources such as sunlight have been considered for their natural, sustainable, and cost-effective characteristics [204, 215, 220-222].

Figure 2. *Examples of different stimuli for actuating the response of 4D printed materials.* ***a.*** *Laser-assisted magnetization profile in magneto-active polymers [163].* ***b.*** *Digital photographs of a temperature-*

responsive 4D printed chameleon. Reproduced with permission [172]. Copyright 2022, Elsevier. The scale bar represents 5 mm. ***c.*** *A magneto-active SMP controlling the variation of applied/recovery strain in the absence of a magnetic field (red curve) and in the presence of a magnetic field of 600 mT (blue curve) (****i****) Reproduced with permission [181]. Copyright 2019, Wiley-VCH. A schematic drawing depicting the experimental steps involved in the programming and recovery cycles of a magnetically stimulated SMP (****ii****) Reproduced with permission [181]. Copyright 2019, Wiley-VCH. Stage 0 shows the permanent shape of the SMP. Within steps 1-3, the SMP is loaded in the presence of the magnetic field. Then, the SMP recovers its shape within a short time through step 4.* ***d.*** *Electric-responsive mechanical metamaterials based on SMP/CNT. Reproduced with permission [190]. Copyright 2022, Elsevier. The 4D printed metamaterial folds within 60 s under a 70 V electric field.* ***e.*** *Water- and solvent-responsive 4D printed structures depicted at the macro- (****i.****). Reproduced with permission [200]. Copyright 2019, Wiley-VCH and microscales (****ii,*** *[23] and* ***iii,*** *Reproduced with permission [9]. Copyright 2021, Wiley-VCH). Scale bars in* ***e.i****,* ***e.ii****, and* ***e.iii*** *represent 1 cm, 20 µm, and 20 µm.* ***f.*** *Light-responsive 4D printed structures, which are shifted from temporary states to permanent shapes, mimicking the opening and closing of an umbrella and butterfly. Reproduced with permission [217]. Copyright 2022, Wiley-VCH.* ***g.*** *A schematics drawing of a mechanical loading stimulus (rubbing) and its effect on the changing luminescent color of a thin film substrate. Reproduced with permission [225]. Copyright 2009, Springer Nature.*

5.3.1.6 Acoustic waves

Acoustic waves are another type of physical stimulus to activate 4D printed materials. These stimuli can manifest in various forms including vibrations, audible sound, ultrasound, and infrasound, each capable of being generated from distinct sources. For instance, vibration can be generated by exciting piezoelectric materials using an electric field.

Ultrasound refers to sound waves above the audible limit of the human hearing and can be categorized into low-frequency, medium-frequency, and high-frequency domains. Each domain has unique penetration depths and focal points. Low-frequency ultrasound, for example, can penetrate deeper into the tissues, but lacks the capacity to concentrate its energy into a smaller area [88]. In contrast, high-frequency ultrasound is capable of localizing its energy, but its depth of penetration is comparatively shallow.

High-frequency ultrasound can induce local heating due to its elevated scattering properties. Utilizing this characteristic, therapeutic ultrasound-responsive hydrogels, such as one based on melamine-enhanced PVA have been developed [223]. However, ultrasound also exhibits non-thermal effects that may cause undesired consequences. One such effect is cavitation, wherein small gas bubbles are formed within the tissue due to acoustic vibrations generated by the ultrasound. These bubbles can expand to twice their original size within the tissue [88]. The subsequent collapse of these bubbles produces shock waves, which can act as micro-reactors within biological systems [88].

5.3.1.7 Mechanical loading

Mechanical is another form of physical stimulus that, although abundant in nature, has been relatively underexplored in the field 4D printing [224, 225]. Various

mechanically responsive materials exist, including organic molecules, polymers, and metal nanoparticles. These materials offer more than mere shape-morphing capabilities, they can also provide activation energy required for specific chemical responses in polymeric structures [224, 226] (*e.g.,* spiropyran polycarbonate [227]).

The application of mechanical stimuli can lead to significant changes in the electronic configurations of chemical bonds within these materials. Such changes have the potential to modify a broad array of material properties, including chemical, optical, electrical, and magnetic characteristics [224]. Hence, integrating mechanically responsive materials with rational designs is crucial for achieving desired mechanically induced outcomes in 4D printed structures.

Mechanical stimuli can be synergistically integrated with other forms of stimuli, such as chemical stimuli, to create materials with dual responsiveness (*i.e.*, mechano-chemo-responsive or mechano-chromic materials). These materials can undergo notable changes in properties such as absorption and/or fluorescence upon the application of mechanical loading [228].

One important example is the class of piezo-chromic luminescent materials, which change the color of their luminescence upon exposure to mechanical stimuli [225]. These materials are primarily constructed from dye-doped polymers and liquid-crystalline substances. A variety of mechanical loading types, including shearing, grinding, or elongation, can induce changes in their photoluminescent color [225]. For instance, the luminescent color of a thin film can be switched, manifesting the sign “UT”, by applying an isothermal mechanical stimulus, such as rubbing with a glass rod at room temperature [225] (Figure 2.g).

5.3.2 Chemical stimulation

To better understand the operating mechanisms of 4D printed biomedical devices that respond to physiological conditions, it is crucial to evaluate their reactions to physiological variables, such as pH levels and ionic concentration. The analysis of these reactions can also aid in optimizing the performance and efficiency of such devices. Furthermore, understanding how 4D printed biomedical devices respond to changes in physiological conditions is essential for ensuring the safety and efficacy of these devices in real-world medical applications.

5.3.2.1 pH

pH, as the acidity level of an aqueous solution, can experience significant fluctuations under various pathological conditions, affecting the different parts of the human body (*e.g.*, the gastrointestinal tract, vaginal tract, or blood vessels [229]). Accordingly, 4D printing technologies have been harnessed to develop pH-dependent systems for biomedical applications, including drug delivery and tissue engineering [229]. These

systems are designed to be responsive across the entire pH spectrum (acidic, alkaline, and neutral). For instance, a 3D printed flow actuating valve constructed of poly (2-vinylpyridine) has been developed that activates when exposed to a pH below 4 [230]. The valve features a globule-to-coil transition that controls its swelling, resulting in decreased water flow [230].

In pH-responsive hydrogels composed of carboxyl groups, polyvinyl chloride is usually added to tune hydrogel stiffness, thereby enabling 3D printing. Altering the pH level influences the ionization of the carboxyl groups in the acrylic acid, allowing control over the stiffness and swelling ratio of the hydrogel [74]. Advances in 2PP have enabled 4D printing of such materials at the microscale [231].

5.3.2.2 Ionic concentration

Ionic concentration serves as a pivotal chemical stimulus in the manipulation of hydrogel-based 4D printed structures. It is particularly instrumental in influencing the mechanical properties and physiological responsiveness of hydrogels. This is manifested in scenarios where hydrogels can achieve a remarkable degree of swelling, up to 60% [232].

A variation in ionic concentration dramatically changes the mechanical properties of hydrogels. An increase in ionic concentration, for example, can enhance rigidity owing to intensified cross-linking between ions and polymer chains [232-236]. Such cross-linking phenomena consequently affect the swelling behavior of hydrogels. For example, elevated ionic concentration can reduce swelling and contribute to a more rigid structure [237]. Furthermore, higher ion concentrations may create an osmotic pressure differential, inducing water influx and potentially increasing hydrogel volume.

Technological innovations have led to the 4D bioprinting of ion-sensitive hydrogel-based hollow tubular structures. Notably, structures sensitive to Ca^{2+} ions have been synthesized using methacrylate alginate and hyaluronic acid hydrogels [43]. Another application example is the fabrication of anatomically accurate and mechanically heterogeneous aortic valves using PEGDA [238].

Ion-sensitive hydrogels have been employed effectively in drug-delivery systems. They can be used for extended or regulated therapeutic release, responding dynamically to the surrounding ionic environment [239-241]. Such hydrogels offer the capability for site-specific drug delivery. For example, calcium-ion-sensitive hydrogels target areas of the body with elevated calcium concentrations, such as bone tissue [236, 242]. The drug release kinetics can be rationally controlled through the hydrogel's swelling or shrinking in response to ionic concentration changes, thereby optimizing therapeutic effectiveness.

Beyond single responsiveness, hydrogels can be engineered to respond to multiple stimuli. For example, hydrogels comprised of poly γ-glutamic acid and ε- polylysine are designed to respond to temperature, pH, and ionic concentration simultaneously [232]. Such multi-stimuli responsive hydrogels offer a wider range of applicability in biomedical applications, including but not limited to drug delivery and tissue engineering.

5.4 Design strategies towards shape morphing

In 4D printing, the shape transformation process is the results of a complex interplay between numerous factors the most notable of which can be categorized into three fundamental motifs: the rational design of macro- and micro-architectures, parameters associated with the AM process, and the configuration of the applied external stimuli. The complexity and level of detail of this multidimensional framework calls for an in-depth analytical approach, bringing together materials science, engineering design, and computational modeling.

The motif concerning the rational design of architectures deserves particular attention because of its centrality to the way the shape-morphing process of 4D printed objects relates to the underlying design parameters. The relevant design parameters may include a complex layering of multiple materials as well as engineered nano- and micro-patterns. Notably, nature often serves as an inspirational source for these designs, with adaptations from floral morphologies [83], the helical structure of DNA [243], biomechanical characteristics of specific animals, such as geckos [23], and even anthropomorphic features [146, 244] used by many research groups to program complex shape transformations.

The second motif focuses on the variables inherent to the AM process. During fabrication, such factors as imperfections or temperature gradients can be introduced, which significantly impact the structural properties and subsequent shape-morphing capabilities of the printed constructs [83, 245, 246]. A multi-faceted understanding of these variables and their interactions during the AM process is crucial for both optimization and quality control of 4D printing processes. For instance, the programmability and shape morphing of PLA-based 2D flat disks can be controlled through controlling the deposition of micro-defects during the FDM 3D printing [247]. This shows how phenomena that are generally considered to be undesirable can be harnessed to extend the programmability of 4D printed materials and their range of possible shape transformations.

The third motif relates to the external stimuli that induce the shape-morphing behavior. These stimuli can range from temperature and humidity fluctuations to magnetic fields, and their integration demands precise calibration with the material and structural design for predictable and controlled shape transformations [248].

Beyond these fundamental motifs, another layer of complexity is introduced when discussing multi-material 4D printed objects, particularly smart composites. The unique properties of such objects can result from differences in the properties of various layers [244, 249], their orientations (*e.g.,* anisotropic distribution of fibers [83, 245, 246]), or the use of multiple stimuli. For example, Figure 3.a illustrates a 4D printed hydrogel inspired by the blossoming of flowers, which can achieve complex 3D shape morphing when in contact with water. The rational distribution of fibers in a soft matrix (hydrogel) leads to twisting and bending of the structure [83]. Concerning multi-material 4D printing, Figure 3.b shows a human face that is 3D printed with multiple hydrogels, exhibiting pattern transformation from a flat shape to an out-of-plane shape similar to a human face [244]. Pattern transformations can also be achieved using the differences in the thermal expansion coefficients of the different compartments of multi-material 4D printed objects (*e.g.,* [248]). Moreover, by integrating two distinct phases, such as an elastic element and a smart material (*e.g.*, a SMP), a multi-functional object can be fabricated. The interaction between both phases can result in unusual phenomena, such as the stiffening/softening effect, SME, and debonding, leading to exciting shape transformation behaviors [243, 250-254]. On the one hand, the softening effect is favorable for achieving complex shape-morphing and self-folding origami structures. On the other hand, it compromises the mechanical load-bearing function of such structures. Because of the competition between self-folding characteristics and final stiffness, there exists a theoretical limit to how high the stiffness of 4D printed (lattice) structures can be [255]. Such theoretical limits should be taken into account in the design of shape-morphing structures. Rational geometrical design can also achieve sequential self-folding, based on the definition of crease lines for origami-like structures [29].

Proper structural design and the rational placement of a second material (*e.g.,* magnetic particle patterns) into the design of 4D printed objects are very challenging, particularly at the microscale. These challenges involve complexities in predicting the pattern transformations resulting from these placements and the fabrication of microstructures and engineering the distribution of the second phase. From the perspective of the distribution of a second phase, for example, the rational control of the pattern of magnetic iron oxide nanoparticles embedded in a single-layer hydrogel-based sheet results in various 3D shapes with out-of-plane deformations [256] (Figure 3.c). Similarly, it is possible to pattern anisotropic gradients in hydrogels using iron oxide nanoparticles and excite them using a magnetic field, inspired by sea jelly organisms [257]. Instead of magnetic particles, (macro-) permanent magnets can be embedded into a temperature-responsive SMP to create 4D printed mechanical metamaterials with untethered and reversible programming and locking mechanisms [258]. In that study, NdFeB magnets were rationally designed and embedded into PLA during the FDM printing process and included the programming of PLA struts, the displacement between the

magnets, the orientation of the magnets (N-S), and temperature changes [258] (Figure 3.d).

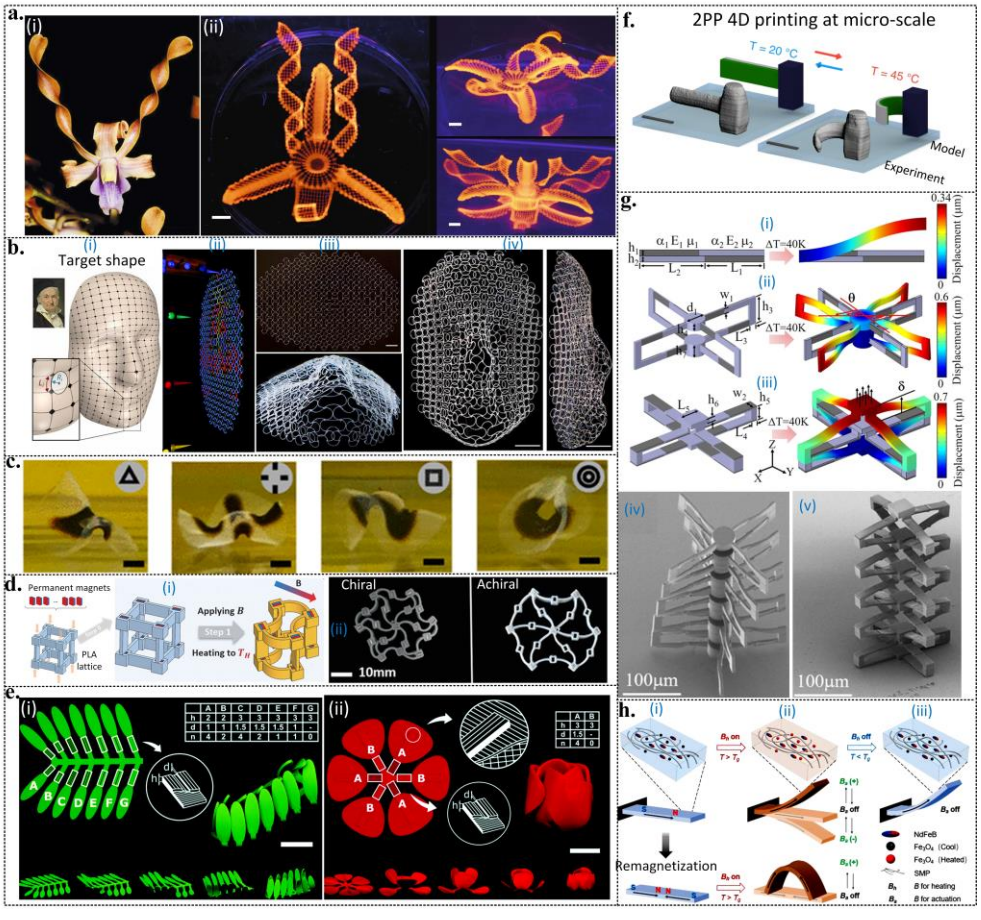

Figure 3. *Examples of complex shape morphing behaviors achieved using 4D printing.* ***a.*** *4D printing and shape-morphing of a flower inspired by a native orchid immersed in water. Reproduced with permission [83] Copyright 2016, Springer Nature. Scale bars represent 5 mm.* ***b.*** *A schematic of a 3D lattice face of Carl Friedrich Gauss's likeness* ***(i.)*** *and the corresponding lattice structure during* ***(ii)*** *and after printing* ***(iii, top)****.* ***iii****,* ***bottom*** *and* ***iv*** *show a 3D scan of the temporary shape of the 4D printed structures triggered by an external stimulus [244].* ***c.*** *The pattern transformation of a composite hydrogel-based sheet made using different ferromagnetic particle distributions while exposed to light [256].* ***d.*** *A magneto-thermo-mechanically setup based on PLA and embedded NdFeB magnets (i) to morph lattice structures into chiral and achiral deformations (ii). Reproduced with permission [258]. Copyright 2022, Wiley-VCH. The scale bar represents 10 mm.* ***e.*** *The shape-shifting and pattern transformation of different architectures. The gradual closure of the leaves of a shy plant-inspired structure* ***(i)*** *and sequential shape-shifting from initially flat petals to a tulip in 20 s* ***(ii)*** *[262].* ***f.*** *A micro-4D printed beam featuring reversible shape-morphing behavior at low temperatures close to those of the human body [24]. Scale bar is 20 μm.* ***g.*** *A 4D printed metamaterial featuring a dynamic Poisson's ratio at the microscale made via 2PP [264].* ***i-iii*** *A FEM-based prediction of the shape morphing behavior of 4D printed structures, working based on the differences in*

thermal coefficients. ***iv-v*** *SEM images of the initial and stimulated configurations of the metamaterial at the microscale.* ***h.*** *An illustration showing the mechanism of pattern transformation in magneto-active SMPs Reproduced with permission [381]. Copyright 2020, Wiley-VCH at low temperatures (**i**), heating up the sample via an alternating magnetic field (**ii**) and heating and cooling the samples via alternating and constant magnetic fields (**iii**).*

From an AM process perspective, the pre-strain or residual stress stored in 4D printed structures and imperfections induced during the AM process are the main reasons for the shape-morphing properties of 4D printed structures [245, 259-263]. The residual stresses can even be generated during simple and inexpensive 3D printing processes, such as FDM-based printing with PLA. Such SMPs can be automatically programmed during the printing process. For example, Figure 3.e demonstrates the sequential shape-morphing behavior resulting from the introduction of porosity into the geometry as well as the adjustment of the printing parameters, such as thickness and printing patterns [262]. Such phenomena also exist in 4D printing at the micro- and nanoscales. Changing the dose in 2PP (depending on the scanning speed and laser power) allows for the control of the mechanical properties and thermal expansions of the polymerized resin. Various 4D printed structures, such as microscale mechanical meta-materials, have been fabricated using this approach (Figures 3.f [24] and 3.g [268]) [17, 24, 264, 265]. For example, the Poisson's ratio of mechanical metamaterials can be controlled through temperature at the microscale (Figure 3.g) [262].

The shape-morphing mechanism accompanied by a locking capability can be also obtained by properly adjusting the base materials and designing an advanced stimulation setup. In this case, fast shape-morphing behavior is achieved, and the structure is locked at its temporary state in the absence of an external field (energy-sufficient) [164]. The composite reported in that study was made of an acrylate-based amorphous SMP consisting of Fe_3O_4 and NdFeB particles. While Fe_3O_4 particles are responsive to inductive heating via a high-frequency magnetic field, NdFeB particles enable the programming of the structure under an actuating magnetic field. The integration of both functionalities results in a locking mechanism, reversibility, and energy-efficient stimulation (Figure 3.h) [164].

5.5 Biomedical applications

The advent of 3D printing has undoubtedly announced a new era in the fabrication of complex structures, particularly for biomedical applications such as tissue engineering. However, its limitation primarily lies in the inability to emulate the dynamic and evolving characteristics of native biological tissues. For example, vascularization within large 3D printed constructs remains an elusive goal, posing a significant impediment to the delivery of essential nutrients and oxygen to engineered tissues.

4D (bio)printing emerges as a transformative solution to these limitations. Unlike its 3D counterpart, 4D bioprinting facilitates the development of artificial tissues endowed with dynamic characteristics. These structures can encapsulate vascular or stem cells, thereby promoting rapid maturation and functional behavior over time [15, 34]. The capacity to undergo dynamic changes makes 4D bioprinted structures highly applicable in the treatment of organ-specific diseases, such as cardiac conditions.

Specifically, in the domain of cardiovascular medicine, the dysfunction of the aortic valve, manifesting either as stenosis or regurgitation, poses serious health risks. The aortic valve is a complex, tri-leaflet structure responsible for regulating the unidirectional flow of blood from the heart to the aorta. Aortic valve stenosis refers to the thickening or stiffening of these cusps, while aortic valve regurgitation is characterized by improper closure, leading to retrograde blood flow. 4D printing technology shows promise in fabricating reversible aortic valves or stents that can adapt to these pathological changes [39] (Figure 4.a).

The applications of 4D printing in the biomedical field extend beyond tissue engineering and cardiovascular treatments. The technology holds potential for developing a myriad of smart medical devices, including but not limited to, occlusion devices, micro-needles for minimally invasive procedures, specialized drug delivery systems, wound closure mechanisms, and various types of implants and scaffolds. Each of these applications leverages the dynamic, adaptive capabilities of 4D printed structures to offer enhanced therapeutic outcomes.

5.5.1 Biomedical devices

4D printing is indeed emerging as a transformative technology in the field of biomedical engineering, significantly contributing to the evolution of minimally invasive medical devices and procedures. One of the most important applications lies in the domain of cardiovascular engineering. For example, self-expanding stents fabricated through 4D printing technologies show considerable promise for the treatment of vascular diseases, as corroborated by multiple studies [266-268]. Similarly, the technique allows for the production of sutureless anastomosis devices, thereby streamlining surgical procedures [270]. In addition, self-fitting scaffolds produced through 4D printing offer enhanced adaptability to diverse tissue topographies.

Furthermore, in the area of bone tissue engineering, 4D printing is increasingly being employed for the fabrication of complex structures such as bone repair tools and orthopedic biomaterials [172, 271]. The technology also holds potential for generating scaffolds that facilitate tissue regeneration. Moving beyond the musculoskeletal system, 4D printing technologies are also being applied in the development of peripheral nerve interfaces for treating ailments such as hypertension and diabetes [272]. Researchers have recently advanced the field by creating a 4D printed nerve cuff electrode

that features self-folding mechanisms, thereby facilitating the treatment of smaller peripheral nerves [272] (Figure 4.b).

In the following sub-sections, we will delve into a detailed examination of these innovative medical devices, elucidating the principles underlying their operation, and assessing the future potential of 4D printing in enhancing their effectiveness and broadening their applicability.

5.5.2 Stents

A stent is a medical device implanted into vascular structures to prevent them from collapsing and to reduce thrombotic risk. 4D printing can minimize the invasiveness of such medical devices by producing self-expanding stents that can be triggered by an external stimulus [273]. This emergent technology has already found applications in the creation of dynamic stents for a diverse array of medical conditions, including vascular, tracheal, and orbital anomalies [274].

5.5.2.1 Vascular stents

The exploration into 4D printing of vascular stents represents a pivotal transformation in the biomedical field, combining advances in material science, computational design, and advanced manufacturing technologies. These stents are employed for a range of medical applications, such as treating cardiovascular diseases (*e.g.,* atherosclerosis), and ureteral-associated diseases (*e.g.,* hydronephrosis) [275]. While traditional stents serve as passive implants, 4D printed stents introduce dynamic functionalities, such as temperature responsiveness, which allows them to expand upon local heating [275].

The operational mechanism of these 4D printed stents is governed by the types of SMPs used and the stimuli that activate them. For instance, stents printed with PLA/Fe_3O_4 composites through DIW are capable of magnetically activated shape recovery [275]. Such multi-functional stents can regain their original form when triggered by a magnetic field. Numerous numerical models and empirical proof-of-concept studies have been conducted to validate self-expanding or self-shrinking stents, further substantiating the potential of this technology [276-281].

Drug-eluting functionalities are another field of application, particularly in the context of ureteral diseases [266, 282]. Water-responsive stents fabricated from zein, a plant-based protein, have been successfully tested in porcine models, demonstrating both biodegradability and functional efficacy [282]. Another noteworthy innovation was the dual-responsive stent fabricated from acrylamide-acrylic acid/cellulose nanocrystal (AAm-AAc/CNC) that could respond to deionized water and Fe^{+3} ions. This design revealed potential for closure in enter-atmospheric fistulas [266] (Figure 4.c).

A promising area of research focuses on enhancing the reliability and longevity of stents through self-healing materials [283]. These include semi-interpenetrating polymer networks of PCL and urethane diacrylate, which offer exceptional stretchability and self-healing properties [283]. Longitudinal studies have started to evaluate the degradation patterns of these stents over extended periods under physiological conditions [284].

A major challenge that some temperature-responsive stents face is the high glass transition temperature, which make them impractical for implantation into the human body. Nevertheless, the operational activation temperatures of stents have also been modulated. In a proof-of-concept study, a vascular stent was 4D printed via DIW from PLMC, featuring a relatively low activation temperature (*i.e.,* 40-45 °C) and a recovery within 30 seconds [285]. However, this activation temperature is still not low enough for either their implantation into body or even *in vitro* mechanobiological studies as cells may not survive. For instance, a poly(glycerol dodecanoate) acrylate (PGDA)-based vascular stent was engineered to recover at the body temperature (20-37 °C) and demonstrated a rapid recovery time (0.4 seconds) in both *in vitro* and *in vivo* settings (Figure 4.d) [68]. One common material to make temperature-responsive stents with a low transition temperature is PNIPAM. That is not only because of the low transition temperature of PNIPAM, but also because of its versatility in tuning the stiffness and inducing complex shape transformations. For example, a stent-inspired tubular structures has been 4D printed via DIW from PNIPAM as the active part and from polyacrylamide as the passive one [286]. The integration of such active and passive components, as a design strategy, induces complex deformations, such as bending, clamping, elongation, and radial expansion, which expands the envelope of achievable shape transformations can be instrumental in eventually making such types of medical devices available to surgeons.

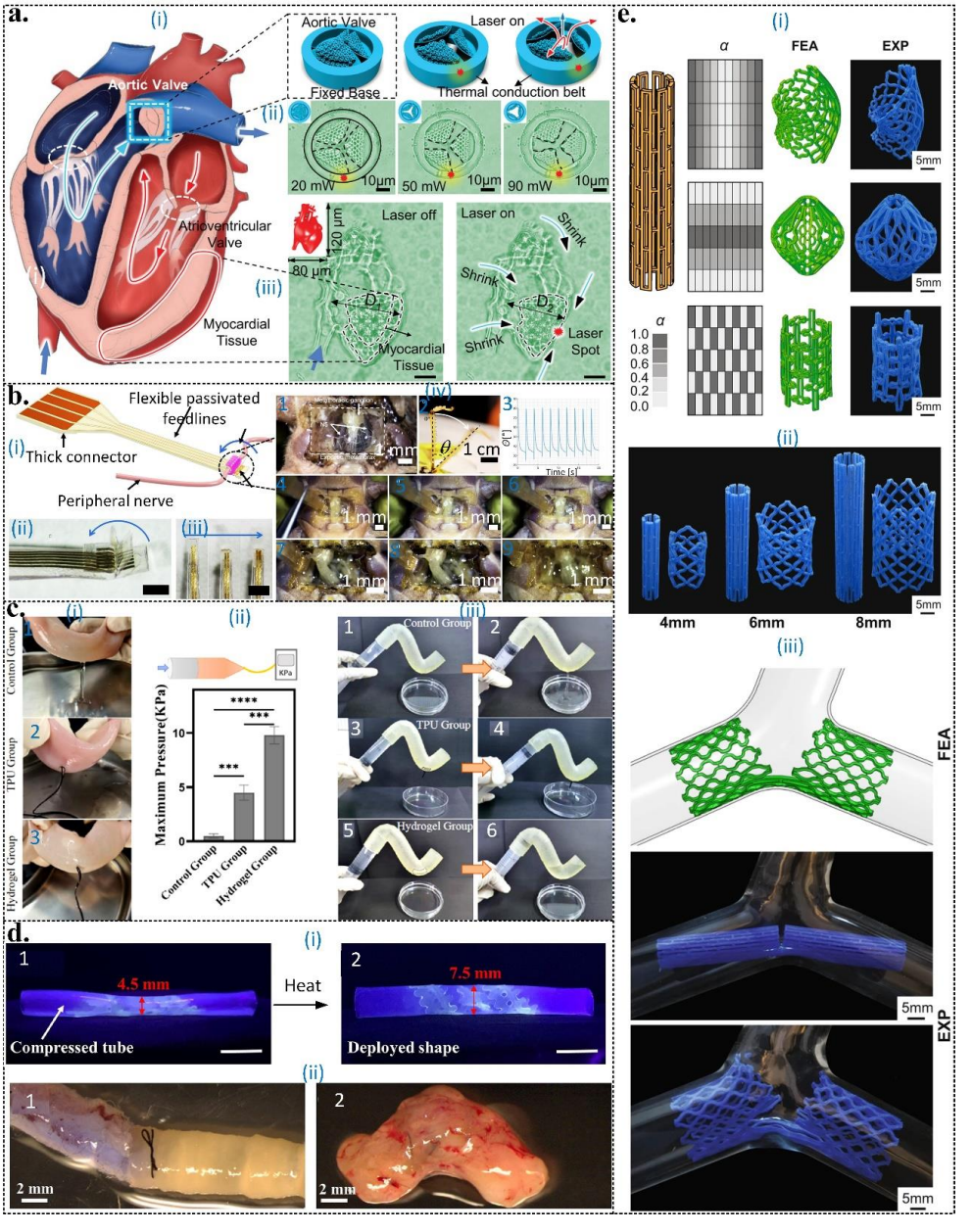

Figure 4. *The applications of 4D printing in biomedical devices and medicine.* ***a.i.*** *A schematic drawing showing a heat-responsive aortic valve. Reproduced with permission [39]. Copyright 2023, Wiley-VCH.* ***a.ii*** *shows the opening and closing of the micro-aortic valve under different laser powers.* ***a.iii*** *illustrates optical micrographs of an artificial 4D printed heart in the presence and absence of light. Scale bar represents 20 μm.* ***b.*** *A 4D printed self-folding nerve cuff electrode [272].* ***i, and ii-iii*** *show a schematic of the cuff electrode design and the 4D printed ones, respectively. The scale bar represents 1 mm.* ***iv*** *depicts the in vivo implantation of the 4D printed cuff electrode in a locust. (**1**) The metathoracic cavity of the locust (**2**)*

*the movement of the hindleg triggered by the nerve, (**3**) the variation of the angle between legs. (**4-9**) the folding and unfolding of the 4D printed cuff electrodes.* ***c.*** *In vitro experiments with a 4D printed hydrogel-based sealing tool in an intestine. Reproduced with permission [266]. Copyright 2022, Elsevier.* ***i.*** *shows the sealing effect of the tool in a hydrogel porcine intestine featuring a hole.* ***ii.*** *Maximum pressure that the intestine can tolerate.* ***iii.*** *Another sealing test in a 4D printed bi-layer hydrogel.* ***d.*** *the in vivo testing of a 4D printed vascular stent based on PGDA. Reproduced with permission [68]. Copyright 2021, Elsevier. The implementation of the stent in a silicone-based blood vessel (temporary shape, **i.1**) and the temperature-based deployment of the vessel (**i.2**). Scale bar is 1 cm. The in vivo implementation of the 4D printed stent in a mouse aorta on days 0 (**ii.1**) and 14 (**ii.2**).* ***e.*** *A proof-of-concept study of a 4D printed stent-like structure made from PLA via FDM [20].* ***i.*** *shows the experimental and FEM results of different designs with different printing parameters to achieve sophisticated shapes and deformations.* ***ii.*** *The effects of dimensional scaling on the performance of 4D printed stents.* ***iii.*** *The implementation of the stents in a vein-like glass and its stimulation via temperature.*

The design space can further be expanded by the incorporation of mechanical meta-materials, offering unique characteristics, such as auxeticity and simultaneous high stiffness and toughness [287, 288]. Several proof-of-concept tabular structures exhibiting auxeticity have been 4D printed using FDM for *in vitro* studies [289-290]. These stent-like structures fabricated through 4D printing have the potential to be used in vascular studies. Stent-like tubes featuring SME based on meta-materials can be simply design through changing the printing parameters. For instance, a stent-like tube was 4D printed from PLA via FDM [20] (Figure 4.e). Through the adjustment of printing speed and patterns, the radial expansion was achieved in aquatic environment. Similarly, stents can be also designed based on the concepts of kirigami (*e.g.,* bifurcated vascular stents from PU-SMPs [290]) and origami (*e.g.,* a vascular stent from a thermoset SMP composite, epoxidized soybean oil [292], and a 4D printed temperature-responsive stent via FDM from PLA [293]) featuring shape morphing and adaptability.

Finally, the capabilities of DLW techniques have been harnessed to create microscale stents that exhibit promising mechanical and functional characteristics [294]. These stents, composed of SMPs, can expand in aqueous environments, opening new opportunities for minimally invasive procedures.

As the horizon of the 4D printing technology continues to expand, future research works may benefit from focusing on the integration of advanced sensing mechanisms, improving biocompatibility, and optimizing the activation parameters for these complex, multi-functional stents. Specific technologies, such as real-time monitoring sensors and nanoscale actuators, could significantly augment the capabilities of these advanced biomedical devices, providing an integrated approach to patient-specific healthcare.

5.5.2.2 Tracheal stents

Tracheal stents, instrumental in treating conditions such as tracheal stenosis and tracheomalacia, represent another frontier of biomedical application for 4D printing technologies [295, 296]. The incorporation of smart biomaterials into tracheal stents has been particularly promising, allowing for precise control over stent opening and thereby potentially mitigating the need for invasive surgical interventions [297].

Among the examples in this emerging field is a bioinspired tracheal stent fabricated from a PLA (and PCL)/Fe_3O_4 composite. This 4D printed construct possesses magnetic activation capabilities [295, 298, 299]. However, it must be noted that comprehensive studies are still needed to determine the cell viability and long-term effects of these magnetic-responsive materials. Moreover, the *in vitro* and *in vivo* feasibility of such 4D printed tracheal stents in the presence of magnetic fields and magnetic fillers remains an area of active investigation.

In pediatric applications, a tracheobronchial splint device made from PCL has been successfully 4D printed to address tracheobronchomalacia [300] (Figure 5.a). Innovatively, the design of this 4D printed splint is such that it can adapt to tissue growth, a feature achieved by careful mechanical design and regulated degradation behaviors [300]. To assess the long-term performance and shape-morphing capabilities of the device, *in vivo* tests were conducted in two infants, thereby substantiating its potential utility.

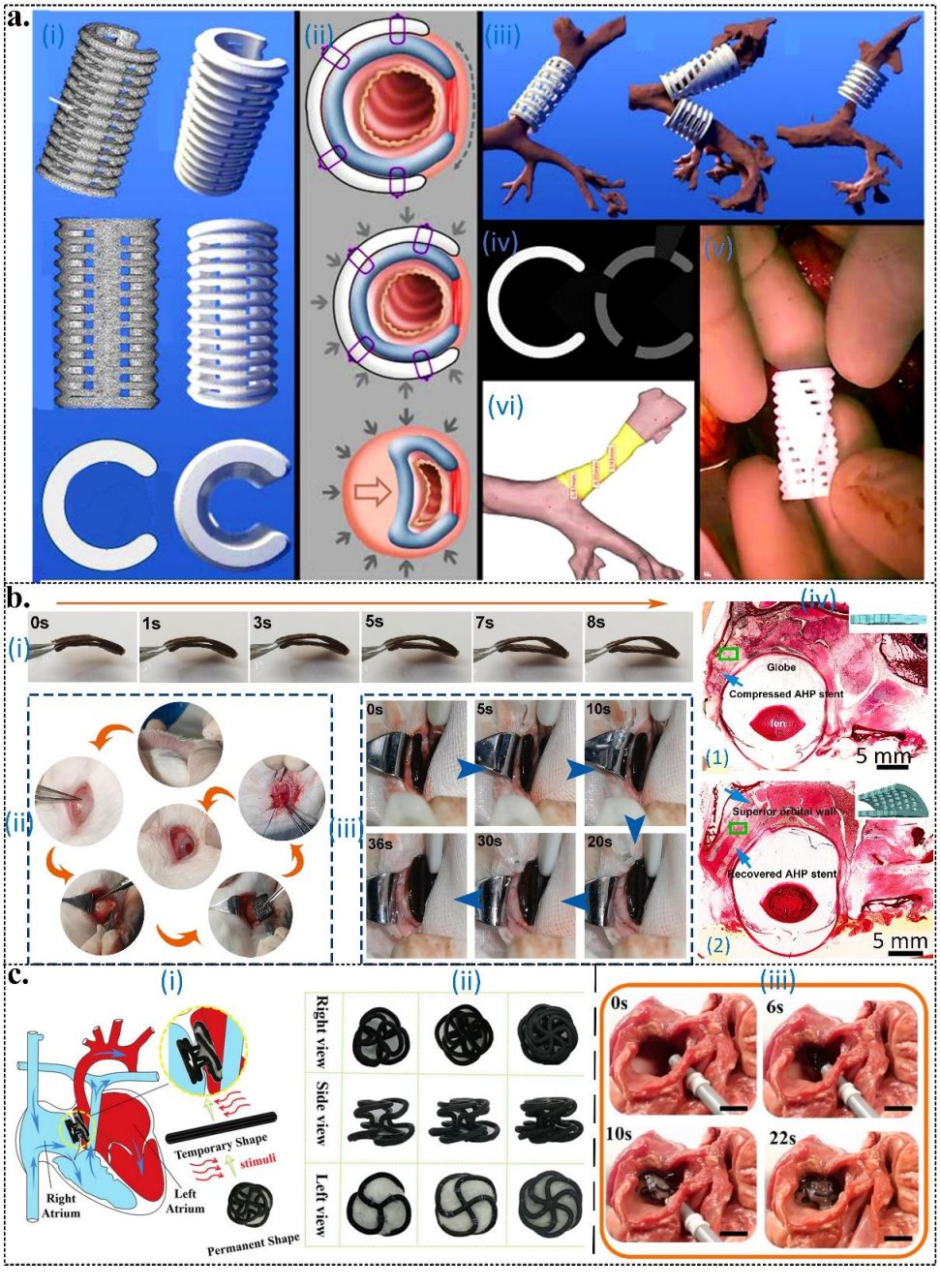

Figure 5. *In vivo testing of 4D printed biomedical devices.* ***a.*** *A 4D printed tracheobronchial splint device made of PCL through SLA (**i**). Reproduced with permission [300]. Copyright 2015, The American Association for the Advancement of Science. The tracheobronchial splint mechanism in treating tracheobronchial collapse in tracheobronchomalacia (**ii**) and its splint over the segmented primary model fits three patients (**iii**). A 2D image of the airway and split wall (**iv**) and the final 4D printed device (**v**) with the 3D model of*

*the patient's airway (**vi**) [300]. **b.** A 4D printed orbital stent to treat enophthalmic invagination. Reproduced with permission [302]. Copyright 2022, Elsevier. **i.** The shape memory recovery of a stent immersed in 44 °C water. **ii.** The implantation steps of a 4D printed stent in the eyeballs of a rabbit. **iii.** The in vivo shape recovery of the stent in a rabbit. The images of the implanted stent when it is compressed (**iv.**) and after recovery (**v**). **c.** 4D printed occluders. A schematic drawing of an atrial septal defect before and after an interventional therapy with an occlude (**i**). Reproduced with permission [52]. Copyright 2019, Wiley-VCH. The final shapes of the 4D printed occlude (**ii**) are shown [52]. In vivo illustration of the magnetic-responsive 4D printed left atrial appendage occlude (**iii**) [53]. The scale bar is 10 mm.*

5.5.2.3 Orbital stents

The application of 4D printing technologies in ophthalmic medicine introduces a paradigm shift, particularly in the treatment of enophthalmos, a condition characterized by the posterior displacement of the eyeball within the orbital cavity [301]. Conventional treatments often employ static implants and stents, which encounter various limitations including, but not limited to, inaccurate contour matching of the orbital coloboma, complications in CT imaging, and suboptimal volumetric filling capabilities [302].

To mitigate these shortcomings, recent innovations in 4D printing have enabled the fabrication of smart orbital stents with features such as controllable shape-morphing and CT-developable capabilities [302]. These advanced stents are typically composed of PU, gold nanoparticles, and nano-hydroxyapatite, thereby integrating mechanical robustness, radiopacity for CT imaging, and bioactivity, respectively. The stent's performance and shape recovery were evaluated both *in vitro* and *in vivo* using a rabbit orbit model. Interestingly, the stent demonstrated promising shape-recovery characteristics when stimulated by a saline solution at 44°C [302] (Figure 5.b). The analytical evaluation of this 4D printed stent [302] not only confirms its theoretical viability but also underlines its empirical effectiveness in a controlled animal model.

Such advancements pave the way for further clinical trials and can help shape the future of personalized ophthalmic treatments. However, for a comprehensive understanding and eventual clinical implementation, several aspects need further investigation. These include long-term biocompatibility of such medical devices, the potential for the bio-integration of the material, and the stent's performance under various physiological conditions. Furthermore, the scalability of this technology to human models and its economic viability are questions that remain to be answered.

5.5.3 Occlusion devices

Interventional therapy, a percutaneous non-surgical procedure, has established itself as a methodology for the treatment of congenital heart diseases [303]. Yet, the field has been persistently confronted with issues related to the precision, biodegradability, and remote controllability of the occlusion devices used. 4D printing technology

provides a groundbreaking avenue to surmount these challenges by enabling the fabrication of personalized, high-precision occlusion devices [52].

Specifically, 4D printed occlusion devices have proven their efficacy in closing atrial septal defects with enhanced treatment accuracy [52, 304] (Figure 5.c.i-ii [52] and Figure 5.c.iii [53]). These devices often incorporate SMPs, as seen in a study where a 4D printed device consisted of a supporting frame made from a PLA/Fe_3O_4 composite [53]. The SMP allows for remote controllability, whereby the device can change its shape *in situ* in response to external stimuli such as temperature or magnetic fields. Covered with thin occluding membranes, these devices further demonstrate biodegradability, durability, and biocompatibility, as was evidenced by a 48-week *in vivo* study on mice [53].

In another proof-of-concept study, a custom-made occluder constructed from porous, radiopaque PU was 4D printed using FDM for interventional radiology applications [305]. An analytical evaluation of the device focused on its mechanical properties, specifically shape recovery ratio and stiffness, thus indicating its potential applicability in real-world clinical scenarios.

The research into 4D printed occlusion devices is ongoing and needs to make further progress before clinical adoptions are feasible. While *in vivo* studies and prototype evaluations are promising, the path to clinical translation demands an exhaustive assessment of various aspects of the performance of such devices. In particular, long-term stability, the potential for immune responses, and real-world mechanical stresses under diverse physiological conditions are yet to be comprehensively understood. Moreover, the economic feasibility and scalability of these 4D printed devices for large-scale clinical use require additional feasibility research.

5.5.4 Microneedles

Microneedles (MNs) represent a paradigm shift in transdermal drug delivery and biosensing technologies, transcending traditional limitations associated with pain and tissue damage. Employed for a plethora of applications including long-term drug delivery (*e.g.*, vaccines and insulin) and biosensing (*e.g.*, glucose and DNA biomarkers), MNs can penetrate the epidermal layer without triggering nerve endings, thus permitting efficient uptake of macro-molecules into the capillaries and lymphatic networks sans pain [306-310]. Furthermore, MNs are being explored for precision drug delivery in oncology [309].

While the physiological advantages of MNs are substantial, their fabrication process plays an important role in their efficacy. Traditional manufacturing techniques for MNs, such as micro-molding, laser cutting, and lithography, have numerous disadvantages including low precision, high costs, and extended processing times [311, 312]. In contrast, micro-4D printing emerges as a revolutionary technology that improve

many of these drawbacks. It confers superior mechanical properties, enhances intracellular drug delivery, offers high printing accuracy, is cost-effective, and simplifies the fabrication workflow [311, 313, 314].

A groundbreaking development in this area is the use of micro-4D printing techniques that synergistically combine micro-DLP and projection micro-SLA. This innovation has led to the creation of bio-inspired MNs featuring backward-facing curved barbs, designed to enhance tissue adhesion [311] (Figure 6.a). Such intricate design features, previously difficult to achieve through conventional methods, become feasible through micro-4D printing. It allows for geometries that can significantly improve the MN's efficiency in drug delivery and biosensing applications.

Considering the pivotal role of MNs in precision medicine and remote monitoring, the evolution of micro-4D printing technologies is likely to have profound impacts. Future research might delve into the exploration of biocompatible and biodegradable materials, the development of MNs with real-time biosensing capabilities, and the application of machine learning algorithms to the optimization of MN design parameters for specific clinical applications.

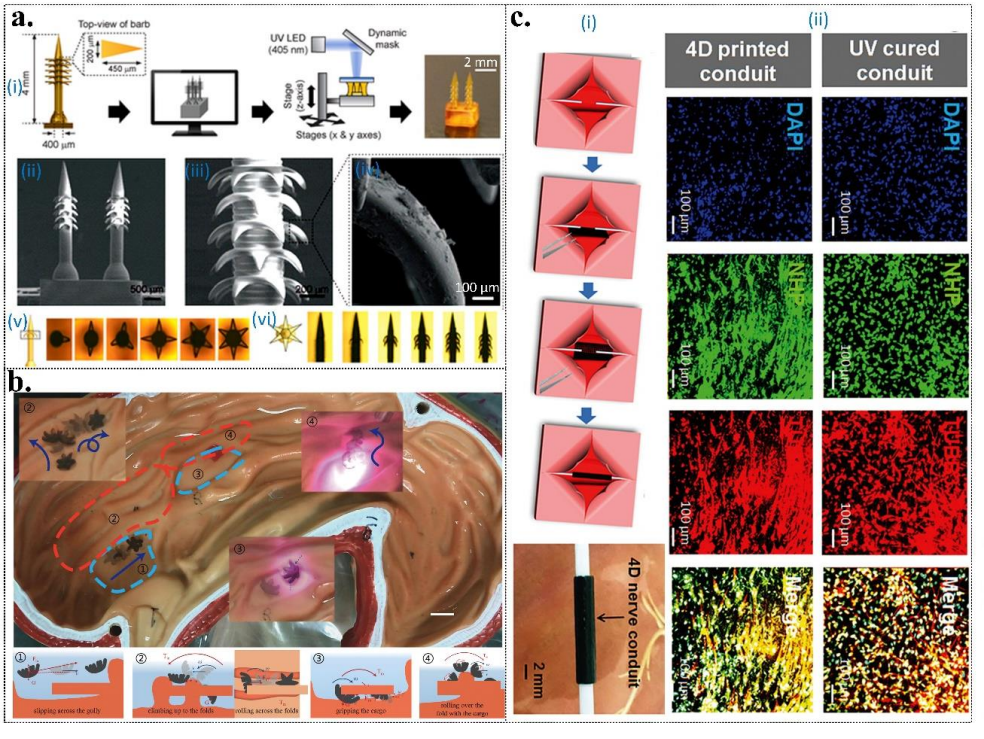

Figure 6. *In vitro testing of 4D printed biomedical devices.* ***a.*** *The 4D printing of a bioinspired MN with triangular backward-facing curved barbs. The schematic drawing depicts the fabrication steps via a light-assisted AM technique (**i**). Reproduced with permission [311]. Copyright 2020, Wiley-VCH. The SEM*

*images of the backward-faced curved barbs are presented in (**ii-iv**). The various configurations of the MN with different barbs can result in different pattern transformations (**v-vi**) [311]. **b.** The movement and delivery of a 4D printed leptasteria-like micro-robot based on NIPAM/NdFeB for drug delivery systems in a stomach model. Reproduced with permission [321]. Copyright 2022, Elsevier. The scale bar corresponds to 6 mm. **c.i**. An illustration showing thermomechanical cycles of the full entubulation of a 4D nerve guidance conduit Reproduced with permission [353]. Copyright 2018, Wiley-VCH. **c.ii**. The immunofluorescence images corresponding to the neurogenic differentiation of human MSCs on the 4D-printed nerve guidance conduit and their UV-cured counterpart. Reproduced with permission [353]. Copyright 2018, Wiley-VCH.*

5.5.5 Drug delivery systems

4D printing technologies offer unparalleled opportunities in controlled drug delivery systems, a topic of substantial importance in the pharmaceutical and biomedical sectors [315]. Employing stimuli-responsive smart materials, 4D printing facilitates the temporal and spatial control of drug release in a programmable manner, triggered by specific biological signals or environmental stimuli (*e.g.*, pathological anomalies *in vivo*) [196].

One example of such applications is the ingestible tablet designed for ulcer treatment, which employs a pH-responsive shell. As the gastric environment turns acidic, the tablet releases a predetermined dose of medication [316]. This innovative approach was later extended in a proof-of-concept study, where an SMP-based capsule was developed to modulate drug release *via* crack propagation mechanisms within the capsule [51].

Another remarkable advancement is the conceptualization and fabrication of "*multi-somes*" complex droplet networks comprising small aqueous droplets encased in a larger oil droplet and suspended in an aqueous medium [317]. Utilizing 3D printing technologies, these droplets can encapsulate aqueous-based drugs and release them responsively based on environmental pH or temperature [317]. These multi-somes are also osmoreactive and can be fabricated into very complex shapes, offering a myriad of possibilities in the drug delivery [318].

Drawing inspiration from the shape-memory effects of 4D printing, researchers have also been experimenting with gastric retention devices aimed at regulating drug release and preventing premature gastric emptying [50, 319, 320]. A key focus of these devices is to maintain retention within the stomach by manipulating the transition from a collapsed configuration to a pre-programmed shape under physiological conditions. For example, an SMP-based device fabricated from PVA was developed that could transform from a compressed to an expanded state upon exposure to aqueous fluids at body temperature, thus prolonging its retention in the stomach [50].

Finally, there is an emergent demand for remote controllability in microscale drug delivery systems. To address this requirement, recent advances have been made in the

4D printing of micro-robots capable of ferrying and releasing drugs upon stimulation by magnetic fields and thermal changes (Figure 6.b) [321].

4D printing has ushered in a new era in drug delivery, offering unprecedented control over the pharmacokinetics and pharmacodynamics of medications. However, the field is still developing, and extensive *in vitro* and *in vivo* studies are required to fully realize the technology's transformative potential. Future investigations could consider employing advanced imaging techniques and multi-physics computational models to better understand the mechanics and kinetics involved in these complex drug delivery systems.

5.5.6 Implants and scaffolds

The application of 4D printing technologies in tissue engineering and regenerative medicine holds significant promise for overcoming the limitations of traditional 3D printed scaffolds and implants. One primary advantage of 4D printed structures is their ability to dynamically adapt to physiological conditions, thereby offering a more robust solution for tissue growth and function restoration [322, 323].

Scaffolds function as 3D matrices that support cellular adhesion, proliferation, and differentiation, leading to tissue regeneration. Implants, on the other hand, serve to replace or augment physiological functions. In the field of regenerative medicine, 4D printing technologies offer a distinctive advantage by allowing for the fabrication of scaffolds and implants with stimuli-responsive features. For instance, a scaffold printed from polyurethane-based SMP demonstrated tunable cellular adhesion properties. This allowed for regulated cell growth when mechanical deformations were applied to the structure, thereby making it more physiologically adaptive [322].

Further studies elucidate the potential for multi-responsiveness in 4D printed scaffolds. A case in point is a 3D porous scaffold manufactured via SLA-based 4D printing, which utilized a biocompatible SOEA resin and facilitated the maturation of multipotent human MSCs [324, 325]. In another innovative application, a dual-responsive scaffold comprising PU and acrylate was fabricated using inkjet-based 3D bioprinting. The resultant structure exhibited responsiveness to both thermal and photonic stimuli [326].

Another avenue for innovation resides in the ability of 4D printing technologies to fabricate geometrically complex implants with intricate surface nanopatterns, a feat not attainable with traditional manufacturing techniques [30]. The incorporation of surface nanopatterns on scaffolds and implants can be highly advantageous for inducing specific cellular responses, such as osteogenic differentiation [327], antibacterial activity [328], and immunomodulation [329]. Pioneering approaches suggest initiating the fabrication process with a flat structure that can be programmed to self-fold into complex 3D architectures upon exposure to external stimuli both for strut-based unit cells

[30] and for sheet-based hyperbolic surfaces, such as triply periodic minimal surfaces [330].

The significance of geometric features, particularly curvature, has been highlighted in recent research, demonstrating its influential role in modulating cellular behavior and thus the progression of tissue regeneration [331]. Given these capabilities, 4D printed structures offer an exceptional platform for advancing the development of scaffolds and implants tailored for the regeneration of various tissue types, including bone, cartilage, and muscle. Thus, this section delves into the myriad potentials and innovative applications of 4D printed scaffolds and implants, specifically focusing on their roles in regenerating bone, cartilage, muscle, and other tissues.

5.5.6.1 Bone and cartilage tissues

The emerging field of 4D printing for bone tissue applications holds transformative potential for orthopedic surgery, presenting areas for reduced infection risks, minimized surgical invasiveness, and enhanced osseointegration. With particular emphasis on the challenge of mimicking the native bone's biomechanical properties [34], current advancements are largely categorized into four groups: *i.* injectable stimuli-responsive hydrogels, *ii.* shape memory scaffolds, *iii.* functional transformation mechanisms, and *iv.* neovascularization and neurogenesis to foster bone growth and mineralization [236].

Firstly, injectable thermo-sensitive hydrogels, such as hydroxypropyl methylcellulose and hydroxybutyl chitosan, offer the advantage of *in situ* gelation at the body temperature [318]. These hydrogels serve as biocompatible matrices for the encapsulation and delivery of cellular components, growth factors, or bone-stimulating inorganic composites, such as hydroxyapatite [236].

Secondly, SMPs serve as a substrate for 3D/4D printed scaffolds, facilitating their deployment through minimally invasive procedures [305]. These SMP-based scaffolds have been shown to enhance osteoblast adhesion, proliferation, and osteogenic gene expression, thereby fulfilling crucial criteria for successful bone repair [332, 333].

In the third approach, functional transformation mechanisms are utilized to design mechanical strategies that augment bone regeneration. An example in this category are mechanically deployable meta-implants [271] (Figure 7.a). This novel application demonstrates how mechanical pattern transformation can contribute to the success of minimally invasive and effective bone regeneration strategies.

The fourth approach addresses the unmet need for vascularization and regeneration of neural networks in bone tissue engineering [34, 236, 334-336]. While 4D printing is yet to be fully exploited for this purpose, it undoubtedly represents a frontier for further research and development.

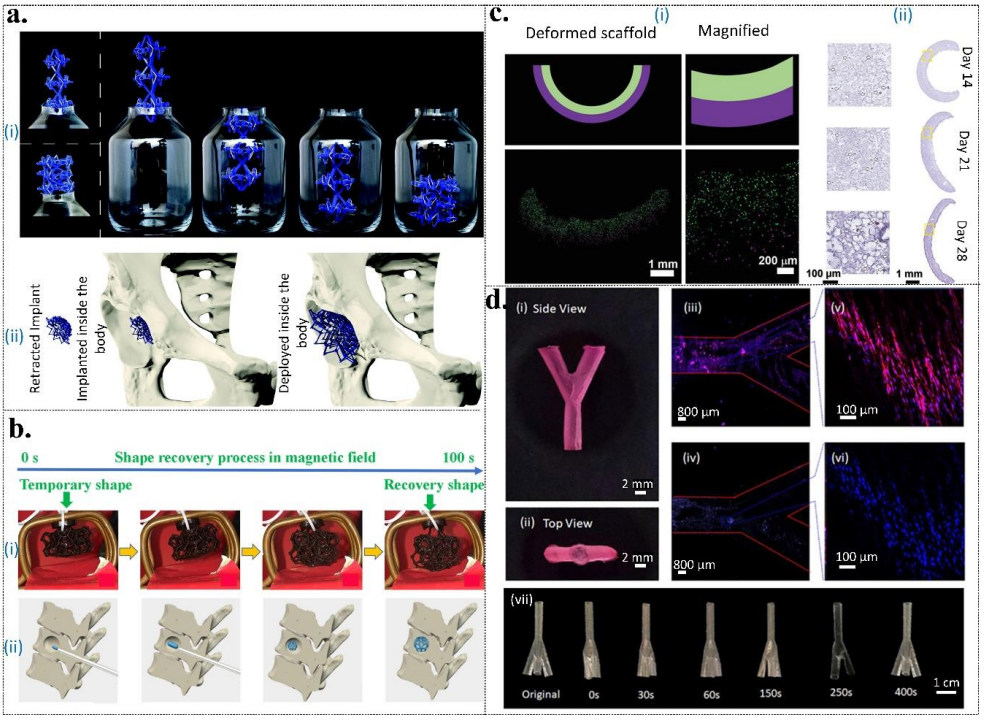

Figure 7. *4D printed scaffolds and implants.* ***a.i*** *An example of deployable structures that expand inside confined environments.* ***(ii)*** *A proof-of-concept-study of a deployable implant to fill damaged bone [271].* ***b.*** *A 4D printed bone scaffold made from PLA/Fe_3O_4, which expands upon exposure to a magnetic field* ***(i.)*** *and can be used to fill bone defects* ***(ii.)****. Reproduced with permission [172]. Copyright 2019, Elsevier.* ***c.*** *4D bioprinted artificial cartilage (scaffold) [15].* ***i.*** *A schematic drawing depicting bi-layer cell-free scaffolds with their corresponding optical images, confirming the presences of cells in both top and bottom layers in green and red, respectively.* ***ii.*** *The histological images of hematoxyline-eosin (H&E staining) on days 14, 21, and 28 with two different magnifications.* ***d.*** *The illustration of 4D anisotropic scaffolds by integrating the staircase effect of FDM printing with a coating technique. Reproduced with permission [349]. Copyright 2019, IOP Publishing.* ***(i-ii)*** *The 4D printed anisotropic scaffolds before seeding.* ***(iii-vi)*** *The confocal images of the seeded scaffolds.*

SMP-based constructs have been tailored for specialized applications in bone repair. Magneto-responsive SMP-based scaffolds were fabricated for personalized bone defect treatment, wherein these structures could be actuated by an external magnetic field to achieve the desired shape [49, 172] (Figure 7.b [172]). Moreover, temperature-responsive SMP scaffolds have been 3D printed to investigate their biomechanical compatibility [324, 337-341]. The piezoelectric properties of certain smart materials have also been investigated for their potential to stimulate osteoblast growth [342].

Advancements in 4D bioprinting have allowed for the incorporation of living cells into the fabrication process, creating dynamic and biocompatible structures. A

hydrogel-based scaffold 4D printed from PEG, alginate, gelatin, and MSCs showed reversible shape morphing behavior and biocompatibility, demonstrating promise for enhanced osseointegration [343].

Turning our attention to cartilage tissue engineering, a plethora of polymers including nanocellulose, alginate, and PU have been employed in various AM techniques, such as SLS and ink-jet bioprinting [344-347]. The use of chondrocytes, which are pivotal for cartilage regeneration, has been notably widespread [351]. A case study involving the 4D bioprinting of a cartilage scaffold demonstrated promising chondrogenesis responses, facilitated by the scaffold's high degree of shape morphing [15] (Figure 7.c). To induce a shape-morphing behavior in the scaffolds, they were fabricated based on dual-layer hydrogels, in which one layer had a lower swelling ratio than the other.

5.5.6.2 Muscle tissues

The intricate nature of skeletal muscle tissues, characterized by their unique anisotropic structures known as myofibers, necessitates advanced techniques for successful tissue engineering [348, 349]. This anisotropy is vital for muscle functionality as it modulates force transmission and regulates muscle contraction [348]. The primary aim in skeletal muscle tissue engineering is the fabrication of scaffolds that not only mimic the anisotropic properties of native tissue but also guide cellular processes, such as proliferation, differentiation, and maturation [249].

Magnetic-based 4D bioprinting has emerged as a sophisticated technique to achieve the desired anisotropic cellular orientation. The strategy involves the utilization of magnetic fields to align collagen fibers at the nanoscale within an agarose-collagen-based hydrogel [40]. In this method, iron nanoparticles are incorporated into the printable hydrogel. When exposed to a magnetic field, these nanoparticles move unidirectionally, forcing the collagen fibers to orient themselves in parallel arrangements. This magnetic field-assisted alignment is a transformative step towards achieving anisotropic scaffolds that closely mimic native skeletal muscle tissue.

Moreover, the layer-by-layer nature of AM processes has been exploited to contribute to the anisotropic orientation of scaffolds. Termed the "staircase effect," this phenomenon can be observed in FDM 3D printing [349]. By combining this staircase effect with subsequent coating techniques, one can achieve shape-specific 4D-printed scaffolds featuring anisotropic properties [349] (Figure 7.d).

5.5.6.3 Wound closure

Trauma-induced organ damage necessitates rapid and effective intervention, with challenges extending to fractures, nerve damage, and other forms of skeletal and soft tissue injuries [350]. In this context, 4D printing has emerged as a transformative technology with significant therapeutic implications. For instance, wound closure – a

relatively emergent application of 4D printing – has demonstrated multi-faceted functionalities, including SME, self-responsiveness, and reversibility [196, 351-353]. Specific cases include the fabrication of multi-responsive SMP-based materials using SLA for nerve repair (Figure 6.c) [353]. Comprising a unique blend of graphene-mixed soybean oil epoxidized acrylate (SOEA), these materials have displayed outstanding physical and chemical signaling properties, further supplemented by electrical conductivity, thereby promoting enhanced nerve regeneration [302].

The use of 3D/4D printing in the preparation of wound dressings marks a significant stride in medical technology. Customized dressings can be produced to fit wounds of diverse shapes, which contributes to accelerated wound healing [354]. Furthermore, these technologies eliminate the need for additional manufacturing resources, thereby generating cost-effective solutions with improved efficacy. In this regard, 3D/4D printed dressings have showcased versatility, incorporating innovative designs, such as porous structures embedded with bacteriophage for sustained release [355] or scaffolds that facilitate continuous exosomes release [356], thereby stimulating cellular repair mechanisms.

One of the important features of 4D printing is its ability to create intricate 3D structures using spatially distributed materials. However, high-fidelity bioprinting cannot yet achieve the functional characteristics of the natural tissue. As such, there is a growing emphasis on the integration of bioactive compounds into biologically functional inks [196, 351-353]. This seeks to ensure the bio-functional relevance of the printed structures in addition to their morphological accuracy.

Another paradigm-shifting innovation is the use of hydrogel-based smart bio-adhesives for sutureless wound closure [350, 357, 358]. These materials possess the capability to adhere to damaged tissue and facilitate wound closure with significantly reduced pain and scarring compared to conventional methods such as sutures and staples. However, a key parameter requiring attention is the temporal span between wound closure and complete healing. To address this, recent studies have introduced hydrogel-based bio-adhesives [350] and hydrogel-forming double-layered adhesive MN patches [359]. These innovations not only demonstrate the capability for efficient wound closure but also present an avenue for post-wound closure care, thereby enhancing the healing process.

5.5.6.4 Other tissues

The domain of nerve tissue engineering has been significantly enriched by the advent of 4D bioprinting technologies. These methods offer the capacity to precisely control the anisotropic orientation of nerve fibers, which is a crucial determinant of functional nerve tissue. Various AM techniques, including SLA, FDM, and inkjet printing, have been harnessed for this purpose [345].

Polymeric substrates, such as collagen, fibrin, PLA, gellan, carboxymethyl chitosan, gelatin methacryloyl (GelMA), PU, and PEGDA, serve as base materials for fabricating various nerve constructs [345, 360]. For instance, a bilayer scaffold was engineered with a combination of aligned PCL and poly(glycerol sebacate), along with randomly aligned hyaluronic acid methacrylate fibers [361]. This construct underwent biological assays involving the culture of PC-12 neuron cells, substantiating its potential for nerve regeneration [361]. A similar milestone was achieved through SLA-based 4D printing of a soft scaffold, characterized by its capacity to integrate seamlessly into void or damaged zones without imposing deformative stress on surrounding tissues. *In vivo* evaluation indicated neovascularization over a two-month cell culture period [362].

Among the recent innovations, the incorporation of electro-responsive biomaterials (*e.g.*, multi-responsive graphene hybrid structures) has opened new avenues in nerve tissue regeneration [353]. These structures offer a lot of benefits: physical guidance, chemical cues, and seamless integration. Given the inherent anisotropic behavior of nerve cells, the orientation of cellular components during the bioprinting process becomes a focal point of consideration [353]. 3D bioprinting has emerged as a robust strategy to mitigate this constraint, enabling the deposition of cells in diverse orientations [345, 363].

Combining 3D/4D printing with other fabrication methods such as electrospinning can further enhance the quality of nerve tissue constructs. For instance, PEGDA scaffolds have been printed on electrospun PCL or PCL/gelatin fibers to enhance nerve tissue properties [364]. An overview of the 4D bioprinting of tissue-engineered constructs is represented in Figure 8 and Table 1.

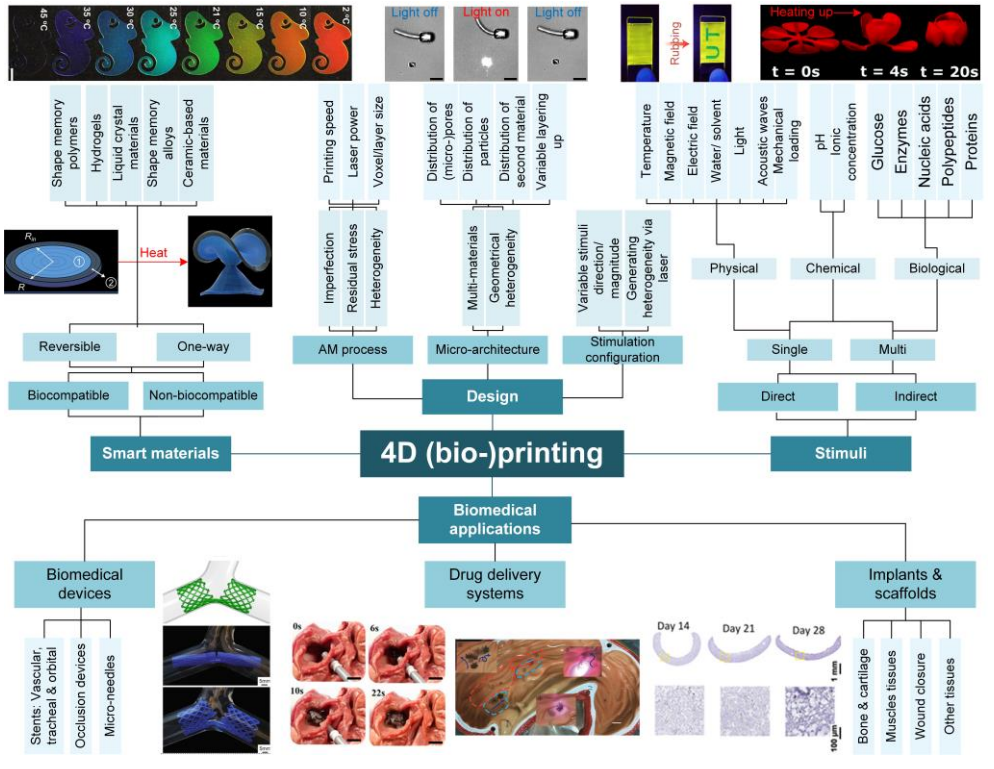

Figure 8. *An overview of the 4D bioprinting of tissue-engineered constructs. The sub-figures are derived from the following references, from top to bottom and left to right: Reproduced with permission [172]. Copyright 2022, Elsevier, [24] Reproduced with permission [225]. Copyright 2009, Springer Nature, [20,247,262], Reprinted with permission [53]. Copyright 2021, American Chemical Society, Reproduced with permission [321]. Copyright 2022, Elsevier [15].*

Table 1. *An overview of the 4D (bio)printing for biomedical applications.*

Method	Applications	Stimuli	3D printing Method	Materials [References]
Smart Materials	Stent	Heat	SLS	PCL [300]
			FDM	PLA [20, 281, 284, 290, 293, 376]
				PU-based SMP [294, 291, 305]
				FlexiFil [377]
				TangoBlackPlus™ & VeroWhitePlus™ [280]
			SLA	α,ω-polytetrahydrofuranether-diacrylate (PTHF-DA) resin [378]
				Methacrylate-based polymer [279, 297]
				Gelatin [294]
			DIW	Polyurethane diacrylate [283]
				PLMC [285]
				Epoxidized soybean oil [292]
				Alginate and hyaluronic acid [43]
				PLA-based nanocomposite [275]
				pNIPAM [282]
				PGDA [68]
				PU/hydroxyapatite/gold nanoparticles [302]
		Magnetic	FDM	PLA/Fe3O4 [295]
			DIW	PLA-based nanocomposite [275]
		Water	DIW	Zein [282]
		Ion		AAm-AAc/CNC [266]
	Occluder	Heat	FDM	PU composite [305]
		Magnetic		PLA/Fe_3O_4 [52, 53]
	Microneedle	-	custom SLA	PEGDA [314]
	Wound closure	Heat	SLA	SOEA [353]
	Drug delivery systems	Heat and magnetic	Custom SLA	pNIPAM/NdFeB [321]
	Scaffold	Heat	-	SMP [341]
			SLA	SOEA [324]
			FDM	PLA [337, 338, 379]
				PU [322]
			DLP and SLA	Acrylate PEG [380]
				SOEA [325, 353]
			Extrusion	PU [326]
		Magnetic	FDM	PLA/Fe_3O_4 [54, 295]
		Light	DIW	PU [326]
		Water	DIW	hyaluronan and alginate [15]
Rational Design	Implant	Mechanical	FDM	PLA [271]

5.6 Discussion and future perspectives

The controllability, repeatability, and reproducibility of 3D printing techniques have been extensively studied. There is, however, a lack of concrete evidence on how 4D bioprinting can contribute to the treatment of various conditions particularly considering the potential mechanobiological implications. Furthermore, the available studies on 4D printed biomedical devices are mostly limited to conceptual designs or proof-of-concept studies and need to be further analyzed *in vitro* or *in vivo*. We, therefore, believe that future studies should focus on the following avenues to advance the state-of-the-art in this exciting area of research.

Fabricating complex structures, such as irregular doubly-curved and inflatable surfaces using custom-built four-axis 3D printers [365, 366] or five-axis 3D printers [367-369] is an area that may further improve the available 4D (bio-) printing technologies. That is because curved-layer manufacturing techniques allow for non-planar lattice shells to be 3D printed, even using three-axis 3D printers. In this method, different non-planar structures can be 3D printed on Bézier surfaces (*i.e.,* a set of control points in space that create smooth curves and surfaces) by using a reusable mandrel [370, 371]. We, therefore, believe that the concept of 4D printing using four or five-axis AM may lead to the production of smart biomedical devices with complex shapes. For example, orthopedic braces with complex geometries can be 4D printed from smart materials so as to allow for remote control of their shape upon application of various stimuli. As a related example, a customized silicone aortic heart valve has been recently fabricated using a custom-built non-planar 3D printer with a flexible degree of freedom [372].

Most studies related to 4D printing have investigated the irreversible behavior of 4D printed structures, particularly the temperature-responsive ones. However, the reversibility and reliability under cyclic loading are highly important factors that need to be considered. For example, a transcatheter 4D-printed aortic valve needs to be reversible and operate cyclically. In soft robotics for biomedical applications, multiple opening and closing cycles of a soft gripper are required to manipulate an object. Therefore, 4D printed structures with two-way behavior may be a solution to these challenges.

So far, the 4D printing of biomedical devices has been mainly limited to conceptual and proof-of-concept studies. For example, a magneto-responsive 4D printed implant was fabricated as a bone repair tool [172], which can be tested *in vivo* (or *in vitro*) in the future. Moreover, AM techniques can be an alternative to conventional techniques for making biomedical devices featuring dynamic behavior (*e.g.,* an SMP-based ureteral stent [373]).

Cell mechanobiology and cell responses in 4D bioprinted-medical devices have not been thoroughly studied yet. Therefore, the response of cells to external stimuli and the

recovery of 4D printed biomedical devices are areas that can benefit from further studies. Moreover, the interaction between external stimuli (*e.g.,* heat or magnetic field) and the body's immune systems is crucial. For instance, when a 4D printed stent is implemented in the body, it should be possible to activate it at temperatures close to those of the human body.

In the context of wound healing applications, 4D printing technology has the potential to create smart wound healing patches and bandages that can dynamically adjust their shape to conform to the wound [315]. This system also has the potential to function as a drug delivery mechanism, releasing medications directly into the wound in addition to adapting its shape. The same concept can be extended to internal sutures within the body. A promising future direction in 4D printing involves the development of self-folding protein-based structures and capsules with self-adjusting drug release profiles.

Multi-material 3D printing has the potential to enhance 4D printing technologies. By using multi-material 3D printing, the deposition of different material phases in the 3D space can be controlled to induce non-affine deformations [374], enable advanced functionalities (*e.g.,* complex shape-morphing), and unique properties (*e.g.,* those found in functionally graded composites [375]).

To create biomedical devices at the microscale, further studies are required to explore advanced AM techniques and stimulation mechanisms. For example, to produce wireless micro-robots for use in drug delivery systems, the manufacturing process, remote actuation mechanism, response time (fast or slow), and energy efficiency need to be further optimized.

The design strategy of 4D bioprinted devices may require a combination of machine learning techniques and multi-physics *in silico* models. The effects of geometrical designs, external stimuli, and mechanical loading in conjunction with cell interaction and tissue growth, while considering the body environment, must be analyzed first. Such models could predict and, thus, improve the interactions of 4D printed medical devices with the human body. Specifically, there is a growing demand for the development of an inverse design approach capable of forecasting the optimal input parameters (*i.e.,* material, geometrical properties, AM parameters and stimulation factors) to achieve any desired function or shape transformation. Furthermore, most existing computational models in 4D printing are stationary (only predicting the final shape or state only). Therefore, there is ample opportunity for enhancement by introducing more dynamic models that can predict both the function and shape morphing at any given moment. This holds particular significance in drug delivery systems, where precise control of drug-release rates is of particular importance.

To gain a deeper comprehension of the process-structure-property (*e.g.,* external stimuli parameters, and rheological properties) and to develop a robust computational platform, more experiments focused on the characterization of 4D printed materials are required under coupled mechanical loading, such as torsion-extension loading or coupled multi-physics conditions, such as magneto-mechanical loading. In this context, measurement monitoring systems of 4D printable materials (*e.g.,* LCEs [100]) are highly recommended. Moreover, mechanical strength, such as fatigue life and longevity of 4D printable biomaterials, need to be further investigated particularly in the context of implantable medical devices.

Finally, the environmental impact of 4D bioprinting technologies has not been adequately assessed and, thus, represents an underexplored domain that requires further explorations and attentions. As 4D bioprinting proliferates within the medical sector, considerations of sustainability, biodegradability, and ecological footprint become indispensable. Investigations into utilizing biocompatible and biodegradable materials could serve as a next step towards achieving environmental sustainability while maintaining medical efficacy.

Moreover, the ethical and regulatory paradigms governing 4D bioprinting are yet to be fully articulated. As this technology transitions from a developing stage to widespread clinical applications, a comprehensive framework that addresses ethical considerations, quality assurance, and safety protocols becomes imperative. Instituting such a framework would not only assure ethical integrity but would also optimize the translational potential of 4D bioprinting technologies.

5.7 Conclusion

4D (bio)printing transforms time-independent 3D printed structures into dynamic and time-dependent ones and offers the ability to program various shape morphing behaviors into biomaterials, bioprinted tissues/organs, and (implantable) medical devices. This enables precise control over shape, function, cell response, and the formation of new tissue over time. Triggered by external stimuli and shape memory effect, 4D bioprinting offers unique and promising features in regenerative medicine and organ transplantation research. These unique behaviors stem from the intrinsic properties of stimuli-responsive materials used in 4D printing. To integrate 4D bioprinting into clinical applications, four vital criteria must be met: *i.* the use of a suitable stimuli-responsive biomaterial, *ii.* the application of an effective and safe external stimulus, *iii.* the adaptation of a rational design strategy to achieve a desired shape morphing, and *iv.* the employment of an effective AM technique. These criteria empower 4D printing as a groundbreaking technology for creating next-generation biomedical devices with unique combination of characteristics, including minimal invasiveness, remote control, and adaptability to the changing dynamics of the body's environment. However, it is essential to acknowledge that 4D printing in biomedicine is still in its early stages.

Indeed, further proof-of-concept (*ex vivo* and *in vitro*) and preclinical studies (*in vivo*) are required in the future to elucidate the interrelationships of the shape morphing behavior and biological functions, for example, within the context of mechanobiology. In the context of drug delivery systems, which requires small-scale 4D printed systems, more studies are required at the microscale to demonstrate high precision remote control. Moreover, for biomedical devices capable of reversibly switching between permanent and temporary shapes without energy loss, the sustainability of 4D printed structures needs to be further improved. We hope that this critical and comprehensive review article serves as a guide for biomedical engineers and scientists engaged in the development of smart biomedical devices.

Bibliography

[1] J. S. Cuellar, G. Smit, D. Plettenburg, A. Zadpoor, Additive Manufacturing 21 (2018) 150.
[2] A. Azarniya, X. G. Colera, M. J. Mirzaali, S. Sovizi, F. Bartolomeu, M. K. S. Weglowski, W. W. Wits, C. Y. Yap, J. Ahn, G. Miranda, F. S. Silva, H. R. Madaah Hosseini, S. Ramakrishna, A. A. Zadpoor, Journal of Alloys and Compounds 804 (2019) 163.
[3] M. J. Mirzaali, A. Azarniya, S. Sovizi, J. Zhou, A. A. Zadpoor, in Fundamentals of Laser Powder Bed Fusion of Metals, (Eds: I. Yadroitsev, I. Yadroitsava, A. du Plessis, E. MacDonald), Elsevier, Oxford 2021, pp. 423–465.
[4] M. J. Mirzaali, V. Moosabeiki, S. M. Rajaai, J. Zhou, A. A. Zadpoor, Materials 15 (2022) 5457.
[5] M. J. Mirzaali, N. Shahriari, J. Zhou, A. A. Zadpoor, in Quality Analysis of Additively Manufactured Metals, (Eds: J. Kadkhodapour, S. Schmauder, F. Sajadi), Elsevier, Oxford 2023, pp. 689–743.
[6] E. Yarali, M. Baniasadi, A. Zolfagharian, M. Chavoshi, F. Arefi, M. Hossain, A. Bastola, M. Ansari, A. Foyouzat, A. Dabbagh, Applied Materials Today 26 (2022) 101306.
[7] P. Fu, H. Li, J. Gong, Z. Fan, A. T. Smith, K. Shen, T. O. Khalfalla, H. Huang, X. Qian, J. McCutcheon, Progress in Polymer Science 126 (2022) 101506.
[8] D.-G. Shin, T.-H. Kim, D.-E. Kim, International Journal of Precision Engineering and Manufacturing-Green Technology 4 (2017) 349.
[9] X. Liu, M. Wei, Q. Wang, Y. Tian, J. Han, H. Gu, H. Ding, Q. Chen, K. Zhou, Z. Gu, Advanced Materials 33 (2021) 2100332.
[10] B. Peng, Y. Yang, T. Ju, ACS Applied Materials and Interfaces 13 (2020) 12777.
[11] S.-D. Wu, S. Hsu, Biofabrication 13 (2021) 045029.
[12] C. Yuan, F. Wang, Q. Ge, Extreme Mechanics Letters 42 (2021) 101122.
[13] C. Xin, D. Jin, R. Li, D. Wang, Z. Ren, B. Liu, C. Chen, L. Li, S. Liu, B. Xu, Y. Zhang, Y. Hu, J. Li, L. Zhang, D. Wu, J. Chu, Small 18 (2022) 2202272.
[14] X. Wan, Y. He, Y. Liu, J. Leng, Additive Manufacturing 53 (2022) 102689.
[15] P. J. Díaz-Payno, M. Kalogeropoulou, I. Muntz, E. Kingma, N. Kops, M. D'Este, G. H. Koenderink, L. E. Fratila-Apachitei, G. J. van Osch, A. Zadpoor, Advanced Healthcare Materials 12 (2022) 2201891.
[16] E. Pei, G. H. Loh, Progress in Additive Manufacturing 3 (2018) 95.
[17] C. A. Spiegel, M. Hippler, A. Münchinger, M. Bastmeyer, C. Barner-Kowollik, M. Wegener, E. Blasco, Advanced Functional Materials 30 (2019) 1907615.
[18] M. Hippler, K. Weißenbruch, K. Richler, E. D. Lemma, M. Nakahata, B. Richter, C. Barner-Kowollik, Y. Takashima, A. Harada, E. Blasco, Science Advances 6 (2020) eabc2648.
[19] C. A. Spiegel, M. Hackner, V. P. Bothe, J. P. Spatz, E. Blasco, Advanced Functional Materials 32 (2022) 2110580.
[20] T. van Manen, S. Janbaz, K. M. Jansen, A. Zadpoor, Communications Materials 2 (2021) 56.
[21] S. Lantean, G. Barrera, C. F. Pirri, P. Tiberto, M. Sangermano, I. Roppolo, G. Rizza, Advanced Materials Technologies 4 (2019) 1900505.
[22] B. Zhang, H. Li, J. Cheng, H. Ye, A. H. Sakhaei, C. Yuan, P. Rao, Y. F. Zhang, Z. Chen, R. Wang, Advanced Materials 33 (2021) 2101298.
[23] Y. Jia, C. A. Spiegel, A. Welle, S. Heißler, E. Sedghamiz, M. Liu, W. Wenzel, M. Hackner, J. P. Spatz, M. Tsotsalas, E. Blasco, Advanced Functional Materials 33 (2023) 2207826.
[24] M. Hippler, E. Blasco, J. Qu, M. Tanaka, C. Barner-Kowollik, M. Wegener, M. Bastmeyer, Nature Communications 10 (2019) 232.
[25] H. Ouyang, X. Li, X. Lu, H. Xia, ACS Applied Polymer Materials 4 (2022) 4035.
[26] D. Abolhasani, S. W. Han, C. J. VanTyne, N. Kang, Y. H. Moon, Journal of Alloys and Compounds 922 (2022) 166228.
[27] Z. Liu, M. Li, X. Dong, Z. Ren, W. Hu, M. Sitti, Nature Communications 13 (2022) 2016.
[28] B. Q. Y. Chan, Y. T. Chong, S. Wang, C. J. J. Lee, C. Owh, F. Wang, F. Wang, Chemical Engineering Journal 430 (2022) 132513.
[29] T. van Manen, S. Janbaz, M. Ganjian, A. A. Zadpoor, Materials Today 32 (2020) 59.

[30] S. Janbaz, N. Noordzij, D. S. Widyaratih, C. W. Hagen, L. E. Fratila-Apachitei, A. A. Zadpoor, Science Advances 3 (2017) eaao1595.
[31] J. Li, X. Zhang, S. An, Z. Zhu, Z. Deng, Z. You, International Journal of Solids and Structures 244 (2022) 111587.
[32] C. M. Wintersinger, D. Minev, A. Ershova, H. M. Sasaki, G. Gowri, J. F. Berengut, F. E. Corea-Dilbert, P. Yin, W. M. Shih, Nature Nanotechnology 18 (2023) 281.
[33] Y. Wang, H. Cui, T. Esworthy, D. Mei, Y. Wang, L. G. J. Zhang, Advanced Materials 34 (2022) 2109198.
[34] B. Gao, Q. Yang, X. Zhao, G. Jin, Y. Ma, F. Xu, Trends in Biotechnology 34 (2016) 746.
[35] W. Zhu, T. J. Webster, L. G. Zhang, Nanomedicine 14 (2019) 1643.
[36] A. Subash, B. Kandasubramanian, European Polymer Journal 134 (2020) 109771.
[37] M. Y. Khalid, Z. U. Arif, R. Noroozi, A. Zolfagharian, M. Bodaghi, Journal of Manufacturing Processes 81 (2022) 759.
[38] J. M. Zelis, R. Meiburg, J. J. Roijen, K. L. Janssens, M. van't Veer, N. H. Pijls, N. P. Johnson, F. N. van de Vosse, P. A. Tonino, M. C. Rutten, International Journal of Cardiology 313 (2020) 32.
[39] C. Deng, Y. Liu, X. Fan, B. Jiao, Z. Zhang, M. Zhang, F. Chen, H. Gao, L. Deng, W. Xiong, Advanced Functional Materials 33 (2023) 2211473.
[40] M. Betsch, C. Cristian, Y. Y. Lin, A. Blaeser, J. Schöneberg, M. Vogt, E. M. Buhl, H. Fischer, D. F. Duarte Campos, Advanced Healthcare Materials 7 (2018) 1800894.
[41] Y. Xia, Y. He, F. Zhang, Y. Liu, J. Leng, Advanced Materials 33 (2021) 2000713.
[42] Y. Tang, M. Li, T. Wang, X. Dong, W. Hu, M. Sitti, Advanced Materials 34 (2022) 2204185.
[43] A. Kirillova, R. Maxson, G. Stoychev, C. T. Gomillion, L. Ionov, Advanced Materials 29 (2017) 1703443.
[44] T. Uchida, H. Onoe, Micromachines 10 (2019) 433.
[45] Y. Dong, S. Wang, Y. Ke, L. Ding, X. Zeng, S. Magdassi, Y. Long, Advanced Materials Technologies 5 (2020) 2000034.
[46] M. Behl, M. Y. Razzaq, A. Lendlein, Advanced Materials 22 (2010) 3388.
[47] S. Nam, E. Pei, Progress in Additive Manufacturing 4 (2019) 167.
[48] J. Delaey, P. Dubruel, S. Van Vlierberghe, Advanced Functional Materials 30 (2020) 1909047.
[49] W. Zhou, X. Dong, Y. He, W. Zheng, J. Leng, Smart Materials and Structures 31 (2022) 105002.
[50] A. Melocchi, M. Uboldi, N. Inverardi, F. Briatico-Vangosa, F. Baldi, S. Pandini, G. Scalet, F. Auricchio, M. Cerea, A. Foppoli, A. Maroni, L. Zema, A. Gazzaniga, International Journal of Pharmaceutics 571 (2019) 118700.
[51] M. Baniasadi, E. Yarali, A. Foyouzat, M. S. Baghani, European Journal of Mechanics - A/Solids 85 (2021) 104093.
[52] C. Lin, J. Lv, Y. Li, F. Zhang, J. Li, Y. Liu, L. Liu, J. Leng, Advanced Functional Materials 29 (2019) 1906569.
[53] C. Lin, L. Liu, Y. Liu, J. Leng, ACS Applied Materials & Interfaces 13 (2021) 12668.
[54] W. Zhao, Z. Huang, L. Liu, W. Wang, J. Leng, Y. J. C. S. Liu, Composites Science and Technology 203 (2021) 108563.
[55] Q. Li, M. Yang, X. Sun, Q. Wang, B. Yu, A. Gong, F. Du, Materials Today Bio 19 (2023) 100566.
[56] Z. Li, Z. Chen, Y. Gao, Y. Xing, Y. Zhou, Y. Luo, W. Xu, Z. Chen, X. Gao, K. J. B. Gupta, Biomaterials 283 (2022) 121426.
[57] N. Roudbarian, M. Baniasadi, P. Nayyeri, M. Ansari, R. Hedayati, M. Baghani, Smart Materials and Structures 30 (2021) 105006.
[58] J. Hu, Y. Zhu, H. Huang, J. Lu, Progress in Polymer Science 37 (2012) 1720.
[59] J. Wu, C. Yuan, Z. Ding, M. Isakov, Y. Mao, T. Wang, M. L. Dunn, H. Qi, Scientific Reports 6 (2016) 24224.
[60] A. Lendlein, S. Kelch, Angewandte Chemie International Edition 41 (2002) 2034.
[61] S. Y. Leo, W. Zhang, Y. Zhang, Y. Ni, H. Jiang, C. Jones, P. Jiang, V. Basile, C. Taylor, Small 14 (2018) 1703515.

[62] M. Martina, D. W. Hutmacher, Polymer International 56 (2007) 145.
[63] M. J.-L. Tschan, E. Brulé, P. Haquette, C. M. Thomas, Polymer Chemistry 3 (2012) 836.
[64] D. Moura, R. F. Pereira, I. C. Gonçalves, Materials Today Chemistry 23 (2022) 100617.
[65] H. Ramaraju, R. E. Akman, D. L. Safranski, S. J. Hollister, Advanced Functional Materials 30 (2020) 2002014.
[66] S. Erkeçoğlu, A. D. Sezer, S. Bucak, Smart Drug Delivery System, InTech, TX, USA (2016).
[67] B. C. Kholkhoev, K. N. Bardakova, E. O. Epifanov, Z. A. Matveev, T. A. Shalygina, E. B. Atutov, S. Y. Voronina, P. S. Timashev, V. F. Burdukovskii, Chemical Engineering Journal 454 (2022) 140423.
[68] C. Zhang, D. Cai, P. Liao, J.-W. Su, H. Deng, B. Vardhanabhuti, B. D. Ulery, S.-Y. Chen, J. Lin, Acta Biomaterialia 122 (2021) 101.
[69] H. Wu, P. Chen, C. Yan, C. Cai, Y. Shi, Materials & Design 171 (2019) 107704.
[70] C.-Y. Cheng, H. Xie, Z.-y. Xu, L. Li, M.-N. Jiang, L. Tang, K.-K. Yang, Y.-Z. Wang, Chemical Engineering Journal 396 (2020) 125242.
[71] A. Cortés, A. Cosola, M. Sangermano, M. Campo, S. González Prolongo, C. F. Pirri, A. Jiménez-Suárez, A. Chiappone, Advanced Functional Materials 31 (2021) 2106774.
[72] D. Fan, U. Staufer, A. Accardo, Bioengineering 6 (2019) 113.
[73] K. Varaprasad, C. Karthikeyan, M. M. Yallapu, R. Sadiku, International Journal of Biological Macromolecules 212 (2022) 561.
[74] Y. Hu, Z. Wang, D. Jin, C. Zhang, R. Sun, Z. Li, K. Hu, J. Ni, Z. Cai, D. Pan, Advanced Functional Materials 30 (2020) 1907377.
[75] J. Li, C. Wu, P. K. Chu, M. Gelinsky, Materials Science and Engineering: R: Reports 140 (2020) 100543.
[76] Z. Ataie, S. Kheirabadi, J. W. Zhang, A. Kedzierski, C. Petrosky, R. Jiang, C. Vollberg, A. Sheikhi, Small 18 (2022) 2202390.
[77] J. R. Dias, N. Ribeiro, S. Baptista-Silva, A. R. Costa-Pinto, N. Alves, A. L. Oliveira, Frontiers in Bioengineering and Biotechnology 8 (2020) 85.
[78] B. Liu, B. Dong, C. Xin, C. Chen, L. Zhang, D. Wang, Y. Hu, J. Li, L. Zhang, D. Wu, Small 19 (2023) 2204630.
[79] R. Suntornnond, W. L. Ng, X. Huang, C. H. E. Yeow, W. Y. Yeong, Journal of Materials Chemistry B 10 (2022) 5989.
[80] C. Cheng, Y. J. Moon, S. H. Kim, Y.-C. Jeong, J. Y. Hwang, G. T.-C. Chiu, B. Han, International Journal of Heat and Mass Transfer 150 (2020) 119327.
[81] Y. Wang, N. Alizadeh, M. Barde, M. L. Auad, B. S. Beckingham, ACS Applied Polymer Materials 4 (2022) 971.
[82] S. Naficy, R. Gately, R. Gorkin III, H. Xin, G. M. Spinks, Macromolecular Materials and Engineering 302 (2017) 1600212.
[83] A. S. Gladman, E. A. Matsumoto, R. G. Nuzzo, L. Mahadevan, J. A. Lewis, Nature Materials 15 (2016) 413.
[84] J. Lai, X. Ye, J. Liu, C. Wang, J. Li, X. Wang, M. Ma, M. Wang, Materials & Design 205 (2021) 109699.
[85] J. Qu, X. Zhao, P. X. Ma, B. Guo, Acta Biomaterialia 72 (2018) 55.
[86] Z. Shi, X. Gao, M. W. Ullah, S. Li, Q. Wang, G. Yang, Biomaterials 111 (2016) 40.
[87] M.-Y. Choi, Y. Shin, H. S. Lee, S. Y. Kim, J.-H. Na, Scientific Reports 10 (2020) 2482.
[88] D. Qureshi, S. K. Nayak, S. Maji, A. Anis, D. Kim, K. Pal, European Polymer Journal 120 (2019) 109220.
[89] H. Banerjee, M. Suhail, H. Ren, Biomimetics 3 (2018) 15.
[90] Y. S. Zhang, A. Khademhosseini, Science 356 (2017) eaaf3627.
[91] S. J. Woltman, G. D. Jay, G. P. Crawford, Nature Materials 6 (2007) 929.
[92] S. Mayer, R. Zentel, Materials Science 6 (2002) 545.
[93] A. Akram, T. G. Shahzady, S. Hussain, N. A. Saad, M. T. Islam, M. Ikram, Russian Journal of Applied Chemistry 94 (2021) 1585.
[94] K. M. Herbert, H. E. Fowler, J. M. McCracken, K. R. Schlafmann, J. A. Koch, T. J. White, Nature Reviews Materials 7 (2022) 23.

[95] X. Peng, S. Wu, X. Sun, L. Yue, S. M. Montgomery, F. Demoly, K. Zhou, R. R. Zhao, H. J. Qi, Advanced Materials 34 (2022) 2204890.
[96] A. Kotikian, R. L. Truby, J. W. Boley, T. J. White, J. A. Lewis, Advanced Materials 30 (2018) 1706164.
[97] M. Del Pozo, J. A. Sol, A. P. Schenning, M. G. Debije, Advanced Materials 34 (2022) 2104390.
[98] Q. Yang, H. Shahsavan, Z. Deng, H. Guo, H. Zhang, H. Liu, C. Zhang, A. Priimagi, X. Zhang, H. Zeng, Advanced Functional Materials 32 (2022) 2206939.
[99] D. Sun, J. Zhang, H. Li, Z. Shi, Q. Meng, S. Liu, J. Chen, X. Liu, Polymers 13 (2021) 1889.
[100] M. Chen, M. Gao, L. Bai, H. Zheng, H. J. Qi, K. Zhou, Advanced Materials 35 (2023) 2209566.
[101] M. Tabrizi, T. H. Ware, M. R. Shankar, ACS Applied Materials & Interfaces 11 (2019) 28236.
[102] J. Sgotti Veiga, M. Reis Carneiro, R. Molter, M. Vinciguerra, L. Yao, C. Majidi, M. Tavakoli, Advanced Materials Technologies 8 (2023) 2300144.
[103] S. Li, Z. Song, Y. Fan, D. Wei, Y. Liu, Biomimetics 8 (2023) 196.
[104] M. R. Vinciguerra, D. K. Patel, W. Zu, M. Tavakoli, C. Majidi, L. Yao, ACS Applied Materials & Interfaces 15 (2023) 24777.
[105] J. S. Veiga, M. R. Carneiro, R. Molter, M. Vinciguerra, L. Yao, C. Majidi, M. Tavakoli, Advanced Materials Technologies 8 (2023) 2300144.
[106] A. Y. Lee, J. An, C. K. Chua, Engineering 3 (2017) 663.
[107] H. Lu, C. Yang, X. Luo, H. Ma, B. Song, Y. Li, L. Zhang, Materials Science and Engineering A 763 (2019) 138166.
[108] M. P. Caputo, A. E. Berkowitz, A. Armstrong, P. Müllner, C. V. Solomon, Additive Manufacturing 21 (2018) 579.
[109] I. Shishkovsky, V. Scherbakov, Proceedings of SPIE 10523 (2018) 1052311.
[110] C. Wang, X. Tan, Z. Du, S. Chandra, Z. Sun, C. Lim, S. B. Tor, C. S. Lim, C. H. Wong, Journal of Materials Processing Technology 271 (2019) 152.
[111] K. Lu, W. T. Reynolds, Powder Technology 187 (2008) 11.
[112] S. Akbari, A. H. Sakhaei, S. Panjwani, K. Kowsari, A. Serjouei, Q. Ge, Sensors and Actuators A: Physical 290 (2019) 177.
[113] A. N. Alagha, S. Hussain, W. Zaki, Materials & Design 204 (2021) 109654.
[114] S. Saedi, A. S. Turabi, M. Taheri Andani, C. Haberland, H. Karaca, M. Elahinia, Journal of Alloys and Compounds 677 (2016) 204.
[115] S. Gao, F. Weng, O. P. Bodunde, M. Qin, W.-H. Liao, P. Guo, Journal of Manufacturing Processes 71 (2021) 417.
[116] J. Otubo, O. D. Rigo, C. M. Neto, P. R. Mei, Materials Science and Engineering A 438 (2006) 679.
[117] A. Mostafaei, K. A. Kimes, E. L. Stevens, J. Toman, Y. L. Krimer, K. Ullakko, M. Chmielus, Acta Materialia 131 (2017) 482.
[118] M. Nachimuthu, R. P. K., Rapid Prototyping Journal 29 (2023) 437.
[119] K. Sun, X. Meng, Z. Gao, W. Cai, Shape Memory and Superelasticity 9 (2023) 252.
[120] F. Wang, C. Liu, H. Yang, H. Wang, H. Zhang, X. Zeng, C. Wang, W. Zhang, W. Lv, P. Zhu, Additive Manufacturing 63 (2023) 103411.
[121] A. Lai, C. A. Schuh, Physical Review Letters 126 (2021) 015701.
[122] A. Lai, Z. Du, C. L. Gan, C. A. Schuh, Science 341 (2013) 1505.
[123] M. Yarahmadi, P. Barcelona, G. Fargas, E. Xuriguera, J. J. Roa, Ceramics International 48 (2022) 4775.
[124] I. Buj-Corral, J. A. Padilla, J. Minguella-Canela, L. Rodero, L. Marco, E. Xuriguera, Key Engineering Materials 958 (2023) 157.
[125] F. Wang, C. Liu, H. Yang, H. Wang, H. Zhang, X. Zeng, C. Wang, W. Zhang, W. Lv, P. Zhu, B. Li, Additive Manufacturing 63 (2023) 103411.
[126] F. L. Bargardi, H. Le Ferrand, R. Libanori, A. R. Studart, Nature Communications 7 (2016) 13912.
[127] S. Chen, J. Li, H. Shi, X. Chen, G. Liu, S. Meng, J. Lu, Chemical Engineering Journal 455 (2023) 140655.

[128] G. Liu, Y. Zhao, G. Wu, J. Lu, Science Advances 4 (2018) eaat0641.
[129] Y.-J. Kim, Y. T. Matsunaga, Journal of Materials Chemistry B 5 (2017) 4307.
[130] P. Zarrintaj, M. Jouyandeh, M. R. Ganjali, B. S. Hadavand, M. Mozafari, S. S. Sheiko, M. Vatankhah-Varnoosfaderani, T. J. Gutiérrez, M. R. Saeb, European Polymer Journal 117 (2019) 402.
[131] M. Liu, X. Song, Y. Wen, J.-L. Zhu, J. Li, ACS Applied Materials & Interfaces 9 (2017) 35673.
[132] M. Hippler, E. Blasco, J. Qu, M. Tanaka, C. Barner-Kowollik, M. Wegener, M. Bastmeyer, Nature Communications 10 (2019) 232.
[133] D. Zhang, J. Yang, C. Liu, S. Ye, Q. Zhang, R. Liu, International Journal of Nanomedicine (2021) 4901.
[134] A. T. Andrgie, H. F. Darge, T. W. Mekonnen, Y. S. Birhan, E. Y. Hanurry, H.-Y. Chou, C.-F. Wang, H.-C. Tsai, J. M. Yang, Y.-H. Chang, Polymers (2020) 12, 2619.
[135] H. Lu, M. Lei, C. Zhao, Y. Yao, J. Gou, D. Hui, Y. Q. Fu, Composites Part B (2015) 80, 37.
[136] H. Luo, Z. Li, G. Yi, X. Zu, H. Wang, H. Huang, Y. Wang, Z. Liang, S. Zhang, Materials Letters (2014) 137, 385.
[137] A. Chortos, E. Hajiesmaili, J. Morales, D. R. Clarke, J. A. Lewis, Advanced Functional Materials (2020) 30, 1907375.
[138] H. Cui, R. Hensleigh, D. Yao, D. Maurya, P. Kumar, M. G. Kang, S. Priya, X. R. Zheng, Nature Materials (2019) 18, 234.
[139] D. Kuscer, O. Noshchenko, H. Uršič, B. Malič, Journal of the American Ceramic Society (2013) 96, 2714.
[140] I. Kierzewski, S. S. Bedair, B. Hanrahan, H. Tsang, L. Hu, N. Lazarus, Additive Manufacturing (2020) 31, 100963.
[141] Y. A. O. Assagra, R. A. P. Altafim, R. A. C. Altafim, J. Carmo, Electronics Letters (2015) 51, 2028.
[142] A. M. Peterson, Additive Manufacturing (2019) 27, 363.
[143] S. J. Callens, D. Fan, I. A. van Hengel, M. Minneboo, L. E. Fratila-Apachitei, A. A. Zadpoor, Nature Communications (2020) 14, 855.
[144] A. A. Zadpoor, Materials Horizons (2016) 3, 371.
[145] H. M. A. Kolken, K. Lietaert, T. van der Sloten, B. Pouran, A. Meynen, G. Van Loock, H. Weinans, L. Scheys, A. A. Zadpoor, Journal of the Mechanical Behavior of Biomedical Materials (2020) 104, 103658.
[146] E. Hajiesmaili, N. M. Larson, J. A. Lewis, D. R. J. S. A. Clarke, Science Advances (2022) 8, eabn9198.
[147] M. Duduta, F. Berlinger, R. Nagpal, D. Clarke, R. Wood, F. Z. Temel, Smart Materials and Structures (2019) 28, 09LT01.
[148] H. Zhao, A. M. Hussain, M. Duduta, D. M. Vogt, R. J. Wood, D. R. Clarke, Advanced Functional Materials (2018) 28, 1804328.
[149] E. Hajiesmaili, E. Khare, A. Chortos, J. Lewis, D. R. Clarke, Extreme Mechanics Letters (2019) 30, 100504.
[150] S. Rosset, O. A. Araromi, S. Schlatter, H. R. Shea, Journal of Visualized Experiments (2016) 53423.
[151] Y. Chen, H. Zhao, J. Mao, P. Chirarattananon, E. F. Helbling, N. P. Hyun, D. R. Clarke, R. J. Wood, Nature (2019) 575, 324.
[152] M. Duduta, R. J. Wood, D. R. Clarke, Advanced Materials (2016) 28, 8058.
[153] L. Zhou, Q. Gao, J. Fu, Q. Chen, J. Zhu, Y. Sun, Y. He, ACS Applied Materials & Interfaces (2019) 11, 23573.
[154] J. Rossiter, P. Walters, B. Stoimenov, Electroactive Polymer Actuators and Devices (EAPAD) (2009) Proc. SPIE, Bellingham, WA, 72870H.
[155] A. Creegan, I. Anderson, Proc. SPIE (2014) 9056, 905629.
[156] D. McCoul, S. Rosset, S. Schlatter, H. Shea, Smart Materials and Structures (2017) 26, 125022.
[157] A. Chortos, J. Mao, J. Mueller, E. Hajiesmaili, J. A. Lewis, D. R. Clarke, Advanced Functional Materials (2021) 31, 2010643.
[158] J. Maas, D. Tepel, T. Hoffstadt, Meccanica (2015) 50, 2839.

[159] R. L. Truby, M. Wehner, A. K. Grosskopf, D. M. Vogt, S. G. Uzel, R. J. Wood, J. A. Lewis, Advanced Materials (2018) 30, 1706383.
[160] G. Haghiashtiani, E. Habtour, S.-H. Park, F. Gardea, M. C. McAlpine, Extreme Mechanics Letters (2018) 21, 1.
[161] A. H. Zamanian, D. A. Porter, P. Krueger, E. Richer, ASME 2018 Dynamic Systems and Control Conference, Atlanta, Georgia, USA, October 2018.
[162] J. J. Abbott, E. Diller, A. J. Petruska, Robotics and Autonomous Systems (2020) 3, 57.
[163] Y. Kim, X. Zhao, Chemical Reviews (2022) 122, 5317.
[164] Q. Ze, X. Kuang, S. Wu, J. Wong, S. M. Montgomery, R. Zhang, J. M. Kovitz, F. Yang, H. J. Qi, R. Zhao, Advanced Materials (2020) 32, 1906657.
[165] Y. Kim, H. Yuk, R. Zhao, S. A. Chester, X. Zhao, Nature (2018) 558, 274.
[166] S. Qi, J. Fu, Y. Xie, Y. Li, R. Gan, M. Yu, Composites Science and Technology (2019) 183, 107817.
[167] E. Yarali, M. A. Farajzadeh, R. Noroozi, A. Dabbagh, M. J. Khoshgoftar, M. Mirzaali, Composites Structures (2020) 254, 112881.
[168] J. Silva, C. Gouveia, G. Dinis, A. Pinto, A. Pereira, Composites Part B (2022) 243, 110125.
[169] A. Bastola, M. Paudel, L. Li, Journal of Magnetism and Magnetic Materials (2020) 494, 165825.
[170] Z. Wang, Y. Wu, D. Wu, D. Sun, L. Lin, Composites Part B (2022) 231, 109596.
[171] X. Ding, Y. Shi, S. Xu, Y. Zhang, J. Du, J. J. S. Qiu, Small (2023) 19, 2205797.
[172] J. Liao, C. Ye, J. Guo, C. E. Garciamendez-Mijares, P. Agrawal, X. Kuang, J. O. Japo, Z. Wang, X. Mu, W. Li, T. Ching, L. S. Mille, C. Zhu, X. Zhang, Z. Gu, Y. S. Zhang, Materials Today (2022) 56, 29.
[173] A. Lendlein, O. E. Gould, Nature Reviews Materials (2019) 4, 116.
[174] E. Yarali, A. Taheri, M. Baghani, Journal of Intelligent Material Systems and Structures (2020) 31, 1243.
[175] A. Bhargava, K. Peng, J. Stieg, R. Mirzaeifar, S. Shahab, RSC Advances 7 (2017) 45452.
[176] K. Yu, Y. Liu, J. Leng, RSC Advances 4 (2014) 2961.
[177] H. Deng, K. Sattari, Y. Xie, P. Liao, Z. Yan, J. Lin, Nature Communications 11 (2020) 6325.
[178] F. Zhang, L. Wang, Z. Zheng, Y. Liu, J. Leng, Composites Part A 125 (2019) 105571.
[179] S. R. Goudu, I. C. Yasa, X. Hu, H. Ceylan, W. Hu, M. Sitti, Advanced Functional Materials 30 (2020) 2004975.
[180] J. Zhang, R. H. Soon, Z. Wei, W. Hu, M. Sitti, Advanced Science 9 (2022) 2203730.
[181] P. Testa, R. W. Style, J. Z. Cui, C. Donnelly, E. Borisova, P. M. Derlet, E. R. Dufresne, L. J. Heyderman, Advanced Materials 31 (2019) 6.
[182] C. Zhang, X. Li, L. Jiang, D. Tang, H. Xu, P. Zhao, J. Fu, Q. Zhou, Y. Chen, Advanced Functional Materials 31 (2021) 2102777.
[183] M. Mazurek-Budzyńska, M. Y. Razzaq, M. Behl, A. Lendlein, in Functional Polymers, M. A. Jafar Mazumder, H. Sheardown, A. Al-Ahmed (Eds.), Springer International Publishing, Cham 2019, pp. 605–663.
[184] A. M. Schmidt, Macromolecular Rapid Communications 27 (2006) 1168.
[185] T. Pretsch, Polymers 2 (2010) 120.
[186] H. Lu, M. Lei, C. Zhao, B. Xu, J. Leng, Y. Q. Fu, Smart Materials and Structures 24 (2015) 045015.
[187] M. Curcio, U. Spizzirri, G. Cirillo, O. Vittorio, N. Picci, F. Nicoletta, F. Iemma, S. Hampel, RSC Advances 5 (2015) 44902.
[188] X. Shi, Y. Zheng, C. Wang, L. Yue, K. Qiao, G. Wang, L. Wang, H. Quan, RSC Advances 5 (2015) 41820.
[189] X. Wan, F. Zhang, Y. Liu, J. Leng, Carbon 155 (2019) 77.
[190] X. Dong, F. Zhang, L. Wang, Y. Liu, J. S. Leng, Composites Part A 157 (2022) 106925.
[191] D. Samanta, R. Mehrotra, K. Margulis, R. N. Zare, Nanoscale 9 (2017) 16429.
[192] K. M. Lichade, S. Shiravi, J. D. Finan, Y. Pan, Additive Manufacturing 104123 (2024).
[193] S. Tibbits, Architectural Design 84 (2014) 116.
[194] J. Yang, Y. Zheng, L. Sheng, H. Chen, L. Zhao, W. Yu, K.-Q. Zhao, P. Hu, Industrial & Engineering Chemistry Research 57 (2018) 15046.

[195] D. Raviv, W. Zhao, C. McKnelly, A. Papadopoulou, A. Kadambi, B. Shi, S. Hirsch, D. Dikovsky, M. Zyracki, C. Olguin, R. Raskar, S. Tibbits, Scientific Reports 4 (2014) 7422.
[196] Q. Yang, B. Gao, F. Xu, Biotechnology Journal 15 (2020) 1900086.
[197] J. Huang, H. Fu, Z. Wang, Q. Meng, S. Liu, H. Wang, X. Zheng, J. Dai, Z. Zhang, RSC Advances 6 (2016) 108423.
[198] H. Yang, C. Li, M. Yang, Y. Pan, Q. Yin, J. Tang, H. J. Qi, Z. Suo, Advanced Functional Materials 29 (2019) 1901721.
[199] C. Lv, X.-C. Sun, H. Xia, Y.-H. Yu, G. Wang, X.-W. Cao, S.-X. Li, Y.-S. Wang, Q.-D. Chen, Y.-D. Yu, H. B. Sun, Sensors and Actuators B 259 (2018) 736.
[200] M. Jamal, S. S. Kadam, R. Xiao, F. Jivan, T. M. Onn, R. Fernandes, T. D. Nguyen, D. H. Gracias, Advanced Healthcare Materials 2 (2013) 1142.
[201] M. J. Mirzaali, A. Ghorbani, K. Nakatani, M. Nouri-Goushki, N. Tümer, S. J. Callens, S. Janbaz, A. Accardo, J. Bico, M. Habibi, Advanced Materials 33 (2021) 2008082.
[202] S. Parimita, A. Kumar, H. Krishnaswamy, P. J. J. M. P. Ghosh, Journal of Manufacturing Processes 85 (2023) 875.
[203] M. Herath, J. Epaarachchi, M. Islam, F. Zhang, J. Leng, L. Fang, C. Yan, G. D. Peng, W. Schade, Smart Materials and Structures 29 (2020) 047001.
[204] X. Cui, J. Chen, Y. Zhu, W. Jiang, Chemical Engineering Journal 382 (2020) 122823.
[205] Y. Lee, J. Moon, J. Choi, M. Cho, Scientific Reports 7 (2017) 14277.
[206] F. Ercole, T. P. Davis, R. A. Evans, Polymer Chemistry 1 (2010) 37.
[207] Y. Shi, Z. Chen, Journal of Materials Chemistry C 6 (2018) 11817.
[208] S. Q. Wang, D. Kaneko, M. Okajima, K. Yasaki, S. Tateyama, T. Kaneko, Angewandte Chemie International Edition 52 (2013) 11143.
[209] Q. Guo, C. J. Bishop, R. A. Meyer, D. R. Wilson, L. Olasov, D. E. Schlesinger, P. T. Mather, J. B. Spicer, J. H. Elisseeff, J. J. Green, ACS Applied Materials & Interfaces 10 (2018) 13333.
[210] Z. Chen, R. Cao, S. Ye, Y. Ge, Y. Tu, X. Yang, Sensors and Actuators B 255 (2018) 2971.
[211] J. Huang, L. Zhao, T. Wang, W. Sun, Z. Tong, ACS Applied Materials & Interfaces 8 (2016) 12384.
[212] J. Ban, L. Mu, J. Yang, S. Chen, H. Zhuo, Journal of Materials Chemistry A 5 (2017) 14514.
[213] C. Greant, B. Van Durme, J. Van Hoorick, S. Van Vlierberghe, Advanced Functional Materials 33 (2023) 2212641.
[214] R. Matsuzaki, M. Ueda, M. Namiki, T.-K. Jeong, H. Asahara, K. Horiguchi, T. Nakamura, A. Todoroki, Y. Hirano, Scientific Reports 6 (2016) 23058.
[215] H. Yang, W. R. Leow, T. Wang, J. Wang, J. Yu, K. He, D. Qi, C. Wan, X. Chen, Advanced Materials 29 (2017) 1701627.
[216] P. J. Kitson, S. Glatzel, W. Chen, C.-G. Lin, Y.-F. Song, L. Cronin, Nature Protocols 11 (2016) 920.
[217] X. Yang, W. Chen, H. Liu, B. Yang, Y. Xie, Y. Wang, Y. Lei, L. Xue, Advanced Materials Technologies 7 (2022) 2200266.
[218] Y. S. Lui, W. T. Sow, L. P. Tan, Y. Wu, Y. Lai, H. Li, Acta Biomaterialia 92 (2019) 19.
[219] Z.-x. Zhang, J.-x. Dou, J.-h. He, C.-x. Xiao, L.-y. Shen, J.-h. Yang, Y. Wang, Z. Zhou, Journal of Materials Chemistry C 5 (2017) 4145.
[220] F. Li, L. Liu, X. Lan, C. Pan, Y. Liu, J. Leng, Q. Xie, Smart Materials and Structures 28 (2019) 075023.
[221] R. Bayan, N. Karak, New Journal of Chemistry 41 (2017) 8781.
[222] W. M. Xu, M. Z. Rong, M. Q. Zhang, Journal of Materials Chemistry A 4 (2016) 10683.
[223] G. Li, Q. Yan, H. Xia, Y. Zhao, ACS Applied Materials & Interfaces 7 (2015) 12067.
[224] C. Weder, Journal of Materials Chemistry 21 (2011) 8235.
[225] Y. Sagara, T. Kato, Nature Chemistry 1 (2009) 605.
[226] T. J. Kucharski, R. Boulatov, Journal of Materials Chemistry 21 (2011) 8237.
[227] Y. Vidavsky, S. J. Yang, B. A. Abel, I. Agami, C. E. Diesendruck, G. W. Coates, M. N. Silberstein, Journal of the American Chemical Society 141 (2019) 10060.
[228] J. Han, K.-M. Tang, S.-C. Cheng, C.-O. Ng, Y.-K. Chun, S.-L. Chan, S.-M. Yiu, M.-K. Tse, V. A. Roy, C.-C. Ko, Inorganic Chemistry Frontiers 7 (2020) 786.
[229] H. Chen, Y. Li, Y. Liu, T. Gong, L. Wang, S. Zhou, Polymer Chemistry 5 (2014) 5168.

[230] M. Nadgorny, Z. Xiao, C. Chen, L. A. Connal, ACS Applied Materials & Interfaces 8 (2016) 28946.
[231] J. Y. Wang, F. Jin, X. Z. Dong, J. Liu, M. X. Zhou, T. Li, M. L. Zheng, Small 19 (2023) 2303166.
[232] Y. Wang, G. He, Z. Li, J. Hua, M. Wu, J. Gong, J. Zhang, L.-t. Ban, L. Huang, Polymers 10 (2018) 112.
[233] A. G. Tabriz, M. A. Hermida, N. R. Leslie, W. Shu, Biofabrication 7 (2015) 045012.
[234] W. Nan, W. Wang, H. Gao, W. Liu, Soft Matter 9 (2013) 132.
[235] A. Skardal, A. Atala, Annals of Biomedical Engineering 43 (2015) 730.
[236] Z. Wan, P. Zhang, Y. Liu, L. Lv, Y. Zhou, Acta Biomaterialia 101 (2020) 26.
[237] M. Champeau, D. A. Heinze, T. N. Viana, E. R. de Souza, A. C. Chinellato, S. Titotto, Advanced Functional Materials 30 (2020) 1910606.
[238] L. Hockaday, K. Kang, N. Colangelo, P. Cheung, B. Duan, E. Malone, J. Wu, L. Girardi, L. Bonassar, H. Lipson, Biofabrication 4 (2012) 035005.
[239] Y. M. Abul-Haija, G. G. Scott, J. K. Sahoo, T. Tuttle, R. V. Ulijn, Chemical Communications 53 (2017) 9562.
[240] E. Fleige, M. A. Quadir, R. Haag, Advanced Drug Delivery Reviews 64 (2012) 866.
[241] R. A. Siegel, Journal of Controlled Release 190 (2014) 337.
[242] J. Bai, R. Wang, X. Wang, S. Liu, X. Wang, J. Ma, Z. Qin, T. Jiao, Cell Reports Physical Science 2 (2021) 100623.
[243] S. Janbaz, R. Hedayati, A. Zadpoor, Materials Horizons 3 (2016) 536.
[244] J. W. Boley, W. M. van Rees, C. Lissandrello, M. N. Horenstein, R. L. Truby, A. Kotikian, J. A. Lewis, L. Mahadevan, Proceedings of the National Academy of Sciences of the United States of America 116 (2019) 20856.
[245] B. Goo, C.-H. Hong, K. Park, Materials Design 188 (2020) 108485.
[246] S. Weng, X. Kuang, Q. Zhang, C. M. Hamel, D. J. Roach, N. Hu, H. Jerry Qi, ACS Applied Materials & Interfaces 13 (2021) 12797.
[247] V. Moosabeiki, E. Yarali, A. Ghalayaniesfahani, S. J. Callens, T. van Manen, A. Accardo, S. Ghodrat, J. Bico, M. Habibi, M. J. Mirzaali, Communications Materials 5 (2024) 10.
[248] X. Ni, X. Guo, J. Li, Y. Huang, Y. Zhang, J. A. Rogers, Advanced Materials 31 (2019) 1905405.
[249] H. Arslan, A. Nojoomi, J. Jeon, K. Yum, Advanced Science 6 (2019) 1800703.
[250] A. B. Baker, S. R. Bates, T. M. Llewellyn-Jones, L. P. Valori, M. P. Dicker, R. S. Trask, Materials Design 163 (2019) 107544.
[251] C. Song, J. Ju, Extreme Mechanics Letters 100625 (2020).
[252] G. Sossou, F. Demoly, H. Belkebir, H. J. Qi, S. Gomes, G. Montavon, Materials Design 175 (2019) 107798.
[253] T. van Manen, S. Janbaz, A. A. Zadpoor, Materials Today 21 (2018) 144.
[254] X. P. Hao, Z. Xu, C. Y. Li, W. Hong, Q. Zheng, Z. L. Wu, Advanced Materials 32 (2020) 2000781.
[255] T. van Manen, V. M. Dehabadi, M. C. Saldívar, M. J. Mirzaali, A. A. Zadpoor, Communications Materials 3 (2022) 43.
[256] H. Guo, J. Cheng, K. Yang, K. Demella, T. Li, S. R. Raghavan, Z. Nie, ACS Applied Materials & Interfaces 11 (2019) 42654.
[257] J. M. McCracken, B. M. Rauzan, J. C. Kjellman, H. Su, S. A. Rogers, R. G. Nuzzo, Advanced Functional Materials 29 (2019) 1806723.
[258] B. Zou, Z. Liang, Z. Cui, K. Xiao, S. Shao, J. J. Ju, Advanced Materials 35 (2023) 2207349.
[259] Y. Wang, X. Li, Mechanics of Materials 151 (2020) 103628.
[260] Y. Feng, J. Xu, S. Zeng, Y. Gao, J. Tan, Smart Materials and Structures 29 (2020) 085042.
[261] M. Bodaghi, A. Damanpack, W. Liao, Materials Design 135 (2017) 26.
[262] T. van Manen, S. Janbaz, A. A. Zadpoor, Materials Horizons 4 (2017) 1064.
[263] H. Deng, C. Zhang, K. Sattari, Y. Ling, J.-W. Su, Z. Yan, J. Lin, ACS Applied Materials & Interfaces 13 (2021) 12719.

[264] Q. Ji, J. Moughames, X. Chen, G. Fang, J. J. Huaroto, V. Laude, J. A. I. Martínez, G. Ulliac, C. Clévy, P. Lutz, K. Rabenorosoa, V. Guelpa, A. Spangenberg, J. Liang, A. Mosset, M. Kadic, Communications Materials 2 (2021) 1.
[265] J. Qu, M. Kadic, A. Naber, M. J. S. Wegener, Scientific Reports 7 (2017) 1.
[266] G. Qu, J. Huang, Z. Li, Y. Jiang, Y. Liu, K. Chen, Z. Xu, Y. Zhao, G. Gu, X. Wu, Materials Today Bio 16 (2022) 100363.
[267] M. Azaouzi, A. Makradi, S. Belouettar, Materials Design 41 (2012) 410.
[268] D. Stoeckel, A. Pelton, T. Duerig, European Radiology 14 (2004) 292.
[269] W. M. Huang, C. Song, Y. Q. Fu, C. C. Wang, Y. Zhao, H. Purnawali, H. Lu, C. Tang, Z. Ding, J. Zhang, Advanced Drug Delivery Reviews 65 (2013) 515.
[270] L. Wang, Y. Qiu, H. Lv, Y. Si, L. Liu, Q. Zhang, J. Cao, J. Yu, X. Li, B. Ding, Advanced Functional Materials 29 (2019) 1901407.
[271] F. Bobbert, S. Janbaz, A. Zadpoor, Journal of Materials Chemistry B 6 (2018) 3449.
[272] L. Hiendlmeier, F. Zurita, J. Vogel, F. D. Duca, G. A. Boustani, H. Peng, I. Kopic, M. Nikić, T. Teshima, B. Wolfrum, Advanced Materials 35 (2023) 2210206.
[273] W. Zhou, Z. Qiao, E. Nazarzadeh Zare, J. Huang, X. Zheng, X. Sun, M. Shao, H. Wang, X. Wang, D. Chen, Journal of Medicinal Chemistry 63 (2020) 8003.
[274] Y. Li, F. Zhang, Y. Liu, J. Leng, Scientific China Technological Sciences 63 (2020) 545.
[275] H. Wei, Q. Zhang, Y. Yao, L. Liu, Y. Liu, J. Leng, ACS Applied Materials & Interfaces 9 (2017) 876.
[276] P. Cao, J. Yang, J. Gong, L. Tao, T. Wang, J. Ju, Y. Zhou, Q. Wang, Y. Zhang, Journal of Applied Polymer Science 140 (2023) 53241.
[277] Y. Zhou, D. Zhou, P. Cao, X. Zhang, Q. Wang, T. Wang, Z. Li, W. He, J. Ju, Y. Zhang, Macromolecular Rapid Communications 42 (2021) 2100176.
[278] L. Zhang, M. Hanif, J. Li, A. H. Shah, W. Hussain, G. Zhang, Polymers 15 (2023) 390.
[279] Q. Ge, A. H. Sakhaei, H. Lee, C. K. Dunn, N. X. Fang, M. L. Dunn, Scientific Reports 6 (2016) 31110.
[280] M. Bodaghi, A. Damanpack, W. Liao, Smart Materials and Structures 25 (2016) 105034.
[281] H. Jia, S. Y. Gu, K. Chang, Advanced Polymer Technologies 37 (2018) 3222.
[282] Y. Zhang, A. Raza, Y.-Q. Xue, G. Yang, U. Hayat, J. Yu, C. Liu, H.-J. Wang, J.-Y. Wang, Bioactive Materials 23 (2023) 343.
[283] X. Kuang, K. Chen, C. K. Dunn, J. Wu, V. C. Li, H. J. Qi, ACS Applied Materials & Interfaces 10 (2018) 7381.
[284] X. Wang, Y. Zhang, P. Shen, Z. Cheng, C. Chu, F. Xue, J. Bai, Biomaterials Science 10 (2022) 2302.
[285] X. Wan, H. Wei, F. Zhang, Y. Liu, J. Leng, Journal of Applied Polymer Science 136 (2019) 48177.
[286] J. Liu, O. Erol, A. Pantula, W. Liu, Z. Jiang, K. Kobayashi, D. Chatterjee, N. Hibino, L. H. Romer, S. H. Kang, ACS Applied Materials & Interfaces 11 (2019) 8492.
[287] M. Mirzaali, A. Caracciolo, H. Pahlavani, S. Janbaz, L. Vergani, A. Zadpoor, Applied Physics Letters 113 (2018) 241903.
[288] A. A. Zadpoor, Biomaterials Science 8 (2020) 18.
[289] Z. Wu, J. Zhao, W. Wu, P. Wang, B. Wang, G. Li, S. Zhang, Materials 11 (2018) 1357.
[290] C. Lin, L. Zhang, Y. Liu, L. Liu, J. Leng, Scientific China Technological Sciences 63 (2020) 578.
[291] T. Kim, Y.-G. Lee, Scientific Reports 8 (2018) 13911.
[292] J. N. Rodriguez, C. Zhu, E. B. Duoss, T. S. Wilson, C. M. Spadaccini, J. P. Lewicki, Scientific Reports 6 (2016) 27933.
[293] W. Zhao, N. Li, L. Liu, J. Leng, Y. Liu, Composites Structures 293 (2022) 115669.
[294] C. de Marco, C. C. J. Alcântara, S. Kim, F. Briatico, A. Kadioglu, G. de Bernardis, X. Chen, C. Marano, B. J. Nelson, S. Pané, Advanced Materials Technologies 4 (2019) 1900332.
[295] W. Zhao, F. Zhang, J. Leng, Y. Liu, Composites Science and Technology 184 (2019) 107866.
[296] L. Huang, L. Wang, J. He, J. Zhao, D. Zhong, G. Yang, T. Guo, X. Yan, L. Zhang, D. Li, Journal of Thoracic Disease 8 (2016) 3323.

[297] M. Zarek, N. Mansour, S. Shapira, D. Cohn, Macromolecular Rapid Communications 38 (2017) 1600628.
[298] F. Zhang, N. Wen, L. Wang, Y. Bai, J. Leng, International Journal of Smart Nano Materials 12 (2021) 375.
[299] W. Zhao, Z. Huang, L. Liu, W. Wang, J. Leng, Y. J. C. S. Liu, Composites Science and Technology 229 (2022) 109671.
[300] R. J. Morrison, S. J. Hollister, M. F. Niedner, M. G. Mahani, A. H. Park, D. K. Mehta, R. G. Ohye, G. E. Green, Science Translational Medicine 7 (2015) 285ra64.
[301] H.-H. Chen, C.-H. Pan, A.-M. Leow, P.-K. Tsay, C.-T. Chen, Formosan Journal of Surgery 49 (2016) 1.
[302] Y. Deng, B. Yang, F. Zhang, Y. Liu, J. Sun, S. Zhang, Y. Zhao, H. Yuan, Biomaterials 291 (2022) 121886.
[303] F. Godart, A. Houeijeh, M. Recher, C. Francart, A.-S. Polge, M. Richardson, M.-A. Cajot, A. Duhamel, Archives of Cardiovascular Diseases 108 (2015) 57.
[304] C. Lin, Z. Huang, Q. Wang, Z. Zou, W. Wang, L. Liu, Y. Liu, J. Leng, Advanced Healthcare Materials 12 (2023) 2201999.
[305] D. Kashyap, P. Kishore Kumar, S. Kanagaraj, Additive Manufacturing 24 (2018) 687.
[306] K. J. Krieger, N. Bertollo, M. Dangol, J. T. Sheridan, M. M. Lowery, E. D. O'Cearbhaill, Microsystems & Nanoengineering 5 (2019) 42.
[307] K.-Y. Seong, M.-S. Seo, D. Y. Hwang, E. D. O'Cearbhaill, S. Sreenan, J. M. Karp, S. Y. Yang, Journal of Controlled Release 265 (2017) 48.
[308] R. Jamaledin, C. Di Natale, V. Onesto, Z. B. Taraghdari, E. N. Zare, P. Makvandi, R. Vecchione, P. A. Netti, Journal of Clinical Medicine 9 (2020) 542.
[309] J. Yang, X. Liu, Y. Fu, Y. Song, Acta Pharmaceutica Sinica B 9 (2019) 469.
[310] R. Ye, J. Yang, Y. Li, Y. Zheng, J. Yang, Y. Li, B. Liu, L. Jiang, ACS Biomaterials Science & Engineering 6 (2020) 2487.
[311] D. Han, R. S. Morde, S. Mariani, A. A. La Mattina, E. Vignali, C. Yang, G. Barillaro, H. Lee, Advanced Functional Materials 30 (2020) 1909197.
[312] X. Li, W. Shan, Y. Yang, D. Joralmon, Y. Zhu, Y. Chen, Y. Yuan, H. Xu, J. Rong, R. Dai, Advanced Functional Materials 31 (2021) 2003725.
[313] L. Lin, Y. Wang, M. Cai, X. Jiang, Y. Hu, Z. Dong, D. Yin, Y. Liu, S. Yang, Z. Liu, Advanced Functional Materials 32 (2022) 2109187.
[314] J. Kevin, F. Xu, S. Toufanian, K. J. Chan, S. Said, T. C. Stimpson, E. González-Martínez, J. M. Moran-Mirabal, E. D. Cranston, T. Hoare, Acta Biomaterialia 128 (2021) 250.
[315] T. S. Tran, R. Balu, S. Mettu, N. R. Choudhury, N. K. Dutta, Pharmaceuticals 15 (2022) 1282.
[316] Y. Lu, A. A. Aimetti, R. Langer, Z. Gu, Nature Reviews Materials 2 (2017) 16075.
[317] G. H. Yang, M. Yeo, Y. W. Koo, G. H. Kim, Macromolecular Bioscience 19 (2019) 1800441.
[318] G. Villar, A. D. Graham, H. Bayley, Science 340 (2013) 48.
[319] D. B. Mahmoud, M. Schulz-Sigmund, Advanced Healthcare Materials 12 (2023) 2202631.
[320] S. Zu, Z. Zhang, Q. Liu, Z. Wang, Z. Song, Y. Guo, Y. Xin, S. Zhang, Bio-Design and Manufacturing 5 (2022) 294.
[321] X. Hu, Z. Ge, X. Wang, N. Jiao, S. Tung, L. E. Liu, Composites Part B: Engineering 228 (2022) 109451.
[322] W. J. Hendrikson, J. Rouwkema, F. Clementi, C. A. Van Blitterswijk, S. Farè, L. Moroni, Biofabrication 9 (2017) 031001.
[323] C. Zhang, D. Cai, P. Liao, J.-W. Su, H. Deng, B. Vardhanabhuti, B. D. Ulery, S.-Y. Chen, J. Lin, Acta Biomaterialia 122 (2021) 101.
[324] S. Miao, W. Zhu, N. J. Castro, M. Nowicki, X. Zhou, H. Cui, J. P. Fisher, L. G. Zhang, Scientific Reports 6 (2016) 27226.
[325] S. Miao, H. Cui, M. Nowicki, S.-j. Lee, J. Almeida, X. Zhou, W. Zhu, X. Yao, F. Masood, M. W. Plesniak, Biofabrication 10 (2018) 035007.
[326] S.-H. Hsiao, S. Hsu, ACS Applied Materials & Interfaces 10 (2018) 29273.
[327] K. Modaresifar, M. Ganjian, L. Angeloni, M. Minneboo, M. K. Ghatkesar, P. L. Hagedoorn, L. E. Fratila-Apachitei, A. A. Zadpoor, Small 17 (2021) 2100706.

[328] M. Ganjian, K. Modaresifar, M. R. Ligeon, L. B. Kunkels, N. Tümer, L. Angeloni, C. W. Hagen, L. G. Otten, P. L. Hagedoorn, I. Apachitei, Advanced Materials Interfaces 6 (2019) 1900640.
[329] M. Nouri-Goushki, A. Isaakidou, B. Eijkel, M. Minneboo, Q. Liu, P. Boukany, M. Mirzaali, L. Fratila-Apachitei, A. Zadpoor, Nanoscale 13 (2021) 14304.
[330] S. J. Callens, N. Tümer, A. A. Zadpoor, Applied Materials Today 15 (2019) 453.
[331] S. J. Callens, R. J. Uyttendaele, L. E. Fratila-Apachitei, A. A. Zadpoor, Biomaterials 232 (2020) 119739.
[332] D. Zhang, O. J. George, K. M. Petersen, A. C. Jimenez-Vergara, M. S. Hahn, M. A. Grunlan, Acta Biomaterialia 10 (2014) 4597.
[333] M. Bao, X. Lou, Q. Zhou, W. Dong, H. Yuan, Y. Zhang, ACS Applied Materials & Interfaces 6 (2014) 2611.
[334] A. S. Neto, J. M. Ferreira, Materials 11 (2018) 1702.
[335] G. D. Barabaschi, V. Manoharan, Q. Li, L. E. Bertassoni, Engineering Mineralized and Load Bearing Tissues, Springer, Berlin (2015) pp. 79–94.
[336] B. P. dos Santos, B. Garbay, M. Fenelon, M. Rosselin, E. Garanger, S. Lecommandoux, H. Oliveira, J. Amédée, Acta Biomaterialia 99 (2019) 154.
[337] F. S. Senatov, K. V. Niaza, M. Y. Zadorozhnyy, A. V. Maksimkin, S. D. Kaloshkin, Y. Z. Estrin, Journal of the Mechanical Behavior of Biomedical Materials 57 (2016) 139.
[338] F. Senatov, M. Y. Zadorozhnyy, K. Niaza, V. Medvedev, S. Kaloshkin, N. Y. Anisimova, M. Kiselevskiy, K.-C. Yang, European Polymer Journal 93 (2017) 222.
[339] L. Zhang, G. Yang, B. N. Johnson, X. Jia, Acta Biomaterialia 84 (2019) 16.
[340] S. Miao, P. Wang, Z. Su, S. Zhang, Acta Biomaterialia 10 (2014) 1692.
[341] S. Miao, W. Zhu, N. J. Castro, J. Leng, L. G. Zhang, Tissue Engineering, Part C 22 (2016) 952.
[342] B. Tandon, J. J. Blaker, S. H. Cartmell, Acta Biomaterialia 73 (2018) 1.
[343] A. Ding, S. J. Lee, S. Ayyagari, R. Tang, C. T. Huynh, E. Alsberg, Bioactive Materials 7 (2022) 324.
[344] X. Yang, Z. Lu, H. Wu, W. Li, L. Zheng, J. Zhao, Materials Science and Engineering, C 83 (2018) 195.
[345] D. G. Tamay, T. Dursun Usal, A. S. Alagoz, D. Yucel, N. Hasirci, V. Hasirci, Frontiers in Bioengineering and Biotechnology 7 (2019) 164.
[346] S. Camarero-Espinosa, C. Tomasina, A. Calore, L. Moroni, Materials Today Bio 6 (2020) 100051.
[347] Y. Deng, F. Zhang, Y. Liu, S. Zhang, H. Yuan, J. Leng, ACS Applied Polymer Materials 5 (2023) 1283.
[348] S. Jana, S. K. L. Levengood, M. Zhang, Advanced Materials 28 (2016) 10588.
[349] S. Miao, M. Nowicki, H. Cui, S.-J. Lee, X. Zhou, D. K. Mills, L. G. Zhang, Biofabrication 11 (2019) 035030.
[350] S. Li, N. Chen, X. Li, Y. Li, Z. Xie, Z. Ma, J. Zhao, X. Hou, X. Yuan, Advanced Functional Materials 30 (2020) 2000130.
[351] B. Mirani, E. Pagan, B. Currie, M. A. Siddiqui, R. Hosseinzadeh, P. Mostafalu, Y. S. Zhang, A. Ghahary, M. Akbari, Advanced Healthcare Materials 6 (2017) 1700718.
[352] P. Mostafalu, A. Tamayol, R. Rahimi, M. Ochoa, A. Khalilpour, G. Kiaee, I. K. Yazdi, S. Bagherifard, M. R. Dokmeci, B. Ziaie, Small 14 (2018) 1703509.
[353] S. Miao, H. Cui, M. Nowicki, L. Xia, X. Zhou, S. J. Lee, W. Zhu, K. Sarkar, Z. Zhang, L. G. Zhang, Advanced Biosystems 2 (2018) 1800101.
[354] L. Zhou, T. Min, X. Bian, Y. Dong, P. Zhang, Y. Wen, ACS Applied Bio Materials 5 (2022) 4055.
[355] H.-Y. Shen, Z.-H. Liu, J.-S. Hong, M.-S. Wu, S.-J. Shiue, H.-Y. Lin, Journal of Controlled Release 331 (2021) 154.
[356] M. Wang, C. Wang, M. Chen, Y. Xi, W. Cheng, C. Mao, T. Xu, X. Zhang, C. Lin, W. Gao, ACS Nano 13 (2019) 10279.

[357] J. Deng, Y. Tang, Q. Zhang, C. Wang, M. Liao, P. Ji, J. Song, G. Luo, L. Chen, X. Ran, Z. Wei, L. Zheng, R. Dang, X. Liu, H. Zhang, Y. S. Zhang, X. Zhang, H. Tan, Advanced Functional Materials 29 (2019) 1809110.
[358] R. Jain, S. Wairkar, International Journal of Biological Macromolecules 137 (2019) 95.
[359] E. Y. Jeon, J. Lee, B. J. Kim, K. I. Joo, K. H. Kim, G. Lim, H. J. Cha, Biomaterials 222 (2019) 119439.
[360] W. Zhu, J. K. George, V. J. Sorger, L. G. Zhang, Biofabrication 9 (2017) 025002.
[361] I. Apsite, G. Constante, M. Dulle, L. Vogt, A. Caspari, A. R. Boccaccini, A. Synytska, S. Salehi, L. Ionov, Biofabrication 12 (2020) 035027.
[362] A. C. Weems, M. C. Arno, W. Yu, R. T. Huckstepp, A. P. Dove, Nature Communications 12 (2021) 3771.
[363] F.-Y. Hsieh, H.-H. Lin, S. Hsu, Biomaterials 71 (2015) 48.
[364] S.-J. Lee, M. Nowicki, B. Harris, L. G. Zhang, Tissue Engineering, Part A 23 (2017) 491.
[365] F. B. Coulter, B. S. Coulter, E. Papastavrou, A. Ianakiev, 3D Printing and Additive Manufacturing 5 (2018) 17.
[366] F. B. Coulter, B. S. Coulter, J. R. Marks, A. Ianakiev, 3D Printing and Additive Manufacturing 5 (2018) 5.
[367] H. Shen, H. Diao, S. Yue, J. Fu, Rapid Prototyping Journal 24 (2018) 548.
[368] M. A. Isa, I. Lazoglu, Journal of Manufacturing Systems 50 (2019) 69.
[369] A. Haleem, M. Javaid, R. Vaishya, Journal of Clinical Orthopaedics and Trauma 10 (2019) 809.
[370] J. C. S. McCaw, E. Cuan-Urquizo, Materials and Design 160 (2018) 949.
[371] D. Zhao, T. Li, B. Shen, Y. Jiang, W. Guo, F. Gao, Rapid Prototyping Journal 26 (2020) 1079.
[372] F. B. Coulter, M. Schaffner, J. A. Faber, A. Rafsanjani, R. Smith, H. Appa, P. Zilla, D. Bezuidenhout, A. R. Studart, Matter 1 (2019) 266.
[373] A. T. Neffe, B. D. Hanh, S. Steuer, A. Lendlein, Advanced Materials 21 (2009) 3394.
[374] M. J. Mirzaali, H. Pahlavani, E. Yarali, A. A. Zadpoor, Scientific Reports 10 (2020) 11488.
[375] M. Mirzaali, A. H. de la Nava, D. Gunashekar, M. Nouri-Goushki, R. Veeger, Q. Grossman, L. Angeloni, M. Ghatkesar, L. Fratila-Apachitei, D. Ruffoni, Composite Structures 237 (2020) 111867.
[376] W. Zhang, F. Zhang, X. Lan, J. Leng, A. S. Wu, T. M. Bryson, C. Cotton, B. Gu, B. Sun, T.-W. Chou, Composite Science and Technology 160 (2018) 224.
[377] M. S. Cabrera, B. Sanders, O. J. Goor, A. Driessen-Mol, C. W. Oomens, F. P. Baaijens, 3D Printing and Additive Manufacturing 4 (2017) 19.
[378] W. Meyer, S. Engelhardt, E. Novosel, B. Elling, M. Wegener, H. Krüger, Journal of Functional Biomaterials 3 (2012) 257.
[379] A. Pandey, G. Singh, S. Singh, K. Jha, C. Prakash, Journal of the Mechanical Behavior of Biomedical Materials 108 (2020) 103781.
[380] C. D. Devillard, C. A. Mandon, S. A. Lambert, L. J. Blum, C. A. Marquette, Biotechnology Journal 13 (2018) 1800098.
[381] Q. Ze, X. Kuang, S. Wu, J. Wong, S. M. Montgomery, R. Zhang, J. M. Kovitz, F. Yang, H. J. Qi, R. Zhao, Advanced Materials 32 (2020) 1906657.

6

4D printing of poly(N-isopropylacrylamide)-based hydrogel microarchitectures: two-photon polymerization for reversible shape morphing

Yarali, E., Mubeen A., Cussen K., Lennart V., Vahid M., Zadpoor, A., Accardo, A., & Mirzaali, M. J. (2024). 4D printing of poly(N-isopropylacrylamide)-based hydrogel microarchitectures: two-photon polymerization for reversible shape morphing. *Communications Materials*, under review.

Incorporating shape morphing capability into micro 3D printing enables the 4D printing of 3D microarchitectures for potential tissue engineering and drug delivery applications that mimic *in vivo* properties and dynamically interact with surrounding cellular microenvironments. The ability to remotely actuate these devices allows for precise, non-invasive, and controlled activation of the engineered structures. This work aims to develop smart 3D microarchitectures featuring reversible shape morphing in response to temperature, particularly tissue-friendly temperature. The microstructures were fabricated from a biocompatible pNIPAM-based photoresist via 2PP-based DLW technique. Systematic studies were performed to evaluate the correlation between the printing parameters (*i.e.,* laser power, scanning speed, and hatching angle) and the concentration of pNIPAM components (*i.e.,* monomer and crosslinker) in terms of shape morphing and printability. The thermomechanical properties of the hydrogels, including the elastic modulus, thermal expansion coefficients, and angular deflection, were also measured at different printing doses and activation temperatures. We also developed a thermomechanical model to predict shape morphing in 4D-printed soft microarchitectures. To incorporate the developed protocol into real-world settings, we 4D printed proof-of-concept microenvironments under the application of soft grippers and drug delivery systems. The microstructures exhibited reversible, robust shape-morphing and reliable printability and paved the way for future applications in cell mechanobiology and tissue engineering.

6.1 Introduction

Toward the fabrication of intelligent drug delivery systems or soft grippers with shape-morphing behavior, 4D printing offers a transformative approach by integrating stimuli-responsive biomaterials with 3D printing technology [1, 2]. The addition of time as the fourth dimension in 4D printing allows for the creation of devices that can be pre-programmed to change their shape or other functions, such as stiffness, in response to external stimuli [3].

To fabricate smart 3D microarchitectures for biomedical applications via 4D printing, two general criteria must be satisfied, depending on the applications [1]: *i.* The smart biomaterial used must exhibit sufficient biocompatibility, as the 4D-printed devices are employed in direct contact with cells or tissues in the body. *ii.* The applied stimulation (external stimuli) must be biocompatible. This remains challenging because there are few stimuli that can be used for *in vivo* stimulation and cause no damage to tissues and cells. While these two criteria are relevant to all biomedical applications, two others may be relevant depending on the application. First, the reversibility of the 4D printed devices is required in some applications, such as soft robotics, when multiple cycles of shape morphing are needed. Second, the 4D printing technique should be applicable to various length scales from nano- to macroscale to fabricate

miniaturized devices capable of operating at very small scales with deployability features for minimal invasiveness applications or drug delivery systems. One microfabrication technique that has found widespread applications in the field of multi-scale manufacturing and meets the four criteria mentioned earlier is direct laser writing two-photon polymerization (2PP) [4-6], based on the simultaneous absorption of two photons in a photoresist to initiate the polymerization reaction, thus resulting in extremely high accuracy of printing [7].

Among all smart biomaterials, such as shape memory polymers [8, 9], shape memory alloys [10], shape memory ceramics [11, 12], liquid crystalline polymers [13], and hydrogels [14, 15], poly(N-isopropyl acrylamide)pNIPAM-based hydrogels [2, 4, 16] meet the four criteria for 4D printing of biomedical devices. It exhibits a hydrophilic behavior at room temperature due to the hydrogen bonds between the polymer chains and water molecules. Suppose the temperature increases beyond its monomer's lower critical solution temperature (LCST) (i.e., NIPAM). In that case, the polymer chains rapidly transition from hydrophilic to hydrophobic, resulting in significant (and reversible) volume change and dramatic shrinking [17, 18], Figure 1a. Since the LCST of pNIPAM is very close to the human body temperature (*i.e.,* ~32-35 °C [19-21]) and owing to its good biocompatibility, pNIPAM hydrogels are well-suited for biomedical applications [22]. Moreover, pNIPAM is a suitable candidate as a photoresist for fabricating miniaturized biomedical devices via 2PP, as its chemical composition and mechanical properties can be tuned accordingly (Figures 1a and c). pNIPAM also features a reversible shape morphing by changing the temperature from above LCST to below LCST.

Additionally, the properties of pNIPAM-based hydrogels, such as elastic modulus, can be tuned upon changing their chemical composition or printing parameters. Another technique is the patterning of pNIPAM hydrogels via reinforcing particles to induce orientation-dependent properties, resulting in complex shape morphing [23]. The printing parameters include laser power and scanning speed, which induce changes in the degree of polymerization. This change in the polymerization level induces local heterogeneity and stiffness tunability in pNIPAM [4, 24]. Consequently, varying degrees of polymerization occur within the photoresist, giving rise to bi-beams in which different layers (or voxels) exhibit distinct physical and mechanical properties, giving rise to shape morphing [24, 25]. When these bi-layered microarchitectures are subjected to external stimuli, each layer of the bi-beams exhibits different thermomechanical properties (*e.g.,* thermal expansion coefficient and elastic modulus), leading to complex shape-morphing behaviors.

To date, 2PP 4D printing of pNIPAM has mainly been used for different shape morphing applications, such as simple beam bending [4, 26], grippers and micro-actuators [27-29], and microfluidic systems [22]. These applications mainly rely on

adjusting printing parameters, mechanical design, and incorporating stimuli-responsive modifications (*e.g.,* adding Fe_3O_4 particles to pNIPAM to enable NIR light responsiveness [28]). However, to design a controlled and predictable shape morphing in an application, such as a drug delivery system, a comprehensive knowledge of the relationship between 2PP 4D printing-inducing shape morphing and the thermomechanical properties of pNIPAM is required.

In this study, we mainly focused on characterizing pNIPAM hydrogels through nanoindentation to measure its Young's modulus, investigating strain rate effects on mechanical properties, and analyzing how printing parameters (*e.g.,* laser power, scanning speed, hatching angle, and hatching distance) influence shape morphing. Additionally, we assessed the influence of pNIPAM's chemical composition (*e.g.,* monomer and crosslinker concentrations) on its shape-morphing behavior. To further predict and control shape morphing, we developed a finite element model (FEM), calibrated and validated through experimental characterization. Finally, we demonstrate the versatility of our fabrication method and computational model in two proof-of-concept applications of soft grippers and drug delivery systems.

6.2 Results and discussion

We intentionally introduced heterogeneity and mechanical anisotropy to demonstrate shape morphing in single-material 2PP 4D-printed structures. We employed a bi-layered design, where each layer exhibited a different level of heterogeneity. This was achieved by polymerizing the layers using varying doses of laser energy (*i.e.,* different laser powers and scanning speeds) (Figures 1a and 1b). It is important to note that all the microarchitectures were 4D printed using this bi-layered beam concept, with one layer referred to as the high laser power (HLP) layer and the other as the low laser power (LLP) one. When the temperature of the bi-layered beams dipped in water increases by 60 °C via a heater, the microstructures morph.

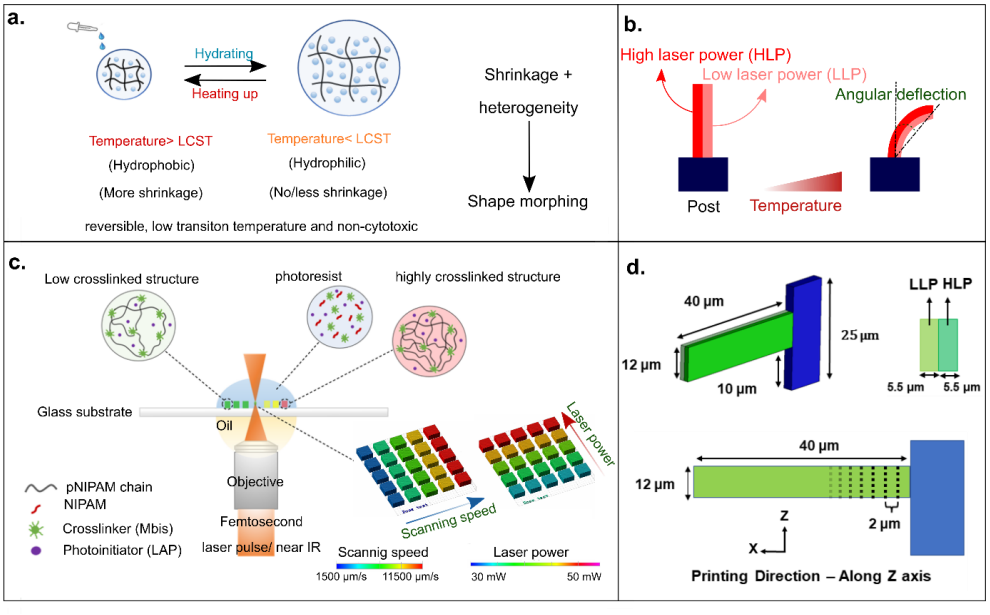

Figure 1. ***a.*** *A schematic drawing illustrating the molecular mechanism of the pNIPAM when temperature exceeds LCST. A reversible transition between hydrophilic and hydrophobic states makes the hydrogel responsive to temperature. It also indicates that sophisticated shape morphing can be achieved if the deformation is heterogeneous.* ***b.*** *A schematic drawing showing the bending of a 4D printed bi-layered beam from a single material (i.e., pNIPAM) and the angular deflection. The red and light red layers represent the high laser power dose (i.e., HLP) and low laser power dose (i.e., LLP). The blue object indicates the post, which is 3D printed with a very high dose.* ***c.*** *The 2PP 4D printing setup for creating pNIPAM-based microstructures. The microstructures are 3D printed via oil configuration with different laser powers and scanning speeds.* ***d.*** *The geometrical configuration of the bi-layered beam. The beams were discretized into smaller slices along the X direction, and the print was done in each slice along the Z direction to increase the mechanical stability.*

6.2.1 Optimal laser power and scanning speed of the 2PP process

The optimal manufacturing range for the laser power and scanning speed ranged between 76-100% (max power = 50 mW) and 6000-11500 µm/s, respectively, based on the dose test study on a series of test blocks (11 × 11) (Figure 2a, highlighted with light blue). For smaller values of the scanning speed (*i.e.,* < 6000 µm/s) and higher values of laser power (*i.e.,* > 75%), the photoresist burned, leading to the generation of bubbles. On the other hand, increasing the scanning speed and choosing a relatively high laser power (*e.g.,* 76-100%) resulted in more solid 3D print blocks. It is noted that the criteria for selecting the right laser power and scanning speed were based on the printability (or mechanical stability) of the blocks (not burnt) and their overall shrinkage. For instance, at a higher scanning speed (*i.e.,* > 6000 µm/s), the blocks printed with a laser power of 76% exhibited a very high level of shrinkage compared to those printed

with a laser power of, say, 100%. Such differences in the shrinkage ratio are due to the degree of polymerization in the photoresist and, thus, differences in the stiffness of the blocks, which results in a different contraction or shrinkage.

Nevertheless, the printed microarchitectures must also be mechanically stable after chemical development (see the section "Materials and methods"). Depending on the geometry of the microarchitectures, selecting the right laser power and scanning speed can be challenging. For instance, to print bi-layered beams with a high aspect ratio (*i.e.*, a high length), more systematic studies are required to find the optimal dose for the LLP and HLP. Apart from the high aspect ratio of the beam, the fact that the beams do not adhere to the glass substrates and are, instead, printed in a photoresist makes the process more challenging. It should also be noted that there was a pre-deflection in the printed beams in some cases (Figure 2b) due to the development process of the pNIPAM in which the specimens were transformed from ethylene-glycol to water [4]. Nevertheless, this pre-deflection vanished after one cycle when the microarchitectures were reheated.

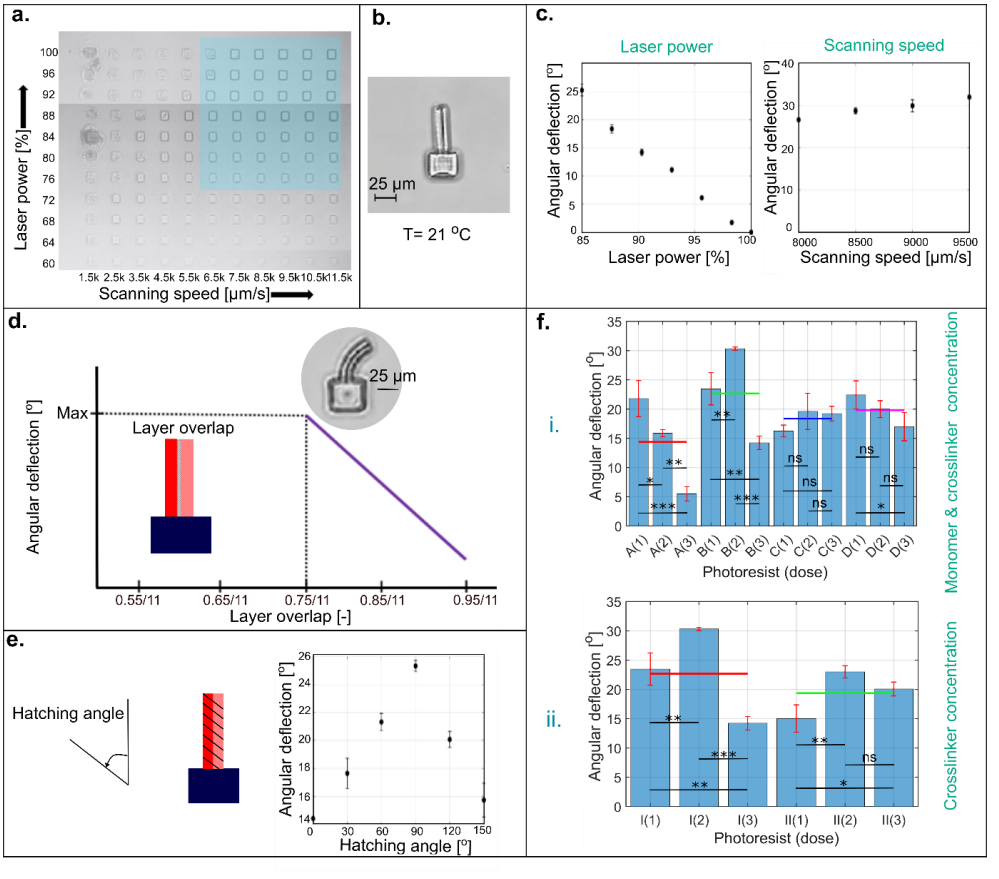

Figure 2. *a. An optical image of the dose test study performed on a pNIPAM photoresist (400 mg NIPAM, 40 mg Mbis, and 15 mg LAP in 450 µL of ethylene glycol (= ~501 mg)) in which the laser power and scanning speed were changed within [60% 100%], and [1500 11500] µm/s, respectively. The blue highlight indicates a region with the optimal dose for 4D printing of the pNIPAM. b. An optical image of the 4D-printed beam at a temperature of 21 °C. c. The effects of the laser power and scanning speed on the angular deflection of the beam (in degree). d. The effects of the overlap between the HLP and LLP layers on the angular deflection of the beam. e. The assessment of the hatching angle, as a printing parameter, on the angular deflection of the beam. f. The effects of the chemical composition of the pNIPAM (i.e., monomer and cross-linker) on the angular deflection of the beam. A, B, C, D, and I and II represent various types of pNIPAM with different chemical composition concentrations. The numbers 1, 2, and 3 indicate a specific dose for each resin, which can be found in Tables 1 and 2. The horizontal solid lines correspond to the average angular deflection in each photoresist. Statistical significance is denoted by ns, *, **, *** corresponding to p-value> 0.05, p-value< 0.05, p-value< 0.01, and p-value< 0.001, respectively. Also, note that DF_n and DF_d for our ordinary ANOWA test for each set of experiment (n = 3) were respectively 2 and 6.*

6.2.2 Effect of laser power and scanning speed on angular deflection

To elucidate the effects of energy dose (*i.e.,* laser power and scanning speed) on the angular deflection of the bi-layered beam, we independently varied the laser power and the scanning speed and measured the angular deflection. Regarding the laser power test, we varied the laser power from 76% (LLP) to 100% (HLP) while maintaining a constant scanning speed of 8000 µm/s (Figure 2c). The angular deflection changed from 26° to 0° (*i.e.,* 100% changes) when the LLP varied from 85% to 100%. Such a reduction in angular deflection upon increasing laser power is due to lower laser power differences in the beam layers and, thus, more minor differences in the shrinkage of the beam, which decreases beam deflection. It should be noted that a LLP below 85% resulted in beams collapsing during the development.

Similarly, to explore the effects of the scanning speed, we fixed the HLP and LLP at 100% and 85% (at the maximum angular deflection based on the laser power study), respectively, and varied the scanning speed from 8000 µm/s to 9500 µm/s (Figure 2c, scanning speed). Unlike the effects of the laser power on the angular deflection, the scanning speed contributed less to angular deflection, as it merely changed the angular deflection from 26° to 32° (*i.e.,* 18.76%). That suggests that laser power influences the polymerization level of photoresists more than the scanning speed. Previous studies have also reported the more pronounced effect of laser power than the scanning speed on the angular deflection and stiffness of 2PP 3D printed structures [30].

6.2.3 Effect of overlap and hatching angle on angular deflection

Another way to increase the deflection of the beam was the overlap between the LLP and HLP layers (Figure 2d, the gray area of the beam). The higher the overlap, the lower the deflection is expected to be, as it increases the rigidity of the beam. However, a small overlap may also result in the delamination of the layers, particularly after the

development process. Therefore, we systematically studied the effects of the normalized overlap magnitude on the angular deflection (Figure 2d). We changed the normalized overlap from 0.55/11 to 0.95/11, in which the delamination happened for overlaps below 0.75/11. Increasing the normalized overlap from 0.75/11 to 0.95/11 drastically decreased the angular deflection. Therefore, we chose the normalized overlap of 0.75/11 as an optimal value between the HLP and LLP layers in this study.

In addition to the dose, an important parameter that determines the mechanical and thermal properties in 2PP 3D printed structures is the printing pattern (*e.g.,* hatching angle, which is the angle between the hatching line direction and the y-axis), similar to other printing techniques [3, 31]. It consequently influences the angular deflection. Therefore, we systematically studied the right hatching angle for the HLP and LLP layers (Figure 2e). We changed the hatching angle from 0° to 150° and measured the angular deflection (Figure 2e). We concluded that the hatching angle of 90° exhibited the maximum deflection (*i.e.,* angular deflection of 25.5°), and therefore, we 3D printed all other specimens with the same hatching angle. This is because the printing patterns can induce anisotropic thermal expansion coefficients (or shrinkage) in 3D printed structures, resulting in different shape morphing [32]. It should also be noted that the variation of the angular deflection vs. hatching angle was almost symmetric with respect to the hatching angle of 90° as the geometry of the beams was symmetric (Figure 2e). The reason that the plot of the angular deflection vs. hatching angle is not entirely symmetric is because of potential imperfections caused by the 2PP 3D printing process, heterogeneity in the photoresist, errors in optical imaging of the specimens, and the experimental measurement of the angular deflection.

6.2.4 Effect of the chemical composition of the pNIPAM on the angular deflection

Apart from the printing parameter, another factor that significantly affects the angular deflection is the chemical composition of the photoresist, as it can influence the stiffness, thermal expansion coefficient, printability, and the LCST of the pNIPAM [33, 34]. For instance, the lower the crosslinker concentration (*i.e.,* Mbis), the lower the storage modulus and the larger the volume of the water released in pNIPAM hydrogels [34]. We fixed the molar ratio at 0.073 and changed the concentration of the monomer and the crosslinker accordingly (Table 1), and the results are illustrated in Figure 2f-i. The corresponding results of the angular deflection of photoresists A, B, C, and D (Figure 2f-i) show that by increasing the concentration of NIPAM as the thermosensitive component of the photoresist and increasing the Mbis, the angular deflection changes irregularly in a way that the photoresist B showed the highest angular deflection (Figure 2f-i). However, this increase made the photoresist more viscous and more opaque, resulting in a much more thermosensitive photoresist, which is associated with more difficulty in terms of printability and reproducibility as the photoresists with higher

concentrations were much more likely to crystalize. This could be due to the constant volume of the solvent, ethylene glycol, (450 µL). While this was sufficient for the lower NIPAM concentrations, at higher concentrations, this may not be sufficient to obtain a fully dissolved mixture. Based on these results and the practical considerations relating to reproducibility and resin homogeneity, the photoresist B (Section "Materials and methods") was determined to exhibit the highest angular deflection of 22.7° across the three sets of doses chosen to print with and featured a maximum angular deflection of 30.33° (dose 2) while still maintaining a homogeneous resin that contained few crystals (Figure 2f). It should also be noted that in the photoresists A and B, there is a significant difference in the angular deflection in different doses (1, 2, and 3), indicating a more expansive design space regarding doses in these resins. Therefore, more consideration was needed for these photoresists to find the optimal printing parameters.

Table 1. *The compositions of the pNIPAM hydrogels when the molar ratio was fixed at 0.073 (i.e., types A, B, C, and D). The corresponding laser power and scanning speed for the HLP and LLP of each photoresist have also been reported as samples 1, 2, and 3. Note that the molar ratio was calculated by dividing the moles of NIPAM by the moles of Mbis, considering molar masses of 113.16 g/mol and 154.15 g/mol, respectively, for NIPAM and Mbis. Moreover, all chemical components were dissolved in 450 µL ethylene glycol.*

Photoresist	Nipam [mg]	Mbis [mg]	Molar ratio [-]	Sample	High dose (laser power / scanning speed)	Low dose (laser power / scanning speed)
A	400	40	0.073	1	84% / 4500	64% / 11500
				2	92% / 5500	68% / 8500
				3	100% / 8000	85% / 8000
B	450	45	0.073	1	88% / 5500	64% / 10500
				2	84% / 7500	72% / 11500
				3	100% / 6500	64% / 11500
C	500	50	0.073	1	92% / 7500	64% / 11500
				2	84% / 5500	68% / 10500
				3	80% / 4500	76% / 11500
D	600	60	0.073	1	92% / 7500	64% / 11500
				2	88% / 4500	64% / 10500
				3	100% / 8500	68% / 11500

Similarly, the results of the photoresists I, II, III, and IV (fixing the concentration of NIPAM and changing the molar ratio, Table 2) did not show an ordered pattern for the angular deflection when the concentration of the Mbis increased (Figure 2f-ii). While a lower molar ratio may produce more swelling, especially at low temperatures [35], practical considerations concerning printing suitability, mechanical stability, and the final hydrogel structure's ability to carry its own weight limit the possible cross-linker concentration reduction. As the molar ratio was reduced, the range of suitable doses decreased. The reduced number of suitable doses also may be prohibitive in

achieving a large deflection as the HLP and LLP doses become closer to each other, thus effectively canceling out any gains achieved through increased swelling. After selecting suitable doses for each resin based on their dose tests, an attempt was made to print the bilayer beam for a selection of doses for each of the four photoresists. Photoresists III and IV could not provide the necessary structural support for the bilayer, leading to it collapsing under its weight and resulting in no successful bilayers. This is likely due to the reduced crosslinker concentration, thus resulting in an unsuitable photoresist for this study. However, successful beams were 3D printed using resins I and II (Figure 2f-ii). We selected a molar ratio of 0.0734 with 450 mg of NIPAM and 45 mg of Mbis for printing all other specimens based on these two tests.

Table 2. *The compositions of the pNIPAM hydrogels when the NIPAM concentration was fixed at 450 g (i.e., types I, II, III, and IV). The corresponding laser power and scanning speed for the HLP and LLP of each photoresist have also been reported as samples 1, 2, and 3. Note that the molar ratio was calculated by dividing the moles of NIPAM by the moles of Mbis, considering molar masses of 113.16 g/mol and 154.15 g/mol, respectively, for NIPAM and Mbis. Moreover, all chemical components were dissolved in 450 µL ethylene glycol.*

Photoresist	Nipam [mg]	Mbis [mg]	Molar ratio [-]	Sample	High dose (laser power / scanning speed)	Low dose (laser power/ scanning speed)
I	450	45.00	0.073	1	88% / 5500	64% / 10500
				2	84% / 7500	72% / 11500
				3	100% / 6500	64% / 11500
II	450	30.70	0.05	1	88% / 5500	68% / 11500
				2	80% / 5500	64% / 10500
				3	88% / 7500	64% / 11500
III	450	12.30	0.02	1	96% / 7500	76% / 8500
				2	88% / 6500	80% / 10500
				3	84% / 5500	76% / 9500
IV	450	6.15	0.01	1	NA	NA
				2	NA	NA
				3	NA	NA

Following Figure 2f-ii, both photoresists enabled the printing of a self-supporting structure and achieved significant deflection upon exposure to a high temperature. Moreover, the photoresist II resulted in slightly less angular deflection on average (22.7° vs. 19.4°) across the three doses. However, this difference is noticeably less than the difference between each photoresist in Figure 2f-i. However, as noted in [35], the impact of a reduced crosslinker-to-monomer molar ratio is more evident at lower temperatures than at higher temperatures. At higher temperatures (*i.e.,* above LCST), the monomer determines the volume of a shrunken pNIPAM [35]. Therefore, in this study, as our focus lies on achieving optimal angular deflection at high temperatures, we

decided to proceed with resin B (2) only with a higher molar ratio of 0.073 (*i.e.,* a laser power of 84% and a scanning speed of 7500 µm/s for the HLP layer and a laser power of 72% and a scanning speed of 11500 µm/s for the LLP layer). However, it can be noted that photoresist II was still capable of achieving acceptable deflection at high temperatures (Figure 2f-ii) but it may be a more suitable photoresist for applications in lower-temperature environments.

6.2.5 Effect of temperature on the angular deflection and FEM validation

The deflection of the beams is also dependent on the temperature. The higher the temperature, the higher the angular deflection is (Figure 3a). Nevertheless, it should be noted that at a specific high temperature (*i.e.,* 60 °C), the beam did not deform anymore (Figure 3a, the plateau of the angular deflection at about 30°). Regarding the cell-friendly feature of the pNIPAM, the 4D printed beams here are partially deformed (about 18° angular deflection) at a body-friendly temperature (37 °C) (Figure 3a-ii).

According to the experimental results of the temperature-dependent angular deflection, we also validated our FEM predictions (Figure 3a-i and Section "Materials and methods"). At temperatures of 21 °C and 30 °C, the experimental and the FEM predictions showed a good match. However, for a temperature of 40 °C, the discrepancy between the experiments and FEM was slightly high. This is likely due to the possible propagation errors in measuring the thermal expansion coefficients, the variation of temperature and relative humidity in the environment, 2PP 3D printing-induced imperfections, assumptions of temperature-independent elastic modulus and temperature-independent thermal expansion coefficients, and errors in measuring the experimental temperature. Particularly, to determine the temperature-independent thermal expansion coefficient of the LLP (in the depth and width directions) and the HLP (in the depth direction), we calculated the linear slope of the plot in Figure 3b.iv. However, not all data points adhere fully to this linear assumption. This nonlinearity, therefore, contributes to the observed discrepancy between the FEM predictions and the experimental results.

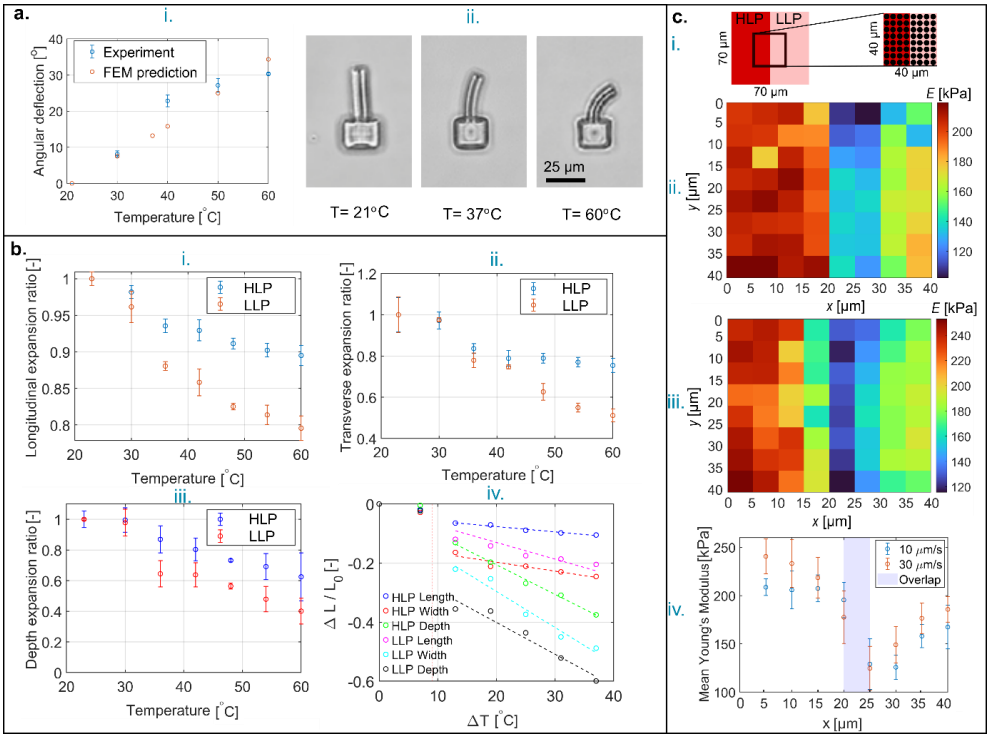

Figure 3. *Thermomechanical characterization of pNIPAM. a. The effects of temperature on the angular deflection of the beam when it changes from 21 °C to 60 °C, experimentally and numerically (i). The optical images show the deflection of the beam at different temperatures of 21 °C, 37 °C, and 60 °C (ii). b. Thermal expansion coefficients (longitudinal, i, transverse, ii, depth, iii) of the HLP and LLP beam as a function of temperature. The variation of the expansion ratio in different directions for each HLP and LLP (iv). c. The elastic modulus measurement of pNIPAM at two different loading rates and a temperature of 21 °C. The schematic drawing shows the configuration for measuring the elastic modulus of pNIPAM with LLP, HLP, and at the interface between the doses (i). The heat map shows the elastic modulus of pNIPAM at a low loading rate of 10 µm/s (ii). The heatmap represents the elastic modulus distribution within pNIPAM at a high loading rate of 30 µm/s. The spatial variation of the elastic modulus of pNIPAM printed with LLP, HLP, and at the interface at different loading rates.*

6.2.6 Thermal expansion coefficients of the pNIPAM bi-layered beams

We measured the thermal expansion coefficients of the beam along its length (longitudinal expansion ratio), width (transverse expansion ratio), and thickness (depth expansion ratio) (Figure 3b) for both HLP (*i.e.,* a laser power of 84% and a scanning speed of 7500 µm/s) and LLP (*i.e.,* a laser power of 72% and a scanning speed of 11500 µm/s) beams. The LLP beams exhibited a higher thermal coefficient for all the directions (Figure 3b-i, ii, and iii) as they were less polymerized. The thermal expansion coefficients in all the directions were lower for lower temperatures (*e.g.,* 30 °C) than those

at higher temperatures (*e.g.*, 60 °C). Moreover, as the temperature increases beyond 30 °C, the difference between the thermal expansion coefficients of the HLP and LLP beams becomes greater. Such a difference in the depth direction is less than that of the longitudinal direction. Additionally, a plateau happens at a specific temperature (around 60 °C), and the thermal coefficient no longer changes. We also plotted the variation of the dimension change to the initial dimension vs. temperature change in which its slope indicates the thermal expansion coefficients (in 1/°C) (Figure 3b-iv). We finally reported the magnitude of the thermal expansion coefficients of the beam at the HLP and LLP in Table 3.

Table 3. *The thermal expansion coefficients of the pNIPAM hydrogel in different directions for the HLP and LLP.*

Direction	HLP [1/°C]	LLP [1/°C]
X	-0.0018	-0.0057
Y	-0.01	0.0107
Z	-0.0030	-0.0122

The results of this experiment demonstrated that shrinkage was highly dependent on the direction of the beam (*i.e.,* anisotropic thermal expansion coefficients). The differences in the transverse and longitudinal thermal expansion ratios for the same dose are likely a result of the complex relationship between the printing direction, hatching angle, printing method, and photoresist properties. Following Figure 3b-iv, at temperatures below the LCST, the variance in the thermal expansion coefficients (*i.e.,* the slope in the graph) is much less noticeable than those above the LCST. However, the data below the LCST does not closely follow a linear trend, possibly due to fewer data points or because these values are closer to the LCST temperature than the range of data above the LCST. The lower expansion ratios below the LCST can be explained by the change in how the monomer chains are arranged at the LCST, where the thermo-response of the NIPAM becomes much more apparent.

6.2.7 Elastic modulus of the pNIPAM

The average elastic modulus of each dose used in the bilayer (*i.e.,* LLP and HLP), and specifically the elastic modulus at the interface of the two different doses, ranged from 120 kPa to 240 kPa at a temperature of 21 °C (Figure 3c). The LLP layer resulted in a lower elastic modulus for both loading rates (150.3 kPa on average for the low rate, 10 μm/s, and 170.4 kPa for the high rate, 30 μm/s), as compared to the HLP, which is more crosslinked and thus stiffer (207.3 kPa for the low rate and 230.8 kPa for the high rate) (Figure 3c-ii, iii, and iv). The spatial distribution of the average elastic modulus of the HLP layer at a lower loading rate (Figure 3c-ii) is more homogeneous than that of the higher rate. This is likely due to the imperfections created during the specimens' printing and the heterogeneity of the photoresist. This is highlighted in the LLP layer

at both low and high loading rates. It should also be noted that the elastic modulus was reported at a fixed temperature of 21 °C in this study. Further investigations are necessary to examine the temperature-dependent Young's modulus of pNIPAM in future studies.

The differences in the elastic modulus corresponding to different loading rates are due to the viscoelastic behavior of the hydrogel. Considering the time-dependency of the hydrogel, it exhibits stiffer at a higher loading rate (*i.e.,* 30 µm/s) as it does not have sufficient opportunity to rearrange its molecular chains in response to the mechanical load [36]. On the other hand, a lower loading rate gives the specimens more time for internal re-arrangement and/or stress (re-)distribution, allowing the hydrogel to exhibit a lower elastic modulus. Both loading rates resulted in the minimum elastic moduli value (within 125 kPa and 190 kPa) being recorded at the interface between the LLP and HLP, Figure 3c-iv. Around this overlap, the measured average elastic modulus values dropped below the single dose specimen's average elastic modulus. This could be because we printed the HLP layer first. Thus, when the second layer (LLP) was printed, some imperfections, such as pores, occurred at the interface, resulting in a lower value for the elastic modulus. Moreover, at the interface (*i.e.,* x within 20 and 25 µm), the standard deviation is the largest compared to the two single doses. This further suggests that the interface resulted in high variability in the elastic modulus (Figure 3c-iv). This is likely due to the surface properties of the interface, such as topology, where a heterogeneous distribution may exist.

6.2.8 Shape recovery of the pNIPAM bi-layered beams after dehydration

The pNIPAM performance in this study was also assessed under different conditions, such as when the hydrogel dried out. For this purpose, we dried out the 4D-printed beam and it consequently, lost water and shrank significantly (supplementary VideoS2). The dried specimens returned to their initial shapes once they were rehydrated by immersion in water (supplementary VideoS3). This indicated how robust our developed hydrogels are at the microscale.

It should be noted that our developed pNIPAM hydrogel exhibited reversible shape morphing, meaning that it could deform in several cycles. Some studies also show the reversibility of the 2PP 4D printed pNIPAM in several cycles (up to around 20 cycles) [4, 37].

6.2.9 Proof-of-concept applications of the 2PP 4D printing of pNIPAM in soft robotics and drug delivery

To obtain sophisticated shape morphing based on 2PP 4D printing of pNIPAM, we first analyzed simple shape morphing by various combinations of beams and the

location (*i.e.*, left/ right or top/bottom) of the HLP and LLP layers. We, therefore, illustrated the undeformed and deformed configuration of the beams and the contour of the von Misses stress predicted by our computational model (the color bar, in terms of MPa) underneath each application (Figure 4a). Note that all the beams were 4D printed at the same height (*Z*) on a single post. Moreover, it should be noted that the activation time for our proposed applications here is less than 1 s, which is relatively fast compared to some other temperature-responsive 4D-printed structures [38].

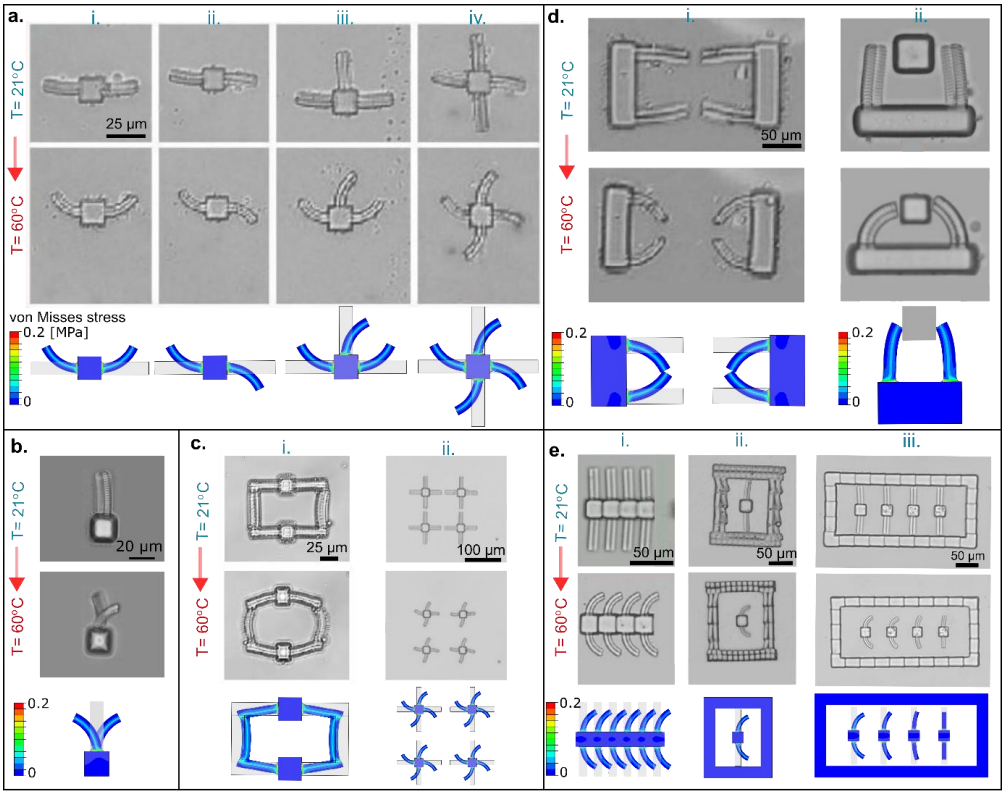

Figure 4. *Optical images of shape morphing behavior in proof-of-concept applications of 2PP 4D printed specimens with their corresponding FEM prediction. Note that the contour indicated the distribution of von Misses stress in terms of MPa.* ***a.*** *The in-plane bending deformation of beams (**i**), twisting/shrinkage deformation (ii), three-beam bending/twisting deformation (**iii**), and fully twisting deformation (**iv**).* ***b.*** *The out-of-plane bending deformation at different heights (Z).* ***c.*** *A unit cell of a meta-biomaterial featuring a switchable Poisson's ratio when the temperature increases (**i**). A unit cell block representing a meta-biomaterial featuring an NPR when the temperature increased by 60 °C (**ii**).* ***d.*** *A simple grasping mechanism (**i**), and a proof-of-concept application of a soft gripper, in which it holds an object (**ii**).* ***e.*** *A proof-of-concept drug delivery application of the 2PP 4D printing with shape morphing capability. A series-bending mechanism that can open up a membrane as a valve simultaneously or sequentially (**i**), and a drug delivery mechanism in which increasing the temperature leads to potential drug release (**ii**). A 4D printed proof-of-concept drug delivery system in which the beams are activated gradually from the maximum (left beam) deflection to the minimum (right beam) when the temperature increases by 60 °C (**iii**).*

In Figure 4a-i, a simple bending deformation, which is very fundamental, was demonstrated. This deformation is used to make sophisticated movements and can also serve as a soft sensor to detect a physical touch in a cyclic loading or as a gripper (if the beam is long enough). To print such a simple deformation, the order of the HLP and LLP should be similar. The second deformation was twisting, created by inverting the order of the HLP and LLP layers (Figure 4a-ii). In this application, the system not only twists but also contracts, a phenomenon known as coupled twisting and shrinkage deformation. The third in-plane application was created by adding another beam to the twisting/shrinkage deformation system (Figure 4a-iii). This was designed to show the potential of in-place deformation when the number of beams increases in the system. The last one combines two twisting/shrinkage mechanisms so that the whole system twists and shrinks (Figure 4a-iv). This system can perform as a unit cell for meta-biomaterials [39], where isotropic twisting and shrinkage are demanded [40]. It should be noted that in all these applications, the beams are not connected to another part apart from the post. Otherwise, the deformation will be compromised due to the boundary conditions. Moreover, the post is slightly deformed here, although it was printed with a much higher dose. Such slight deformations cause difficulties in achieving our desired deformation for the beams. Regarding the prediction of our computational model for the in-plane applications, there is a high degree of agreement between the experiments and computational models. The distribution of the von Misses stress in all the in-place applications is similar as the beams are all connected only from one side (Figure 4a). Moreover, at the interface, the von Misses is higher than the other locations of the beams due to the overlap between the HLP and LLP layers.

The out-of-plane deformation was also achievable by 4D printing two beams at different heights, *Z* (Figure 4b). The computational prediction also proved von Misses stress similar to in-place applications. Such deformation is helpful in soft robotics, where different *Z* values are demanded.

Combining the in-plane deformations and the beam constraint could result in creating a unit cell of non-stochastic meta-biomaterials (Figure 4c). In non-stochastic metamaterials [39], a unit cell refers to a repetitive geometric pattern that represents the overall properties of the material, with the entire meta-biomaterial composed of an array of such unit cells [39]. We aimed at 4D printing a unit cell whose Poisson's ratio (*i.e.,* the negative ratio of lateral strain to longitudinal strain) changes over time by changing temperature. However, it is noted that the difficulty level increases when the number of unit cells increases, mainly due to the geometrical constraints, which depend on the stiffness of the struts. The 3D printed unit cell (Figure 4b-i) is rectangular, representing nearly zero Poisson's ratio [41] at 21 °C. When the temperature rose to 60 °C, its shape shifted to a honeycomb-like structure, generating a positive Poisson's ratio [41] (Supplementary VideoS4). Nonetheless, the horizontal struts were supposed not to deform. However, as the post is still deformable, undesired deformation in the beams

also occurred. In this application (Figure 4c-i), the two vertical struts were made of bi-layered beams, and a single-layered beam made the other two horizontal with a high laser power dose. Our computational model predictions do not perfectly mimic the deflection of the bi-layered beam in the unit cell, mainly because we considered the post as a non-deformable object.

A similar idea was used to generate meta-biomaterials using four independent block boxes of beams and posts (Figure 4c-ii). The unit cell was created by arranging the twisting/ shrinkage mechanism such that the whole structure shrank upon exposure to higher temperatures, mechanically indicating auxetic meta-biomaterials with NPRs. Our computational predictions exhibited a high degree of agreement with these experimental observations.

To fabricate proof-of-concept soft robotics, we first 4D printed a simple mechanism (Figure 4d-i) in which two beams were printed on a large post. It featured a grasping mechanism when the temperature increased by 60 °C. Regarding the prediction of our FEM, the discrepancy in the deflection of the beams is mainly because of the thermal expansion coefficients and 3D printing imperfections. To predict the maximum force generated by the deflection of the beams, we proposed another design (Figure 4d-ii). In this case, we 4D printed an extra post with the same printing parameter for the post as an object. When the temperature increased by 60 °C, the beam deformed and thus stopped deforming when they touched the extra post. To predict the force applied to the post or generated by the beam, we used FEM (Figure 4d-ii). The maximum predicted force is approximately 0.085 μN, which is desirable in mechanobiological measurements at a small scale, such as AFM of cells [42].

We also proposed a proof-of-concept application for drug delivery systems comprising a chamber and valves, in which changing the temperature controls the opening of the valves. Such a stimuli-responsive opening mechanism could be used to control the release of a drug. When the temperature rises, the beams deform; consequently, the potential drug can go to the other side of the chamber (Figure 4e). The current proof-of-concept drug delivery system could be upgraded by incorporating the 4D printing of multiple beams/posts with a controlled deformation (Figure 4e-i). Moreover, the deformation of the beams could be controlled gradually, meaning a gradient release of a potential drug release (Figure 4e-iii). In this application, we 3D printed four beams with the same LLP as before (*i.e.,* 72% laser power and 11500 μm/s scanning speed) while varying the HLP layer for each beam. The laser power and scanning speed of the HLP layer decreased by 4% and 1334 μm/s for each beam, from left to right (Figure 4e-iii). The FEM predictions of our gradient drug delivery system also indicate a high level of accuracy of our model in terms of the beam deflection.

6.3 Conclusions

In conclusion, we used a single material and single-step fabrication process based on 2PP direct laser writing and pNIPAM-based hydrogels to fabricate smart 3D microstructures with reversible and rapid shape morphing upon triggering by cell-friendly thermal stimulus. We initially elucidated the effects of different photoresist compositions, monomers, and crosslinker densities on the angular deflection of a cantilever beam. We found the hydrogel's optimal composition, considering the structures' printability, mechanical stability, and angular deflection. To model the thermomechanical behavior of the 2PP 4D printed microarchitectures, we developed a computational model based on the thermomechanical characterization of the hydrogel. The thermomechanical characterization included thermal expansion coefficients at different temperatures and the elastic modulus of the hydrogel at various loading rates. Based on the prediction of the developed model, we proposed several proof-of-concept biomedical applications, including drug delivery systems and soft grippers. The shape morphing behavior in these applications was induced by introducing anisotropy within the fabricated microstructures by locally varying the printing parameters (laser power, scanning speed, and hatching angle). Finally, it was demonstrated that the success of 4D printing in biomedical applications strongly depends on photoresist composition and printing parameters, and each should be thoroughly investigated to meet the targeted application. Our developed 2PP 4D printing of thermo-responsive pNIPAM paves the way for developing smart 3D microstructures in drug delivery systems and soft robotics. However, further investigations are required to evaluate its efficiency, such as studying *in vitro* drug release by incorporating drug particles into the 4D printed shape morphing systems.

6.4 Materials and methods

6.4.1 Photoresist composition and preparation

NIPAM (see weights in Tables 1 and 2) was added to 450 µL of ethylene glycol (EG) and magnetically stirred for 3 hours. After complete dissolution, the cross-linker N, N-methylenebis(acrylamide) (Mbis) (Tables 1 and 2) and 15 mg (1.49 %w/w) of the photo-initiator lithium phenyl(2,4,6-trimethylbenzoyl)phosphinate (LAP) were added under yellow light conditions and stirred again for 3 hours. Following this, the brown bottle containing the photoresist solution was wrapped in an aluminum foil to avoid unnecessary exposure to light.

As the photoresist's chemical composition significantly affects the beams' angular deflection, we varied the ratios of the NIPAM and Mbis. Consequently, we made eight different types of photoresists (*i.e.,* A, B, C, D, and I, II, III, IV) (Tables 1 and 2). In photoresists A, B, C, and D, the molar ratio of the crosslinker-to-monomer was fixed at 0.073, and the ratios of the monomer and the crosslinkers were varied accordingly.

Note that the molar ratio was calculated by dividing the moles of NIPAM by the moles of Mbis, considering molar masses of 113.16 g/mol and 154.15 g/mol, respectively, for NIPAM and Mbis. On the other hand, in photoresists I, II, III, and IV, the ratio of NIPAM was fixed at 450 g, but the Mbis ratio was varied. It should be noted that the notations "1", "2" and "3" indicate the different doses (laser power and scanning speed) for each photoresist. This is because we performed a new dose test for each photoresist and selected different doses to measure the angular deflection of the beams. We printed the beams with the same printing setting, and the printing parameters were chosen based on the corresponding dose test (Tables 1 and 2).

6.4.2 Fabrication and post-processing of the microarchitectures

All structures in this study were fabricated using a commercial direct laser writing setup (Photonic Professional GT+, Nanoscribe GmbH) (Figure 1c). The initial designs (*i.e.,* beams) were generated using SolidWorks (Dassault Systèmes, France), a commercial CAD software, and then exported as .stl files. These files were imported into DeScribe software (Nanoscribe, Germany) to generate General.gwl files, which were subsequently utilized in the Nanowrite software (printing software, Nanoscribe, Germany) to interface with the 2PP 3D printer, enabling the fabrication process. The printing was executed using a Photonic Professional GT+ 3D printer (Nanoscribe).

The conventional direction of printing in DeScribe (software for print job preparation from Nanoscribe) is along the *X*-*Y* plane (*i.e.,* individual layers are printed along the *X*-*Y* plane), and the layers are stacked upon each other along the *Z*-axis to obtain the desired structure. However, due to the low scanning speed of printing the microstructures (8,000 µm/s), delamination was observed between two consecutive layers along the Z-axis. Therefore, the printing strategy was changed such that small sections of 2 µm in length were printed along the *X*-axis (length of the beam) (Figure 1d). To identify the maximum thickness of the slices along the *X* direction, we conducted a parametric study and concluded that 2 µm is the desirable size. It should also be noted that the shape morphing, and the stability of the beams were dependent on the 3D printing sequence of the HLP and LLP layers. Here, we initially started printing from the HLP layer. An overlap of 0.75 µm (equivalent normalized overlap of 0.75/11) was provided between the HLP and LLP layers to prevent delamination in the structure when subjected to thermal loads. Additionally, between the beam element and the fixed post, an overlap of 2 µm was chosen to ensure the structural stability of the overhanging structure. Moreover, we employed the piezo scanning mode instead of *z*-drive for the stage movement due to the small dimensions of our specimens and to increase the stability of the photoresists. It should also be noted that in the oil configuration, we are limited to the working distance of the employed 25×, which is 380 µm. Considering the thickness of the coverslip substrates, which is 170 µm, a maximum of ~210 µm high microstructures can be 3D printed.

Prior to printing the microstructures, a rounded glass substrate with a 30 mm diameter and a thickness of 170 μm (Thermo Scientific Inc., USA) was first cleaned using isopropanol and acetone (both from Sigma-Aldrich, Germany). This was followed by oxygen plasma (Diener electronic GmbH, Germany) treatment of the glass substrate at a power of 80 W with a gas flow rate of 5 cm3 min-1 and a pressure of 0.12 bar for 15 minutes. The treated glass substrate was then placed in a petri dish containing a thin layer of 3-(Trimethoxysilyl)propyl methacrylate (stabilized with BHT, 98.0%, Sigma-Aldrich, Germany) for 1 hour. This process, commonly called silanization, ensures that the microstructures printed on the glass substrate adhere firmly to it, thereby reducing the chances of delamination of the structures. Following silanization, the glass substrate was again cleaned using isopropanol. The glass substrate was then firmly mounted onto the substrate holder using tape to hold it in place. Since the oil configuration was used for fabricating the structures, a drop of immersion oil (Immersol 518F, ZEISS) was placed on the side of the substrate facing the objective.

Next, a drop of the pNIPAM-based photoresist was placed on the other side of the glass substrate, and the sample holder was loaded into the printer. A 25× oil immersion objective (numerical aperture of 0.8 from ZEISS) was used for printing the microstructures. Once the printing process was completed, the excess precursor solution was rinsed away using acetone, followed by rinsing with ultrapure water.

Post-processing of the 3D printed microstructures included the substrate being dipped into acetone for 30 s, followed by 10 minutes of upright immersion in a glass full of demi-water. Afterward, the substrate was attached to a petri dish using two drops of silicone glue, and the substrate was covered with demi-water for 5 minutes (ensuring the silicone glue was not wetted) to allow the silicone glue to dry out. Finally, the rest of the petri dish was filled with demi-water (approximately 5 mm deep) and left at room temperature for 2-3 hours to allow the hydrogel structures to rehydrate before any tests were performed.

6.4.3 Beam deflection

To find the optimal printing parameters and materials compositions and to quantify our developed hydrogel, we first performed our experiments on a beam with a size of 40×11×12 μm3 alongside x, y, and z (Figure 1b and 1d). Each beam was joined at one end to a 20×20×25 μm^3 base (the blue block in Figure 1b), which is adhered to the glass substrate. The beam's deflection level was indicated via the angular angle, as illustrated in Figure 1b. The angular deflection of the beam is defined as the angle between the midpoint at the end of the bilayer beam and the line orthogonal to the interface's face between the support structure and the bilayer (Figure 1b).

After finding the optimal dose (laser power and scanning speed) from a dose test (Figure 2a), we printed three beams (with the post) for each application and

assessment. It should be noted that the beams had a pre-deflection in some cases due to the pNIPAM development process. Nevertheless, this pre-deflection vanished after reheating them, releasing the residual stress.

6.4.4 Mechanical characterization

Mechanical characterization of the samples consisted of determining the thermal expansion coefficients of the beams, as well as nanoindentation, to determine the elastic modulus of the pNIPAM at different loading rates. Three beams ($n = 3$) were 3D printed with the same dimensions as before to determine how the beam shrinks at various temperatures. However, only one dose throughout was used (*i.e.,* either HLP or LLP). The angular deflection vs. temperature was recorded. Moreover, the thermal expansion ratios were determined by submerging the specimens in a water bath at different temperatures and then comparing the longitudinal, depth, and transverse dimensions before and after exposure to hot water.

Nanoindentation was used to determine the elastic modulus of the beam. This is a process whereby the mechanical properties of the specimens are characterized using an optical interferometry-based nanoindenter (Chiaro, Optics11 life, The Netherlands). During the application of the load, the displacement of the cantilever, equipped with a spherical glass probe, is recorded, resulting in a force-displacement curve from which the sample's mechanical properties can be determined. The nanoindenter employed in this work had a 2.5 μm radius probe with a nominal stiffness of 0.43 N/m. All nanoindentations were performed with the sample submerged in demi-water. Cuboids measuring 70×70×20 μm3 were printed using the doses described above and left for 20 hours before nanoindentation to ensure the samples had reached a swelling equilibrium and to ensure repeatability in the measurements. The elastic modulus of each specimen was calculated using the Hertzian model, considering the assumption of incompressibility. This model applies to soft biomaterials, such as the one used in this work. The loading regime used was a peak indentation waveform with a controlled maximum load of 0.4 N (which corresponded to approximately 1 μm indentation depth). Two different loading rates were used, initially a loading rate of 10 μm/s, followed by a loading rate of 30 μm/s. Following the HLP and LLP layers interface, a 4.75 μm overlap (maintaining the same overlap-to-width ratio as in the bi-layered beams) was selected. It should also be noted that we first printed the HLP layer and then the LLP layer.

6.4.5 Computational mdoeling

We used the commercial software suite Abaqus/CAE 2023.HF2 (Dassault Systèmes Simulia Corp., Johnston, RI, USA) for finite element analysis. The analysis incorporated nonlinear geometric effects to capture the large deflections observed in the bilayer beams. Linear thermally-coupled brick elements with full integration (C3D8T,

Abaqus) were utilized to model the behavior of the bi-layered microarchitectures. A systematic mesh convergence study was performed to find the optimal mesh size by changing the mesh size from 3 μm to 0.5 μm. The angular deflection did not change anymore within a tolerance of 5% by considering a mesh size of 1 μm, and therefore, we chose this mesh size for modeling the microarchitectures. A uniform temperature, ranging from ambient temperature (20 °C) to 60 °C, was applied to conduct a coupled temperature–displacement steady-state analysis. The material model included elastic moduli (*i.e.,* E) and orthotropic thermal expansion coefficients to replicate the anisotropic behavior observed in experiments. These material properties were derived from experimental data (Figures 3c and Table 3).

The computational model was discretized with a maximum element size of 1 μm to achieve sufficient resolution. For the analysis of bilayer deflection, the angular displacement between the beam tips at the interface of HLP and LLP layers was quantified relative to the initial interface line (Figure 1b). The beam substrates were modeled as fixed, with extremely high mechanical properties (*e.g.,* $E = 100$ MPa) assigned to ensure substrate rigidity. Standard surface-to-surface contact was defined for simulations involving a gripper and object, with hard contact in the normal direction and friction modeled using a penalty coefficient of 0.2. The object was represented as an analytical rigid part, further simplifying the interaction modeling.

6.4.6 Statistical analysis

We used Prism (9.4.1, GraphPad, US) software for the statistical analysis (*i.e.,* mean values, standard deviations and the p-values) of the effect of the chemical compositions of the pNIPAM on the angular deflection of the bi-layered beams. All the experiments were repeated three times ($n = 3$). Prior to calculating the p-value, we first performed a normality test using the Shapiro–Wilk test with alpha= 0.05 to determine the normality of the data. After ensuring the normality of data in each group (at each dose), we performed an ordinary one-way ANOVA test, followed by post-hoc analysis using Tukey's multiple comparison test to calculate the p-value between groups. We considered a p-value< 0.005 as statistically significant for all the experiments. It should also be noted that the DF_n and DF_d presented in the caption of Figure 2 indicate the degree of freedom for the numerator of the F ratio and the denominator, respectively.

Bibliography

[1] E. Yarali, M.J. Mirzaali, A. Ghalayaniesfahani, A. Accardo, P.J. Diaz-Payno, A.A. Zadpoor, 4D printing for Biomedical Applications, Advanced Materials (2024) 2402301.
[2] L. Tan, Y. Yang, L. Fang, D.J. Cappelleri, Shape-Programmable Adaptive Multi-Material Microswimmers for Biomedical Applications, Advanced Functional Materials (2024) 2401876.

[3] V. Moosabeiki, E. Yarali, A. Ghalayaniesfahani, S.J. Callens, T. van Manen, A. Accardo, S. Ghodrat, J. Bico, M. Habibi, M.J. Mirzaali, Curvature tuning through defect-based 4D printing, Communications Materials 5(1) (2024) 10.
[4] M. Hippler, E. Blasco, J. Qu, M. Tanaka, C. Barner-Kowollik, M. Wegener, M. Bastmeyer, Controlling the shape of 3D microstructures by temperature and light, Nature communications 10(1) (2019) 1-8.
[5] S. Peng, X. Lei, S. Sun, Y. Zhu, J. Qiu, H. Yang, Magnetic-Driven Micro-Gear Pair Fabricated by Femtosecond Laser Writing, Advanced Engineering Materials 26(10) (2024) 2301960.
[6] E. Yarali, A.A. Zadpoor, U. Staufer, A. Accardo, M.J. Mirzaali, Auxeticity as a mechanobiological tool to create meta-biomaterials, ACS Applied Bio Materials 6(7) (2023) 2562-2575.
[7] W. Wang, Z.-Q. Chen, B. Lin, M.-C. Liu, Y. Zhang, S.-J. Liu, Y. Li, Q. Zhao, Two-photon polymerization-based 3D micro-scaffolds toward biomedical devices, Chemical Engineering Journal (2024) 152469.
[8] H. Li, B. Zhang, H. Ye, B. Jian, X. He, J. Cheng, Z. Sun, R. Wang, Z. Chen, J. Lin, Reconfigurable 4D printing via mechanically robust covalent adaptable network shape memory polymer, Science Advances 10(20) (2024) eadl4387.
[9] T. van Manen, V.M. Dehabadi, M.C. Saldívar, M.J. Mirzaali, A.A. Zadpoor, Theoretical stiffness limits of 4D printed self-folding metamaterials, Communications Materials 3(1) (2022) 43.
[10] J. Zeng, Y. Yang, H. Peng, P. Wang, C. Liu, Z. Chen, W. Chen, X. Liu, Y. Wu, Z. Liu, Additive manufacturing of high entropy shape memory alloy with outstanding properties through multi-remelting in-situ alloying, Additive Manufacturing (2024) 104253.
[11] R. Wang, C. Yuan, J. Cheng, X. He, H. Ye, B. Jian, H. Li, J. Bai, Q. Ge, Direct 4D printing of ceramics driven by hydrogel dehydration, Nature Communications 15(1) (2024) 758.
[12] L. Wan, Z. Mao, H. Liu, Y. Xie, F. Lyu, Z. Cao, Y. He, J. Yin, X. Han, W.Y.K. Chan, Direct 4D printing of gradient structure of ceramics, Chemical Engineering Journal 465 (2023) 142804.
[13] P. Sartori, R.S. Yadav, J. Del Barrio, A. DeSimone, C. Sánchez-Somolinos, Photochemically Induced Propulsion of a 4D Printed Liquid Crystal Elastomer Biomimetic Swimmer, Advanced Science (2024) 2308561.
[14] B. Liu, H. Li, F. Meng, Z. Xu, L. Hao, Y. Yao, H. Zhu, C. Wang, J. Wu, S. Bian, 4D printed hydrogel scaffold with swelling-stiffening properties and programmable deformation for minimally invasive implantation, Nature Communications 15(1) (2024) 1587.
[15] C. Deng, J. Qu, J. Dong, Y. Guo, X. Wu, Y. Fang, X. Sun, Y. Wei, Z. Li, 4D printing of magnetic smart structures based on light-cured magnetic hydrogel, Chemical Engineering Journal (2024) 152992.
[16] S. Li, H. Yang, G. Chen, J. Zheng, W. Wang, J. Ren, C. Zhu, Y. Yang, Y. Cong, J. Fu, 4D printing of biomimetic anisotropic self-sensing hydrogel actuators, Chemical Engineering Journal 473 (2023) 145444.
[17] I. Sanzari, E. Buratti, R. Huang, C.G. Tusan, F. Dinelli, N.D. Evans, T. Prodromakis, M. Bertoldo, Poly (N-isopropylacrylamide) based thin microgel films for use in cell culture applications, Scientific reports 10(1) (2020) 6126.
[18] S. Khumngern, I. Jeerapan, Synergistic convergence of materials and enzymes for biosensing and self-sustaining energy devices towards on-body health monitoring, Communications Materials 5(1) (2024) 135.
[19] L. Chen, M. Liu, L. Lin, T. Zhang, J. Ma, Y. Song, L. Jiang, Thermal-responsive hydrogel surface: tunable wettability and adhesion to oil at the water/solid interface, Soft Matter 6(12) (2010) 2708-2712.
[20] N. Lopez-Larrea, S. Wustoni, M.I. Peñas, J. Uribe, A. Dominguez-Alfaro, A. Gallastegui, S. Inal, D. Mecerreyes, PNIPAM/PEDOT: PSS Hydrogels for Multifunctional Organic Electrochemical Transistors, Advanced Functional Materials (2024) 2403708.
[21] J. Liu, L. Jiang, S. He, J. Zhang, W. Shao, Recent progress in PNIPAM-based multi-responsive actuators: A mini-review, Chemical Engineering Journal 433 (2022) 133496.

[22] C. Barwig, A. Sonn, T. Spratte, A. Mishra, E. Blasco, C. Selhuber-Unkel, S. Pashapour, Two-Photon Direct Laser Writing of pNIPAM Actuators in Microchannels for Dynamic Microfluidics, Advanced Intelligent Systems (2024) 2300829.
[23] R.M. Erb, J.S. Sander, R. Grisch, A.R. Studart, Self-shaping composites with programmable bioinspired microstructures, Nature communications 4(1) (2013) 1712.
[24] J. Zheng, H. Yu, Y. Zhang, J. Wang, H. Guo, H. Luo, X. Wang, Y. Qiu, L. Liu, W.J. Li, 4D Printed Soft Microactuator for Particle Manipulation via Surrounding Medium Variation, Small (2024) 2311951.
[25] Y. Zhang, H. Yu, X. Zhang, J. Zheng, J. Wang, H. Guo, Y. Qiu, X. Wang, L. Liu, W.J. Li, A Novel Multifunctional Material for Constructing 3D Multi-Response Structures Using Programmable Two-Photon Laser Fabrication, Advanced Functional Materials (2024) 2313922.
[26] G. Decroly, A. Chafaï, G. de Timary, G. Gandolfo, A. Delchambre, P. Lambert, A Voxel-Based Approach for the Generation of Advanced Kinematics at the Microscale, Advanced Intelligent Systems 5(7) (2023) 2200394.
[27] T. Spratte, S. Geiger, F. Colombo, A. Mishra, M. Taale, L.Y. Hsu, E. Blasco, C. Selhuber-Unkel, Increasing the efficiency of thermoresponsive actuation at the microscale by direct laser writing of pNIPAM, Advanced Materials Technologies 8(1) (2023) 2200714.
[28] C. Zheng, F. Jin, Y. Zhao, M. Zheng, J. Liu, X. Dong, Z. Xiong, Y. Xia, X. Duan, Light-driven micron-scale 3D hydrogel actuator produced by two-photon polymerization microfabrication, Sensors and Actuators B: Chemical 304 (2020) 127345.
[29] Y. Tao, C. Lu, X. Wang, Z. Xin, X. Cao, Y. Ren, Monolayer heterojunction interactive hydrogels for high-freedom 4D shape reconfiguration by two-photon polymerization, International journal of bioprinting 9(3) (2023).
[30] P.F. van Altena, A. Accardo, Micro 3d printing elastomeric ip-pdms using two-photon polymerisation: A comparative analysis of mechanical and feature resolution properties, Polymers 15(8) (2023) 1816.
[31] L. Mogas-Soldevila, J. Duro-Royo, D. Lizardo, G.G. Hollyer, C.M. Settens, J.M. Cox, J.T. Overvelde, E. DiMasi, K. Bertoldi, J.C. Weaver, Driving macro-scale transformations in three-dimensional-printed biopolymers through controlled induction of molecular anisotropy at the nanoscale, Interface Focus 14(3) (2024) 20230077.
[32] B. Goo, C.-H. Hong, K. Park, 4D printing using anisotropic thermal deformation of 3D-printed thermoplastic parts, Materials & Design 188 (2020) 108485.
[33] S. Xu, S. Wu, R. Zhu, Z. Qiu, Y. Yan, Fully Physically Crosslinked PNIPAM Ionogels with High Mechanical Properties and Temperature-Managed Adhesion Achieved by H2O/Ionic Liquid Binary Solvents, Advanced Functional Materials (2024) 2405965.
[34] M.M. Rana, H. De la Hoz Siegler, Tuning the properties of PNIPAm-based hydrogel scaffolds for cartilage tissue engineering, Polymers 13(18) (2021) 3154.
[35] D. Han, Z. Lu, S.A. Chester, H. Lee, Micro 3D printing of a temperature-responsive hydrogel using projection micro-stereolithography, Scientific reports 8(1) (2018) 1963.
[36] H.F. Brinson, L.C. Brinson, Polymer engineering science and viscoelasticity, Springer 2008.
[37] Y. Hu, Z. Wang, D. Jin, C. Zhang, R. Sun, Z. Li, K. Hu, J. Ni, Z. Cai, D. Pan, Botanical-inspired 4D printing of hydrogel at the microscale, Advanced Functional Materials 30(4) (2020) 1907377.
[38] T. Van Manen, S. Janbaz, A.A. Zadpoor, Programming 2D/3D shape-shifting with hobbyist 3D printers, Materials horizons 4(6) (2017) 1064-1069.
[39] A.A. Zadpoor, Meta-biomaterials, Biomaterials science 8(1) (2020) 18-38.
[40] Y.Y. Lee, R.M. Kim, S.W. Im, M. Balamurugan, K.T. Nam, Plasmonic metamaterials for chiral sensing applications, Nanoscale 12(1) (2020) 58-66.
[41] M.J. Mirzaali, H. Pahlavani, E. Yarali, A. Zadpoor, Non-affinity in multi-material mechanical metamaterials, Scientific reports 10(1) (2020) 11488.
[42] L. Andolfi, A. Battistella, M. Zanetti, M. Lazzarino, L. Pascolo, F. Romano, G. Ricci, Scanning probe microscopies: imaging and biomechanics in reproductive medicine research, International Journal of Molecular Sciences 22(8) (2021) 3823.

7

Discussion and conclusion

7.1 Main findings

In this dissertation, we developed 3D meta-biomaterials with transversely isotropic, cubic, and fully isotropic properties to investigate bone cell response to pore shapes, exploring effects on cell proliferation, morphology, and differentiation. The primary objective was to elucidate the role of Poisson's ratio as a biophysical cue influencing the response of preosteoblast cells. A key component of this research was the isolation of Poisson's ratio from other properties, including elastic modulus, shear modulus, anisotropy level, porosity, pore size, tortuosity, surface-to-volume ratio, connectivity, and permeability.

The initial design of our meta-biomaterials considered Poisson's ratio, effective elastic modulus, porosity, and pore size. By categorizing the meta-biomaterials based on similar porosity and effective elastic modulus, we isolated the effects of Poisson's ratio with a deviation of 24%. The 2PP-additively manufactured meta-biomaterials were subsequently seeded with preosteoblast cells *in vitro*. Cellular assessments revealed that cell growth was significantly higher in meta-biomaterials with a PPR than in auxetic meta-biomaterials. This result was notably contrary to existing literature, which we attribute to the previous studies' failure to isolate Poisson's ratio effectively.

We further refined our design methodology to effectively isolate Poisson's ratio by incorporating additional parameters, including elastic modulus, shear modulus, anisotropy level, porosity, pore size, tortuosity, surface-to-volume ratio, connectivity, and permeability. Our findings demonstrate that isolating Poisson's ratio from these parameters is feasible with a less than 9% deviation.

We subsequently implemented 4D bioprinting at the microscale to fabricate dynamic microarchitectures with shape-morphing capabilities. To achieve this, we developed a photoresist for 2PP based on a thermo-responsive hydrogel, pNIPAM, which functions effectively at physiological temperatures. Below, we summarize the key findings of this dissertation:

- Strut-based meta-biomaterials offer significant potential for mechanobiological studies. Their mechanical, morphometric, and mass transport properties, particularly Poisson's ratio, can be widely tuned, ranging from negative to positive.
- 2PP is currently the most suitable advanced light-assisted additive manufacturing technique for fabricating meta-biomaterials at the microscale.
- The 3D printing of auxetic meta-biomaterials, characterized by support-needed struts, requires more careful handling than those with PPRs.

- Auxetic meta-biomaterials exhibit a lower effective elastic modulus compared to those with PPRs (Figure 2, Chapter 4).
- It is possible to isolate Poisson's ratio from various other parameters, such as elastic modulus, shear modulus, anisotropy level, porosity, pore size, tortuosity, surface-to-volume ratio, connectivity, and permeability, with a deviation of less than 9% (Figure 4, Chapter 4).
- The less mechanically anisotropic the meta-biomaterial is, the less challenging it is to isolate Poisson's ratios.
- Meta-biomaterials generally provide a suitable environment for preosteoblast cells in terms of growth and differentiation, as observed through SEM images and Runx2 and ARS assessments (Figure 3 and 5, Chapter 3).
- Meta-biomaterials with PPRs create a more favorable environment for the growth of preosteoblast cells (Figures 3 and 4, Chapter 3).
- The developed thermoresponsive hydrogel, activating at around 32 °C, was suitable for 4D printing meta-biomaterials with shape-morphing capabilities (Figures 3 and 4, Chapter 6).
- Various 2D and 3D micro-architectures were successfully 4D printed using pNIPAM and 2PP (Figure 4, Chapter 6).

7.2 General discussion

This dissertation discusses a multidisciplinary study that addresses mechanical design, biomaterial development, 3D printing at both micro- and mesoscales, *in vitro* cell culture, cellular assessments, and 4D bioprinting to tackle key challenges in the mechanobiology of biophysical cues. We reflect on the relevance of our findings for the intended applications and discuss emerging challenges.

7.2.1 Mechanical design of meta-biomaterials

Mechanobiological modeling is a promising approach for designing meta-biomaterials with tailored properties, from mechanical properties to mass transport characteristics. The term "*mechanobiological modeling*" reflects its aim to mimic specific trabecular bone properties, such as pore size, porosity, and other structural features. Various methodologies exist for designing meta-biomaterials with specific or isolated properties, including direct FEM, analytical solutions, homogenization-based FEM, topology optimization, and machine learning. Each technique offers unique advantages regarding simulation time, accuracy, data handling, and computational complexity. An extensive number of simulations is often required when isolating a single parameter, such as Poisson's ratio, from others. Thus, employing a model that offers both efficiency and speed is essential.

In this dissertation, we employed two modeling techniques: direct FEM (Chapter 3) and homogenization-based FEM (Chapter 4). Initially, direct FEM was used to

design five distinct meta-biomaterials with varying Poisson's ratios, accounting for pore size, porosity, and effective elastic modulus, Figure (1, Chapter 3) [1]. This approach utilized 3D solid elements and limited the number of simulations due to high computational costs. Additionally, the resulting meta-biomaterials demonstrated significant anisotropy, characterized by more than five independent elasticity parameters, including two elastic moduli, three Poisson's ratios, and multiple shear moduli. This complexity complicated the isolation of Poisson's ratio. Generally, the fewer the independent elastic parameters, the easier it is to isolate specific properties.

Considering the longitudinal properties (*i.e.,* E_l) and porosity, we designed three meta-biomaterials (NPR, PPRs, and Hybrid) with different Poisson's ratios but almost similar porosity and longitudinal elastic modulus with a deviation of less than 24% (Table 1 Chapter 3). However, along the transverse direction, the deviation of the effective elastic modulus was 60%. It was very challenging to lower the deviation of the parameters via direct FEM. Moreover, there was a difficulty in decoupling other independent properties, such as shear modulus, and it was not included in the first version of our meta-biomaterials.

One limitation in the design of the first version of our meta-biomaterials was that it was based on honeycomb unit cells. These meta-biomaterials possess only two PPRs, with the third being negative (*e.g.,* the meta-biomaterial PPRs exhibited $v_{yz} = 0.74$, $v_{xz} = -0.22$ and $v_{xy} = 0.33$, (Table 1 Chapter 3) [1]). This limitation is highlighted more in the cell culture of the meta-biomaterials, as it is essential to mechanically fix the meta-biomaterials in the cell medium (*i.e.,* along x, y, or z). Nevertheless, in our study, we seeded the meta-biomaterials along y, and therefore, the meta-biomaterial manifests only a PPR (*i.e.,* v_{yz}).

We further improved our computational modeling in the next iteration of our meta-biomaterial design (Chapter 4). We could successfully isolate Poisson's ratio while keeping many other parameters, from mechanical to mass transport properties, constant with a deviation of less than 8% (Figure 4, Chapter 4). In the second iteration, we used a homogenization FEM-based technique [2], in which we could perform an extensive number of simulations (*i.e.,* 43,000) within a relatively short time. The homogenization-based FEM method offers a relatively high level of accuracy and very low simulation time. We considered beam-based elements, unity displacement matrix, and periodic boundary conditions to calculate the homogenized constitutive matrix (Figure 1, Chapter 4). The homogenized constitutive matrix can calculate all the mechanical properties, including effective elastic moduli, shear moduli, and Poisson's ratios in different directions.

In the new version of our meta-biomaterials, we introduced geometrically symmetric unit cells with increased isotropy. This means that the meta-biomaterials

exhibited only two independent parameters (*i.e.,* effective elastic modulus and Poisson's ratio for the isotropic meta-biomaterials) or three parameters (*i.e.,* effective elastic modulus, effective shear modulus, and Poisson's ratio, for the cubic meta-biomaterials). Compared to our first design version, we reduced the number of independent parameters from 6 to 3 (in the cubic meta-biomaterials), making isolating the Poisson's ratio much less challenging.

In addition to mechanical properties, we calculated the morphometric properties for all the 43,000 generated meta-biomaterials (Figure 3, Chapter 4). To achieve this, we derived explicit geometrical relationships for the unit cells and explored the design space, focusing on critical values (supplementary material of Chapter 4). The meta-biomaterial designs were generated by varying only three input parameters: strut angle, strut length, and strut diameter. Adjusting these parameters across their entire range allowed us to achieve a broad range of morphometric properties. Interestingly, the distribution of most morphometric properties as a function of Poisson's ratio exhibited a random pattern, suggesting a complex optimization process for isolating Poisson's ratio.

One main challenge in meta-biomaterials design is tuning the ratio of the effective elastic modulus to Poisson's ratio [3]. As we also showed, the auxetic meta-biomaterials with extreme NPRs exhibit much lower effective elastic moduli than meta-biomaterials with PPRs (Figure 2, Chapter 4). This is a critical challenge in the design of meta-biomaterials when a high value of effective elastic modulus is required. A similar challenge exists for the relationship between the anisotropy level and Poisson's ratio [3]. We also showed that auxetic meta-biomaterials exhibit a higher level of anisotropy than meta-biomaterials with a PPR (Figure 2, Chapter 4). One method to tune these relationships is to design hollow struts. In this case, the effective elastic modulus can be tuned without changing the overall strut diameter and outer curvature. However, the main challenge is printing complex 3D meta-biomaterials with hollow struts. For instance, in 2PP, the photoresist will be stuck inside the struts, and removing them afterward will be very challenging. Another method can be changing the 3D printing parameters, effectively tuning the mechanical properties [4, 5].

We also showed that tuning the relationship between Poisson's ratio and strut diameter (or porosity) is challenging. We demonstrated that the sign of Poisson's ratio changes from negative to positive when the strut diameter exceeds 25/300 (Figure 2, Chapter 4). This means that the auxetic meta-biomaterials with extreme NPRs exhibit a very high porosity, which might make it challenging to mimic the porosity range of trabecular bone (50%-90% [6]).

7.2.2 AM of meta-biomaterials

Advanced AM technologies enable the fabrication of geometrically complex 3D meta-biomaterials with tailored microarchitectures. The choice of the AM technique depends on specific application requirements, including biocompatibility, printing time, scale, accuracy, and tunability of mechanical properties. This research employed PolyJet and 2PP to 3D print meta-biomaterials at the macro- and microscales, respectively. Our findings demonstrate that 2PP is highly suitable for mechanobiological studies at the microscale, offering advantages in printability, photoresist biocompatibility, and high-resolution fabrication.

The availability of soluble support materials facilitated the use of PolyJet for large-scale 3D printing of meta-biomaterials, eliminating the need for manual support removal. This approach is essential for printing highly porous and complex meta-biomaterials, as supports are required during printing. However, the supports can be easily dissolved by immersing the specimens in water at room temperature. We utilized PolyJet to fabricate larger-scale meta-biomaterials specifically for mechanical characterization (Figure 5, Chapter 4). However, cell analysis was not conducted on these larger constructs due to their scale.

This dissertation's primary 3D printing technique was 2PP, which enabled us to conduct mechanobiological studies on microscale meta-biomaterials. Selecting the appropriate printing settings is crucial for this technique. These settings include various parameters, such as laser power, scanning speed, printing configuration (*e.g.,* piezo or *Z*-drive), substrate choice (*e.g.,* glass or silicon), and the type of photoresist (*e.g.,* hard or soft). The selection of the latter two factors depends on the specimens' scale. To achieve our goal of printing meta-biomaterials with relatively stiff photoresists at scales of hundreds of microns, we utilized IP-Q as the photoresist and silicon as the substrate. In terms of printing configuration, we found that the piezo configuration was optimal for fabricating auxetic meta-biomaterials, as it allows the stage to remain stationary during each slice. This stability is essential for these meta-biomaterials, consisting of support-needed struts, as it ensures that the photoresist maintains mechanical stability and minimizes micromovement during printing.

We also conducted a systematic study to optimize printing parameters, including scanning speed, laser power, number of contours, and stage acceleration. This investigation was carried out on small blocks and individual unit cells of meta-biomaterials, serving as a representative model for all meta-biomaterials (Chapter 3).

After 3D printing the meta-biomaterials using 2PP, we conducted micromechanical tests to measure their effective elastic modulus and validate our computational modeling (Figure 2, Chapter 3). Ideally, this testing would be performed using a high-precision machine like the FemtoTools device. However, the cross-section of the largest

tip available for the FemtoTools was insufficient to cover the entire surface area of our meta-biomaterials, making its use impractical. Consequently, there is a pressing need to develop a specialized micromechanical testing machine capable of characterizing meta-biomaterials at the meso- and microscales.

7.2.3 Bone cell response

We assessed the biological responses of preosteoblast cells seeded on the initial version of meta-biomaterials. Biological evaluations were conducted to ensure non-cytotoxicity, including live/dead assays and metabolic activity assessments. SEM imaging was performed on preosteoblast-laden meta-biomaterials to examine cell adhesion, morphology, and cell-induced deformation. Additionally, cytoskeletal morphology was analyzed to visualize F-actins, while Runx2 and ARS staining were used to evaluate preosteoblast differentiation. All mechanobiological responses were assessed under static conditions, with the meta-biomaterials fixed on one side of a substrate.

Our preliminary results on pedestals 3D printed from the base material, IP-Q, indicated that this photoresist is non-cytotoxic and supports strong adhesion of preosteoblast cells (supplementary material of Chapter 3). These findings suggest that IP-Q is suitable for 3D printing complex micro-architectures for cell mechanobiological studies. However, IP-Q's inherent auto-fluorescence, particularly in the red spectrum, may interfere with fluorescence imaging. To address this, techniques like photo-bleaching (*i.e.,* exposing structures to UV light) or applying fluorescence-quenching coatings, such as Sudan Black B [7], can help reduce the auto-fluorescent properties of IP-Q.

We observed preosteoblast cells deform the meta-biomaterials differently over time (up to day 17 of cell culture), depending on the structure type (Figure 3, Chapter 3). For example, the meta-biomaterial PPRp exhibited the highest deformation (46.1%, excluding structural shrinkage), resulting in a pyramid-like shape (Figures 3 and 4, Chapter 3). This phenomenon is likely influenced by two factors: the Poisson's ratio and the elastic modulus of the meta-biomaterial. PPRp displayed a very low elastic modulus in the transverse direction compared to the longitudinal one (0.6 MPa *vs.* 15.0 MPa), Table 1, Chapter 3. Poisson's ratio was positive in two directions but negative in another. This anisotropic behavior in elastic modulus and Poisson's ratio contributed to the observed deformation.

The additively manufactured meta-biomaterials also exhibited variations in cell growth and differentiation. Meta-biomaterials with a PPR showed higher metabolic activity and cell-induced deformation than auxetic meta-biomaterials, likely due to differences in pore microarchitecture (Figure 4, Chapter 3). This finding contrasts with previous literature, which we attribute to insufficient isolation of Poisson's ratio in those studies [8,9]. We recommend further biological assessments on a new version of meta-biomaterials where Poisson's ratio is as effectively decoupled as possible.

7.2.4 4D printing of meta-biomaterials

4D printing of meta-biomaterials is gaining significant attention due to its potential to create dynamic structures that respond to external stimuli over time. However, it presents more important challenges than conventional 3D printing of meta-biomaterials. These challenges arise from several factors, including the complexity of mechanical design, the development of suitable biomaterials, and the mechanisms for stimulation and responsiveness. Unlike their 2D counterparts, this complexity is particularly pronounced when working with 3D meta-biomaterials.

Various biomaterials and 4D printing techniques can be employed to fabricate dynamic meta-biomaterials. However, two primary issues persist: the scalability of the produced meta-biomaterials and the biocompatibility of the base materials or stimulation mechanisms used. For example, due to its favorable mechanical properties and biodegradability, PLA has been widely utilized in biomedical applications, such as drug delivery systems. Nonetheless, a significant limitation of PLA is its requirement for high processing temperatures during the fabrication [10, 11] as well as its high glass transition temperature, which can be unsuitable for *in vivo* applications. Such thermal constraints may hinder the integration of PLA-based structures within the human body, raising concerns about biocompatibility and physiological response.

To advance the field of 4D bioprinting, it is crucial to explore alternative materials that can maintain the desired mechanical properties while being compatible with biological systems. We, therefore, developed a thermo-responsive hydrogel, pNIPAM for 2PP 4D printing of microarchitectures, particularly 2D meta-biomaterials (Figure 4, Chapter 6). However, further efforts are required to 4D print 3D meta-biomaterials with higher number of unit cells at the microscale. Moreover, developing innovative stimulation mechanisms, such as light, heat, or magnetic fields, can enhance the functionality of 4D-printed meta-biomaterials. Addressing these challenges will be vital for realizing the full potential of 4D bioprinting in creating adaptive and responsive biomedical solutions.

7.3 Recommendations for future research

This dissertation has substantially contributed to a multidisciplinary project involving mechanical design, micro-scale additive manufacturing, mechanical testing, bone cell culture, cellular analysis, and 4D (bio)printing. However, significant challenges persist in understanding the mechanobiological role of Poisson's ratio in meta-biomaterials and advancing meta-implants toward clinical application. The following section provides recommendations and outlines potential avenues for future research to address these challenges.

1. **Unit cell mechanobiological study:** Investigating meta-biomaterials at the unit cell level provides a focused approach to understanding cellular interactions

within the core structural elements (*i.e.,* bottom-up approach). By seeding only the unit cell, the localized mechanobiological responses can be elucidated, allowing for the isolation of specific cellular behaviors within distinct pore shapes. Additionally, 3D printing unit cells at varying scales may explain the effects of length scale on cellular responses, potentially revealing how length scale affects the influence of Poisson's ratio on cell proliferation, differentiation, and migration. This approach could be instrumental in linking microstructural design to cellular outcomes at the most fundamental level.

2. **Randomized meta-biomaterial design:** Designing meta-biomaterials with random network structures introduces variability that mimics the heterogeneity observed in natural tissues, expanding the design space beyond the constraints of ordered architectures [12]. Random-network designs offer extensive property combinations, enhancing the potential for creating biomaterials with tailored mechanical and functional responses [12]. However, controlling pore size within these random structures poses significant challenges, as uniform pore distribution may not be achievable. This challenge necessitates advancements in fabrication and design methodologies to ensure pore size precision and, thus, maintain desired cellular environments.
3. **Machine learning for computational modeling:** Machine learning algorithms, when trained with extensive datasets from homogenization-based FEM could serve as predictive tools for new meta-biomaterial designs by rapidly identifying behavior patterns linked to specific microarchitectures and Poisson's ratios. Further advancement could involve a reverse engineering approach, where desired mechanical and biological properties are used as target inputs, enabling the algorithm to identify or generate corresponding structural designs [12, 13]. Such an approach could significantly accelerate the design process, offering real-time predictions and optimizations within a vast, complex design space.
4. **Preosteoblast differentiation studies:** The non-significant differentiation observed in preosteoblast cells warrants additional investigation. This further research is essential to validate the efficacy of these biomaterials in supporting bone regeneration, as osteogenic differentiation is a crucial indicator of implant biofunctionality. Incorporating gene-level assessments, such as polymerase chain reaction (PCR), could provide a more comprehensive evaluation of cellular responses, particularly differentiation within meta-biomaterials. Gene expression profiling, especially of markers linked to osteogenesis, mechanotransduction, and stress response, would offer deeper insights into the underlying biological processes. This level of analysis is necessary to understand how structural variations in meta-biomaterials, like changes in Poisson's ratio, influence cellular gene expression and phenotype at a molecular level.

5. **Dynamic loading effects on cellular response:** The mechanobiological response of cells in meta-biomaterials under dynamic loading conditions requires in-depth exploration. Changes in pore structure and Poisson's ratio under load may alter cellular behavior, potentially affecting cell adhesion, signaling, and differentiation pathways. Investigating these dynamic conditions will clarify whether the mechanotransductory effects observed under static conditions are consistent with those under physiologically relevant cyclic loading, providing crucial insights for applications in load-bearing implants.
6. **Multi-cell-type seeding:** Employing various cell types, such as MSCs, could provide insights into the cell-type-specific response to Poisson's ratio variations. As MSCs exhibit distinct mechanosensitivity compared to preosteoblasts, observing their behavior within the meta-biomaterial matrix could clarify if and how different cellular lineages respond uniquely to structural cues. This approach could help ascertain whether the mechanobiological impacts of Poisson's ratio are universally applicable or are cell-specific, thus informing broader applications in tissue engineering.
7. **Precision micromechanical characterization:** For the accurate mechanical characterization of meta-biomaterials fabricated via 2PP, selecting a testing apparatus with high precision in displacement and force measurement is critical. The intricacies of the meta-biomaterial structure, combined with the microscale resolution of 2PP, require a mechanical testing setup with minimal noise and high sensitivity. Ensuring equipment compatibility with the material's properties can lead to more reliable mechanical data, essential for predicting *in vivo* performance.
8. **Advancements in 4D printing:** Exploring the fabrication of dynamic 3D meta-biomaterials using 2PP with 4D printing capabilities could open new avenues for *in vitro* cellular behavior studies. 4D printing allows structures to undergo post-fabrication transformations in response to stimuli, which could introduce adaptive features to the biomaterials, potentially enhancing cellular responses. By evaluating how cells interact with these dynamically changing environments, researchers can assess the potential for creating implants that adapt in real-time to biological conditions, further advancing tissue regeneration applications.

Overall, the research presented in this dissertation highlights the significant potential of meta-biomaterials to modulate bone cell responses. These findings encourage further investigations into the *in vivo* and *in vitro* performance of meta-implants with newly designed unit cells, mainly focusing on their longevity, mechanical stability, and cellular interactions.

Bibliography

[1] E. Yarali, M. Klimopoulou, K. David, P.E. Boukany, U. Staufer, L.E. Fratila-Apachitei, A.A. Zadpoor, A. Accardo, M.J. Mirzaali, Bone cell response to additively manufactured 3D micro-architectures with controlled Poisson's ratio: auxetic vs. non-auxetic meta-biomaterials, Acta Biomaterialia 177 (2024) 228-242.
[2] G. Dong, Y. Tang, Y.F. Zhao, A 149 line homogenization code for three-dimensional cellular materials written in matlab, Journal of Engineering Materials and Technology 141(1) (2019) 011005.
[3] T. Meier, R. Li, S. Mavrikos, B. Blankenship, Z. Vangelatos, M.E. Yildizdag, C.P. Grigoropoulos, Obtaining auxetic and isotropic metamaterials in counterintuitive design spaces: an automated optimization approach and experimental characterization, npj Computational Materials 10(1) (2024) 3.
[4] P.F. van Altena, A. Accardo, Micro 3d printing elastomeric ip-pdms using two-photon polymerisation: A comparative analysis of mechanical and feature resolution properties, Polymers 15(8) (2023) 1816.
[5] M. Belqat, X. Wu, L.P.C. Gomez, J.-P. Malval, S. Dominici, B. Leuschel, A. Spangenberg, K. Mougin, Tuning nanomechanical properties of microstructures made by 3D direct laser writing, Additive Manufacturing 47 (2021) 102232.
[6] V. Karageorgiou, D. Kaplan, Porosity of 3D biomaterial scaffolds and osteogenesis, Biomaterials 26(27) (2005) 5474-5491.
[7] Sharaf, A. M. S. E., et al. "Suppression of auto-fluorescence from high-resolution 3D polymeric architectures fabricated via two-photon polymerization for cell biology applications." Micro and Nano Engineering 19 (2023): 100188.
[8] Tang, Aimin, et al. "Nanocellulose/PEGDA aerogels with tunable poisson's ratio fabricated by stereolithography for mouse bone marrow mesenchymal stem cell culture." Nanomaterials 11.3 (2021): 603.
[9] Yan, Yuanwei, et al. "Pluripotent stem cell expansion and neural differentiation in 3-D scaffolds of tunable Poisson's ratio." Acta biomaterialia 49 (2017): 192-203.
[10] V. Moosabeiki, E. Yarali, A. Ghalayaniesfahani, S.J. Callens, T. van Manen, A. Accardo, S. Ghodrat, J. Bico, M. Habibi, M.J. Mirzaali, Curvature tuning through defect-based 4D printing, Communications Materials 5(1) (2024) 10.
[11] M. Mehrpouya, H. Vahabi, S. Janbaz, A. Darafsheh, T.R. Mazur, S. Ramakrishna, 4D printing of shape memory polylactic acid (PLA), Polymer 230 (2021) 124080.
[12] H. Pahlavani, K. Tsifoutis-Kazolis, M.C. Saldivar, P. Mody, J. Zhou, M.J. Mirzaali, A.A. Zadpoor, Deep Learning for Size-Agnostic Inverse Design of Random-Network 3D Printed Mechanical Metamaterials, Advanced Materials 36(6) (2024) 2303481.
[13] M. Abu-Mualla, J. Huang, Inverse design of 3D cellular materials with physics-guided machine learning, Materials & Design 232 (2023) 112103.

Acknowledgements

As I am writing this part of my thesis, while keep getting numerous rejections and uninspiring offers for my next job! it feels like a bit of guilty pleasure! Anyhow, as I reach the end of my PhD journey (the defense not the end of contract!), it feels right to take a moment to reflect on this experience that has been more than just research and technical challenges. First, I would like to answer this question, "*why did I do a PhD?*" the answer is simple, because I was a nerd and a little bit stupid (do not get me wrong, I am joking!)! I got very interested into healthcare and biomedical challenges and therefore, as I like doing research, I decided to pursue a PhD in this field. With this, I could benefit from my engineering background while also expanding my knowledge in bioengineering. Beyond this, as my soft skills were horrible! Like in social interaction, communication, presentation, and so on. I find PhD a very suitable and multi-cultural environment to improve my soft skills. You tell me now if seeing any improvements?! However, these milestones would not have been ever possible without the invaluable support of a remarkable group of people. It is to them that I dedicate this section, with deep gratitude and appreciation.

I first became interested in the topic of meta-biomaterials after reading **Amir**'s single-author articles in 2018. From then on, I followed Amir's group and their exciting works on meta-biomaterials, additive manufacturing and bone tissue engineering. Amire, our paths crossed in 2019 when I had the opportunity to attend a lecture you gave on meta-biomaterials. This eventually led to the reality of joining your research team a year later, where I began my PhD trajectory. **Amir**, your contribution to my PhD project has been significant and undeniable. Unfortunately, in the first two years of my PhD, it did not happen to meet often and discuss my project. However, over the last two years, I noticed how incredibly useful it is if I have more meetings with you. Over these two years of interaction with you about my research and life, I noticed your intelligence, meticulousness, open-mindedness and, of course, your kind-hearted nature. I also remember our late-working time conversations about my project when almost no one else was around. These moments were not just about research; we had quite a lot of moments discussing other aspects of life, such as politics. By the way, I still do not get how it is possible that you would appear behind me all of a sudden when I was casually chatting with my friends even outside of the faculty!! This happened at least three times. I felt very embarrassed because of this until I shared this with you! Also, I can barely remember a time when you weren't smiling, and that positivity was always a source of motivation for me! Believe me!

I am gonna talk a lot about my supervisors as I had many! Five! My first interaction with you, **Mohammad**, was in 2019 when you contacted me on Skype for an interview

after Amir forwarded my CV to you. Over the next year, before I officially started my PhD, we stayed in touch, and our collaboration resulted in three manuscripts! (cannot believe it now tho!), which one getting very popular😊. I would like to express my gratitude for all your support and feedback throughout my PhD journey, especially during the many ups and downs. I know I took a lot of your energy at times, especially when misunderstandings would happen (maybe because of my horrible soft skills in the beginning! who knows!). Plus, I was your first official PhD candidate, with your name at the end of the author list in our manuscripts! I have learned so much from you, from drafting and revising manuscripts to performing experiments, and even receiving your friendly advice about my future career and academic life. Your guidance has been invaluable and I hope to stay in touch with you.

I am very excited to talk about my other co-promotor, **Angelo**! Over times, particularly in the last two years of my PhD, our relationship felt more like a friendship than a supervisor-student dynamic, and your motivation and appreciation for my research made a significant impact. Your office door was always open, and I could knock anytime I faced challenges, whether related to my PhD or personal feelings. I would like to deeply appreciate your efforts in arranging a research visit to Canada to work on nanocellulose crystals with Prof. Jose. Although it did not happen because of issues with extending my PhD contract for three more months (Covid was never useful for me!). **Angelo**, Although I learned a lot about 2PP with you, your "3P" technique (*i.e.,* patience, passion, and perseverance) was also fantastic. It could guide me through tough times of my PhD trajectory. I will always cherish the memories of the two conferences we attended together, BioCube and MNE, and the fantastic fun we had, as well as our coffee meetings at Coffee Star and the dinners and drinks that added so much joy to my PhD journey. You were an exceptional teacher to me who I could grow with and always feel appreciated and of course I learned a lot from you.

In engineering projects, having a physicist to delve into the complicated details of phenomena is often priceless, and I was incredibly fortunate to have **Urs** involved in my project as a co-promotor. Although it was not officially possible from the TU Delft graduate school to register you as a promotor, your contributions were very valuable. I always looked forward to our monthly meetings, where we would dive deeply into the details of the project, engaging in countless brainstorming sessions that shaped my PhD journey. Beyond research, we also had quite a lot of chats about academic life and its challenges. **Urs**, you are a true symbol of kindness, intelligence, meticulousness, and a generous heart, and I am deeply grateful for your guidance and emotional support throughout these four years.

Lidy, I am deeply grateful to have such a supervisor, guiding me on the biological aspects of my PhD trajectory. Your patience and positivity created a safe environment for me to continually learn the biological aspects. Our regular CCB lab meetings were

incredibly insightful, allowing me to explore and satisfy my curiosity in this field. I only wish there had been more time and opportunities to work further on the biology part of my thesis so that I could have learned even more from you. Your kindness, constant smile, and caring meant great to me, and I will never forget it.

One spicy part of PhD at TU Delft is how to get into technical knowledge! Especially those that I had zero knowledge in. I, therefore, would like to express my gratitude to those who offered invaluable lab supports during my PhD journey. **Ahmed**, no idea how to thank you. The term "Nanoscribe" always remind me of you. All those time that you dedicate to others and me, particularly at off-working hours when the 3D printer would not function properly. I also greatly appreciated your advice on PhD life and its challenges. On the biological side, **Maria**, I am incredibly grateful for all you taught me about cell culture and cellular assessments. I remember our first appointment for cell training did go well as I had delay! But then fortunately we built a wonderful friendship beyond work. **Sander**, a legend of BME! (next to who? Gabi), the Gaz and Tahchin lover. In my book, you are a wonderful lab manager and person. I wish I had worked on metals as well, so I could have had the chance to collaborate with you more as you're the master of metals! BTW, I never forget our lectures on life challenges like fashion-style relationship! Plus, I would like to thank PME lab technicians, **Alex** (Chemical and NanoScribe labs), **Rob** (everything!), **Patrick** (optical lab and the dynamic mechanical test machine), **Gideon** (the laser cutter), and **Bradley** (our coffee chats 😊) for their supports.

Now it's time to dedicate some space to acknowledge my friends, and colleagues, those who shared in my nags, happiness, achievements, complaints, fun moments, and everything in between during my PhD journey. **Ines**, we met in 2022 when you were a (little!) master's student here, and we had countless coffee breaks together, especially in the kitchen on the third floor as they were also free 😊. You were one of those friends I could always turn to, sharing both the good and the not-so-good moments of my PhD life and your life. I'll never forget all those times we spent together with our friends, and I'm so happy to have built such a wonderful friendship with you. BTW, I am still looking forward to the day when you will finally pronounce "Eda" correctly instead of "Ella"! **Nastran**, I truly appreciate our friendship and all the great moments we had together; whether at the BioCube and MNE conferences, on road trips, during campus lunches, or at parties. You were always there for me, a great friend I could share the ups and downs of my PhD life with.

Let's talk about the legend of BME, the strong rider, **Gabrielle**! I was so lucky to get to know you and will never forget all the laughs, fun, and, of course, serious moments we shared. One of the coolest things was how close our birthdays are (mine on November 13th and yours on November 11th), which gave us the perfect excuse to combine our birthday parties! You also introduced the master cooking classes, an awesome

and fun way to explore different cuisines at X. And who could forget our hilarious moments with **Sander**, chatting about life's topics like the *trust-mustache length relationship* or *fashion-style relationship*? **Solmaz**, **Mehrab**, **Sayeh**, **Hoda** and **Marjan**, I'm truly grateful to have you as (Persian) friends here. We celebrated so many moments together and shared our life stories, creating memories that I will always cherish. Our parties and Persian cooking gatherings were always filled with laughter and joy. Together, we shared the challenges of migration and how to adapt to a new environment, which made the journey so much more bearable and meaningful.

There were some moments where I would get very excited when saw some people like? Yes, **George** (Geooooooorgeeeee!), the guy who I met for the first time online in this PhD defense. I remember I asked two challenging questions as our project was very similar. I am still ok if you hated me by then! But once I saw you in person, we clicked greatly and built a strong friendship. We always have endless things to talk about, and we laugh so much together. You're just a sweetheart of a person. You introduced me to the Greek culture as well! As I was lucky and was into Greek culture, a year after you joined the team, another funny Greekkie joined us, **Stavros**! Even though I was almost in the last year of my PhD, we had so much fun together. Let's keep the good times rolling! **Mohammad** (Mahmuuuudi), meeting you in the last year of my PhD was a real highlight. Though we didn't expect to bond so strongly at the start, we have become such good friends now. BTW, I love your unique interpretations of everything!:) You were always the one I would call whenever I needed a chat or a drink. **Federica** (Aspeta), **Vishrut** (Mushroom), **Morteza** (the philosophical AI boy), and **Riccardo** (the curly-haired classic guy), I met all of you toward the end of my PhD, but what a blast we have had! From the parties and id pub drinks to psor pub hangouts and countless coffee moments, it's been so much fun. Let's stay in touch and keep enjoying life together!

Ruben, I have known you almost from the very beginning, and you have been such a smart and sweet friend. I will always remember our zoo visits, especially to Apenheul, your trick on how to get monkeys on our shoulder! Let's definitely keep in touch! **Pierre** (the master of French! and metamaterials!), **Qais** (the master of negotiations, Wikipedia source, ChatGPT source, and the bad luck for public transports), and **Serena** (the master of colors, although I still do not know the differences between winter and summer colors!). We have shared so many great moments, from coffee breaks and lunch meetings to parties and conferences. You've all been such good friends to me. **Francesco** (Super funny and open-minded), **Mohammad Javad (MJ)**, **Saleh**, **Ali**, **Hava**, **Hande**, **Santiago**, **Pieter**, **Jurga**, **Celine**, **Vallery**, **Azza**, **Novinda**, **Vijay**, **Zhilin**, **Zohre**, **Sahar**, **Paulina**, **Himanshu**, **Giulio**, **Filippo**, **Martin** (with that lovely French accent! And now an assistant professor) and **Giovanni**, you've all been a part of my PhD journey. From lunch meetings and coffee breaks to dinner outings, we've created so many great memories. I would like also to

mention some PME professors, **Paula** (thanks for chairing the MNE weekly meetings!), **Davood**, **Farbod**, **Marcel**, **Murali**, **Ivan**, and **Andres** plus **Marlie** (secretary), where we had some chats through these four years and indeed I found your advice very useful.

As part of my PhD life was involved with supervising EXCEPTIONAL master students, lets share some moments with them here. **Ava**, you were my first master student and also the one who showed me around the campus in the beginning. While our project had its ups and downs, you did an incredible job, and I'm so glad we built a friendship along the way with **Behrooz** as well! BTW, I'm happy that both of you are on your way to becoming doctors soon! **Michelle**, you joined us for a short but impactful time (around six months) to work on metamaterials. You did great work, and we had so much fun outside the campus too, especially with **Antonio** (our football superfan!). **Thomas**, even though your project was not directly aligned with my PhD work, I really enjoyed collaborating with you and had a lot of fun along the way! **Ayman**, you were such an impressive person in my eyes; both brilliant and great to chat with. I always see you as a true engineer, and I'm happy we've stayed in touch and still meet sometimes. **Kai**, my last master's student, I really admired your persistence and patience, especially when we had to change your project midway. You handled it so well, and I'm glad we shared some fun moments together too.

Let's get back to the BME department! **Vahid**, you were one of the first people I met on campus when I started my PhD. We shared office for almost four years and collaborated on two manuscripts. Your experience and advice were invaluable. Thank you for always being there. **Lorenzo**, I truly enjoyed our chats and hope we stay in touch (though I'm still a little upset you missed my 30th and 31st birthday parties!). We also had so much fun in Switzerland with **Churu** and **Yerong**. **Monika**, **Ludovica**, **Jinlai** (my funny boy), and **Katerina**, I shared so many great moments with you. I loved our chats and exchanging life stories, and I learned so much from each of you. Thank you for being part of this journey!

Here, I'd like to mention other amazing BME colleagues who were part of my PhD journey, including **Sara** (A true symbol of niceness), **Kasra** (the master of badminton), **Teddy** (our funny doctor, especially your jokes when you drink a lot!), **Dirk** (**Pieter**'s BFF, our trip to Switzerland together), **Sara** and **Mattia** (the fashionable Italian couple), **Giacomo** (the bouldering expert! thank you for introducing me to such an interesting sport!), **Shima** (the Shirazi and genius colleague!), **Lennart** (the formal but friendly colleague), **Judith** (the fast-speaking Spanish creature!), **Edwin** (interesting human!), **Mauricio** (another interesting human!), **Helda** (the always-smiley former officemate), **Shahram** (a true scientist), **Khashayar** (thank you for helping me with cell culture tasks), **Mahya** (kind!), **Pedro** (I appreciate the ccb lab tour and your collaboration on my massive review article), **Niko** ("sssss, behave Ebi", sorry for being

annoying to you 😊), **Keyu** (the quiet but sweetest person), **Jinsong** (the smart magician), **Jelle** (the bioprinto-bouldering guy), **Hassan** (your beautiful laughs), **Christoph** (the symbol of a professional PhD and indeed the god of bouldering), **Antonio** (superfan of fancy and classic? cars), **Thomas** (the burger story when we were at the BME conference), **Marije** (the permanent member of the ccb lab!), **Daniel** (the sweet German friend), **Rogier** (very friendly and sweet! But tallllll! Always feel insecure when I stand next to you!), **Suzanne** (the master of sport, especially armwrestling!!), **Federica** (very kind and friendly!), **Sabrina** (quiet and always-smiley person), **Bea** (kind and always smiley), **Silvia** (the wood printing girl), **Abbi** (the hard-working guy), **Jose** (the new but fun member), **Gavin** (our lucky cocktail suggestions!), **Jonathan** (great guy, especially when you have mustache!), **Zahra**, **Saeed**, **Robin**, **Kardelen**, **Rick**, **Giulia**, **Karien**, **Karin**, **Anneke**, **Bob**, **Hamed**, **Suzanne**, **Luca**, **Jiahui**, **Alessia**, **Jenna**, **Matthew**, **Benjamin**, **Marina**, and **Kate**. And then there's **Pier**, someone I initially thought was very quiet. Although we didn't get along at first, you proved me wrong and showed me how kind and respectful you are. By the way, I'll never forget how you helped me get home when I overdrank for the first time in my life.

There was always that one office completely opposite to ours, so quiet and super focused. Which one? **Jette**'s office, of course! **Jette**, **Vera** (echt ee?? 😊), **Esther**, **Merle**, **Kirsten**, **Mostafa**, **Indra** (Nynke), and **Nynke (**Nyndra**)**. I was always a bit scared to knock on your door! I would feel so guilty every time I saw you all working so hard. But honestly, I loved chatting with you whenever I got the chance. A big shoutout to everyone else in BME too, especially on the third floor, **Roderick** (our young and super kind assistant professor), **Julian** (full of passion and hard work), **Nazli** (so dedicated), **Jie** (A symbol of NICE professor), **Paul** (our afternoon "*Hoooiii*" moments with your apple), **Ajay**, **Matthias**, **Behrooz**, **Gerwin**, **Angelique**, **Amanda**, and **Marjolijn**. You all made it such a great place to be!

Menno (a super fun friend and future dad!), **Dimitris** (the sweetest friend, seriously, I still can't get over how quickly you fall asleep with your military sleeping technique!), **Justin** (the mulberry enthusiast) and **Kartik**. We got to know each other thanks to Ines, and I have had so much fun with all of you! **Soheil** (the friendliest person on the planet), **Alireza** (serious but a great friend), **Hidde**, and **Alberto** we got to know each other at the end of my PhD but I had great time chatting with you guys. **Kiril**, meeting you at BioCube 2023 was amazing; we clicked instantly and had an incredible week together. Seeing you again at MNE 2024 made me so happy. **Verindi**, **Elena**, and **Alireza**, I'm so glad we connected at BioCube 2023 and have stayed in touch since. **Matin**, my bachelor buddy, you and your fiancé **Casandra** are such patient and kind friends. I always enjoy our gatherings, especially when we share our bachelor- life stories!

Morteza and **Milad**, my high school friends, I can't even put into words how much fun we have had together. The endless laughs, jokes, smiles, and even the sad moments we have shared will always be unforgettable. Another chapter of my life was intertwined with amazing friends I met during my Master's study: **Mahdi** (aka Shadmehr Aghili, smart and incredibly friendly), **Reza** (our "*professor*"), **Armin** (Shire Kamyaran), and **Saman** (so hardworking, I never forget your imaginary dogs, Tami and Teddy!).

I would also like to express my gratitude to those who initially motivated and supported me during my high school years. **Farhang** (**Abdolmalaki**), our school manager, you were the first person to instill confidence in me. I still remember when you encouraged me to register for the National Physics Olympiad 2011. At the time, I immediately rejected the idea because I had zero confidence. But then you drove me home one day and spoke to me like a true friend, saying, "*Believe in yourself. I believe in you, and you deserve to go for this contest.*" That conversation was a turning point in my life, and I'll never forget it. **Morteza** (**Abdolmaleki**), my mathematics teacher, you were another key figure in helping me realize my potential. I can still hear the respectful and passionate way you would call me (آقای یارعلی), and it always gave me a sense of pride. Lastly, **Mr. Shawkati**, you were my favorite physics teacher. I truly admired your teaching style and the seriousness you brought to every lesson. Your dedication to preparing me for the National Physics Olympiad 2011 was invaluable, and I'll always be thankful for your guidance.

In the end, I would like to conclude my acknowledgment by dedicating the final, and most important, section to my family. I plan to write it in Persian and Kurdish so that my mom and dad can read it.

داده و آضه (مامان و بابا) نمیدونم چجوری و با چه زبونی از اون همه سختی هایی که کشیدین واسه ما بچه ها، ازتون تشکر کنم. دوران سختی داشتیم ولی خدارو شکر داره کم کم بهتر میشه. **آضه**، یاد اون دوران به خیر که وقتی بچه بودیم با بعید، همیشه کنارت بودیم روی تراکتور و مواظب بودی که خوابمون نبره. اون دورانی که مجبور بودیم همیشه تا دیروقت کار کنیم باهم. خیلی سخت بود اما گذشت! وقتی هم که رفتیم دبیرستان و دانشگاه، تابستونا (سه ماه) سخت کار کشاورزی می کردیم باهم. امیدوارم که بتونم یک مقدار کوچکی از اون همه سختی هایی که به خاطر ما کشیدی رو جبران کنم. **داده**، من تو رو باهوش ترین آدمی که تا حالا میشناسم میبینم، مخصوصا هوش اجتماعی ات. به خاطر ما مجبور بودی چند سالی از آغم دور زندگی کنی و شبا تا دیروقت به خاطر ما بیدار باشی. یادم نمیره که موقع دبیرستان، مخصوصا کنکور، پا به پای ما تو هم کتاب میخوندی، کتاب شیعر مخصوصا، که ما هم امید بیشتری داشته باشیم. امیدوارم بتونم ذره ای کوچک از سختی هایی که کشیدی رو جبران کنم. عاشق خنده هاتم 😊 **سادان**، برادر بزرگترم، تو اگر نبودی، من قطعا اینجا نمی بودم. خیلی کمک کردی. سختی زیاد کشیدیم باهمدیگه. هیچ وقت ناامید نمیشدی و همیشه به ما امید دادی. دوران خیلی خوبی باهم داشتیم. امیدوارم هرچه

زودتر خودت و پریسا رو ببینم . پروانه، خواهرم، چهره همیشه خندان این روزاااای من، هرچند بچه بودیم بعضی وقتا دعوا می کردیم! دختری قوی تر از تو ندیدم من! بت افتخار میکنم .عاشقتم . اما سعید، برادر کوچکترم، هرچند از لحاظ سنی کوچکتر از منی اما فک کنم از بقیه لحاظ بزرگتر از من باشی! واقعا بت افتخار میکنم که هم میتونی درس های پزشکی تو جلو ببری هم به عنوان یک شنوایی شناس در کنارش کار کنی. واقعا تلاش شبانه روزیتو و مخصوصا واسه خونواده فراموش نخواهم کرد. خیلی باااااهم سختی کشیدیم اما امیدوارم کم کم زمان واسه تغییر باشه. بهترین دوست من، یک دقیقه حرف زدن با تو کل غربت مهاجرت رو میشوره میبره! خیلی دوست دارم.

List of publications

Journals

- **Yarali, E.**, Mirzaali, M. J., Ghalayaniesfahani, A., Accardo, A., Diaz-Payno, P. J., & Zadpoor, A. A. (2024). 4D printing for Biomedical Applications. *Advanced Materials*, 2402301.
- **Yarali, E.**, Klimopoulou, M., David, K., Boukany, P. E., Staufer, U., Fratila-Apachitei, L. E., ... & Mirzaali, M. J. (2024). Bone cell response to additively manufactured 3D micro-architectures with controlled Poisson's ratio: Auxetic vs. non-auxetic meta-biomaterials. *Acta Biomaterialia*, *177*, 228-242.
- Moosabeiki, V., **Yarali, E.**, Ghalayaniesfahani, A., Callens, S. J., van Manen, T., Accardo, A., ... & Zadpoor, A. A. (2024). Curvature tuning through defect-based 4D printing. *Communications Materials*, 5(1), 10.
- **Yarali, E.**, Zadpoor, A. A., Staufer, U., Accardo, A., & Mirzaali, M. J. (2023). Auxeticity as a mechanobiological tool to create meta-biomaterials. *ACS Applied Bio Materials*, 6(7), 2562-2575.
- Mirzaali, M. J., Pahlavani, H., **Yarali, E**., & Zadpoor, A. A. (2020). Non-affinity in multi-material mechanical metamaterials. *Scientific reports*, 10(1), 11488.
- **Yarali, E.**, Mubeen A., Cussen K., Lennart V., Vahid M., Zadpoor, A., Accardo, A., & Mirzaali, M. J. (2024). 4D printing of poly(N-isopropylacrylamide)-based hydrogel microarchitectures: two-photon polymerization for reversible shape morphing. *Communications Materials*, under review.
- **Yarali, E.**, Urs S., Fratila-Apachitei L. E., Mahdavi R., Zadpoor, A., Accardo, A., & Mirzaali, M. J. (2024). Decoupling mechanical and morphometric properties in meta-biomaterials. *Nature Communications*, revised.

Conferences and summer schools

- **Yarali, E.**, Summer school course on “bone cell and tissue mechanics”, 2021, Italy
- **Yarali, E.**, *et al*, 31st the Netherlands Society for Biomaterials and Tissue Engineering (NBTE) annual meeting 2022, The Netherlands, oral presentation
- **Yarali, E.**, *et al*, 33rd annual conference of European Society for Biomaterials (ESB), 2023, Switzerland, oral and poster presentations
- **Yarali, E.**, 2nd BIOCUBE winter school, 2023, Italy, oral presentation

- **Yarali, E.**, *et al*, 26th Engineering Mechanics symposium, 2023, The Netherlands, oral and poster presentations
- **Yarali, E.**, *et al*, 50th Micro- and Nano Engineering (MNE) conference, 2024, France, oral presentation

Curriculum Vitae

Ebrahim Yarali, born on November 13, 1993, in Iran, pursued his passion for engineering by earning a BSc in Mechanical Engineering (Manufacturing and Production) from Amirkabir University of Technology (Tehran Polytechnic) between 2012 and 2016, where he was a top-ranked student in his field. He worked on developing magnetorheological suspension systems for automotive industry in collaboration with Indamin Saipa for his bachelor thesis and documented it as a patent. He completed his MSc in Mechanical Engineering (Applied Mechanics) at the University of Tehran in 2019, focusing on the development of the constitutive models for shape memory polymers and their 4D printing at the Smart Materials and Structures Lab. Motivated to address healthcare challenges, he began a PhD in Biomechanical Engineering & Precision and Microsystems Engineering at Delft University of Technology (TU Delft) in 2020. His PhD research focused on the mechanobiology of meta-biomaterials, their rational design, advanced micro-additive manufacturing, and biological assessments for bone tissue engineering. He is also interested in clinical applications of 4D bioprinting of stimuli-responsive biomaterials, such as temperature- and magneto-responsive hydrogels, for drug delivery systems and tissue engineering at the microscale.


TUDelft